

Microstructural evolution of Mn-based maraging steels and their influences on mechanical properties

By

Feng Qian



Thesis submitted for the degree of Doctor of Philosophy

Department of Materials Science & Engineering

The University of Sheffield

March 2015

Abstract

A set of Mn-based maraging TRIP steels was designed by Max-Planck-Institut für Eisenforschung GmbH (MPIE) for light weight and safe automotive applications. According to their research, these Mn-based maraging TRIP steels exhibited a simultaneous increase in both strength and ductility upon aging. They attributed this surprising effect to the combination of precipitation strengthening mechanism and TRIP effect of reverted/retained austenite.

This thesis carried out a further study on this type of steels with minor modification of chemical composition (7-12 wt.% Mn, with additional ~ 1 wt.% Al). The unknown precipitates were characterized as L2₁-ordered Ni₂TiAl intermetallic phase for the first time. This type of precipitates is not only coherent but also coplanar with the martensite matrix. Their special orientation relationship together with the small lattice misfit (1.24%) led to the precipitates remaining coherent with the martensite matrix even after a long-term aging for 10080 min. Analyses on precipitate size revealed that the coarsening rate constants follows the diffusion-controlled coarsening kinetics form $\bar{r}^3 \sim Kt$ predicted by LSW theory, but the experimental precipitate size distributions (PSDs) is much broader than the theoretical PSD function. In addition, a core/shell structure was observed within the precipitates, but the exact structure of this structure is still not clear.

The formation of reverted austenite nanolayers initiated at the onset of aging by a diffusionless shear mechanism since the critical Mn concentration for austenite reversion at the interface is very low. The accumulated Mn segregation at grain boundaries in the following aging led to the austenite nanolayers that grew to lath-like reverted austenite, which means the lateral growth of austenite was supported by the diffusion of Mn. Due to the low diffusion rate of Mn and the thermodynamic resistance to coalescence, the growth rate of lath-like reverted austenite is slow and thus the austenite maintained in the range 70-200 nm for a long time. The segregation of Ti and Mo on grain boundaries in the initial aging stage resulted in the Mn concentration of austenite nanolayers being far from that indicated by the equilibrium Fe-Mn phase diagram. The segregation of Ti and Mo gradually vanished

Abstract

with the enrichment of Mn during the succeeding aging process. The TEM-EDS analyses revealed the Mn concentration of lath-like austenite was at the level of ~24 at.% which is higher than that of retained austenite (8-12 at.%) reported in conventional Mn-based TRIP or Q&P steels. Nanoindentation testing revealed that the high stability of reverted austenite in Mn-based maraging steels was mainly attributed to the high Mn concentration of austenite. The nano-size of reverted austenite was also considered to be responsible for the high stability.

Severe embrittlement occurred in samples aged at lower temperatures or for short times. Increasing aging temperatures and duration can significantly improve the embrittlement phenomena. An ultimate tensile strength (UTS) of 1120 MPa with total elongation (TE) of 18.4% was obtained in the 12% Mn alloy by aging at 500 °C for 5760 min. It was demonstrated that the dense precipitates contributed to the increase in yield strength whereas the work hardening of reverted austenite contributed to the enhanced strength and ductility after yielding. The TRIP effect of reverted austenite reported by Raabe et al. does not occur to any significant amount owing to the high stability of reverted austenite in Mn-based maraging steels.

Acknowledgements

First of all, I would like to express my sincere gratitude to Professor W. Mark Rainforth, for his support and supervision throughout my PhD study. Although he is very busy with teaching, research and administration jobs, Professor Mark Rainforth is always inspiring to me. He is really good at encouraging students and has given me lots of freedom to realize my idea. Moreover, he is always enthusiastic to share the latest news and information in the materials world which largely broaden my vision. I also admire his remarkable knowledge of electron microscopy and his tutorial on electron microscopy will definitely benefit my future career.

I greatly acknowledge University of Sheffield, Department for Business Innovation & Skills (BIS) and China Scholarship Council (CSC) for giving me the opportunity to study in UK and their generous financial support. Another important contributor is Tata Steel who provided the materials for this project. I am very grateful to Professor Andy Howe for the delight and helpful conversations with him and his efforts on the project coordination with industry as well. Dr Eric Palmiere and Dr Martin Jackson are also appreciated for their suggestions given in the viva for annual report.

I must express my sincere appreciation to Dr Peter Kogul, Dr Peng Zeng, Dr Le Ma and Dr Cheryl Shaw for the training and technical help at Sorby Centre for Electron Microscopy and Microanalysis. They are always here when I meet problems. Thank you all. Special thanks go to Dr Joanne Sharp for her helps on precipitation characterization using high-end TEM facilities. I am also thankful for Miss Dawn Bussey's instruction on nanoindentation tests. Many thanks are given to Dr Amit Rara, Dr Andy Williams and Mrs Vanessa Dalton who helped me a lot on daily research work.

I am very lucky to meet and work with a number of kind technical staff in the Department of Materials Science and Engineering. Thanks a lot to Mr Dean Haylock, Mr Kyle Arnold, Dr Lisa Hollands, Mr Michael Bell, Mr Richard Kangley, Mr Ian Watts and Mr Stuart Bater for their day-to-day helps on various experimental works which made this thesis possible.

Acknowledgements

I would like to thank my dear friends who helped me a lot on my research work during these years. Particular thanks are given to Dr Yonghao Gao for those heavy work and IT support. Dr Lin Sun, who helped me a lot with the MatCalc software, is also appreciated. The experience of discussing thermodynamics and TEM with Mr Xiaoming Yuan and Mr Dongdong Xiao across jet lag will be one of the most valuable treasures in my life. I am also grateful for the joy and happiness brought by all friends and colleagues in the department which made this journey enjoyable.

Words are not enough to convey my deepest gratitude to my family for their unconditional love and support. My open-minded parents give me their greatest patience and understanding through all these years. They give me enough freedom to do what I like and to pursue what I want. I am so proud to have them in my life.

Table of Contents

Abstract	i
Acknowledgements	iii
Table of Contents	v
List of Figures	x
List of Tables	xviii
Chapter 1 Introduction	1
Chapter 2 Literature review	6
2.1 The development of Mn TRIP steels.....	6
2.2 The development of maraging steels.....	7
2.2.1 The role of alloying elements in maraging steels.....	9
2.2.2 Behaviour of intermetallic precipitates in conventional maraging steels..	10
2.2.3 Precipitation behaviour in newly-developed maraging steels strengthened by other intermetallic phases.....	12
2.2.4 The Mn embrittlement in Fe-Ni-Mn and Fe-Mn alloys.....	21
2.3 Evolution of precipitates.....	24
2.3.1 Critical size in precipitation.....	24
2.3.2 Growth and Coarsening of precipitates.....	25
2.3.3 Precipitate coarsening theory.....	27
2.3.4 The effect of precipitate size on precipitation strengthening.....	29
2.4 Austenite reversion in maraging steels.....	31
2.4.1 Influence of reverted austenite on mechanical properties.....	32
2.4.2 The formation mechanism of reverted austenite.....	41
2.5 Grain refinement in maraging steels.....	44
2.5.1 Conventional methods to refine grains.....	44

Table of Contents

2.5.2 Effective grain size in lath martensitic steels.....	45
2.5.3 Methods of grain refinement in lath martensitic steel	46
Chapter 3 Materials and Experimental Methods	48
3.1 Alloys and processing details	48
3.1.1 Alloys and Composition Analysis	48
3.1.1 Hot rolling and heat treatment procedure	48
3.2 Sample preparation.....	50
3.2.1 Mircopreparation	50
3.2.2 Etching.....	50
3.2.3 TEM thin foil preparation.....	51
3.2.4 Carbon extraction replicas	51
3.3 Characterization techniques.....	52
3.3.1 Qualitative and quantitative analyses by X-ray diffraction (XRD).....	52
3.3.2 Grain size analysis by optical microscopy.....	55
3.3.3 Scanning electron microscopy.....	56
3.3.4 Transmission electron microscopy	56
3.4 Mechanical property testing	60
3.4.1 Vickers hardness measurement.....	60
3.4.2 Tensile testing.....	60
3.4.3 Nanoindentation.....	61
Chapter 4 Brief study on microstructure and mechanical properties of Mn-based maraging steels	63
4.1 Thermodynamic calculation	63
4.2 The effect of Mn content on grain refinement	65
4.3 Phase identification by XRD and SEM.....	67
4.4 Hardness evolution	71

Table of Contents

4.5 Tensile results.....	74
4.5.1 Tensile behaviour of solution-treated samples	74
4.5.2 The embrittlement of aged samples	75
4.5.3 The improvement of mechanical properties in overaged samples.....	76
4.6 Fractography analyses	81
4.6.1 The fracture surface after solution heat treatment	81
4.6.2 Intergranular brittleness in aged 7% Mn alloy.....	82
4.6.3 Improved fracture behaviour in aged 12% Mn alloy.....	83
4.7 Summary	85
Chapter 5 Characterization of L2₁-ordered Ni₂TiAl intermetallic phase and its precipitation behaviour	87
5.1 Introduction	87
5.2 Experimental details	87
5.3 Microstructural evolution	88
5.3.1 The effect of Mn content on the precipitation	88
5.3.2 The effect of aging temperature.....	90
5.4 Coarsening of precipitates	91
5.4.1 Size distribution of precipitates	91
5.4.2 The growth and coarsening kinetics of precipitate	95
5.5 Chemical composition of precipitates	98
5.6 Crystal structure of precipitates.....	104
5.6.1 Determination of crystal structure	104
5.6.2 The orientation relationship between the precipitate and martensite matrix	110
5.7 Core/shell precipitates	112
5.8 Discussion	116

Table of Contents

5.8.1 The effects of volume fractions on the coarsening behaviour	116
5.8.2 The formation mechanism of core/shell structure	119
5.8.3 The effect of Mn on the precipitation	122
5.9 Summary	123
Chapter 6 The formation mechanism of reverted austenite and its mechanical stability	126
6.1 Introduction	126
6.2 SEM observation	127
6.2.1 The effect of aging parameters on austenite reversion	127
6.2.2 The effect of Mn content on austenite reversion	130
6.3 TEM investigation	131
6.4 XRD quantitative analyses	137
6.5 Nanoindentation	139
6.6 Discussion	142
6.6.1 The size of reverted austenite grains.....	143
6.6.2 Chemical composition of reverted austenite.....	144
6.6.3 The volume fraction of reverted austenite	148
6.6.4 The formation mechanism of reverted austenite.....	149
6.6.5 The stability of reverted austenite.....	152
6.7 Summary	155
Chapter 7 Strengthening mechanisms of Mn-based maraging steels	158
7.1 The solid-solution and grain refinement strengthening.....	162
7.2 Precipitation strengthening mechanism.....	163
7.3 Austenite engineering in overaged stage	166
7.3.1 The effect of reverted austenite on strengthening.....	167
7.3.2 The effect of reverted austenite on ductility	171

Table of Contents

7.4 Summary	172
Chapter 8 Conclusions and future work.....	175
8.1 Phase identification	175
8.2 Hardness and tensile results	175
8.3 Precipitation behaviour of L2 ₁ -ordered Ni ₂ TiAl phase	176
8.4 Reverted austenite and its mechanical stability.....	177
8.5 Optimal heat treatment suggestions	179
8.6 Future work	180
References	181
Appendix Crystallographic information of the phases in maraging steels	203

List of Figures

Figure 1-1 Global tensile strength-elongation profile for various kinds of steels [1]..2	
Figure 2-1 Stress-strain curves of samples with different heat treatment conditions in Ti-containing alloy [84].	15
Figure 2-2 (a) An atomic resolution high-angle annular dark-field (HAADF)-scanning transmission electron microscope (STEM) image along the $[001]_{\text{bcc-Fe}}$ zone axis; (b) magnified HAADF-STEM image of the precipitate/matrix interface in (a); (c) Dark-field image of the precipitates using the unique 111 reflection of $L2_1$ -ordered Ni_2TiAl phase where the B2-ordered NiAl zones are indicated by arrows [85].	16
Figure 2-3 (a) Three dimensional atom probe tomographic reconstructions of rod-shaped precipitates after treated for 3600 seconds and (b) corresponding Ni+Ti isoconcentration surfaces [46].	18
Figure 2-4 Atomic distribution of representative precipitates in the (a) 1 h, (b) 4 h and (c) 1024 h aging stages [102]; (d) HAADF image of the core/shell precipitates and (e) Enlarged HAADF image of yellow rectangle part in (d) [45].	20
Figure 2-5 The evolution of precipitate size during aging in terms of precipitation kinetics, after [29].	27
Figure 2-6 (a) Matrix austenite at prior austenite grain boundaries [147] (b) the lamellar structure of alternate lath-like austenite and residual martensite [27] and (c) a recrystallized austenite grain free of defects [146].	36
Figure 2-7 Different orientation relationships between fcc and bcc phases: (a) Bain, (b) K-S, and (c) N-W. Blue atoms belong to bcc unit cell and green atoms belong to fcc unit cell [179].	41
Figure 2-8 Schematic illustration of (a) abnormal $\alpha' \rightarrow \gamma$ transformation and (b) normal $\alpha' \rightarrow \gamma$ transformation [192].	43

List of Figures

Figure 2-9 (a) The typical microstructure of a martensitic steel constituted by packets of martensite laths, (b) the dislocated laths which is at nano-scale in thickness. Both are the micrographs of a 10% Mn maraging steel after water quenching from solution heat treatment.	46
Figure 3-1 Schematic diagram of processing conditions	49
Figure 3-2 Schematic steps of making the carbon extraction replication [207].	52
Figure 3-3 Schematic diagram of linear intercepts for the measurement of grain size.	55
Figure 3-4 The construction of Ewald sphere after [207].	57
Figure 3-5 The geometric relationship between reciprocal lattice and electron diffraction pattern after [207].	58
Figure 3-6 Geometry of the standard rectangular tension test sample.	61
Figure 3-7 (a) a standard Berkovich indenter where $\alpha = 65.03^\circ$; (b) a standard cube corner indenter where $\alpha = 35.26^\circ$	62
Figure 3-8 A typical schematic of load-displacement curve for nanoindentation test.	62
Figure 4-1 The equilibrium phase fractions as a function of temperature in (a) 7% Mn, (b) 10% Mn and (c) 12% Mn alloys.	64
Figure 4-2 Microstructure of the three alloys in the SHT state by EBSD analyses. Left column: phase maps showing martensite phase (blue) with grain boundaries (black lines, $>15^\circ$). Right column: inverse pole maps of the same area, showing the orientation distribution of the martensite.	66
Figure 4-3 X-ray diffraction patterns of solution-treated 7% Mn, 10% Mn and 12% Mn alloys.	67

List of Figures

Figure 4-4 (a) SEM micrograph of Ti-rich carbide present in 10% Mn alloy in the SHT state with (b) EDS line scan and (c) EDS spot detection results; (d) TEM micrograph of Ti-rich carbide existing in aged 7% Mn alloy in 500 °C / 10080 min state.	68
Figure 4-5 X-ray diffraction patterns of (a) 10% Mn and (b) 12% Mn alloys aged at 500 °C for various durations.	69
Figure 4-6 (a) Schumann’s martensitic transformation diagram of the Fe-Mn system [154]; (b) schematic map of the phase fractions after cooling to room temperature based on Schumann’s description [215].	70
Figure 4-7 SEM micrographs of (a) lath-like austenite and precipitate-decorated martensite matrix and (b) homogenously distributed precipitates in 12% Mn alloy in 500 °C / 2880 min state.	71
Figure 4-8 Vickers hardness as a function of aging time at (a) 420 °C, (b) 460 °C and (c) 500 °C for Mn-based maraging steels, respectively.	73
Figure 4-9 Engineering stress vs. strain of 7%, 10% and 12% Mn alloys in the SHT state.	74
Figure 4-10 (a) Engineering stress-strain curves of 10% Mn alloy in 460 °C / 10080 min state and 7% Mn alloy in 500 °C / 60 min state with their corresponding fracture images: (b) 10% Mn alloy in 460 °C / 10080 min state and (c) 7% Mn alloy in 500 °C / 60 min state.	76
Figure 4-11 Engineering stress vs. engineering strain of 10% Mn alloy aged at 500 °C for different durations.	77
Figure 4-12 Engineering stress vs. strain of 12% Mn alloy aged at 500 °C for different durations.	78
Figure 4-13 Engineering stress-strain curves of 12% Mn alloy aged for 10080 minutes at different temperatures.	79

List of Figures

Figure 4-14 Engineering stress-strain curves of 7% Mn, 10% Mn and 12% Mn alloys in 500 °C / 10080 min state.....	80
Figure 4-15 Comparison of UTS and TE between 10% Mn and 12% Mn alloys aged at 500 °C for different durations.	81
Figure 4-16 The fracture surface of solution-treated (a) 7% Mn; (b) 10% Mn and (c) 12% Mn alloys.	82
Figure 4-17 The fracture surface of 7% Mn alloy aged at: (a) 420 °C / 10080 min; (b) 460 °C / 10080 min; (c) 500 °C / 60 min and (d) 500 °C / 10080 min.....	83
Figure 4-18 The fracture surface of 12% Mn alloys aged at 460 °C for (a)(b) 4320 min and (c)(d) 10080 min. The right column is the enlarged fractographs.	84
Figure 4-19 The fracture surface of 12% Mn alloys aged at 500 °C for (a) 10 min; (b) 1440 min and (c)(d) 10080 min.	85
Figure 5-1 Bright-field TEM micrographs of precipitates formed at 500 °C. Left: 7% Mn alloy for (a) 480 min (c) 2880 min and (e) 10080 min; right: 12% Mn alloy for (b) 480 min (d) 2880 min and (f) 10080 min.	89
Figure 5-2 TEM micrographs of precipitates on carbon extraction replicas of 12% Mn alloy aged at (a) 420 °C, (b) 460 °C and (c) 500 °C for 10080 min.....	91
Figure 5-3 Examples of PSDs plotted for various aged samples: 7% Mn alloy (a) 500 °C / 480 min, (b) 500 °C / 2880 min and (c) 500°C / 10080 min; 10% Mn alloy (d) 500 °C / 480 min, (e) 500 °C / 2880 min and (f) 500°C / 10080 min; 12% Mn alloy (g) 500 °C / 480 min, (h) 500 °C / 2880 min and (i) 500°C / 10080 min. The histograms of the PSD function, g, are plotted as a function of reduced precipitate radius ($\rho = r/r$). Theoretical LSW distribution is presented as well for comparison.	94
Figure 5-4 Evolution of the mean precipitate size r as a function of aging time at 500 °C in (a) 7% Mn alloy and (b) 12% Mn alloy.....	95

List of Figures

Figure 5-5 Evolution of the mean precipitate radius r_3 as a function of aging time t , in 7% Mn, 10% Mn and 12% Mn alloys aged at 500 °C.....	96
Figure 5-6 (a) Bright-field TEM image of 7% Mn alloy aged at 500 °C for 12960 min and TEM-EDS spectra of (b) precipitate and (c) matrix.....	99
Figure 5-7 STEM micrograph of precipitates in 12% Mn alloy aged at 500 °C for 2880 min and EDS results of concentration profiles measured along the red line. .	100
Figure 5-8 Crystal structure of the B2-ordered NiAl phase and simulated electron diffraction patterns along low-index zone axis directions simulated using ICDD PDF-4+ software.	105
Figure 5-9 Crystal structure of the L2 ₁ -ordered Ni ₂ TiAl phase and its simulated electron diffraction patterns along low-index zone axis directions simulated using ICDD PDF-4+ software.	106
Figure 5-10 (a) Eight unit cells of the B2-ordered NiAl for a better comparison with (b) the unit cell of L2 ₁ -ordered Ni ₂ TiAl; diffraction patterns along the [011] zone axis of (c) B2-ordered NiAl and (d) L2 ₁ -Ni ₂ TiAl simulated using ICDD PDF-4+ software.	108
Figure 5-11 HREM micrographs of precipitates in 12% Mn alloy aged at 500 °C for 10080 min, (a) [011] zone axis; (b) IFFT of (a); (c) [111] zone axis; (d) IFFT of (c).	109
Figure 5-12 (a) Bright-field TEM micrograph of 7% Mn alloy aged at 500 °C for 10080 min along [011] zone axis and (b) corresponding dark-field micrograph using the [111] superlattice spots of precipitates (inset is the corresponding diffraction pattern).	110
Figure 5-13 Selected area diffraction patterns taken on thin foil samples (500 °C / 10080 min, 10% Mn alloy) along (a) [001], (b) [011] and (c) [111] zone axes.....	110
Figure 5-14 Two-beam bright field micrographs of (a) 7% Mn and (b) 10% Mn alloys after aging at 500 °C for 10080 min.	112

List of Figures

Figure 5-15 Left column: representative bright-field TEM micrographs. Right column: magnified carbon extraction replica TEM micrographs of precipitates. (a) 7% Mn alloy, 500 °C / 10080 min; (b) 10% Mn alloy, 500 °C / 10080 min and (c) 12% Mn alloy, 500 °C / 2880 min.....	113
Figure 5-16 HAADF image of core/shell precipitates in 12% Mn alloy aged at 500 °C for 2880 min.....	114
Figure 5-17 HREM micrographs of the precipitate in 12% Mn alloy aged at 500 °C for 10080 min. (a) The low-magnification images of precipitates, (b) core/shell structure at a higher magnification and (c) lattice information at the periphery of precipitate.....	115
Figure 5-18 The precipitate size distribution as a function of reduced precipitate radius R/\bar{R} for different volume fractions of precipitate f_p [226].	117
Figure 6-1 SEM micrographs showing the morphologies of reverted austenite in the 12% Mn alloy during aging. (a) Thin austenite layers formed along boundaries and (b) highly dispersed fine precipitates at 420 °C / 10080 min state; (c) evident matrix austenite and austenite layers at 460 °C / 2880 min state; (d) the amount of austenite increased after aging at 460 °C for 10080 min.	128
Figure 6-2 (a) Fine precipitates and (b) thin matrix austenite at the onset of aging in the 12% Mn alloy (500 °C / 10 min state); (c) the lath-like austenite became dominant after aging for 2880 min; (d) a lamellar structure of alternative lath-like austenite and residual martensite in the 10080 min aged sample.	129
Figure 6-3 (a) Reverted austenite in the 12% Mn alloy after aging at 540 °C for 10080 min; (b) reverted austenite is free of precipitates.....	130
Figure 6-4 SEM observation of (a) 7% Mn alloy (500 °C / 2880 min state); (b) 7% Mn alloy (500 °C / 10080 min state); (c) 10% Mn alloy (500 °C / 2880 min state); (d) 10% Mn alloy (500 °C / 10080 min state).	131

List of Figures

Figure 6-5 Matrix austenite formed along prior austenite grain boundaries in (a) 10% Mn alloy at 500 °C / 1440 min state and (b) 7% Mn alloy at 500 °C / 10080 min state.	132
Figure 6-6 TEM micrographs of lath-like austenite in (a) 12% Mn alloy aging at 500 °C for 2880 min and (b) 12% Mn alloy aging at 540 °C for 2880 min; (c) and (d) are the corresponding images from a different orientation.	133
Figure 6-7 Bright-field TEM images of austenite in the martensite matrix and the corresponding selected area diffraction patterns presenting (a) K-S relationship and (b) Nishiyama relationship between austenite and martensite.	137
Figure 6-8 The evolution of volume fractions (vol.%) of reverted austenite formed as a function of aging time at the temperature of 500 °C.	138
Figure 6-9 Load-displacement curves of martensite and austenite in the 12% Mn alloy in the 500 °C / 10080 min state.	140
Figure 6-10 Hardness distribution of austenite and martensite phases in (a) 10% Mn alloy, in 500 °C / 10080 min state and (b) 12% Mn alloy, in 500 °C / 10080 min state.	141
Figure 6-11 Load-displacement curve recording the martensitic transformation of an austenite grain.	142
Figure 6-12 Average width of lath-like reverted austenite after aging at 500 °C for different times in the 10% Mn and 12% Mn alloys.	144
Figure 6-13 Average width of reverted austenite aged at different temperatures for 10080 min in the 12% Mn alloy.	144
Figure 6-14 Equilibrium phase diagram of the Fe-Mn system.	146
Figure 6-15 Arrhenius plot for the determination of the activation energy of austenite formation in the 10% Mn and 12% Mn alloy.	151

List of Figures

Figure 6-16 (a) The average hardness of austenite and martensite in the 10% Mn and 12% Mn alloys aged at 500 °C for 10080 min; (b) the hardness of austenite and martensite in the 12% Mn alloy as a function of aging temperature.	154
Figure 7-1 The optical micrographs of 7% Mn alloy (a) at SHT state and (b) 500 °C / 2880 min state.	163
Figure 7-2 (a) The engineering stress-strain curves of 12% Mn alloy in different heat treatment conditions; (b) the corresponding hardness evolution of 12% Mn alloy aged at 500 °C.	165
Figure 7-3 SEM images of samples after-tensile (a) 10% Mn and (b) 12% Mn alloys aged at 500 °C for 5760 min. (c) The volume fractions (vol.%) of reverted austenite as a function of aging time at the temperature of 500 °C (solid lines: before tensile testing; dash lines: after tensile testing).	167
Figure 7-4 Hardness evolution vs. volume fraction of austenite as a function of time in (a) 10% Mn and (b) 12% Mn alloys when aged at 500 °C.	168
Figure 7-5 (a) The true stress-strain curves of the 12% Mn alloy in different heat treatment conditions; the true stress-strain curves of the 10% Mn alloy in the 500 °C /5760 min state is also displayed for comparison.	170
Figure 7-6 SEM images of 12% Mn alloy aged at 540 °C for 360 min: (a) reverted austenite formed along grain boundaries and (b) nano-precipitates.	174

List of Tables

Table 2–1 Overview of the different orientation relationships between fcc and bcc crystals [168].	39
Table 3–1 Chemical compositions (wt.%) of the investigated Mn-based steels.	48
Table 3–2 Parameters for hot rolling process	49
Table 3–3 Calculated theoretical intensity ratios $\frac{R_V^{hkl}}{R_\alpha^{hkl}}$ using Co K_α radiation [206].	55
Table 4–1 Summary of the mechanical properties of 7% Mn, 10% Mn and 12% Mn alloys in the SHT state.	75
Table 4–2 Summary of the mechanical properties of 10% Mn alloys aged at 500 °C for different durations.	77
Table 4–3 Summary of mechanical properties of 12% Mn alloy aged at 500 °C for different durations.	79
Table 5–1 Experimental mean size of precipitates (r) and coarsening rate constant (K_R) of different alloys aged at 500 °C.	97
Table 5–2 Average chemical composition in at.% of the nano-sized precipitates evolved at 500 °C measured by TEM-EDS.	103
Table 5–3 The diffusion rates of the constituent elements in bcc-Fe at 500 °C	121
Table 5–4 The mixing enthalpy of elements in the Mn-based maraging steels [238].	122
Table 6–1 Chemical compositions (at.%) of reverted austenite and martensite in the 7% Mn alloy obtained by TEM-EDS.	135
Table 6–2 Chemical compositions (at.%) of reverted austenite and martensite in the 12% Mn alloy under various heat treatment conditions obtained by TEM-EDS.	136

List of Tables

Table 6–3 The volume fractions (vol.%) of reverted austenite formed in different aging conditions.	138
Table 6–4 A summary of the equilibrium Mn concentration (at.%) and volume fraction (vol.%) of austenite and ferrite phases at different aging temperatures based on the Fe-Mn phase diagram in Figure 6-14.....	148
Table 7–1 Summary of the tensile properties of Mn-based steels.	159
Table 7–2 Lattice parameter (Å) of α' -martensite in the three alloy in different heat treatment conditions.....	162

Chapter 1 Introduction

Steels possessing a good balance of mechanical properties (tensile strength \times elongation) are of great importance to their applications. Specifically in the automotive industry, they are regarded as the future key materials for light-weight strategies and related fuel and car emissions savings. The huge commercial demand therefore has driven both industry and academia to make great progress in developing various high strength steel (HSS) grades and corresponding processing technology.

High-strength low-alloy (HSLA) steels, as the most conventional HSS group, have a microstructure of fine ferrite grains strengthened by carbides and/or nitrides of Ti, V or Nb. Generally their strength is at the level of 700-800 MPa. As this type of steels can be manufactured by simple processing paths, they have been widely used in automotive applications. In order to further improve the combining properties of strength and ductility, other alloying elements have been added and hence more sophisticated alloy systems have been designed, such as Dual Phase (DP) steels, Transformation Induced Plasticity (TRIP) steels, Twinning Induced Plasticity (TWIP) steels and martensitic (MART) steels. Global tensile strength-elongation profile of those steel families is displayed in Figure 1-1 [1]. Dual phase steels are mainly constituted of soft ferrite with dispersed islands of hard martensite. Their strength is dependent on the amount of martensite and its morphology and distribution [2][3][4][5]. TRIP steels are multiphase grades which utilize specially designed alloying additions and processing paths to retain certain amount of austenite down to room temperature within a ferritic matrix. This metastable austenite transforms to martensite when subjected to plastic deformation, which leads to a volume and shape change of the resulting martensite and matrix to accommodate the transformation misfit and thus increases the ductility [6][7][8]. TWIP steels normally have a fully austenitic microstructure at room temperature. The formation of mechanical twins of austenite during deformation induces high strain hardening and prevents necking, which maintains a very high strain capacity and achieves a better balance of strength and ductility [9][10][11]. Another group of HSS is martensitic (MS) steels, among

which maraging steels is the most widely studied category. Maraging steels are known for its ultrahigh strength which is attributed to the heavily strained martensite matrix upon quenching and further precipitation strengthening by aging treatment. These precipitates act as highly efficient obstacles against dislocation motion via Orowan mechanism. The detailed microstructure and properties of maraging steels will be introduced in Section 2.2.

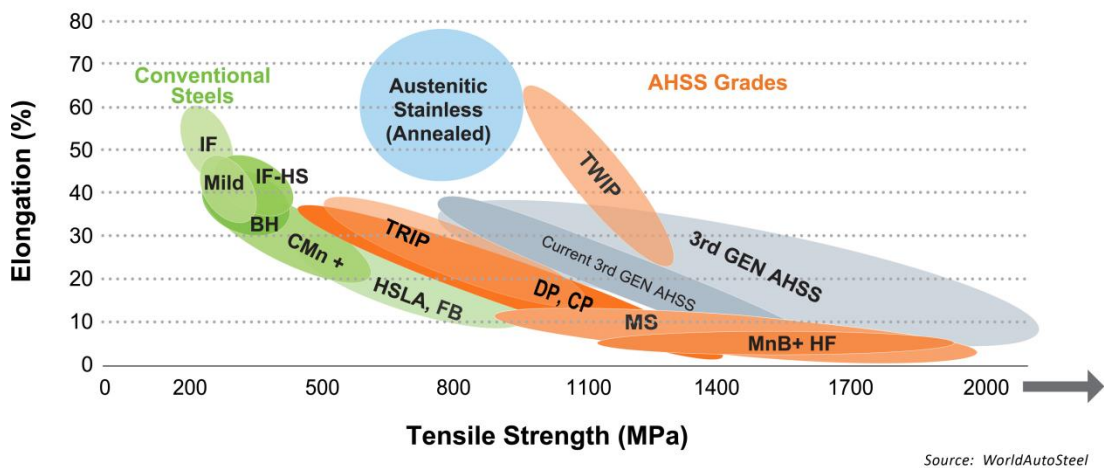


Figure 1-1 Global tensile strength-elongation profile for various kinds of steels [1].

It is recognized that deformation-induced martensitic transformation plays an important role in improving the mechanical properties of TRIP steels. Conventionally, high level of carbon content is added to retain austenite at room temperature, but the poor weldability resulting from high carbon addition restricts its application in the automotive industry. Hence, Mn, as another effective austenite stabilizer, is used to substitute carbon. In 1960s, Goldshtein et al. first reported an excellent toughness obtained in a low-carbon TRIP steel (0.1 wt% C, 8 wt.% Mn) with a considerable amount of austenite [12]. Since then many researches on medium Mn steels have been carried out [13][14][15][16]. A recent study by Luo et al. [17] reported a 5Mn steel, which contained more than 30 vol.% austenite, exhibited an ultimate tensile strength (UTS) of 1-1.5 GPa with total elongation (TE) of 31-44%.

On the other hand, it is generally accepted that the superior mechanical properties in maraging steels are attributed to the formation of strengthening nano-precipitates

upon aging. In fact, as the aging process is normally performed at the two-phase field, another phase transformation reaction, the partial reversion of martensite to austenite, is expected to occur. Evidence has demonstrated that austenite reversion can significantly affect the mechanical properties [18][19][20]. The most classical maraging group is nickel-based maraging steels (18 wt.% Ni) with considerable additions of elements such as Co (8 wt.%), Ti, Cr and Mo. Owing to the sharp drop of the availability of Co since the 1960s, many researchers have focused on developing alternatives to expensive Co and Ni containing maraging steels. Among them, studies on Mn-based maraging steels have made great progress in minimising the strength sacrifice resulting from the absence of Co and Ni.

Based on the above discussion, the strategy of combining the two strengthening mechanisms in the form of Fe-Mn alloys was proposed. According to this strategy, a microstructure including hard martensite strengthened by nano-precipitates and ductile austenite in which transformation-induced plasticity can occur should be attained. Raabe et al. [18] designed a type of low carbon content (0.01 wt.% C), 9-12 wt.% Mn steels with minor additions of Ni, Ti and Mo (1-2 wt.%). Contradictory to the common knowledge that the increase in strength is accompanied by a decrease in ductility (Figure 1-1), those steels exhibited a simultaneous increase in strength and ductility. A UTS of ~1300 MPa with a tensile elongation of 21% was reported in a 12 wt.% Mn maraging TRIP steel.

This great achievement opens a new approach to develop ultra-high steels at relatively lean alloying costs. However, there are still some unsolved questions about this new type of steels, e.g. the nature and composition of precipitates are debated. The respective formation mechanisms governing the austenite reversion and precipitation are not clear. Given that the chemical composition, morphology and grain size of reverted austenite are different from those of retained austenite, the deformation mechanism of reverted austenite in these steels is supposed to be different from that of retained austenite. The strengthening mechanism of this type of steels is also worth studying. Therefore, it is necessary to carry out a detailed study on this type of steels and based on the study, the optimal microstructure and related processing paths can be proposed.

Chapter 1 Introduction

The present work is undertaken in collaboration with Tata Steel. The aim was to proceed with a further study on a series of 7-12% Mn maraging steels. Characterization of the unknown precipitates is the primary task of this work. Then the formation mechanism of precipitates and reverted austenite are discussed, respectively. Based on the investigation on the strengthening mechanisms, optimal chemical composition and processing techniques are determined.

This thesis continues with Chapter 2 which presents a general survey of relevant literature for the study on Mn-based maraging steels. After the introduction on the development of Mn TRIP steels and Mn maraging steels, various precipitation behaviours in different maraging steels are reviewed. Subsequently, the basic knowledge about precipitate coarsening is given. Then, the discussion on the mechanical stability of austenite and its formation mechanism is followed by a brief overview of grain refinement in maraging steels.

Chapter 3 provides the information about the materials studied in this thesis and the relevant processing paths. Various sample preparation methods and characterization techniques are also described.

Chapter 4 presents the results of some basic analyses on these steels to give the most straightforward understanding about Mn-based maraging steels, e.g. the thermodynamic calculation results, phase identification by X-ray diffraction (XRD), hardness and tensile testing results, etc.

In Chapter 5, microstructural evolution of nano-scale precipitates during aging is described. Based on the observation, the precipitate coarsening kinetics is discussed. Then the chemical composition and crystal structure of precipitates are studied to identify the precipitates. In addition, their orientation relationship with martensite matrix and the core/shell structure are also investigated.

Chapter 6 mainly focuses on the austenite reversion in maraging steels. Apart from the microstructural observation on reverted austenite in various aging conditions, the quantity and chemical composition of reverted austenite are measured to provide information about its mechanical stability. Then, the analyses of nanoindentation results of different samples are given. Based on these results, the factors which are normally considered to affect the mechanical stability of reverted austenite, such as

Chapter 1 Introduction

morphology, orientation relationship, grain size and chemical composition etc., are discussed successively.

After a brief comparison of the mechanical properties of Mn-based maraging steels in this work with other medium Mn steels reported in the literature, the focus of Chapter 7 is concerned with the definition of strengthening mechanisms mainly involving solid-solution strengthening, grain-refinement strengthening, precipitation strengthening and phase transformation strengthening mechanisms (TRIP effect).

Chapter 8 draws conclusions of this thesis based on the results and discussion of all chapters and future work are proposed as well.

Chapter 2 Literature review

2.1 The development of Mn TRIP steels

Two primary motivations have been driving the development of advanced high strength steel (AHSS) for automotive applications. The first motivation is to decrease the consumption of fuel and car emissions by mass reduction. The second is the increasing requirement for comfort, safety and speed of vehicles. From this point of view, AHSSs with high strength to weight ratio are the key materials for automotive manufactures [1][21][22]. The first-generation automotive-grade AHSSs (Figure 1-1), such as DP steels, TRIP steels and complex-phase (CP) steels which possess multi-phase microstructures comprised of different percentages of bainite, martensite and carbon-rich austenite, have been extensively investigated in the past [1][22]. The second-generation AHSSs are the twinning-induced plasticity (TWIP) steels. These high Mn (> 15 wt.%) austenitic-based steels yield a combination of strength and ductility superior than those of the first-generation AHSSs [10][11], but the high alloying additions (e.g. Mn, Al and C) and complicated processing technology limited their application in automotive industry [23]. Recently, the development of third-generation AHSSs with medium Mn contents (5-12 wt.%) have been designed and developed. In these steels, varying fractions of metastable austenite with fine grain size were produced by adjusted intercritical tempering [16][24][25][26]. It is reported that the medium Mn steels containing sub-micro austenite grains can achieve a high ultimate tensile strength and excellent total elongation [27][22][26]. This is because the plasticity of the austenite is not only dependent on the mobile dislocations, two other plastic modes, i.e., strain-induced martensitic transformation and mechanical twinning, are also involved in the deformation of austenite. The operation of specific deformation modes is determined by the microstructural characteristics of austenite (which will be discussed in Section 2.4). This feature is significant in the design of medium Mn steels containing austenite. Recent studies on 5-7 wt.% Mn steels revealed that elongation of up to 45% can be achieved by optimized intercritical tempering. However, so far the yield

strength of this steel grade hardly goes beyond 1 GPa, which obviously cannot meet the demand for the various intrusion application of hole-expanded components in automotive industry [26]. Therefore, strategies to improve the strength of these steels in which the excellent ductility can be retained are the focus of current study.

2.2 The development of maraging steels

Maraging steels are a special group of ultrahigh-strength martensitic steels which are hardened by intermetallic precipitates instead of universal carbide precipitates. Therefore, the carbon content in maraging steels is controlled to be as low as is commercially practicable [28]. The term ‘maraging’ refers to the aging of martensite. The supersaturated martensite is obtained by fast cooling from the austenite phase field and the martensite with low carbon content is very soft but heavily dislocated. This microstructural feature is believed to benefit the hardenability, toughness and formability before aging [29], and more importantly, provide an excellent nucleation condition for precipitation. The subsequent aging treatment leads to the formation of intermetallic precipitates. The nature of precipitates largely depends on the alloying compositions and aging parameters. The detailed discussion about the precipitation in maraging steels will be given in Section 2.2.3. On the other hand, the excessive softening of martensite matrix by recovery during aging should be avoided if a good balance between strength and toughness is required.

The development of maraging steels initiated in 1962 with the publication of a paper by Decker et al. [30] on 18 wt.% Ni steels containing significant levels of Co (8 wt.%) and Mo (5 wt.%) but low carbon content (0.01-0.03 wt.%). According to their report, tensile strengths of up to 2068 MPa, 12% elongation, 60% reduction in area, low ductile-brittle transition temperature (DBTT) and notch tensile strengths of ~3034 MPa were achieved. Additionally, excellent stress-corrosion resistance and weldability were inherent in these alloys [30]. The following researches led to the development of the well-known maraging systems, such as 18Ni (200 (ksi)), 18Ni (250) and 18Ni (300) alloys. However, the costly alloying additions of maraging steels restricted their applications in the most critical industry. The sharp drop of the availability of cobalt during the period 1978-1980 promoted the exploitation of

alternatives to Co-containing maraging steels. Intensive efforts were directed at reducing the concentration of expensive alloying elements, such as Co and Ni. As a result, a new class of Co-free maraging steels containing Fe, Ni, Mo and Ti emerged. These Co-free steels generally presented inferior mechanical properties compared to Co-containing steels, but their mechanical properties appeared sufficient for typical applications of maraging steels [31][32]. Moreover, due to the similarity of the equilibrium phase diagrams between Fe-Ni and Fe-Mn systems, the partial substitution of Ni by Mn was applied in the development of lean maraging steels. An excellent combination of strength and ductility was reported in an Fe-20.8Ni-2.13Mn-0.8Ti maraging steel after aging at 550 °C for 1 h which exhibited a yield strength (YS: 1371 MPa) and total elongation (TE: 18.8%) [33]. It should be noted, however, steels with high Mn contents were found to suffer from embrittlement after aging for short times.

The main strength of maraging steels is generally attributed to the dense precipitation of fine intermetallic compounds in a soft but heavily dislocated martensite matrix. In some cases, reverted austenite may form when aging at high temperatures or for a long period. The effect of reverted austenite on the mechanical properties is controversial. It is generally accepted that the toughness of quenching and partitioning (Q&P) steels for low-temperature service can be improved via the formation of metastable reverted austenite after fast cooling from intercritical tempering (holding in the temperature range where the austenite and ferrite phases coexist) [27][34][26]. However, in maraging steels, different opinions exist on the effect of reverted austenite on mechanical properties (which will discuss in detail in Section 2.4.1) [19][35][36][37].

Maraging steels are known for their excellent combination of ultrahigh strength with an acceptable ductility. Due to the low carbon content, they exhibit excellent machinability and weldability in the solution-treated condition. Besides, they also possess high strength to weight ratio and dimensional stability during aging. All of these attractive properties make maraging steels as a class of promising materials and numerous researches have been carried out on the development of maraging steels. More recently, a newly-developed 12 wt.% Mn maraging TRIP steel with minor addition of Ni, Ti, Mo and Al was reported to possess an excellent combination of

strength and ductility (UTS (ultimate tensile strength): 1.3 GPa, TE (total elongation): 21%) due to precipitation strengthening mechanism and TRIP effect of austenite. But there are some unsolved questions about this new materials, i.e. the nature of precipitates, the formation mechanism of retained/reverted austenite and its contribution to strengthening [18].

2.2.1 The role of alloying elements in maraging steels

The high Ni content in maraging steels, which significantly lowers both the equilibrium γ/α transformation temperature (A_{e3}) and martensite start temperature (M_s), ensures the formation of martensite after quenching from solid-solution treatment. Precipitation strengthening by aging is subsequently acquired via aging at 480-510 °C for a range of times [29]. Ni, Co, Ti, and Mo are normally added as essential elements to generate intermetallic precipitates. In recent studies on Cu-bearing maraging steels, Cu precipitates were demonstrated to accelerate the nucleation of intermetallic precipitates [38][39][40]. In some maraging steels, the additions of high levels of Cr are required to achieve effective aging hardening in stainless grades resistant to corrosion [41][42][43]. As mentioned above, the price jump of Co and Ni drove extensive researches to develop lean maraging steels. In recent years, the development of lean maraging steels by substituting Ni with cheaper elements such as Mn (the price of Ni: 14410 USD/t, Co: 27750 USD/t, Mn: 2200 USD/t by Aug 2013) has made remarkable progress. As an alternative austenite stabilizer, Mn can take over the role of Ni in conventional maraging steels. Besides, experimental evidence indicated that Mn was also involved in the precipitation of Mn-containing maraging steels [44][45] and Mn additions were found to accelerate the age hardening process [46]. However, high maraging strength at the expense of dramatic loss in ductility was found in several Fe-Ni-Mn steels [33][47][48]. Some researchers suggested that the segregation of Mn to grain boundaries was responsible for the embrittlement phenomena in those alloys (which will discuss in Section 2.2.4) [47][49]. While further study on these Mn-containing maraging steels revealed that the embrittlement vanished by proceeding segregation of Mn at grain boundaries leading to the austenite reversion [50].

2.2.2 Behaviour of intermetallic precipitates in conventional maraging steels

Since the development of maraging steels in the 1960s, numerous researches have been carried out on the precipitation behaviour in this steel grade. Thanks to the development of advanced characterization techniques, such as high resolution electron microscopy (HREM) and atom probe tomography (APT) which enables the characterization of extremely fine precipitates, the nature and composition of those intermetallic precipitates in maraging steels have been generally understood. Most of studies agreed that in conventional 18Ni maraging steels, $\text{Ni}_3\text{Ti}(\text{Mo},\text{V},\text{W})$ -type phases generally appear at the very early aging stage, whereas a more stable $\text{FeMo}(\text{W})$ -type phase is formed after long-term aging [51].

The formation of $\text{Ni}_3\text{Ti}(\text{Mo})$ -type phases at the initial aging stage in conventional maraging steels had been proposed since this type of steels was invented. The modern techniques which allow atomic-scale resolution make the direct observation on the nano-precipitates possible and finally confirm the existence of $\text{Ni}_3\text{Ti}(\text{Mo})$ phase (η -phase) in those steels. The morphology of Ni_3Ti precipitates was found to be needle-like [31][52], plate-like [53] or rod-like [31]. The Ni_3Ti phase exhibits hexagonal lattice with $a = 0.255 \text{ nm}$ and $c = 0.42 \text{ nm}$ [38]. Selected area electron diffraction (SAED) analyses indicate that the orientation relationship between η - Ni_3Ti and α' -martensite matrix is $(011)_{\alpha'} \parallel (0001)_{\eta}$, $[1\bar{1}1]_{\alpha'} \parallel [11\bar{2}0]_{\eta}$ [54]. There was debate about the formation mechanism of Ni_3Ti phase in the literature. Most studies suggested the heterogeneous nucleation on dislocations followed by growth via pipe diffusion [48][54]. Other researchers insisted that the precipitate nucleation occurs homogeneously, or at larger undercooling, by spinodal decomposition [55]. There were also divergent opinions about the dominant strengthening effect of each type of precipitates in these steels. Some studies revealed that in maraging steels where both Ti and Mo were present, Ti was much more active in the beginning due to its rapid diffusivity in martensite at the specific aging temperature. Apart from the kinetic advantage, the smaller lattice misfit between Ni_3Ti and martensite and consequently a lower barrier for nucleation is another reason for the formation of

Ni_3Ti in the early stage of aging (just a few minutes or even faster). Therefore, a sharp rise in hardness shortly after the onset of aging was usually observed in Ti-containing maraging steels (C-300 and T-300 steels) [51]. At this stage, Mo is more likely to be incorporated into the Ni_3Ti phase and partially substitute Ti atoms. As the substitution is limited, there are still sufficient Mo atoms for the following formation of FeMo-type phases. Conversely, the growth of FeMo phase would consume the Mo atoms in $\text{Ni}_3\text{Ti}(\text{Mo})$ phase and therefore the stoichiometry of $\text{Ni}_3\text{Ti}(\text{Mo})$ becomes more closer to that of Ni_3Ti . The activity of Mo has been shown to be strongly affected by other elements. The presence of Co is generally found to promote the formation of Mo-rich precipitates. When Co is absent, the driving force for the precipitation of Mo-rich precipitate is significantly reduced. In this case, the precipitation of Mo-rich phases would take 3 to 8 hours to occur [56]. Thus the major precipitates in Co-free maraging steels are entirely Ni_3Ti phase and thus higher Ti content is required to achieve the same level of precipitation strengthening. In addition, the stoichiometry of FeMo-type phase is still debated. Previous TEM and SAED studies suggested it as Fe_2Mo Laves phase [54][56], whereas the compositional result by a more recent ATP analysis corresponded to Fe_7Mo_6 μ phase. Moreover, the possibilities of FeMo and Fe_3Mo_2 cannot be excluded as well.

Apart from the primary $\text{Ni}_3\text{Ti}(\text{Mo})$ -type and FeMo-type phase, several other intermetallic phases may also form as well due to the composition variation of maraging steels. In Ti-free maraging steels, the role of Ti is taken over by Mo. A precipitation sequence of Ni_3Mo followed by equilibrium FeMo-type phase was reported in Ref. [56]. Besides, a type of metastable ω phase (ordered isothermal phase enriched in Ni, Co and Mo) was always generated before the formation of the more stable Ni_3Mo phase. Researches revealed that this ω phase had a higher level of coherency with the matrix and hence was easier to form [57][58]. In addition, the precipitation of $\text{Ti}_6\text{Si}_7\text{Ni}_{16}$ (G-phase) was found to be responsible for the precipitation hardening of Cr-containing high-Si steels [59].

2.2.3 Precipitation behaviour in newly-developed maraging steels strengthened by other intermetallic phases

Maraging steels strengthened by intermetallic phases have complex precipitation behaviours, which vary with the chemical compositions. In this section, some less-known intermetallic precipitates in steels are briefly introduced.

2.2.3.1 NiAl-strengthened Fe-Cr-Ni-Al steels

Precipitation-strengthened ferritic steels are candidate materials for applications such as high-pressure steam piping and heaters in ultra-supercritical fossil-energy power plants [60][61][62]. These applications generally require a creep strain rate $\sim 3 \times 10^{-11} \text{ s}^{-1}$ at temperatures of 760 °C and stress of 35 MPa [63][64]. Therefore, creep resistance is one of the most significant properties. Currently, most creep-resistant ferritic steels are strengthened by carbides. However, the coarsening of incoherent carbides in long-term high temperature application often leads to the decrease of creep resistance [65][66][67][68][69]. Consequently, a number of studies have been carried out to improve the creep properties of steels [70][71][72][73][74]. On the other hand, the investigation on the strengthening behaviour of high temperature materials suggests a uniform dispersion of coherent precipitates is beneficial to enhancing the strength [74]. The most classical group is the nickel-based superalloys where coherent $L1_2$ -ordered precipitates are generated to strengthen the fcc matrix. Analogously in steels, B2-ordered (CsCl-type) NiAl phase ($a = 0.2887 \text{ nm}$) [75] is known to have a similar crystal structure to α -Fe matrix ($a = 0.2866 \text{ nm}$) [75]. Its orientation relationship with matrix is $(100)_\alpha \parallel (100)_{NiAl}$, $[001]_\alpha \parallel [001]_{NiAl}$, which means the NiAl phase is not only coherent but also coplanar with α -Fe matrix [76]. NiAl-strengthened ferritic steels have been found to possess better thermal conductivity, lower thermal expansion and production cost compared to other materials applied in high temperature [77]. Besides, it is believed that the additions of Al which varies from several to more than 10% contributes to the feature of lower density ($\sim 7 \text{ g}\cdot\text{cm}^{-3}$) [60]. All these advantages allow the NiAl-strengthened ferritic steels to be nominated as a promising substitution for carbide-containing ferritic

steels, austenitic steels and nickel superalloys applied in the high temperature field. Therefore, a series of NiAl-strengthened ferritic superalloys have been designed.

High strength and toughness with an improved creep resistance have been achieved by the formation of B2-ordered NiAl precipitates in these alloys [61][62][73][76]. Tailard [76] reported an Fe-20Cr-4 Ni-2Al alloy aged at 550-650 °C which hardened rapidly in the initial stage owing to the precipitation of B2-ordered NiAl phase. Maximum hardening of ~420 HV was achieved at around 1000 minutes / 550 °C followed by the decrease in hardness due to precipitate coarsening. In terms of morphology, NiAl phase initially remains coherent with the α -Fe matrix and presents a spherical shape. Then it gradually transforms to a non-equiaxed cuboidal morphology up to 150 nm and eventually lose coherency at the dimension of 150-300 nm after an extremely long time aging. This continuous growth in size during aging indicates that the resistance to coarsening of NiAl phase needs to be improved.

In addition, the high volume fraction of NiAl precipitates leads to a better creep resistance, whereas the ductility is inversely related to the volume fraction of NiAl precipitates [60][61]. Moreover, the ductility is found to decrease with the increasing addition of Al in α -Fe matrix. Therefore, an improved microstructure which possesses (1) a volume fraction of 20% NiAl precipitates, (2) a solubility of Al below 4% in the α -Fe matrix and (3) appropriate Ni and Al additions to avoid the austenite reversion, has been proposed to achieve a better balance between the creep resistance and ductility [61][62].

On the other hand, some other studies were devoted to developing potential stainless maraging steels also strengthened by NiAl precipitates for application in machinery, aircraft and sports fields [78][79][80][81][82]. Ultra-fine NiAl precipitates (1–6 nm) with a high number density ($10^{23-25} \text{ m}^{-3}$) were found homogeneously distributed in martensite matrix at the early stage when aging at 450-620 °C [82]. The size and elemental concentrations of precipitates were found to increase moderately with the aging temperature while the number density decreased. A maximum yield strength (YS) of ~1500 MPa was reported in an Fe-13Cr-8Ni-2.5 Mo-2Al stainless maraging steel aged at 510 °C [82]. It has been demonstrated that B2-ordered NiAl phase formed in stainless maraging steels remained fully coherent with the matrix even

after a significant coarsening [80][81][82]. According to Seetharaman's calculation, the critical diameter of losing the coherency between NiAl phase and α -Fe matrix was ~150 nm [80].

2.2.3.2 The co-precipitation of NiAl and Ni₃Ti phase in Fe-Cr-Ni-Ti-Al steels

Ti is one of the most active elements in maraging steels due to its rapid, and strong precipitation effect during aging [56], hence a number of studies have been carried out to investigate the influence of Ti addition on the precipitation evolution in maraging steels [32][78][83][84]. Accelerated hardening was observed in an Fe-Ni-Al-Ti-Cr stainless steel aged at 525 °C where ~86% of the total increase in hardness was achieved within 0.25 h [32]. The uniformly dispersed clusters formed at the initial aging stage were enriched in Ni, Al and Ti. At the peak hardness (525 °C / 3h), a splitting of the clusters occurred and two independent intermetallic phases, B2-ordered NiAl phase and η -Ni₃(Ti,Al) which were both responsible for precipitation hardening, were formed. In addition, the enrichment of Fe and Cr at the expense of Ni and Al was found in NiAl precipitates by Atom Probe tomography (APT), but the concentrations of Fe and Cr progressively decreased with aging time. In contrast, no substituting elements were found in Ni₃Ti precipitates which indicated the Ni₃Ti phase had a low solubility of other elements and maintained the chemical stability during aging [32].

Lately Leitner and co-workers further reported a supplement of Si in Fe-Cr-Ni-Ti-Al steels [78][84]. A heterogeneous nucleation sequence at dislocation lines was found in the very beginning of aging which resulted in a more significant increase in the cluster formation and hence the hardness of the alloy. This undefined precursor phase then acted as nuclei for the formation of precipitates after a long-time aging treatment. Therefore, two intermetallic precipitates, a spherical phase Ni₁₆Si₇Ti₆ (G-phase) and a rod-shaped η -Ni₃(Ti,Al) phase were generated during aging either simultaneously or separately depending on the chemical composition of alloys [78][84]. Both of the two precipitates were demonstrated to be correlated to the precipitation hardening. Despite the strong increase in strength at the early aging stage, the alloy suffered from severe intergranular embrittlement (Figure 2-1). It is

speculated that the higher number density of undefined precursor precipitates was correlated to the embrittlement since neither precipitation nor segregation on the prior austenite grain boundaries was found at this stage. The embrittlement phenomenon was improved after prolonged aging due to the evolution of the precipitates and the reversion of austenite.

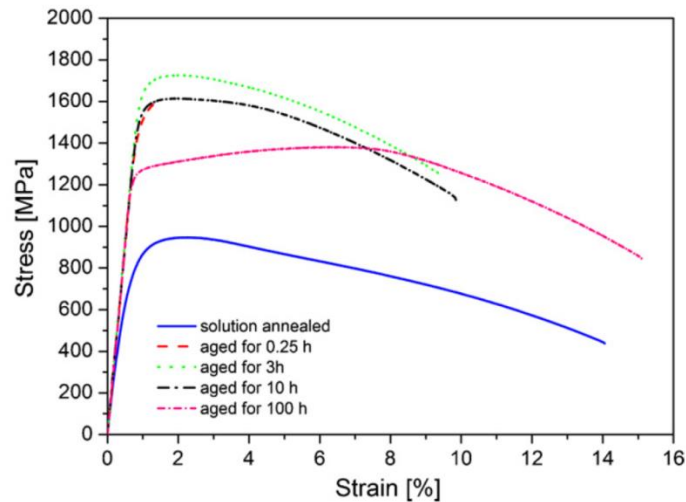


Figure 2-1 Stress-strain curves of samples with different heat treatment conditions in Ti-containing alloy [84].

2.2.3.3 $L2_1$ -ordered Ni_2TiAl type precipitates in Fe-Cr-Ni-Al-Ti steels

In contrast to the co-precipitation of Ni_3Ti and $NiAl$ described in Section 2.2.3.2, some studies demonstrated that the addition of Ti to Fe-Cr-Ni-Al steels led to a type of precipitates which had rarely been reported in Fe-based alloys [62][85]. The nano-sized precipitates which were observed in the as-quenched state presented a cuboidal morphology with an aspect ratio of ~ 2 and an average width of 15 nm. The structure was determined as $L2_1$ -ordered and was fully coherent with the α -Fe matrix (Figure 2-2(a) and (b) [85]). The precipitation of $L2_1$ -ordered Ni_2TiAl phase from a supersaturated B2 TiNi matrix has been reported in several Ni-Ti-Al shape-memory alloys [86][87][88][89][90], but it was seldom observed in Fe alloys. During the further aging, the precipitates grew to an elongated shape with an average width of 40 nm and decomposed into a substructure with a network of B2-ordered NiAl zones

in $L2_1$ -ordered Ni_2TiAl precipitates as shown in Figure 2-2(c). The $L2_1/B2$ two-phase system, with ordered structures based on a bcc lattice is analogous to the classical γ/γ' system with an fcc lattice in Ni-based superalloys [89][90]. Evidence showed that Ni_2TiAl phase exhibited a better creep resistance than NiAl phase. In most creep-resistant form, the creep strength of $L2_1$ - Ni_2TiAl between 1026 and 1273 K was about three times that of NiAl [91]. Further investigation revealed that the best creep properties in Ni-Al-Ti alloys was obtained by a two-phase microstructure of NiAl phase embedded in Ni_2TiAl matrix [85]. Therefore, the formation of a similar two-phase precipitate which is composed of B2-ordered NiAl and $L2_1$ -ordered Ni_2TiAl is a potential strategy to optimize the mechanical properties of precipitation-strengthened ferritic alloys.

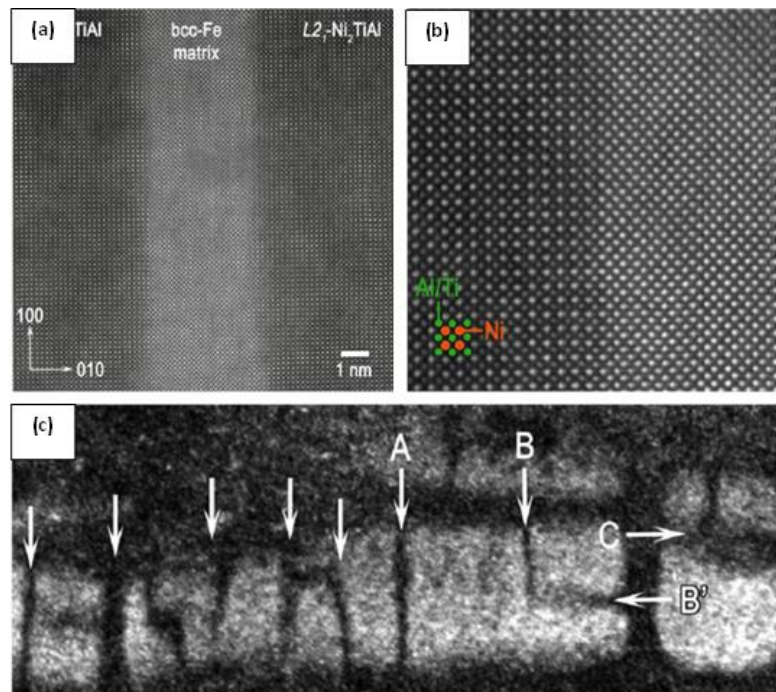


Figure 2-2 (a) An atomic resolution high-angle annular dark-field (HAADF)-scanning transmission electron microscope (STEM) image along the $[001]_{bcc-Fe}$ zone axis; (b) magnified HAADF-STEM image of the precipitate/matrix interface in (a); (c) Dark-field image of the precipitates using the unique $1\bar{1}\bar{1}$ reflection of $L2_1$ -ordered Ni_2TiAl phase where the B2-ordered NiAl zones are indicated by arrows [85].

2.2.3.4 Effect of Mn on the precipitation in Fe-Ni-Mn-Ti-Al steels

As discussed in Section 2.2.1, efforts of partial substitution of Ni by lean element such as Mn, which provides similar effects upon the austenite-martensite transformation, have led to the development of Fe-Ni-Mn-Ti-Al alloys. The increase of Mn content at the expense of Ni content is correlated to a considerable acceleration of the age hardening. A significant increase of hardness by ~200 VHN within 5 s was reported in an Fe-20Ni-1.8Mn-1.5Ti-0.59Al alloy aged at 550 °C and the yield strength increased by ~215 MPa to above 900 MPa [48]. Initially the co-clustering involving the Ti+Al and Mn+Fe was observed before the formation of plate-shaped $(\text{Ni,Fe})_3\text{Ti}$ precipitates and spheroidal $(\text{Ni,Fe})_3(\text{Al,Mn})$ precipitates after aging for ~60 seconds [46]. Out of these four alloying elements, Ti possesses the highest diffusion rate followed by Mn and Al, whereas Ni has the slowest rate. Therefore, the Ti-rich clusters normally acted as nuclei for the subsequent formation of $\eta\text{-Ni}_3\text{Ti}$ precipitates [46]. On the other hand, the $(\text{Ni,Fe})_3(\text{Al,Mn})$ precipitates were found predominantly at two sites: homogeneously within the matrix or the periphery of plate-shaped $(\text{Ni,Fe})_3\text{Ti}$ particles which indicated the segregation of Al and Mn at the interface between the $(\text{Ni,Fe})_3\text{Ti}$ phase and surrounding matrix (Figure 2-3). This segregation of Al+Mn atoms was attributed to the high thermodynamic affinity between Al and Mn [92][93][94] and the tendency of Mn atoms in steels to segregate on the interfaces [95][96].

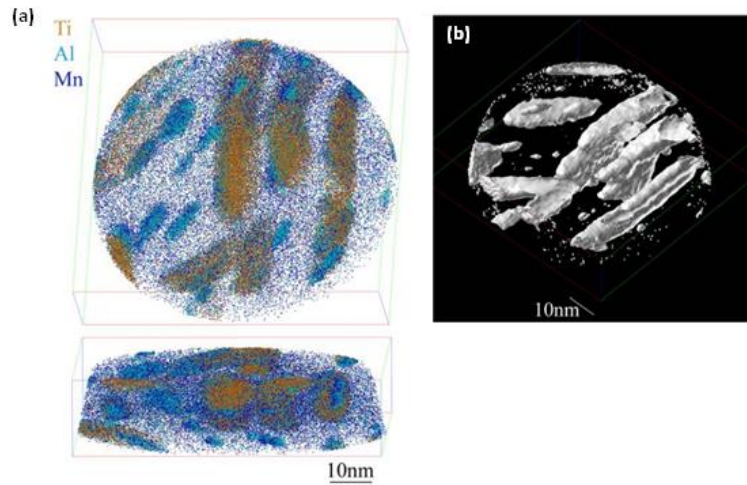


Figure 2-3 (a) Three dimensional atom probe tomographic reconstructions of rod-shaped precipitates after treated for 3600 seconds and (b) corresponding Ni+Ti isoconcentration surfaces [46].

2.2.3.5 Cu-rich precipitation strengthened steels

As Cu has limited solubility in Fe [97][98], Cu precipitates can serve as homogeneous nucleation sites for other precipitates [39][99]. It is also demonstrated that Cu accelerates the nucleation process due to a reduction in the activation energy when Cu is incorporated into precipitates [38][39]. Therefore, nano-sized Cu precipitates are extensively utilized in the development of precipitation-strengthened steels, and numerous studies have been carried out to study the hardening effect by Cu and Cu-rich precipitates [38][39][40][45][97][99][100][101][102][103][104].

Investigations on the Cu-containing steels revealed that Cu precipitates had a wide size range from 1 nm to 30 nm during aging [105][106]. Precipitation sequence was initiated with the rapid formation of metastable bcc copper phase which exhibited a spherical shape due to the coherency with bcc matrix [107]. The maximum hardness was achieved before Cu precipitates grew to the critical diameter of ~ 5 nm after which the precipitates gradually lost the coherency and transformed to an intermediate 9R structure [106][107]. The precipitate/matrix orientation relationship was proposed as $(11\bar{4})_{9R-Cu} \parallel (011)_{\alpha-Fe}$, $[\bar{1}10]_{9R-Cu} \parallel [1\bar{1}1]_{\alpha-Fe}$ [45][108]. The twinned 9R

precipitates maintained a spherical shape before coarsening to ~ 17 nm [105]. Then a more stable 3R structure followed by an equilibrium fcc structure were observed in Cu precipitates during further aging. The rod-like fcc Cu precipitates regained the untwinned structure and were aligned along the Kurdjumov-Sachs orientation relationship $((111)_{\text{fcc-Cu}} \parallel (110)_{\alpha\text{-Fe}}, [110]_{\text{fcc-Cu}} \parallel [111]_{\alpha\text{-Fe}})$ with the bcc matrix [100][102][105].

Despite of the advantages discussed above, steels strengthened by Cu precipitates suffered from low hardness and rapid precipitate coarsening during annealing. Therefore, minor additions of Ni, Ti, Al and Mn are introduced to develop the co-precipitation strategy so as to ultimately enhance the strengthening effect of Cu precipitates [38][40][102][109][110]. Two types of intermetallic precipitates, B2-ordered NiAl and $\eta\text{-Ni}_3(\text{Ti},\text{Al})$, were generated into Cu-containing maraging steels [38][39][40][45][102][103]. Experimental evidence revealed that the addition of Cu accelerated the nucleation of the two precipitates and in turn, the two phases restrained the coarsening of Cu precipitates.

It is worth discussing the different effects of Cu on the nucleation of the two precipitates. In the case of B2-ordered NiAl phase, approximately 10 at.% Cu was detected within the Ni+Al clusters in the as-quenched state [39] and this level remained constant during the following aging treatment. It is commonly believed that the incorporation of Cu reduced the nucleation energy by reducing the lattice misfit and thus promoted the precipitation of NiAl [38][39]. Moreover, Cu-rich NiAl precipitates exhibited a stability in both the size and morphology compared to the NiAl precipitates in Cu-free Fe-Ni-Al alloy [40]. In view of the rapid coarsening of both Cu precipitates and NiAl precipitates when present separately, it is supposed that there is an interaction effect between Cu and NiAl phase in terms of the resistance to coarsening.

On the other hand, a different Cu-rich precipitation behaviour was reported in other Fe-Ni-Al alloys [45][102][103]. The initial precipitation was similar as described above: short-range ordering occurred before aging followed by the formation of B2-ordered Ni-Al-Cu precipitates at the beginning of aging as shown in Figure 2-4(a) [45]. Then a decomposition of the primary precipitates led to a kind of core/shell

precipitates with Cu-rich core surrounded by a periphery enriched in Ni and Al (Figure 2-4(b) and (c)). The thermally stable B2-ordered shells hindered the diffusion-controlled growth of Cu-rich core, and more importantly, reduced the misfit between the fcc Cu-rich core and the bcc matrix, Figure 2-4(d) and (e) [45][102]. The low interfacial energy together with the atomic ordering of B2-ordered shells allowed the precipitates to grow moderately without sacrificing the high-density feature during further aging, and moreover provided a complex obstacle for dislocation motion [103].

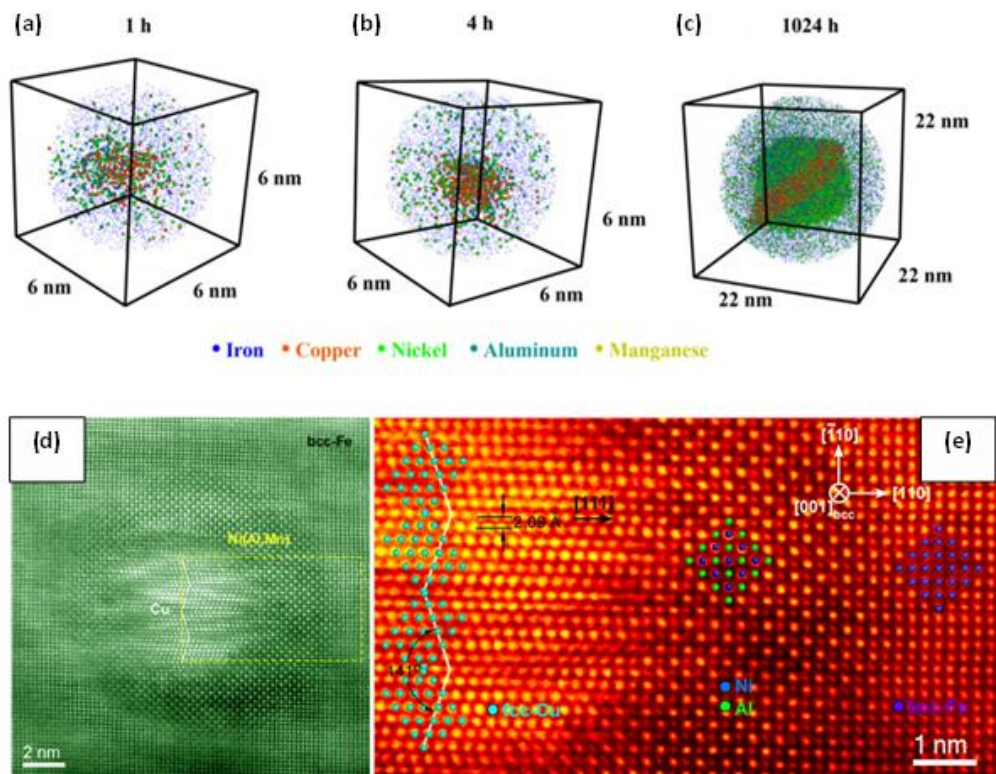


Figure 2-4 Atomic distribution of representative precipitates in the (a) 1 h, (b) 4 h and (c) 1024 h aging stages [102]; (d) HAADF image of the core/shell precipitates and (e) Enlarged HAADF image of yellow rectangle part in (d) [45].

In terms of the Ni_3Ti -strengthened steels, as the solubility of Cu in Ni_3Ti phase is much lower than that in NiAl phase, the independent Cu-rich clusters were usually observed in the beginning of aging and acted as nucleation sites for $\text{Ni}_3(\text{Ti},\text{Al})$ phase. The precipitation of $\text{Ni}_3(\text{Ti},\text{Al})$ occurred mainly adjacent to the Cu-rich clusters [39].

Other studies reported that the formation of η -Ni₃Ti in Cu-containing maraging steels was restrained when NiAl precipitates were also present, as Cu could only be incorporated in NiAl phase and thereby, to a larger extent, accelerating the formation of NiAl phase in the initial aging stage[38].

2.2.4 The Mn embrittlement in Fe-Ni-Mn and Fe-Mn alloys

As mentioned in Section 2.2.1, attempts have been made to develop cheaper alternatives to the conventional Ni-based maraging steels. Experimental studies on a series of Fe-Ni-Mn steels revealed that this type of steels exhibited a remarkable maraging strengthening owing to the formation of fine f.c.t θ -NiMn phase [111][112]. In some cases, the addition of Ti to Fe-Ni-Mn alloys was found to generate very fine and thermally stable Ni₃Ti precipitates [33]. Other phases such as MnNi, fcc Ni₃Mn and ordering were also considered as possible precipitation-strengthening contributor [113][114]. Therefore, this grade of steels used to be regarded as a promising alternative to conventional maraging steels.

Unfortunately, serious grain-boundary embrittlement was observed to occur at the very beginning of aging treatment in Fe-Ni-Mn steels [95][115][116][117]. A lot of researches were carried out on the source of grain boundary embrittlement and some possibilities have been proposed. It is generally accepted that the grain boundaries act not only as barriers against dislocation motion but also as zones where interface segregation may occur. More specifically, Raabe et al. [50] summarized the conceivable pathways by which the solute segregation could behave: (i) the segregation might increase the coherence and preferential bonding at the interface (grain boundary strengthening); (ii) the reverse could lead to a further loss of coherence and unfavourably directed bonding at the interface (grain boundary weakening); (iii) phase transformation might occur at the grain boundaries (grain boundary phase transformation); (iv) the formation of one or more second phases at the decorated interface could be initiated (grain boundary precipitation); (vi) discontinuous precipitation might be promoted.

Squires and Wilson [95] first stated that the intergranular fracture observed in an Fe-12Ni-6Mn alloy was associated with the segregation of embrittling elements like Mn

and P to prior austenite grain boundaries. A later study on a similar alloy complementally reported that the Ni and N were also found at the fractured grain boundaries [115]. Heo and Lee [117] tracked the segregation and desegregation of Mn at the prior austenite grain boundaries on the fracture surfaces of an Fe-8Mn-7Ni alloy in the embrittled condition. They pointed out that the embrittlement and de-embrittlement of the alloy was directly correlated to the segregation and desegregation of Mn, but they also suggested that considering the low enrichment level of Mn, such serious embrittlement was not likely to be solely attributed to the Mn segregation alone [92].

In contrast, Suto and Murakami argued that the slight segregation of Mn and Ni at grain boundaries detected would not result in the transition to brittle state [116]. Raabe and his colleagues [50] also hold an opposite opinion about the correlation between Mn segregation at grain boundary and mechanical behaviours. They believed that the embrittlement was associated with the susceptible crack penetration owing to the low mutual misorientation between adjacent lath boundaries [50]. Unfortunately, as the predominant interfaces in quenched martensite, a large amount of lath boundaries existed. However, given that the variation of bulk grain free energy was negligible, the primary thermodynamic driving force for solute segregation at interfaces was to minimize the interface free energy. As the decrease of the interfacial free energy reduced the driving force for grain growth, materials with reduced grain boundary energy were considered to have a finer and more stable grain size. Therefore, they proposed that the solute segregation at grain boundaries contributes to both strength and toughness by refining grain size, if the specific type of segregation does not lead to grain boundary embrittlement.

On the other hand, other studies suggested the intergranular embrittlement in Fe-Ni-Mn system as the result of the interaction of mobile dislocation with precipitates at grain boundaries. These researchers insisted that the precipitation on grain boundary was the main source of grain boundary failure in Fe-Ni-Mn maraging steels. Lee et al. [118] found θ -NiMn intermetallic precipitates at the grain boundaries in an Fe-10Ni-5Mn alloy when aging at 753 K for short time and this type of precipitate was initially suspected to be responsible for the embrittlement. Later studies conducted by Nedjad et al. [119][120] on Fe-10Ni-7Mn maraging steels confirmed the

correlation between the intergranular failure and precipitation reactions at grain boundaries. They further pointed out that the formation of coarse precipitates at grain boundaries resulted in the soft solute-depleted precipitate-free zones at grain boundaries. Then the large strain localization resulting from the grain boundary weakening triggered the microcracks initiation under negligible macroscopic strains. Alternatively, Mun et al. [113] observed the precipitation of austenite particles along grain boundaries in an Fe-7Ni-8Mn steel and it was assumed that the austenite-ferrite interface boosted the intergranular fracture. However, Wilson and his colleagues [37][121] argued that the driving force for Mn segregation to prior austenite grain boundaries was indeed to form precipitates and reverted austenite, but the primary factor of grain boundary embrittlement was still the segregation of Mn rather than precipitation or austenite reversion.

Binary Fe-Mn alloys in the range of 4-10 wt.% Mn, which possess a soft but heavily dislocated lath martensite after quenching, generally exhibit similar microstructural features to Fe-Ni-Mn maraging steels. Studies on their mechanical behaviours revealed that Fe-Mn alloys suffered from brittleness as well [121][122]. After cooling from the austenite phase field, brittle fracture occurred mainly by cleavage. While tempering at 250-500 °C increased the DBTT and the failure mode below DBTT was intergranular fracture. The maximum embrittlement was reported at 450 °C [121]. Elevated temperature, e.g. 600 °C, has shown to overcome the embrittlement due to a faster kinetics to form ductile austenite [50][28].

Therefore, the embrittlement is of key importance in the mechanical behaviour of Fe-Ni-Mn and Fe-Mn alloys. To understand the embrittlement mechanism can provide not only an insight into the alloying element interaction in these alloys during thermal treatment but also pathways to improve their possible commercial exploitation. However, to the author's best knowledge, the mechanism of intergranular fracture in Fe-Ni-Mn and Fe-Mn systems is still not clear yet and remains the subject of debate in the literature.

2.3 Evolution of precipitates

Generally, the precipitation process is generally described as successive nucleation and growth followed by coarsening. In this section, the discussion about precipitate evolution will mainly focus on the growth of nuclei and then on the coarsening.

2.3.1 Critical size in precipitation

The real precipitation process is always complicated. It is worth introducing several critical sizes during the evolution of precipitation before discussing the precipitation mechanism. The critical precipitate radius (r_c) below which the precipitate will dissolve is usually determined by [29]:

$$r_c = 2c_\alpha\Gamma/(c_0 - c_\alpha) \quad (2.1)$$

where c_α is the solute concentration in the matrix phase during aging, c_0 is the solute concentration in the matrix before aging. The capillarity constant Γ is described as [29]:

$$\Gamma = \frac{\sigma_{\alpha/\beta}N_A\Omega_\beta(1 - c_\alpha)}{RT(c_\beta - c_\alpha)} \quad (2.2)$$

where $\sigma_{\alpha/\beta}$ is the interfacial energy per unit area between the precipitate and matrix, N_A is Avogadro's number, Ω_β is the atomic volume of precipitates, c_β is the solute concentration in the precipitate, R is the idea gas constant and T is the absolute temperature.

The first critical precipitate radius r_{c1} is defined to distinguish the growth mechanism of precipitates above which the interfacial-limited growth is taken over by the diffusion-limited growth. After that, further precipitation results in another critical precipitate radius r_{c5} above which the diffusion-limited coarsening occurs. In Section 2.3.2, the detail about the growth and coarsening of precipitates will be discussed.

As the interfacial free energy $\sigma_{\alpha/\beta}$ (Equation (2.2)) varies depending on the nature of coherency, two more critical sizes, r_{c0} and r_{c3} , are introduced. r_{c0} is the critical

radius below which precipitates will dissolve when the interface is coherent and r_{c3} is the critical radius below which precipitates will dissolve when the interface is incoherent.

Another two critical sizes relating to the precipitation strengthening are also taken into consideration. r_{c2} stands for the critical radius above which the coherency strengthening starts to decrease, whereas r_{c4} indicates the critical radius above which the interaction between dislocation and the precipitate transforms from shear-cutting mechanism to looping mechanism.

In order to better understand the precipitation process, efforts have been made to sort out the order of these critical sizes. It is not difficult to understand that $r_{c1} < r_{c5}$ and $r_{c0} < r_{c2} < r_{c3}$. As r_{c0} and r_{c1} are very small, they are usually considered as zero [29]. In most cases, the Orowan looping occurs when precipitates are incoherent with the matrix, thus we can obtain $r_{c3} < r_{c4}$ (dislocation looping may also occur when the coherent precipitate is too large or strong to be cut through). Thus what is uncertain is the relationship of r_{c5} with the other three critical sizes r_{c2} , r_{c3} and r_{c4} and this will be further discussed in Section 2.3.4.

2.3.2 Growth and Coarsening of precipitates

During the early stage of precipitation, the nucleus is surrounded by a supersaturated matrix with a solute concentration gradient which provides the driving force for solute diffusion and promotes the precipitate growth. There are two factors which are considered to affect the growth rate: the interface reaction and the lattice diffusion [123]. When the average size of precipitates is below r_{c1} , as the distance of diffusion field is rather short, the interface reaction is the rate-controlling step. The precipitate size is proportional to the aging time: $\bar{r} = r_{c0} + G_0 t$ (Figure 2-5), where G_0 is the growth rate during the interface-limited growth. In the case of larger precipitates ($r > r_{c1}$), the driving force for lattice diffusion gradually decreases owing to the continuous depleting of solute atoms in the matrix, the diffusion becomes the rate-controlling step [123][124]. The relationship between the precipitate size and growth time follows the equation [29][125]:

$$\bar{r} = (r_{c1}^2 + 2D \frac{c_0 - c_\alpha^e}{c_\beta - c_\alpha^e} (t - t_1))^{1/2} \quad (2.3)$$

where D is the diffusion coefficient in the matrix, c_0 is the initial solute concentration, c_α^e is the equilibrium solute concentration in the matrix, c_β is the solute concentration in the precipitate and t_1 is the time the diffusion-limited growth starts.

At the end of the diffusion-limited growth period, Equation (2.3) cannot describe the dynamic evolution of precipitate size anymore which indicates that the diffusion-limited coarsening initiates. It is difficult to accurately distinguish the diffusion-limited growth and diffusion-limited coarsening. Generally, the diffusion-limited growth process is defined as a stage when the solute is from the surrounding matrix; whereas the solute for diffusion-limited coarsening is from the dissolving of smaller precipitates. According to the Gibbs-Thomson equation, the solubility of smaller precipitates which possess a larger ratio of surface area to volume is higher than that of larger precipitates. This size-dependent solubility results in a further size-dependent driving force for coarsening. Based on the Gibbs-Thomson equation, the growth rate is positive for large precipitates with $\bar{c} < c_R$ and negative for small precipitates with $\bar{c} > c_R$, namely, larger precipitates grow at the expense of smaller precipitates which dissolve back into the matrix. Therefore, the coarsening process is featured by the decrease of number density and the broadening of size distribution. But in reality, coarsening may take place simultaneously with the growth process or even in the nucleation stage if the initial solid solution supersaturates [124]. In addition, due to the increase in the distances of diffusion field, the size increment rate in the coarsening stage is slower than that in the growth stage (Figure 2-5). The precipitate size in most coarsening process obeys the LSW (Lifshitz and Slyozov [126] and Wagner [127]) theory which suggests the time exponent is 1/3 (Figure 2-5).

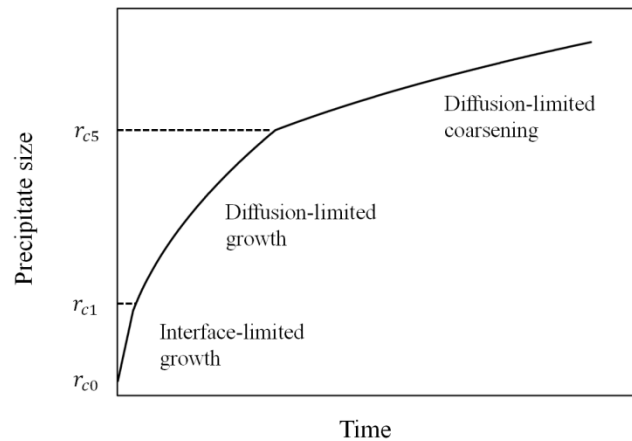


Figure 2-5 The evolution of precipitate size during aging in terms of precipitation kinetics, after [29].

2.3.3 Precipitate coarsening theory

Although it is difficult to describe the coarsening of randomly dispersed precipitate, Lifshitz and Slyozov [126] and Wagner [127] developed a theory attempting to interpret the diffusion-limited coarsening. The theory which is referred to as LSW theory has later achieved great success in the experiment application. Certain assumptions are made to confine the application [124][128]:

1. Dilute solution theory applies and the linearized version of the Gibbs-Thomson equation is valid.
2. Diffusion fields of precipitates do not overlap and the particles only interact with the matrix, thereby limiting the precipitate volume fraction to zero.
3. Coarsening takes place in a stress-free matrix.
4. Precipitates possess a spherical morphology.
5. The composition of precipitates is the same as given by the equilibrium phase diagram.

Based on the above assumptions, the LSW theory provides three equations to describe the diffusion-limited coarsening. The first equation predicts the increase of the average precipitate radius, \bar{r} , with respect to the coarsening time according to:

$$\bar{r}^3 - r_{c5}^3 = \frac{8DV_\beta\sigma_{\alpha/\beta}}{9(c_\beta^e - c_\alpha^e)^2 G_\alpha''} t \quad (2.4)$$

where D is the diffusion constant, V_β is the molar volume of β phase, $\sigma_{\alpha/\beta}$ is the interfacial energy per unit area between the precipitate and matrix, c_α^e and c_β^e are the equilibrium solute concentration in the matrix and precipitates respectively, G_α'' is the second derivative of the molar Helmholtz energy of the α phase.

The second equation reveals that the decrease in the precipitate number density, N_V , follows:

$$N_V \cong \frac{3f_p}{4\pi K_R f_3} t^{-1} \quad (2.5)$$

where f_p is the volume fraction of precipitate, K_R is the coarsening rate constant in Equation (2.4) and f_3 is the third moment of the time-independent precipitate size distribution function $f(r/\bar{r})$ when $V_p \rightarrow 0$ (will be discussed later).

The relationship between the solute concentration within the matrix, C_i^α , and coarsening time is derived:

$$\Delta c = \frac{9(c_\beta^e - c_\alpha^e)}{4D} K_R^{2/3} t^{-1/3} \quad (2.6)$$

Numerous experimental studies on two-phase alloys have been carried out to examine the LSW coarsening theory. Advanced techniques such as CTEM[76][129], HREM, STEM and HAADF-STEM [45][130] provide direct observations of the local structural characteristics. In some studies, small-angle X-ray scattering (SAXS) and small-angle neutron scattering (SANS) approaches are applied for the quantitative analyses of average precipitate size, interparticle distance and volume fraction based on huge numbers of precipitates [97][131][132]. Moreover, SAXS can also provide information about the chemical heterogeneity of precipitates [133][134]. Recently, state-of-the-art APT offers not only an accurate quantitative measurement of precipitates [130][135] but also a three dimensional observation on the atomic distribution within the material. If combined with the complementary studies on the resistivity and hardness evolution, global information about the coarsening of precipitates can be obtained.

Most of these experimental studies revealed that the experimental plot of \bar{r}^3 or N_V^{-1} vs. t roughly fitted the straight lines given by LSW theory. However, experimental results also indicates that the shapes of size distribution function are much broader than that of the theoretical $f(r/\bar{r})$. This deviation has later been demonstrated to be associated with the non-zero volume fraction of precipitate in reality. Therefore, many studies have been carried out to modify the LSW theory for better applications in cases where the volume fraction of precipitate has to be taken into consideration. The major challenge of this work is to determine the effects of interparticle diffusional interactions on the coarsening behaviour of a precipitate with a specific size. Modified theories [136][137][138][139] are all in agreement that the exponents of the Equations (2.4), (2.5) and (2.6) and the time-independence of precipitate size distribution will not change when the volume fraction of precipitates is taken into consideration. However, the values of K_R and K_N along with the shape of size distribution function will change. According to the modified theories, with the increase of precipitated volume fraction, the average distance of diffusion field become shorter and thus the concentration gradients will be larger, thereby resulting in the increase of the coarsening rate. Besides, the local diffusional interactions give rise to spatial correlations between adjacent precipitates which further leads to the broadening and symmetry of size distribution function.

2.3.4 The effect of precipitate size on precipitation strengthening

It is easy to get confused when discussing the relationship of coherency, coarsening and strengthening mechanism. It is generally thought that in the under-aged stage the growth of coherent precipitates leads to an increase in the strength with shear-cutting mechanism. While in the overaged stage, the coarsening of precipitates results in the incoherency and thus activates the looping softening mechanism. Although most precipitation-strengthened alloys obey this rule, there are several concepts which are confusing.

First, the term ‘strengthening’ is usually utilized to describe the strength increase in the underaged stage and ‘softening’ means the decrease of strength during the

overaged stage. But it is worth noting that, the strength at both of the two stages is higher than that before aging, therefore both of two terms are actually defined as strengthening mechanisms.

Secondly, although the softening during the overaged period is generally considered to result from lose of the coherency, a number of studies have shown that the extremely large coherent precipitate and the modulus difference between the precipitate and matrix can also lead to the decrease of strength. In the case of large precipitates, considerable flexing of dislocation occurs owing to the increase of the interparticle spacing (assuming the volume fraction of precipitate is constant), thereby resulting in the coherency softening. Namely, the coherency softening may occur before the lose of coherency. Another possible is the modulus difference which is suggested to result in the softening as well, but so far there is no experimental evidence to support this viewpoint yet [29].

Thirdly, the strengthening mechanism is only associated with the precipitate size regardless of how the precipitate approaches the critical size, by growth or coarsening. It means that r_{c2} and r_{c4} are irrelevant to r_{c5} . But according to Sha and Guo's conclusion [29], the value of r_{c2} should be somewhere between r_{c1} and r_{c5} .

Based on the discussion, a more comprehensive precipitation-strengthening process is comprised of three stages: when the precipitate is small, coherency strengthening takes effective by cutting mechanism, the strengthening effect increases with the precipitate size; with the growth of precipitate size, the stress required to cut through precipitate is so high that Orowan looping mechanism takes place. Orowan strengthening is inversely related to the interpartical spacing, so initially the precipitate growth which reduces the interpartical spacing lead to the Orowan strengthening. The following coarsening of precipitate featured with the decrease of number density and thus the increase of interpartical spacing results in the Orowan Softening mechanism. On the other hand, the structure of the interface is also very important. For example, if the precipitates are small but have incoherent interface, the looping mechanism take place. Conversely, if the precipitates have a large size but coherent interface and a small misfit strain, the shearing will be the dominant mechanism.

It is worth emphasizing that apart from the coherency mechanism and modulus mechanism, there are more strengthening mechanisms, such as chemical (softening), stacking-fault (strengthening), order (strengthening), etc. As the effects of these mechanisms on the strengthening are irrelevant to the precipitate size, they are not taken into consideration when discussing the relationship between the strengthening and precipitate size.

2.4 Austenite reversion in maraging steels

As previously stated, engineering steels suffer from the fact that the increase of strength generally corresponds to a decrease in ductility. This inverse strength-ductility relationship largely limits their application as structural materials. In order to overcome this problem, dual-phase microstructure, such as hard martensite with ductile ferrite or austenite which can coordinate during deformation, is developed. Moreover, for steels containing austenite, the deformation-induced martensitic transformation of austenite under external load can provide additional strength and elongation. This type of steels has now found wide applications in the body frame sector of automotive manufacture. Their high strength-to-weight ratio, low yield-to-ultimate strength ratio, high initial work hardening rate and good formability make them particularly suitable for this application [140].

Austenite in steels is generally derived from two different processing technologies. The austenite phase retained after cooling from two-phase field is known as retained austenite and it has been investigated extensively in TRIP steels [141][142][143][144]. Austenite phase which is formed by a partial reversion from martensite when aging at two phase field but a lower temperature is defined as reverted austenite [145][146][147]. Compared to retained austenite, reverted austenite normally provides more significant microstructural synergy with martensite, as it creates thin compliant interlayers along both prior austenite grain boundaries and martensite lath boundaries.

The influence of reverted austenite on the mechanical properties of maraging steels has been investigated by many studies. Conventionally, the intermetallic precipitates in maraging steels are thought to be the main contributor to the strength

enhancement upon aging [31][48][148][149][150][151]. However, it has been gradually recognized that reverted austenite formed in some maraging steels also has a pronounced effect on the mechanical properties [18][19][20][145][152][153]. It is proposed that [121]:

1. Austenite can act as a sink for impurities; in this case, reducing N and P embrittlement during heat treatment.
2. The ductile phases, ($\gamma+\epsilon$ (ϵ martensite)), may act as compliance layers or mechanical buffer regions impeding crack propagation otherwise prevalent along the $\{100\}$ planes of martensite laths, which has been considered to improve toughness and reduce DBTT [36].
3. Transformation of austenite to martensite may occur during deformation which also improves toughness.

2.4.1 Influence of reverted austenite on mechanical properties

Many researches have been carried out to study the effects of reverted austenite on mechanical properties in maraging steels. Vylezhnev et al. [153] proposed that the poor ductility at low temperatures in a 18Ni maraging steel resulted from the fracture of reverted austenite along martensite lath boundaries. Viswanathan et al. [19] noticed that the austenite reversion in a 18Ni maraging steel corresponded to the decrease in both yield strength and ultimate tensile strength but the increase in ductility at the initial overaged stage. Vijay et al. [54] attributed the high strength after long-term aging in a Co-free, high-Ti 18Ni maraging steel to the high coarsening resistance of precipitates and a small amount of reverted austenite, whereas in the case of a Co-containing, low-Ti 18Ni maraging steel, the high volume fraction of reverted austenite are considered to result in the loss of strength at long aging times. Overall, the debate on this issue has been chaotic for years. However, recent researches tend to hold the same opinion that the formation of reverted austenite can lead to the increase of strength and toughness in Co-free maraging steel. Nakagawa et al. [20] reported a significant improvement in the balance of strength and ductility during the overaged stage in Cu-containing maraging steels, and they suggested this improvement is due to the increase in the amount of reverted austenite.

Raabe et al. [18], reported a significant increase in both strength and ductility upon aging in a 9 wt.% Mn maraging TRIP steel with the ultimate tensile strength increased by 25% (from 810 MPa to 1 GPa) and total elongation increased by more than 150% (from 6% to 15%), which is considered as a result of nano-precipitation and nano-scale austenite reversion.

As revealed by these researches, the mechanical properties is directly associated with the quantity of austenite. An appropriate quantity of reverted austenite can lead to a good balance between strength and toughness. Generally, the quantity of austenite is determined by the chemical composition, aging temperatures and durations [27][18]. In addition to the quantity, the stability of reverted austenite also plays a critical role in the mechanical properties of maraging steels. As the literature about the stability of reverted austenite is limited, retained austenite may be discussed alternatively in this study. In TRIP and Q&P steels, retained austenite with proper stability to induce martensitic transformation is desirable. Retained austenite with low stability would transform at small strains and cannot improve the ductility; whereas extremely high stability does not lead to the TRIP effect and contributes little to ductility either. The stability of austenite is generally governed by the chemical composition [154][34][155][156][157][158][159], temperature [160][161], size [154][34][158][159][162][163], morphology [164][165], adjacent microstructure [157][159][165] and crystallographic orientation relationship [166][167][168][169]. The following part will discuss reverted/retained austenite in terms of these factors.

2.4.1.1 Composition

The chemical driving force for martensitic transformation of austenite involving the most potential austenite stabilizing elements, carbon and manganese, is described as [170]:

$$\Delta G^{ch} = -7381.6 + 19296X_{Mn} + 69447X_C - 38776X_{Mn}X_C + (6.7821 - 33.45X_C)T \quad (2.7)$$

where ΔG^{ch} is the chemical driving force for martensitic transformation, X_{Mn} is the mole fraction of manganese, X_C is the mole fraction of carbon and T is the absolute temperature. As shown in Equation (2.7), the increase in the mole fraction of

manganese and carbon leads to the increase of the driving force for martensitic transformation at specific temperature, namely, the addition of carbon and manganese is beneficial to the stability of austenite.

Similarly, Ni, as another efficient austenite stabilizer, contributes to the austenite stability as well; whereas elements which are defined as ferritic stabilizer, such as Ti and Al, are demonstrated to decrease the austenite stability.

2.4.1.2 Temperature

The effect of temperature can be expressed by the equation [142]:

$$\frac{\partial \Delta G^{ch}}{\partial T} = 6.7821 - 33.45X_c \quad (2.8)$$

According to the Equation (2.8), a positive fluctuation in ΔG^{ch} is expected when a positive fluctuation in temperature occurs with a constant carbon content, i.e. austenite is more stable at higher temperature. This view point has been confirmed by tensile tests conducted at a range of temperatures which reveals the variation of austenite stability depending on temperatures [160][161].

2.4.1.3 Size

Yang and Bhadeshia described the relationship between austenite grain size and M_s temperature as:

$$M_s^0 - T = \frac{1}{b} \ln \left[\frac{1}{V_\gamma} \left\{ \exp \left(\frac{\ln(1 - f_M)}{m} \right) - 1 \right\} + 1 \right] \quad (2.9)$$

where the constant b is 0.2689 for α' -martensite [162] and 0.19 for ε -martensite [26], V_γ is the average grain volume of austenite, f_M is the volume fraction of martensite, m is the aspect ratio of the martensite (α' -martensite: 0.05; ε -martensite: 0.03), and T is the temperature at which f_M is measured. In this equation, $M_s^0 - T$ becomes $M_s^0 - M_s$ if f_M is set to be the first detectable fraction of martensite, $V_\gamma \rightarrow \infty$ and so $M_s \rightarrow M_s^0$. According to their conclusion, the small size of austenite suppresses the M_s temperature and therefore contributes to the stability of austenite. The size effect on the austenite stability in steels has been extensively investigated by experiment as

well. In carbon TRIP steels, both experimental results and thermodynamic modelling have demonstrated that M_s temperature decreases as the carbon concentration of retained austenite increases or the mean size of retained austenite decreases [161]. In Mn-containing TRIP steels, it is shown that the size effect of ultrafine austenite grain and the partitioning of Mn to austenite during intercritical annealing were the two primary reasons for the high mechanical stability of retained austenite [34].

In contrast, recent work by Wang et al. [171] reported that small austenite grains were less stable against the deformation-induced martensitic transformation in a 9 wt.% Mn TRIP maraging steel. They suggested the deformation-induced martensitic transformation was suppressed by the mechanical twinning in larger austenite grains while in smaller austenite grains, mechanical twinning is less favoured. Other work [166] proposed that because the intrinsic strength of austenite is lower than that of the martensite matrix, a parabolic distribution of the von Mises stress exists in reverted austenite, namely the stress in the outer layer is higher than that in the centre. Besides, there is an inverse distribution of austenite stabilizing element concentrations in the reverted austenite grains. Hence, it is easier for the outer layer of reverted austenite to transform into martensite during the deformation. Generally, the fraction of the outer layer region is smaller in the reverted austenite with a larger dimension and so it is proposed that the larger reverted austenite is more stable than the smaller one.

2.4.1.4 Morphology

Reverted austenite, which is distinguished from retained austenite, exhibits different morphologies [146][147]. Evidence indicates that the morphologies are correlated to the alloy compositions and processing paths [147]. Reverted austenite in maraging steels generally appears either an elongated or granular shape. More specifically, reverted austenite is classified into three types, i.e. matrix austenite, lath-like austenite and recrystallized austenite [146]. Matrix austenite is defined as an austenite phase that either develops from retained austenite and thus has the same orientation, or grows at the prior austenite grain boundaries and forms a single austenite grain (Figure 2-6(a)). Lath-like austenite can be generated along and within the martensite laths, thereby generating a lamellar structure of alternate austenite

laths and residual martensite laths (Figure 2-6(b)). Recrystallized austenite normally nucleates at high aging temperatures or after long aging times and it is characterized by a polygonal shape with low dislocation density, as shown in Figure 2-6(c). In addition, in high Ni alloyed and Ti-containing maraging steels, a type of Widmanstätten austenite was reported to become dominant when aging at high temperatures for a long time [52][172]. In terms of its effect on the austenite stability, the morphology does not directly affect the mechanical stability of austenite, it is actually the adjacent microstructure that determines the mechanical stability of reverted austenite and this will be discussed in the next section.

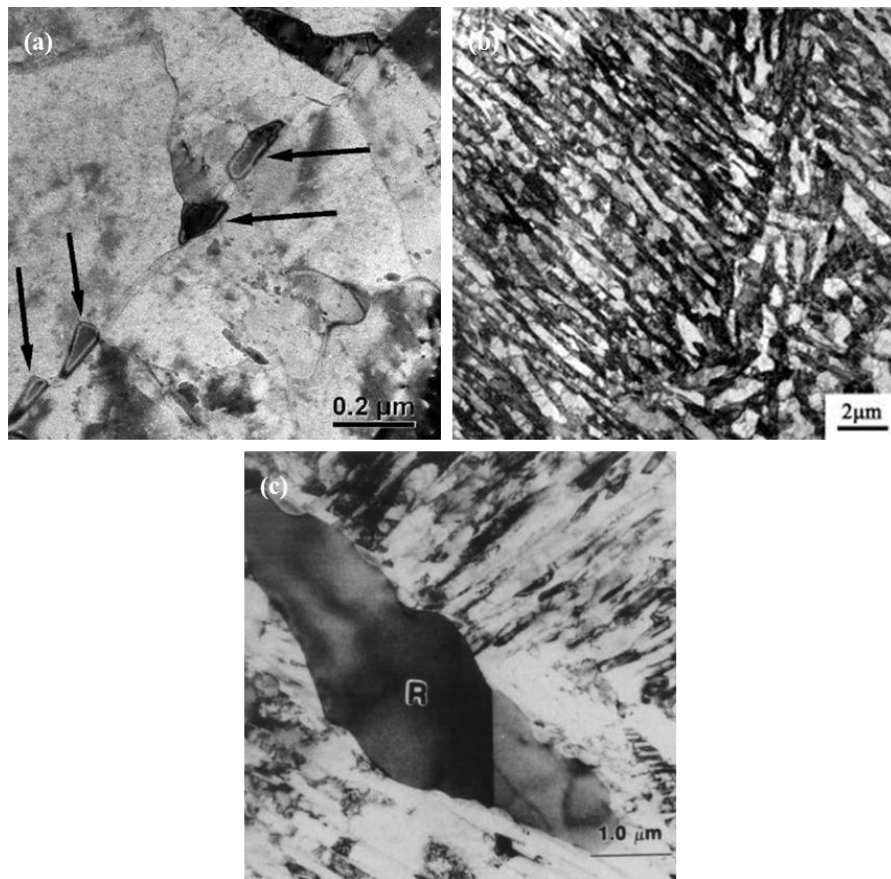


Figure 2-6 (a) Matrix austenite at prior austenite grain boundaries [147] (b) the lamellar structure of alternate lath-like austenite and residual martensite [27] and (c) a recrystallized austenite grain free of defects [146].

2.4.1.5 Adjacent microstructure

Many studies on TRIP and Q&P steels reveal that the stability of retained austenite is also associated with the adjacent microstructure [142][164][165][173]. For example in TRIP steels, retained austenite in bainitic ferrite is found more stabilized than that in polygonal ferrite. Two possible mechanisms are given to explain this phenomenon. Grajcar [173] stated that the retained austenite surrounded by bainitic ferrite had a shorter diffusion path to carbon atoms and thus was more thermally stable. Another explanation is that the bainitic ferrite can stabilize retained austenite by stress partitioning. The stress partitioning mechanism points out that a harder phase adjacent to retained austenite can decrease the hydrostatic stress without affecting the equivalent stress, which in turn decreases the mechanical driving force for transformation as following [155]:

$$\frac{\partial \Delta g^\sigma}{\partial \bar{\sigma}} = -0.715 - 0.3206 \frac{\sigma_h}{\bar{\sigma}} \quad (2.10)$$

where σ_h is the hydrostatic stress and $\bar{\sigma}$ is the equivalent stress. The harder bainite may restrain the phase transformation of retained austenite as the adjacent bainite would have to deform so as to coordinate the volume expansion resulting from the martensitic transformation. Therefore, compared to polygonal ferrite, the harder bainitic ferrite can better shield the retained austenite located nearby and suppress phase transformation. It is worth noting that the morphology of retained austenite in bainitic ferrite is different from that in polygonal ferrite which may also be a reason for the difference in stress partitioning.

A similar mechanism was proposed on the stability of retained austenite in a Q&P steel [164]. According to their study, the martensitic transformation occurred at the onset of deformation in blocky retained austenite surrounded by proeutectoid ferrite; while film-like retained austenite in lath martensite, despite having a lower carbon content, is more stabilized against deformation. Apart from the martensite/bainite shielding effect, Jacques et al. [157] speculated that the small size effect of film-like retained austenite, may also contribute to the higher mechanical stability of retained austenite. The discussion on multi-phase steels is never simple as the mechanical stability of austenite is generally determined by more than one factor.

2.4.1.6 Crystallographic orientation relationships

Different crystallographic orientation relationships have been found between fcc and bcc crystals. Three relationships, i.e., Kurdjumov-Sachs (K-S) relationship [52][146][174][175], Nishiyama-Wassermann (N-W) relationship [146][176][177] and Pitsch relationship [178] are the most commonly known relationships in steels. A summary of these orientation relationships is displayed in Table 2-1 [169]. The Bain orientation relationship is the simplest one among those relationships, but has rarely been observed in steels. It is shown here as a reference relationship when discussing the orientation relationship. The Pitsch orientation is usually regarded as ‘inverse NW’ orientation. To better explain these orientation relationships, the crystallographic structures are illustrated in Figure 2-7 [179]. The orientation relationships are interpreted by presenting the crystallographic planes and directions of the two phases. For example, in the case of Kurdjumov-Sachs (K-S) relationship, it is specified as one $\{111\}_\gamma$ plane being parallel to one $\{100\}_\alpha$ plane and a $\langle 100 \rangle_\gamma$ direction within the $\{111\}_\gamma$ plane being parallel to a $\langle 111 \rangle_\alpha$ direction within the $\{100\}_\alpha$ plane.

The numbers of variants for each orientation relationship are also given in Table 2-1. For example in K-S relationship, there are four different $\{111\}_\gamma$ planes, each $\{111\}_\gamma$ plane has three different $\langle 110 \rangle_\gamma$ directions and each $\langle 110 \rangle_\gamma$ has two different $\langle 111 \rangle_\alpha$ directions which are parallel to it. Therefore, there are 24 variants for K-S orientation relationship in total. The variants of orientation relationships between fcc and bcc phases are important when analysing the twinned austenite in bcc ferrite.

$\langle uvw \rangle / \omega_{\min}$, in the last column of Table 2-1, are the parameters to describe the misorientation between two crystallographic orientations. As the most reported orientation relationships, the difference in angular between K-S and N-W relationships is small, so distinguishing the two relationships by misorientation in experiment is difficult. As shown in Figure 2-7, the $\{111\}_\gamma$ plane is parallel to the $\{011\}_\alpha$ plane in the two types of orientation relationships (K-S: Figure 2-7(b); N-W: Figure 2-7(c)) and the misorientation between the NW variants and any of the two neighbouring KS variants is only 5.26° .

Table 2–1 Overview of the different orientation relationships between fcc and bcc crystals [169].

	Orientation relationship	Number of variants	$\langle uvw \rangle / \omega_{\min}$
Bain (B) [180]	$\{100\}_{\gamma} \parallel \{100\}_{\alpha}$ $\langle 100 \rangle_{\gamma} \parallel \langle 110 \rangle_{\alpha}$	3	$\langle 100 \rangle / 45$
Kurdjumov-Sachs (K-S) [174]	$\{111\}_{\gamma} \parallel \{110\}_{\alpha}$ $\langle 110 \rangle_{\gamma} \parallel \langle 111 \rangle_{\alpha}$	24	$\langle 0.97 \ 0.18 \ 0.18 \rangle / 42.85$
Nishiyama-Wasserman (N-W) [176][177]	$\{111\}_{\gamma} \parallel \{110\}_{\alpha}$ $\langle 112 \rangle_{\gamma} \parallel \langle 110 \rangle_{\alpha}$	12	$\langle 0.98 \ 0.08 \ 0.20 \rangle / 45.98$
Pitsch (P) [178]	$\{100\}_{\gamma} \parallel \{110\}_{\alpha}$ $\langle 110 \rangle_{\gamma} \parallel \langle 111 \rangle_{\alpha}$	12	$\langle 0.08 \ 0.20 \ 0.98 \rangle / 45.98$

Given that the only difference between the two orientation relationships is the rotational angle, it is proposed that the K-S and N-W relationships may co-exist in steels. But studies are in debate on the relatively dominant position between K-S and N-W relationships in steels [143][168][181][182][183]. Katz et al. [184] reported both of the two orientation relationships existed between reverted austenite and martensite matrix in 18Ni maraging steels. Shiang and Wayman [146], who also noticed the two relationships, suggested that the dominant orientation relationship was correlated to the aging temperatures. Suk et al. [167] found that reverted austenite had a specific orientation relationship not only with the surrounding martensite but also with the adjacent precipitates. In addition, the twinned austenite, which has been observed in both maraging steel [185][186] and dual-phase stainless steel [187], was found obeying the K-S orientation relationship [167]. The N-W orientation relationship, however, has not been found yet between the twinned austenite and martensite.

Although some researchers stated that the orientation effect of fcc phase on the strength is negligible [188][189][190], there are others who held a different view [166][191]. It is accepted that the local stress is heterogeneous at the microscopic level when the phase orientations and activated slip systems are taken into consideration. Wang et al., who studied the mechanical stability of reverted austenite in a 13%Cr-4%Ni martensitic steel, suggested that the stress at the α/γ interface with N or K-S relationships was much lower than that without N or K-S relationships [166] and they attributed the difference to the activation of the slip systems. The activation of slip system is normally affected by two factors. One is the external load, the other one is the interaction between phases. In the case of austenite/martensite, plastic strain occurs in the austenite earlier than martensite during deformation due to its lower critically resolved shear stress. Wang et al. [166] stated that when the slip system was activated in reverted austenite, it can penetrate the boundaries and activate the slip system in the adjacent martensite easily with the assist of N or K-S relationship. It means that if the special N or K-S relationship exists, a smaller slip strain in austenite is required to activate the slip systems of the surrounding martensite, and thus the local stress of austenite will decrease to a lower level. On the other hand, when the N-W or K-S relationship is absent, it needs higher stress and strain accumulation in austenite to activate the slip system of nearby martensite. However, the accumulated stress in austenite is highly likely to induce martensitic transformation and hence result in a lower mechanical stability of austenite.

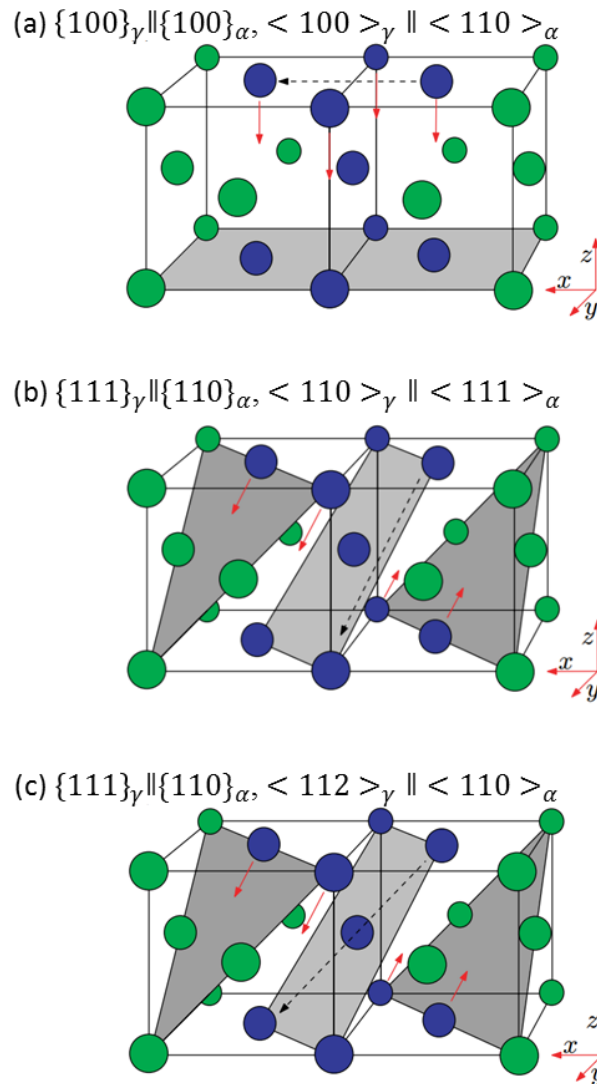


Figure 2-7 Different orientation relationships between fcc and bcc phases: (a) Bain, (b) K-S, and (c) N-W. Blue atoms belong to bcc unit cell and green atoms belong to fcc unit cell [179].

2.4.2 The formation mechanism of reverted austenite

It has been acknowledged that the formation of granular reverted austenite is associated with a diffusion-controlled process. The granular reverted austenite is deemed to result from the dissolving of cementite or precipitates which leads to the enrichment of austenite stabilizing elements in localized areas [27][147][192]. On the other hand, the formation mechanism of lath-like reverted austenite is

controversial [146]. Plichata and Aaronson supposed that the growth of lath-like austenite was also controlled by diffusion [193]. Sinha et al. [194] further pointed out that, instead of precipitate dissolution, the diffusion of Ni atoms in matrix to dislocations or other defects generated the local enrichment of austenite stabilizing elements. Schnitzer et al. [147], Nakagawa et al. [20] and Sinha et al. [194] reported the value of activation energy for reverted austenite formation was about 234-250 kJ/mol which is in the range of the activation energy of Ni diffusion in pure Fe (246 kJ/mol [195]). Conversely, some researchers suggested the formation of lath-like reverted austenite to be a shear-dominated process but assisted by a diffusion mechanism [52][146]. They believed that due to the segregation of solute elements to preferential locations, the reverse transformation start temperature (A_s) at these sites reduces to below the aging temperature. Phase transformation involving shear deformations, which is also referred to as displacive phase transformation, is expected to occur in the similar way as bainitic transformation [172]. The lattice correspondence for this phase transformation normally obeys K-S or N-W relationships. Besides, the twinned lath-like austenite in some maraging steels is another evidence for the occurrence of a shear motion in austenite reversion [146][172]. Lee et al., who studied the austenite reversion in both Fe-3Si-13Cr-7Ni (wt.%) martensitic stainless steel and medium Mn steels, suggested that the formation mechanism of reverted austenite was heating-rate related. Below the critical heating rate (10 K/s for Fe-3Si-13Cr-7Ni martensitic stainless steel and 15 K/s for medium Mn steels), the austenite reversion process was diffusion-controlled and the reverted austenite presented a globular shape with a diameter of 200–250 nm. Besides, a lower dislocation density and a higher Mn concentration were observed in this type of reverted austenite. When the samples were heated faster than the critical heating rates, the phase transformation occurred by a diffusionless shear mechanism. Reverted austenite presented a lath-like shape with 200–300 nm in width and 400–700 nm in length. They also mentioned that despite the diffusionless reverted austenite had a high density of dislocation, it yielded lower mechanical stability owing to the lower Mn concentration and larger grain size. In addition, it is worth noting that, $\alpha' \rightarrow \gamma$ transformation as well as bainitic transformation [196] is not

universally accepted to be shear-controlled. Further studies on the mechanism of $\alpha' \rightarrow \gamma$ transformation are needed to support this viewpoint.

It is suggested that some transformation-induced deformation may be induced during the formation of reverted austenite, and the stored strain energy may act as a driving force to cause recrystallization [146]. For steels in which retained austenite also exists, austenite reversion is governed by the competition between the nucleation of new reverted austenite and the growth of existing retained austenite. There are two mechanisms relating to the $\alpha' \rightarrow \gamma$ transformation, i.e. abnormal $\alpha' \rightarrow \gamma$ transformation and normal $\alpha' \rightarrow \gamma$ transformation [192]. The abnormal $\alpha' \rightarrow \gamma$ transformation proposes that the retained austenite grains within one prior austenite grain normally have the same orientation, therefore their growth may result in the coalescence and further, a reconstruction of the original prior austenite grain boundaries (Figure 2-8(a)). This process is called as the austenite grain memory effect (also known as austenite recrystallization). While the normal $\alpha' \rightarrow \gamma$ transformation proposes that newly formed reverted austenite cannot coalesce as these austenite grains have different orientations.

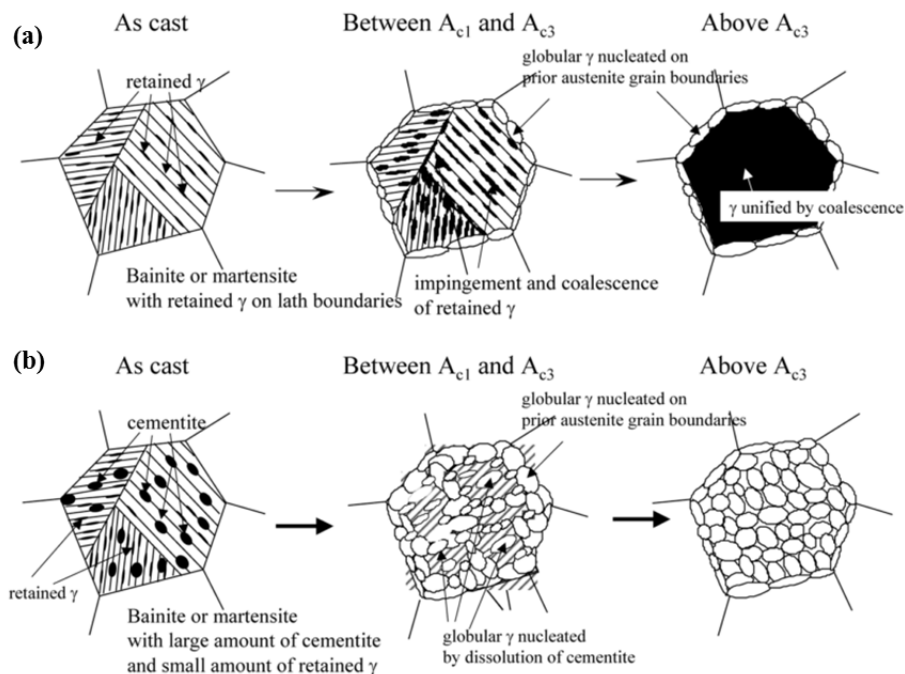


Figure 2-8 Schematic illustration of (a) abnormal $\alpha' \rightarrow \gamma$ transformation and (b) normal $\alpha' \rightarrow \gamma$ transformation [192].

2.5 Grain refinement in maraging steels

It is commonly known that there is an inverse relationship between strength and toughness. One of the methods to improve both simultaneously is the grain refinement. The famous Hall-Petch equation expresses the relationship between yield stress and grain size [197]:

$$\sigma_y = \sigma_0 + k_y d^{-1/2} \quad (2.11)$$

where σ_y is the yield stress, σ_0 is the intrinsic friction stress of an undeformed single crystal oriented for multiple slip, k_y is the Petch constant representing the resistance against the slip propagation across grain boundary and is generally specific to materials, d is the grain size [198].

The fracture strength, which is derived from dislocation theory [199][200] and classical Griffith theory [201], is an indication of the resistance to the propagation of a crack around a dislocation pile-up grain boundary:

$$\sigma_f = 4G\gamma_m k_y^{-1} d^{-1/2} \quad (2.12)$$

where σ_f is the fracture strength, G is the shear modulus, γ_m is the surface energy. According to Equation (2.12), it is apparent that both the yield stress and fracture strength increase when the grain size is refined.

In addition, since σ_0 is strongly dependent on the temperature, σ_y increases significantly as the temperature reduces; whereas σ_f is much less affected by the temperature. Consequently, the critical DBTT, T_c , is introduced when $\sigma_y = \sigma_f$ as:

$$T_c = C^{-1} \ln[Bk_y d^{1/2} / (\beta G \gamma_m - k_y^2)] \quad (2.13)$$

where C , B and β are constants [202]. According to Equation (2.13), T_c can also be decreased by refining grain size.

2.5.1 Conventional methods to refine grains

Thermomechanical processing, as one of the most well-known methods for grain refinement, has been intensively studied in various alloys. It has been demonstrated

that the extraordinary improvement in both strength and toughness can be obtained in steels by refining grain size to $< 1 \mu\text{m}$ via thermomechanical processing [203]. However, in the steel industry it is difficult to perform a uniform plastic deformation through the thickness of plates to produce uniform ultrafine grain size [204]. Therefore, in the case of thick plate steels (or bars and weldments, etc.) with high strength, alternative methods such as cyclic heat treatment are introduced to refine grain size.

2.5.2 Effective grain size in lath martensitic steels

In ferritic steels, as the cleavage normally occurs along $\{100\}_\alpha$ planes [204], the effective grain size, in terms of transgranular cleavage fracture, is determined as the coherent length on $\{100\}_\alpha$ planes, or the average free path of crack propagation along $\{100\}_\alpha$ planes [203].

In martensitic steels, the definition of effective grain size is more complicated. The interfaces in quenched martensite can be classified into several types: prior austenite, martensite packet, block and lath boundaries. They generally possess different energies, structures, misorientations, mechanics and segregation properties [50]. The effective grain size is correlated to the prior thermal processes. A typical microstructure of martensitic steel is illustrated in Figure 2-9. The prior austenite grains are divided into packets of fine, parallel distributed martensite laths (Figure 2-9(b)). The thickness of laths is generally at nano-scale. Electron diffraction studies revealed that the laths within a packet are in close crystallographic alignment and the lath boundaries are low-angle boundaries [204]. It means that the martensite packet is actually a single crystal. Therefore, the size of the packet is defined as the effective grain size of lath martensite.

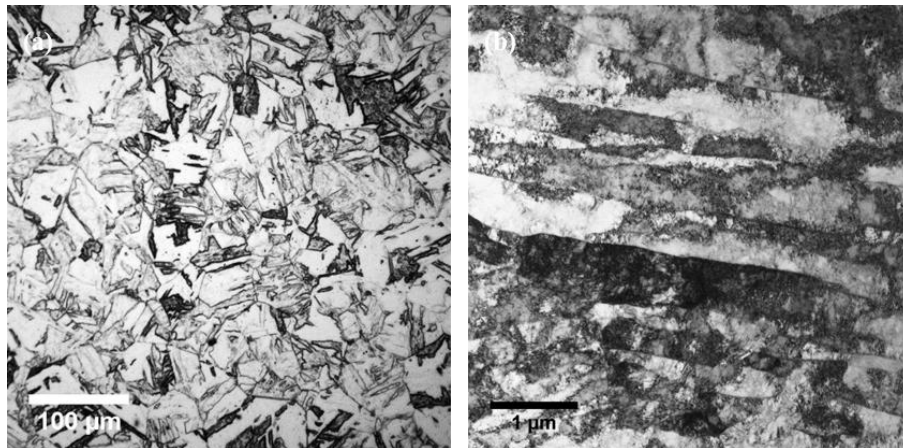


Figure 2-9 (a) The typical microstructure of a martensitic steel constituted by packets of martensite laths, (b) the dislocated laths which is at nano-scale in thickness. Both are the micrographs of a 10% Mn maraging steel after water quenching from solution heat treatment.

2.5.3 Methods of grain refinement in lath martensitic steel

If taking account of the effective grain size of lath martensite, there are mainly three approaches to refine the grain size of martensitic steel. The most common method is by refining the prior austenite grain size. The practical heat treatment to realize it is by quenching from austenization before the austenite grains coarsen, but it has been demonstrated that this method can hardly refine the prior austenite grain size further below 10 μm [203].

A more direct method is to generate high-angle misorientation between the adjacent laths and thereby breaking up the crystallographic alignment of laths within the packets [205]. Although this method seems to be the most direct way to completely refine the effective grain size, it is difficult to control in production. This is owing to the difficulty to design the martensitic transformation and the crystallographic relationships of martensite laths by thermal treatment.

Based on the second approach, the third approach for grain refinement is to form a new phase at boundaries, such as austenite, so as to separate the martensite laths. This type of austenite islands is required to be very thin and remain stable during heat treatment. This is generally achieved by intercritical tempering (in most cases, a

temperature just above A_{c1} is desirable). This mechanism of improving toughness via austenite reversion is a matter of debate. One possible explanation is that the formation of austenite, which generally has K-S or N-W orientation relationships with adjacent martensite, introduces high-angle misorientation between phases. Even when the metastable austenite transforms into martensite during deformation, the fresh martensite with different variant can still disrupt the crystallographic alignment of laths. This method has been widely used to in medium-Ni and medium-Mn steels [27][24][156][206] by Q&P treatment or in maraging steels by aging process [18][19][145][146].

Chapter 3 Materials and Experimental Methods

3.1 Alloys and processing details

3.1.1 Alloys and Composition Analysis

The present study is mainly focused on investigating the microstructure and mechanical properties of Mn-based maraging TRIP steels and hereby developing new alloy compositions to improve the properties. Three as-cast steels, namely, two (10 wt.% Mn, 12 wt.% Mn) based on the compositions mentioned in Ref. [18] with minor addition of Al (1 wt.%) and one with lower Mn content (7 wt.% Mn) were provided by Tata Steel. The chemical compositions of alloys are listed in Table 3–1. The low carbon content (<0.04 wt.%) is to achieve a soft but heavily dislocated martensite after water quenching. Minor elements, such as Ni, Mo, Ti and Al are added to form precipitates. Compared with the conventional 18Ni maraging steels, the main difference exists in the content of austenite stabilizer Mn. 7-12 wt.% Mn are added to ensure that an appropriate amount of austenite is obtained with appropriate stability and yet being substantially lower than the Mn contents in the twinning-induced plasticity (TWIP) steels.

Table 3–1 Chemical compositions (wt.%) of the investigated Mn-based steels

Materials	C	Mn	Ni	Mo	Al	Ti	Si	Cr	Co	Fe
7% Mn	0.033	7.07	2.03	1.03	1.04	1.05	0.07	<0.005	<0.001	bal.
10% Mn	0.015	9.97	2.03	1.19	1.00	0.84	0.07	0.02	0.008	bal.
12% Mn	0.022	11.77	1.97	1.17	1.00	0.82	0.08	0.03	0.009	bal.

3.1.1 Hot rolling and heat treatment procedure

The equilibrium γ/α transformation temperatures (A_{e3}) of 7%, 10% and 12% Mn alloys were calculated as 722 °C, 644 °C and 614 °C, respectively. In order to

minimize the detrimental effect of coarse carbide, the three ingots were first homogenized under argon gas atmosphere at 1150 °C for 1 h and hot rolled between 1140 °C and 850 °C. The thickness of ingots was reduced from 20 mm to 3 mm with six passes and the corresponding reduction ratio was 85%. Inter-stage re-heating to 1150 °C was performed after every two passes. The detailed parameters for hot rolling process are presented in Table 3–2. The subsequent solution heat treatment (SHT) was carried out with argon protection at 1050 °C followed by water quenching. After SHT, the samples were then aged at 420 °C, 460 °C and 500 °C for a range of times from 10 minutes to 168 hours (Figure 3-1).

Table 3–2 Parameters for hot rolling process

Temperature (°C)	1140	1040	1090	950	1030	860
Thickness reduction (mm)	20-14	14-10	10-7	7-5	5-4	4-3
Reduction ratio	30%	28.6%	30%	28.6%	20%	25%

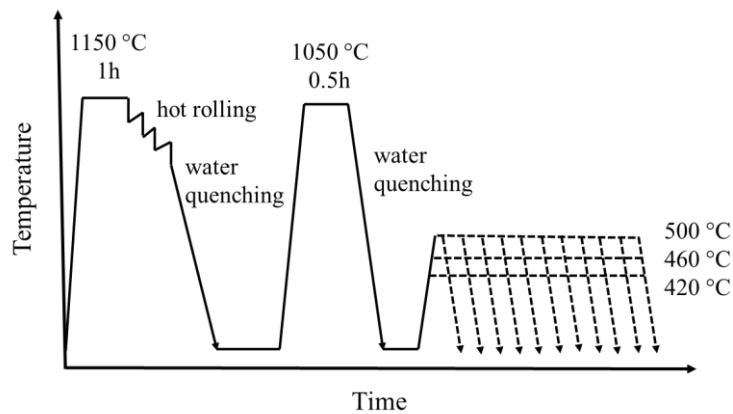


Figure 3-1 Schematic diagram of processing conditions

3.2 Sample preparation

3.2.1 Mircopreparation

All hot-rolling and heat-treatment pieces for characterization were cut from bulk samples after each processing procedure. To avoid deformation-induced phase transformation, all the aged materials were cut by IsometTM 5000 with feeding speeds of 2-4 mm/s. Small pieces of samples were then hot mounted with Bakelite for optical and scanning electron microscopy (SEM) observation. Samples without Bakelite were prepared for X-ray diffraction (XRD) and transmission electron microscopy (TEM) analyses. The subsequent mechanical grinding and polishing process needed to be carefully controlled as any inappropriate operation may induce undesired phase transformation. The grinding operation was carried out successively on 240, 400, 800 and 1200 grade silicon carbide papers with running water. The manual polishing operation was performed on 6 μm and 1 μm polishing cloth with corresponding diamond suspensions. Some techniques such as nanoindentation and electron backscatter diffraction (EBSD) demand an excellent sample surface finish, in these cases, 0.04 μm colloidal silica (silco) suspension was used for the final polishing. Silco suspension has a slight etching effect, thereby being able to remove the residual strain layer from the manual grinding and polishing procedure. The load, rotation speed and duration for each step of grinding and polishing varied depending on the surface condition. Generally a small load (10N) for approximately 5 minutes was desired for final polishing. All the samples were rinsed and dried with isopropanol after each step and final cleaning was done using ultrasonic agitation.

3.2.2 Etching

The 2% nital is the most widely used etchant for general steels. In this study, 2% nital worked effectively on hot-rolled and solution-treated samples, but failed to reveal the reverted austenite in aged samples. It was eventually found that picric acid can clearly distinguish reverted austenite from martensite matrix. The picric acid etchant was a mixed solution of 75 mL saturated picric acid and 25 mL wetting agent. The etching process was performed at 60-70 °C for a few seconds. The etching

temperature and duration was dependent on the amount of reverted austenite. Normally, a lighter etch than the conventional picric acid etch for the observation of prior austenite grain boundaries observation was more appropriate in this study.

3.2.3 TEM thin foil preparation

TEM thin foil samples were prepared by two methods, in which electropolishing was the mainly used one in this study. The bulk samples were manually ground to foils below 150 μm thick. Disks with a diameter of 3 mm were then punched and further thinned to 50-80 μm . Electropolishing was conducted with 5% perchloric acid, 35% butoxyethanol and 60% methanol solution (maintained at approximately $-40\text{ }^{\circ}\text{C}$ by a liquid nitrogen cooling system) running through a twin-jet electropolisher operated at 25-35 V (being adjusted to ensure the current of $\sim 40\text{ mA}$). The whole process lasted approximately 2-3 minutes depending on the operation parameters (such as temperature, jet speed and sensitivity, etc.) and stopped once the foil was perforated. Then the foil was cleaned immediately and stored by methanol.

High quality TEM thin foil can be obtained with carefully controlled parameters for most of steel samples. However, in this study, reverted austenite in aged samples was found disappeared after electropolishing. In this case, a combination of electropolishing with ion milling techniques was employed. Thin foils were thinned by electropolishing and stopped manually before perforation. Then ion milling was performed on Gatan model 600 or Fischione model 1010 for a few hours. Usually a voltage of 3 kV and milling angle of 6° were used for final thinning. Ion milling can be utilized to remove contamination and oxide layer before TEM observation as well.

3.2.4 Carbon extraction replicas

Precipitates, which are normally at the nano-scale size range, can be easily recognized under TEM by using carbon extraction replica, and thus be characterized by selected area electron diffraction (SAED) and energy-dispersive X-ray spectroscopy (EDS) in the absence of bulk matrix. The matrix is generally considered to absorb or overlap the faint signals of precipitates due to their small amount. In order to conduct accurate investigation on nano-size precipitates without

interference from the surrounding matrix (especially in this study the electron beam was distracted by the magnetic field introduced by martensite), carbon extraction replicas were prepared and examined by TEM. Firstly, the polished sample was cleaned carefully by ultrasonic agitation to exclude the particles retained from diamond polishing suspension. Precipitates embedded in the matrix were revealed by etching lightly with picric acid (at 60-70 °C) for approximately 10 seconds. The sample was then coated with amorphous carbon film, usually a thin carbon film is desired for TEM analysis. The carbon film which evaporated small particles from the matrix was scratched into 2mm squares. Then the sample was immersed into 10% nital to dissolve the matrix until the carbon film started to bubble and left the surface with the particles (Figure 3-2) [207]. The 400 square copper meshes were then used to catch those carbon film squares.

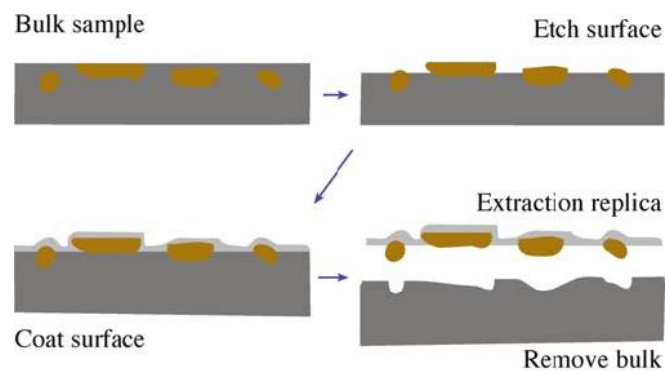


Figure 3-2 Schematic steps of making the carbon extraction replication [207].

3.3 Characterization techniques

3.3.1 Qualitative and quantitative analyses by X-ray diffraction (XRD)

Samples of hot-rolled, solution-treated and aged steels were examined by XRD for phase identification and evaluating the volume fraction of austenite. Samples were cut into pieces with a size of 20 mm × 20 mm × 3 mm. The subsequent metallographic preparation has been described in Section 3.2.

X-ray diffraction work was performed on Siemens D500 Diffractometer using Co K_{α} radiation ($\lambda = 1.78897 \text{ \AA}$) and Siemens D5000 using Cu K_{α} radiation ($\lambda = 1.54178 \text{ \AA}$). Both two diffractometers were operated at the condition of 40 kV and 40 mA. Samples were step scanned (0.02° per step) by a beam size of 0.2 mm covering a range of 2θ angles. For quantitative phase analysis, more than two sites of each sample were scanned. XRD data were collected by WinXPOW (D500) and DIFFRAC plus XRD commander (D5000), respectively. The analyses were undertaken using ICDD PDF-4+.

X-ray diffraction (XRD) measurement was applied to identify the austenite (face-centred cubic, fcc) in martensite matrix (body-centred tetragonal, bct). It is worth noting that, to simplify the discussion, α' -martensite was treated as ferrite (body-centred cubic, bcc) thermodynamically and kinetically in this study. But elevated elemental diffusivity should be taken into consideration when studying the kinetics of phase formation. The XRD patterns were compared to standard diffraction patterns by software to identify phases. Analogous to the illustration in Section 3.3.4.2, each phase has characteristic X-ray peaks which allow them to be identified. The accurate d-spacings were calculated using Bragg's law, $\lambda = 2d\sin\theta$ (λ is the wavelength of target radiation and θ is half of the angle where the peak presents).

XRD technique is considered as one of the most accurate and convenient methods to evaluate the volume fraction of austenite in steels. In this study, the volume fraction of austenite was calculated via comparison method described by Yang et al. [208] and the ASTM standard E975-03 [209]. Specific XRD patterns for each crystalline phase were produced during irradiation. For example, α' -martensite (211) crystalline plane peaks at 82° while austenite (220) crystalline plane peaks at 74° when a Co target is used. The volume fraction of austenite was measured by comparing the integrated intensity of austenite and α' -martensite. For a randomly oriented sample, the integrated intensities of the austenite (γ) and ferrite (α) diffraction peaks are determined by:

$$I_{\alpha}^{hkl} = \frac{KR_{\alpha}^{hkl}V_{\alpha}}{2\mu} \quad (3.1)$$

$$I_{\gamma}^{hkl} = \frac{KR_{\gamma}^{hkl}V_{\gamma}}{2\mu} \quad (3.2)$$

where K is the constant related to the instrumentation geometry and radiation. R is proportional to the theoretical integrated intensity which depends on the interplanar spacing (hkl), Bragg angle θ , crystal structure and composition of the phase. V is the volume fraction of each phase and μ is the linear absorption coefficient of steels.

Therefore, any pair of ferrite and austenite hkl peaks can be written as

$$\frac{I_{\alpha}^{hkl}}{I_{\gamma}^{hkl}} = \frac{R_{\alpha}^{hkl}V_{\alpha}}{R_{\gamma}^{hkl}V_{\gamma}} \quad (3.3)$$

For steels which contain carbides (or intermetallic precipitates in this study),

$$V_{\alpha} + V_{\gamma} + V_c = 1 \quad (3.4)$$

The volume fraction of austenite can be described as

$$V_{\gamma} = \frac{1 - V_c}{1 + \frac{R_{\gamma}^{hkl} I_{\alpha}^{hkl}}{R_{\alpha}^{hkl} I_{\gamma}^{hkl}}} \quad (3.5)$$

It is implied by Equation (3.5) that the volume fraction of austenite is not much influenced by the presence of carbide. For example, when the volume fraction of carbide is 10 vol.%, the volume fraction of austenite is calculated as 9 vol.% by Equation (3.5). While if the carbide is ignored ($V_c = 0$), the volume fraction of austenite is calculated as 10%. But the volume fraction of carbide has to be taken into account when it is over 15 vol.%. In this case, the volume fraction of carbide is normally measured by chemical extraction and metallographic methods or currently TEM and APT techniques are utilized to obtain a more accurate result.

In this study, the integrated intensities of ferrite peaks (200) and (211) and austenite peaks (200), (220) and (311) were measured by ICDD PDF-4+. Calculated theoretical intensity ratios $\frac{R_{\gamma}^{hkl}}{R_{\alpha}^{hkl}}$ using Co K_{α} radiation are illustrated in Table 3–3 [208].

If assuming $V_c = 0$ in Equation (3.5), the volume fraction of austenite can thus be averaged from 6 pairs of ferrite and austenite peaks.

Table 3-3 Calculated theoretical intensity ratios $\frac{R_{\gamma}^{hkl}}{R_{\alpha}^{hkl}}$ using Co K $_{\alpha}$ radiation [208]

	(200) $_{\gamma}$	(220) $_{\gamma}$	(311) $_{\gamma}$
(200) $_{\alpha}$	2.46	1.32	1.78
(211) $_{\alpha}$	1.21	0.65	0.87

3.3.2 Grain size analysis by optical microscopy

Hot-rolled and solution-treated samples for optical observation were prepared as described in Section 3.2.1 and 3.2.2. Optical observation was then undertaken on a Polyvar Optical Microscope to image the prior austenite grains and martensite packets.

Grain size in this study was measured using the linear intercept method. The principle of this method is to count numbers of grain boundaries per unit length. First, parallel lines are drawn on the image of the microstructure as illustrated in Figure 3-3. The number of times each line cross grain boundaries is counted. Thus, the average grain size \bar{L} is given by:

$$\bar{L} = \frac{L_{Total}}{N_L} \quad (3.6)$$

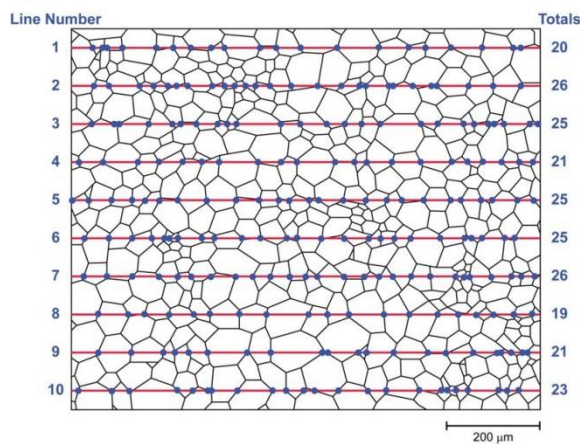


Figure 3-3 Schematic diagram of linear intercepts for the measurement of grain size.

For the grains which are equiaxed, parallel lines can be drawn along random orientation as long as there is sufficient space larger than the grain size between lines. When the grains are not equiaxed, such as deformed materials, lines should be drawn in the rolling direction and the short transverse direction separately. The average grain size should be measured in two separate directions as well.

3.3.3 Scanning electron microscopy

The aged samples for SEM observation were manual prepared with the same standard as samples for optical observation. The picric acid etch was used to reveal reverted austenite and precipitates. The fracture behaviour of the three alloys in different conditions was also investigated by SEM. The fresh fracture surfaces of samples after tensile testing were examined to provide information about the fracture modes and the cause of fracture. In order to further study the damage mechanisms in microscopic level, the microstructure of the fractured samples was also observed by SEM. In addition, the volume fraction of reverted austenite after tensile tests was analysed by X-ray diffraction.

A FEI InspectF FEG-SEM equipped with EDS was utilized for both imaging and EDS analysis. The working conditions were dependent on the characterization purposes. An operating voltage of 15 kV was usually used for microstructural observation and EDS analyses, whereas 10 kV was usually set for fractography.

3.3.4 Transmission electron microscopy

TEM technique was mainly used to analyse the nanoscale features like precipitate and reverted austenite in this study. The morphology, size distribution and composition of precipitates and reverted austenite were examined by conventional transmission electron microscopes. Due to the overlap of diffraction spots between fine precipitates and bcc matrix, high resolution electron microscopy (HREM) was used to explore precipitates. TEM observation was conducted on four different microscopes which are Philips EM 420 operated at 120 kV (for SAED analysis), FEI Tecnai operated at 200 kV (for microstructural observation and EDS analysis), JEOL 2010F at 200 kV (HREM and TEM-EDS) and aberration-corrected FEG JEOL

Z3100R05 at 300 kV (HREM and scanning transmission electron microscopy (STEM)).

3.3.4.1 Identification of the crystal structure by SAED

The crystal structure of precipitates is of vital importance for the study of precipitation-strengthened materials as the structure of precipitates, to a large extent, determines their properties and thus their roles in precipitation-strengthened materials. SAED is one of the most frequently used experimental tools to identify the crystal structure of ultrafine phases which cannot be detected by XRD or SEM. Electron diffraction pattern is unique to the crystal structure and the patterns can provide information about the size and shape of the unit cells and atomic positions in the unit cell as well.

It is known that Bragg's conditions are satisfied when the Ewald sphere cuts a reciprocal lattice point specified by the indices of the reflecting plane, see Figure 3-4.

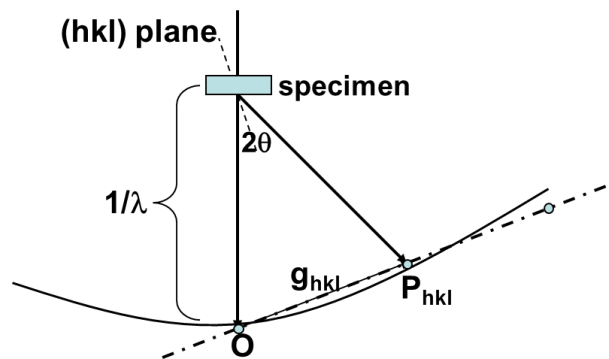


Figure 3-4 The construction of Ewald sphere after [207].

The Bragg's law is given as

$$\sin\theta = \frac{g/2}{1/\lambda} = \frac{\lambda}{2d_{hkl}} \quad (3.7)$$

where O is the origin of the reciprocal lattice;

P_{hkl} is the points of reciprocal lattice;

λ is the wavelength of the electrons, which is determined by the accelerating voltage.

d_{hkl} is the crystal lattice spacing between atomic planes;

θ is the angle between the incident beam and the reflecting planes.

As Figure 3-5 reveals, the distance (r) between the transmitted beam and diffracted beam as measured on the screen is determined by the camera length L ,

$$\tan 2\theta = \frac{r}{L} \quad (3.8)$$

when $\frac{1}{\lambda} \gg g$, it can be expressed as,

$$\tan 2\theta \approx \sin 2\theta \approx 2\theta \quad (3.9)$$

combined with the Bragg equation (Equation (3.7)), d_{hkl} can be obtained

$$d_{hkl} = \frac{L\lambda}{r} \quad (3.10)$$

$L\lambda$ is known as camera constant.

After measuring the nearest r_1, r_2, r_3 , crystal lattice spacing d_1, d_2, d_3 can be calculated using Equation (3.10).

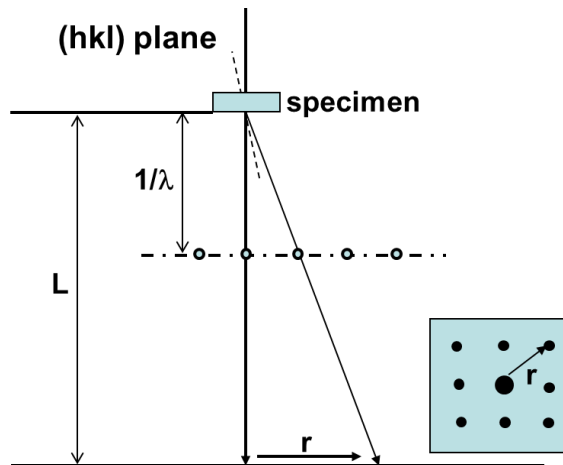


Figure 3-5 The geometric relationship between reciprocal lattice and electron diffraction pattern after [207].

3.3.4.2 Quantitative EDS analysis

It is known that the most straightforward method to study an unknown phase is to identify its elemental constituents. The first step is the qualitative EDS analysis. The further quantitative analysis would be meaningless if the identification of element is inaccurate. The principle of qualitative energy-dispersive X-ray analysis is simple. When the incident beams interact with the host atoms, the secondary electrons escape and leave holes in the electron shells. To stabilize the energy of atoms, electrons from outer shells transfer into the inner shells, thus the X-rays with characteristic energy are emitted from the atoms. For example in an iron atom, when the K shell electron is replaced by an electron from L shell, a 6400 eV K_{α} X-ray is emitted from the sample, or a 704 eV L_{β} X-ray is emitted if L shell electron is replaced by the M shell electron. Namely, each element has characteristic X-ray peaks which allow them to be identified. In addition, since elements with lower atomic number have fewer filled shells, normally they have fewer X-ray peaks.

In general, it is necessary to remove Bremsstrahlung X-rays and spectral artefacts in order to obtain the integrated intensities for quantitative analysis. In so-called standardless quantitative or semi-quantitative analysis, a Gaussian fit of the elemental peaks is performed to obtain the peak intensities. The most popular algorithm is ZAF where Z is the atomic number of the element, A is the absorbance coefficient and F is the fluorescence efficiency. The peak intensities are then converted into weight or atomic percent by sensitivity factors created by taking account of the accelerating voltage of the beam. Instead of fitting a Gaussian profile, fully standardized quantification compares the areas under the peaks to standard files which are reference spectra of the elements collected under the same conditions on the same instrument. As it requires the additional standard spectra, the fully standardized quantitative analysis is time-consuming. It is commonly considered that the advantage of this form of analysis is evident only in the situation when the peaks of the elements overlap or when quantifying the trace elements. Therefore, the quantitative analysis in this study was performed by the standardless analysis which has been proved reliable.

3.4 Mechanical property testing

3.4.1 Vickers hardness measurement

Vickers indentation was performed to measure the hardness of samples in different conditions. Hardness tests were carried out on a CV-430AAT Manual Vickers Hardness Tester with a load of 294 N (30kg) and indentation time of 15 s. Each result was averaged from at least eight measurements.

It is commonly accepted that the strength is in a direct proportion to the Vickers hardness values. Therefore, the strength can be roughly predicted by the Vickers hardness results which are easier to obtain. Dieter [210] reports the conversion equation by which the yield strength can be evaluated:

$$\sigma_y = \frac{H}{3} \quad (3.11)$$

Cahoon [211] presented the expression relating the ultimate tensile strength σ to hardness:

$$\sigma = \frac{H}{2.9} \left(\frac{n}{0.217} \right)^n \quad (3.12)$$

where H (MPa) is obtained by multiplying the Vickers hardness values by 9.807;

n is the strain hardening coefficient.

3.4.2 Tensile testing

Tensile testing was performed to examine the mechanical response of materials and to further study the deformation mechanisms, damage mechanisms and their relationships to the microstructure. All the tensile tests were conducted at room temperature on a Zwick Roell Z050 tensile testing machine at a constant cross head velocity corresponding to an initial strain rate of 0.002 s^{-1} . Flat rectangular tensile samples were machined along the longitudinal direction based on ASTM standard. The dimensions of tensile test samples are given in Figure 3-6. The thickness is thinned to approximately 1.5 mm in order to remove the oxide surface from the preceding heat treatment. The tensile strain was recorded by an attached video

extensometer. Two special stickers attached within the gauge portion of the tensile samples were constantly captured in the video and the distance between them was tracked in real time.

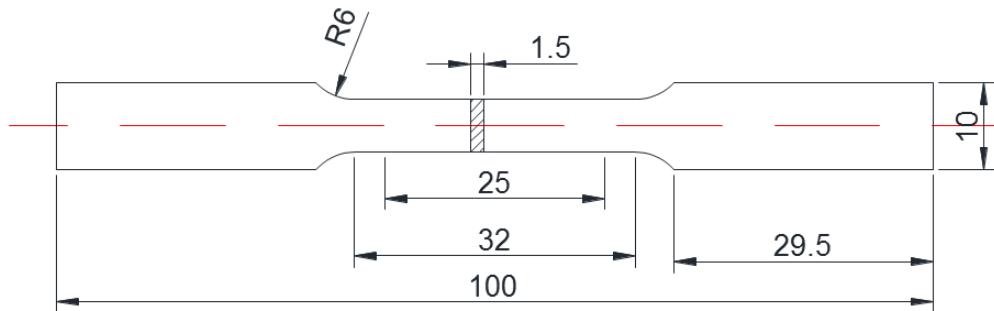


Figure 3-6 Geometry of the standard rectangular tension test sample.

3.4.3 Nanoindentation

As phases are deemed to have different strength, the mechanical response of different phases in the steels was examined by nanoindentation. This technique is based on indenting the selected area with a small load by an indenter tip with a specific geometry. The Berkovich tip is commonly used with the tip radius being at the range of 50-100 nm for a new indenter, see Figure 3-7(a). Since identifying the small area for indentation can be quite difficult, atomic-force microscopy (AFM) or SEM is usually used to image the microstructure and indents. Different from calculating the contact area by measuring the dimensions of indents in the conventional indentation tests, the size of residual impression in nanoindentation is on the order of nanometres and is too fine to be accurately measured even with microscopes. Therefore the depth of penetration is alternatively recorded during nanoindentation [212]. Together with the recorded force, a load-displacement curve can be obtained as shown in Figure 3-8 and different mechanical properties can therefore be evaluated:

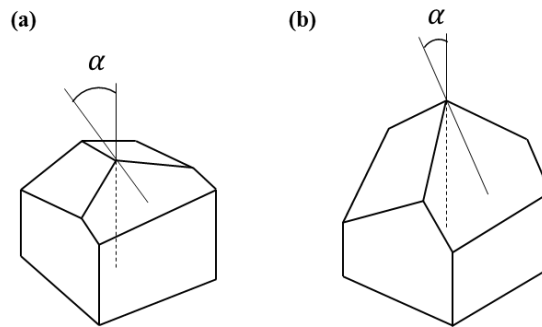


Figure 3-7 (a) a standard Berkovich indenter where $\alpha = 65.03^\circ$; (b) a standard cube corner indenter where $\alpha = 35.26^\circ$.

In this study, reverted austenite displays an elongated shape with the width of approximately 50-100 nm which is difficult to measure with conventional hardness testing. Thus nanoindentation was used to reveal the effects of aging parameters on martensite and austenite phases, respectively. In addition, the contribution of each phase to the strength can also be evaluated. For nanoindentation testing, aged samples were manually polished and etched with picric acid to reveal the microstructure under AFM. A cube corner tip (Figure 3-7(b)) was used for testing the ultrafine austenite grains. A $10 \mu\text{N/s}$ up to a maximum indentation load of $70 \mu\text{N}$ was employed in this study.

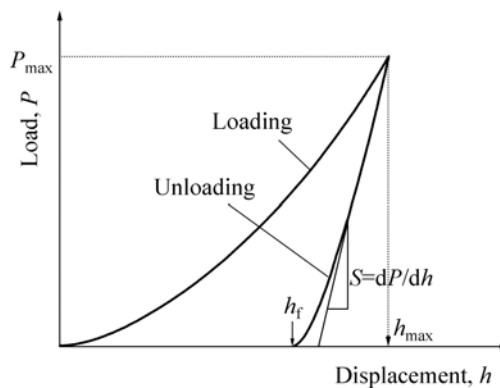


Figure 3-8 A typical schematic of load-displacement curve for nanoindentation test.

Chapter 4 Brief study on microstructure and mechanical properties of Mn-based maraging steels

The Mn-based maraging steels studied in this work contain Ni, Ti, Al and Mo which are deemed to form intermetallic precipitates. The precipitation, which occurred during aging, is expected to increase the strength of martensite, and consequently is referred as martensite aging hardening or maraging. On the other hand, the high Mn content in this type of steel promotes the formation of reverted austenite during aging which is believed to affect the mechanical properties as well. In this chapter, the mechanical behaviour of Mn-based maraging steels in various conditions is evaluated by hardness and tensile testing. The mechanical differences among the three alloys are compared and analysed. The equilibrium phases as a function of temperature are predicted by MatCalc software and XRD analyses are conducted to identify the phase constitutions. Based on these studies, a general concept about the newly-developed maraging steels is presented.

4.1 Thermodynamic calculation

Figure 4-1 presents the equilibrium phase volume fractions as a function of temperature, which was calculated by MatCalc using MC_FE_V2.0 database. The dominant equilibrium phases at the aging temperatures of 420-500 °C are ferrite and austenite. According to MatCalc, The only precipitate phase formed in the two-phase field is Laves phase with a composition close to $\text{Fe}_3\text{Ti}(\text{Mo})$. This type of precipitate forms from ~800 °C and the fraction maintains between 3.45 vol.% to 4.42 vol.% at the temperature 420-500 °C. Another phase which is formed above the equilibrium γ/α transformation temperature (A_{e3}) is fcc TiC. This carbide is thermally stable over a large temperature range up to 1300 °C.

Chapter 4 Brief study on microstructure and mechanical properties of Mn-based maraging steels

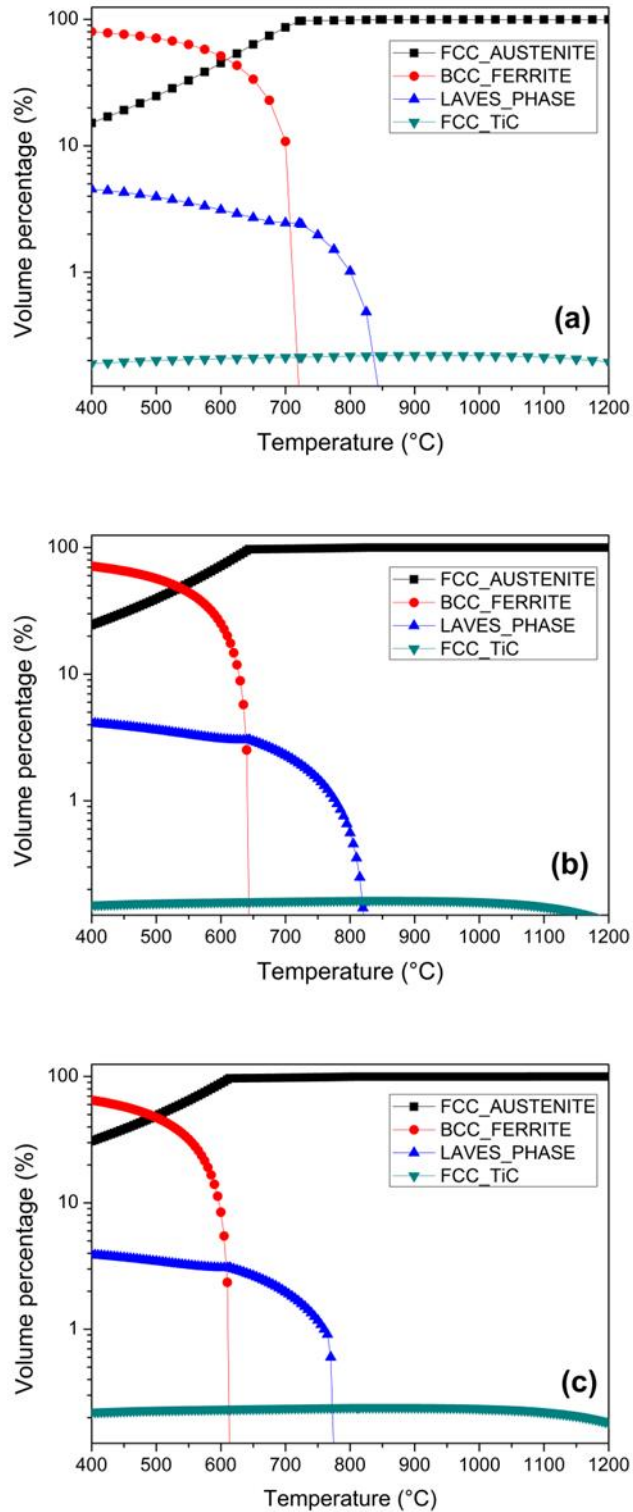


Figure 4-1 The equilibrium phase fractions as a function of temperature in (a) 7% Mn, (b) 10% Mn and (c) 12% Mn alloys.

4.2 The effect of Mn content on grain refinement

The grain size distribution of 7%, 10% and 12% Mn alloys in the SHT state was characterized by EBSD and the results are displayed in Figure 4-2. The left column presents the martensite phase (blue) with grain boundaries (black lines, $>15^\circ$). The EBSD phase maps show that in the solution-treated condition, only martensite was present. This result disagrees with the EBSD observation by Raabe et al. [18] suggesting that a small amount of austenite was retained after quenching in 12 wt.% Mn alloy. Apart from the EBSD resolution limit, there are three possible reasons about this deviation. (i) Raabe may have used a slower cooling rate by which some austenite was retained rather than transformed to α' -martensite. (ii) Both experiment and model simulation demonstrated the dependence of the martensite-start temperature (M_s) on the prior austenite grain size [34][162][213]. It is reported the ultrafine prior austenite grain is one of the reason for the presence of retained austenite. The small grain size suppresses the martensitic transformation, and thereby contributing to the austenite stability during cooling [34][213]. (iii) The addition of Al in the present study increased M_s temperature.

The right column presents the inverse pole coloured orientation maps of the same area, in which the packets of lath martensite can be clearly observed. It is evident that these martensite packets formed via water quenching possessed high-angle misorientation with adjacent packets. Each prior austenite grain was sub-divided into several martensite packets. In other words, the effective grain size was refined owing to the dense high-angle boundaries induced by martensite packets. In addition, it is noticed that the effective grain size was reduced as the Mn content of the alloy increased, which means that the Mn addition contributed to the grain refinement in these alloys. It is known that the addition of Mn lowers both the A_{e3} and M_s temperatures. The reduction of A_{e3} provides an increased driving force for phase transformation and thus a decreased driving force for grain growth. Similarly, a lower M_s temperature leads to the refined packets of lath martensite. Therefore, finer prior austenite grains and martensite packets were observed in 12% Mn alloy in the SHT state compared to other two alloys.

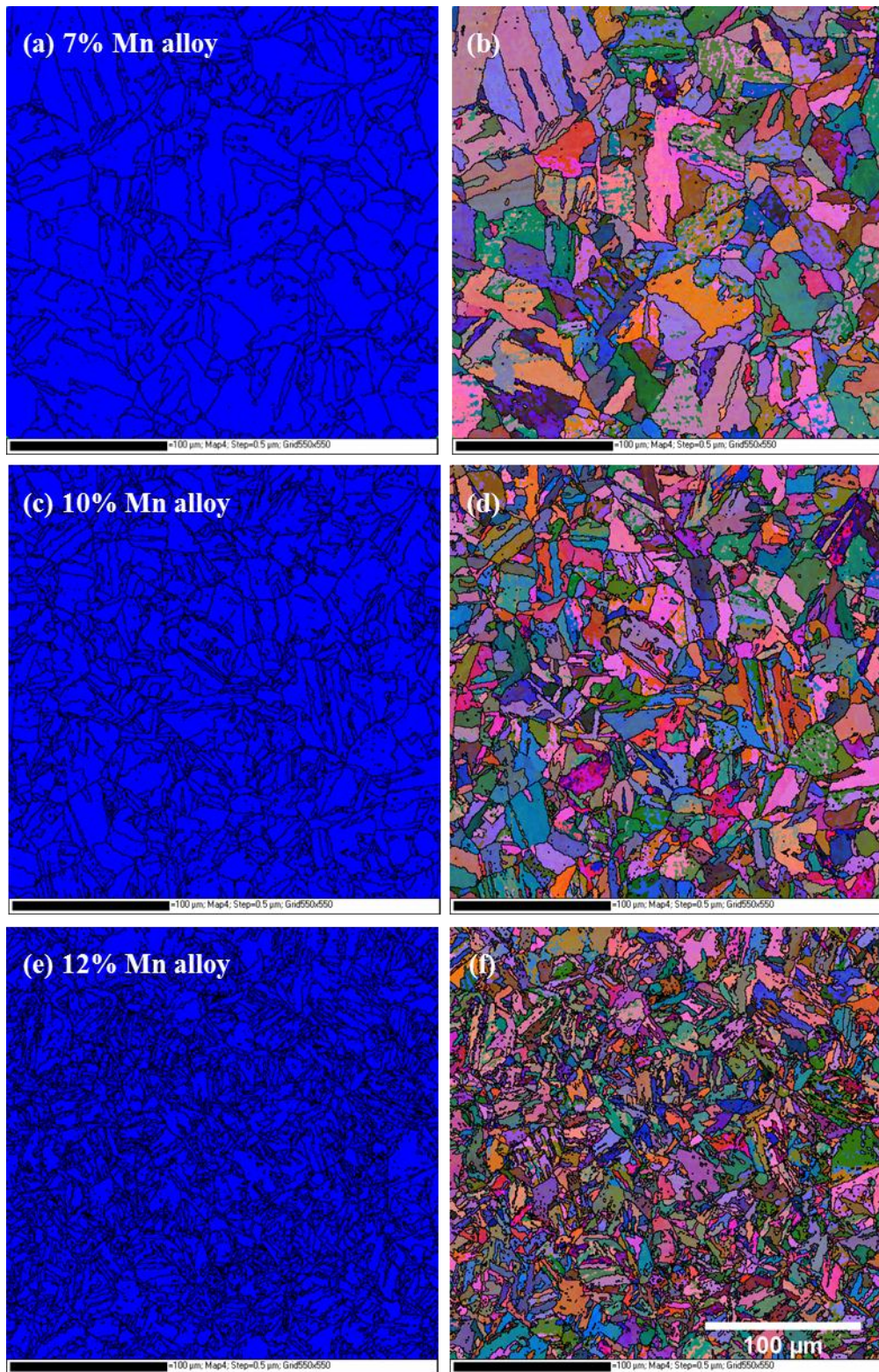


Figure 4-2 Microstructure of the three alloys in the SHT state by EBSD analyses. Left column: phase maps showing martensite phase (blue) with grain boundaries (black lines, $>15^\circ$). Right column: inverse pole maps of the same area, showing the orientation distribution of the martensite.

4.3 Phase identification by XRD and SEM

X-ray diffraction (XRD) analyses were conducted on all the solution-treated and aged samples. Figure 4-3 displays the XRD results of the three alloys in the SHT state, which confirms only martensite could be detected in the three samples.

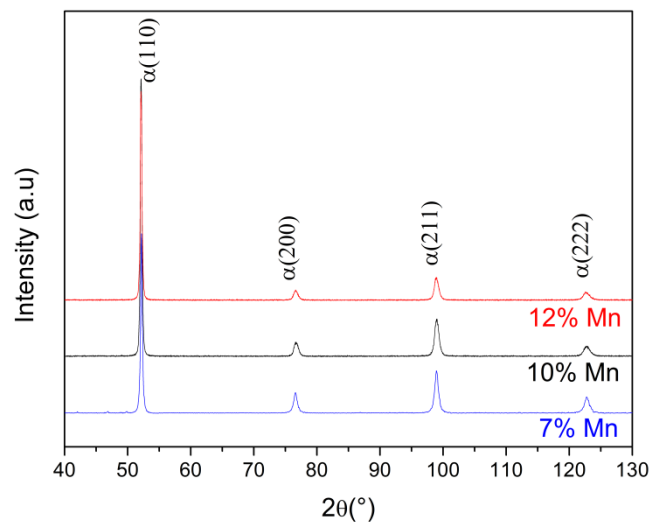


Figure 4-3 X-ray diffraction patterns of solution-treated 7%, 10% and 12% Mn alloys.

Although both XRD and EBSD analyses did not show any evidence of carbide formation, the SEM micrographs in Figure 4-4(a) and (b) reveals the existence of carbide in the SHT state. The SEM-EDS and TEM-EDS analyses (Figure 4-4(b) and (c)) confirm that this type of carbide is Ti-rich as MatCalc predicts. It is shown in Figure 4-4(a) that both the size and the number density of TiC particles are small (0.15-0.22 vol.% provided by MatCalc) and this is the reason why the XRD and EBSD failed to detect carbide. In addition, MatCalc indicated this kind of carbide is very stable and cannot be totally dissolved even heating up to 1300 °C, so in this work the carbides were retained and could be observed in both SHT and aged samples (Figure 4-4(d)).

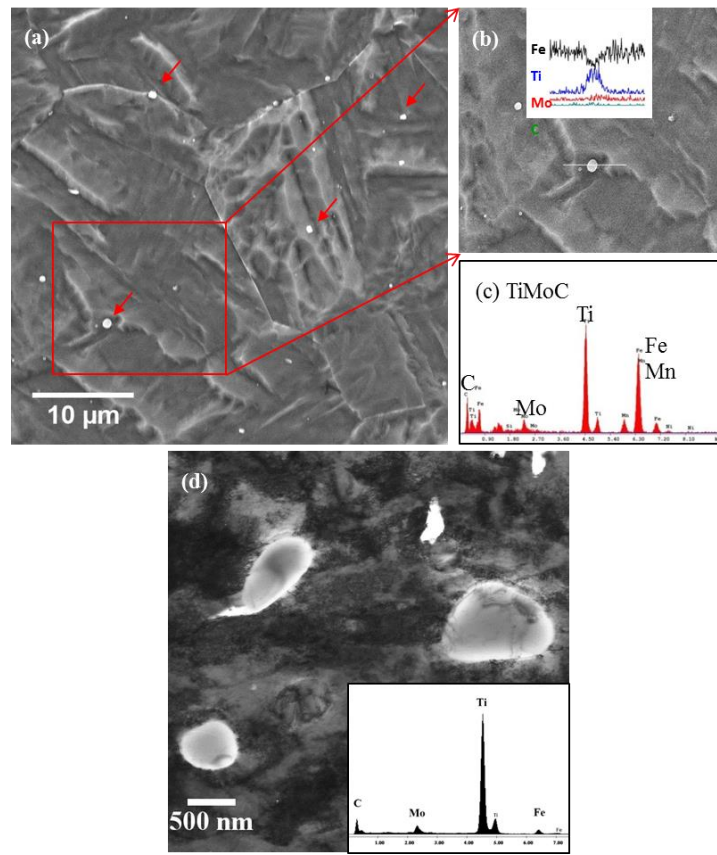


Figure 4-4 (a) SEM micrograph of Ti-rich carbide present in 10% Mn alloy in the SHT state with (b) EDS line scan and (c) EDS spot detection results; (d) TEM micrograph of Ti-rich carbide existing in aged 7% Mn alloy in 500 °C / 10080 min state.

Further aging treatment is supposed to lead to the precipitation and the formation of reverted austenite. However, the X-ray diffraction patterns of most aged samples only reveal the existence of martensite. Distinguishable austenite peaks were mainly observed in 10% and 12% Mn alloys in the overaged stage at 500 °C, see Figure 4-5. At 460 °C, the presence of austenite was only observed after long-term aging (not presented), while at 420 °C, there was no evidence of the formation of reverted austenite in the three alloys (not presented).

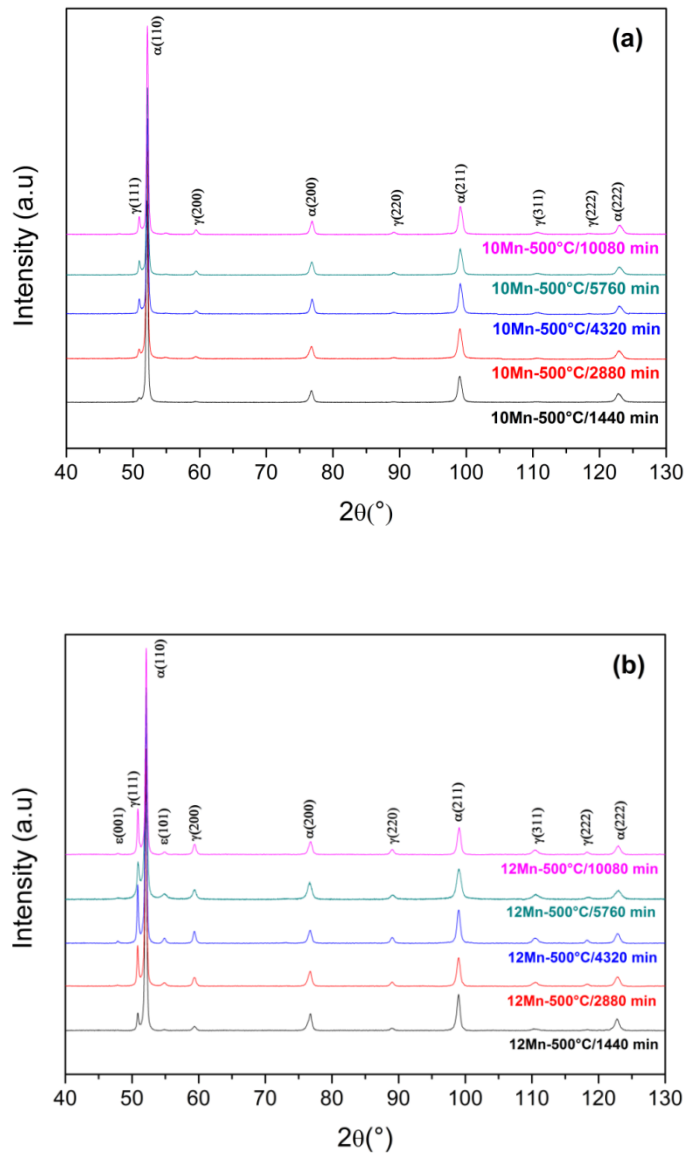


Figure 4-5 X-ray diffraction patterns of (a) 10% Mn and (b) 12% Mn alloys aged at 500 °C for various durations.

Apart from peaks of martensite and austenite, additional peaks were noticed in the samples aged at 500 °C for a long duration (Figure 4-5), which were later demonstrated to be ϵ -martensite phase. The ϵ -martensitic transformation upon cooling has been interpreted by Schumann in his study on Fe-Mn steels [214]. The Schumann's martensitic transformation diagrams are displayed in Figure 4-6 [154][215]. According to Schumann, the martensitic transformation in Fe-Mn steels

Chapter 4 Brief study on microstructure and mechanical properties of Mn-based maraging steels

can be summaries as: (i) when the Mn concentration of austenite is below 10 wt.%, $\gamma \rightarrow \alpha'$ martensitic transformation occurs during cooling and only α' martensite can be obtained at room temperature, (ii) when the Mn concentration is between 10 wt.% and 15wt.%, the M_s temperatures of $\gamma \rightarrow \alpha'$ and $\gamma \rightarrow \epsilon$ transformations are close (Figure 4-6(a)). Although part of the ϵ -martensite may still transform into α' martensite, the presence of both α' - and ϵ -martensite along with untransformed γ phase is expected after cooling, (iii) when the Mn concentration is between 15 wt.% and 25 wt.%, the thermally stable phases at room temperature are ϵ -martensite and γ phase which is retained due to fast cooling rate, (iv) when the Mn concentration is over ~ 25 wt.%, both the M_s temperatures of $\gamma \rightarrow \alpha'$ and $\gamma \rightarrow \epsilon$ transformations have been reduced to below room temperature. In theory the alloy at room temperature should be constituted by fully austenite content, but some studies reported a trace of ϵ -martensite in alloys with Mn concentration higher than 25 wt.% [216]. In addition, it has been demonstrated that the $\gamma \rightarrow \epsilon$ martensitic transformations is controlled by a displacement mechanism and thus there is no change in the concentration after phase transformation [214].

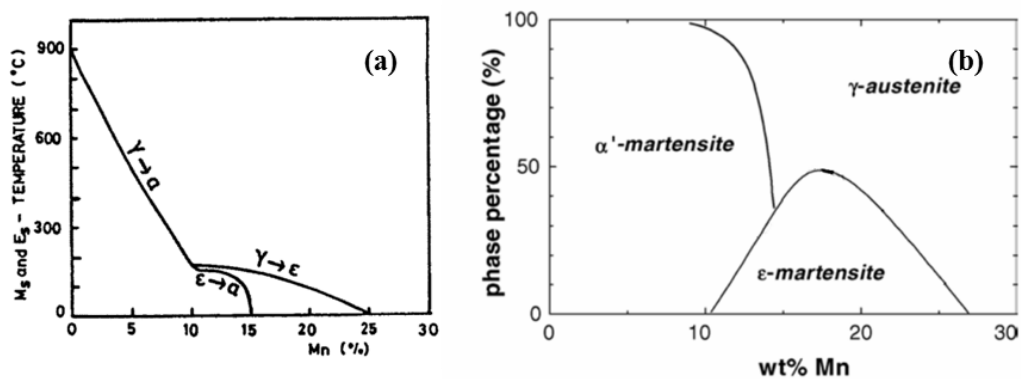


Figure 4-6 (a) Schumann's martensitic transformation diagram of the Fe-Mn system [154];
(b) schematic map of the phase fractions after cooling to room temperature based on Schumann's description [215].

It is worth noting that no peaks corresponding to precipitates were detected by XRD. But a large number of uniformly distributed precipitates were noticed in aged samples under microscope observation, as shown in Figure 4-7. The elongated

islands with brighter contrast are the reverted austenite phase, whereas the nano-scaled spherical phases are the precipitates. A possible explanation is that the diffraction peaks of precipitates are overlapped by those of α' -martensite matrix. A more detailed study on precipitates will be given in Chapter 5.

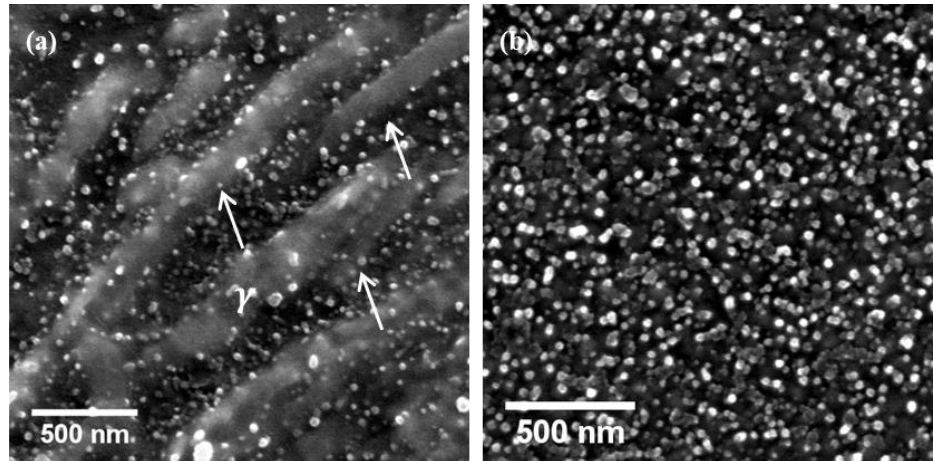


Figure 4-7 SEM micrographs of (a) lath-like austenite and precipitate-decorated martensite matrix and (b) homogeneously distributed precipitates in 12% Mn alloy in 500 °C / 2880 min state.

4.4 Hardness evolution

The hardness curves of precipitation-strengthened alloys generally exhibit four regions: (i) incubation; (ii) a rapid increase in hardness (under-aged region); (iii) a plateau of hardness (peak-aged point) and (iv) a decrease in hardness (overaged region). Figure 4-8 displays the hardness evolution of 7%, 10% and 12% Mn alloys aged at different temperatures.

It is apparent that aging at 420 °C for a limited time up to 10080 minutes did not lead to the peak hardness in the three alloys. As presented in Figure 4-8(a), the three alloys experienced a long incubation and under-aging process which indicated a very slow hardening kinetics in Mn-based maraging steels when aging at 420 °C. It should be noted that higher hardness of alloys with higher Mn content (i.e. $H_{12\% Mn} > H_{10\% Mn} > H_{7\% Mn}$) can be observed for each state (Figure 4-8(a)).

Aging at 460 °C led to the peak hardness in 10% Mn and 12% Mn alloys (Figure 4-8(b)). Although the over-aged region was not that evident in 7% Mn alloy, a

Chapter 4 Brief study on microstructure and mechanical properties of Mn-based maraging steels

decreasing slope of hardness curve leading to a plateau indicates that the peak hardness of 7% Mn alloy aged at 460 °C was achieved within 10080 minutes as well. As expected, 12% Mn alloy was the first who reached the maximum hardness (453 HV, 480 min), followed by 10% Mn alloy approaching the peak (457 HV, 1440 min) and then 7% Mn alloy (454 HV, 5760 min).

Figure 4-8(c) displays the hardness curves of the three alloys aged at 500 °C, which exhibit a typical hardness evolution of precipitation-strengthened alloys. A very rapid increase of hardness was visible in the early aging region of the 10% Mn and 12% Mn alloys, over 90% of the total increase in hardness was achieved within the first 30 minutes. While an incubation in the first 30 minutes was evident in 7% Mn alloy followed by a sluggish hardening process leading to the hardness peak. On the other hand, the maximum hardness of the three alloys are very close (7% Mn alloy: 418 HV at 240 min; 10% Mn alloy: 421 HV at 240 min; 12% Mn alloy: 432 HV at 120 min). It is worth noting that in the over-aged region, what appears to be secondary hardening was observed in both 10% Mn and 12% Mn alloy. Actually, a less evident secondary hardening in the overaged stage could also be observed in the two alloys at 460 °C. This secondary hardening indicates there might be a new phase formed during this period.

Chapter 4 Brief study on microstructure and mechanical properties of Mn-based maraging steels

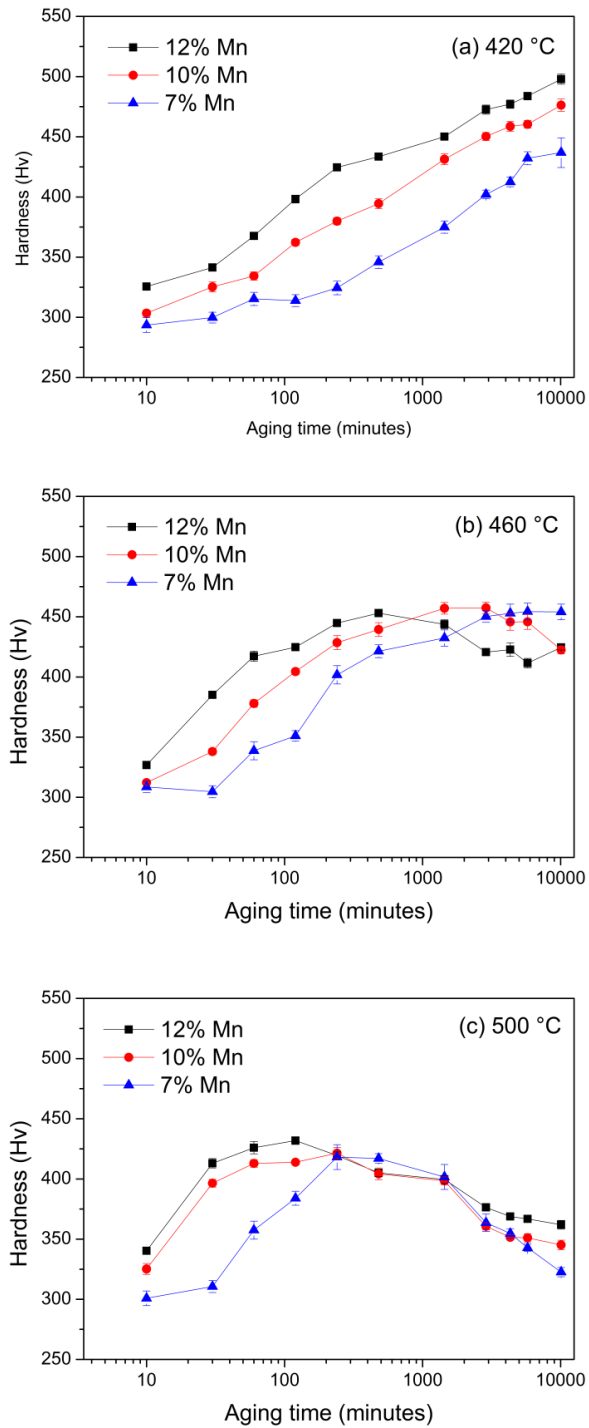


Figure 4-8 Vickers hardness as a function of aging time at (a) 420 °C, (b) 460 °C and (c) 500 °C for Mn-based maraging steels, respectively.

4.5 Tensile results

4.5.1 Tensile behaviour of solution-treated samples

Figure 4-9 displays the engineering stress-strain curves of 7%, 10% and 12% Mn alloys in the SHT state and the summarized data are listed in Table 4-1. It is obvious that the yield strength (YS), ultimate tensile strength (UTS) and tensile elongation (TE) increase with the Mn content of alloys, but the differences among the three alloys are small. It is believed that the more prominent solid solution strengthening owing to higher Mn content is responsible for the higher UTS and TE of 12% Mn alloy. In addition, the Mn addition leading to the refinement of both prior austenite grains and martensite laths which contributes to the improvement of strength and ductility. It should be noted that after reaching the yield point, the increase of engineering stress was small. Instead, an evident decrease of engineering stress as a function of strain was observed. This indicates that the Mn-based maraging steels in the SHT state did not possess a good work hardening during deformation.

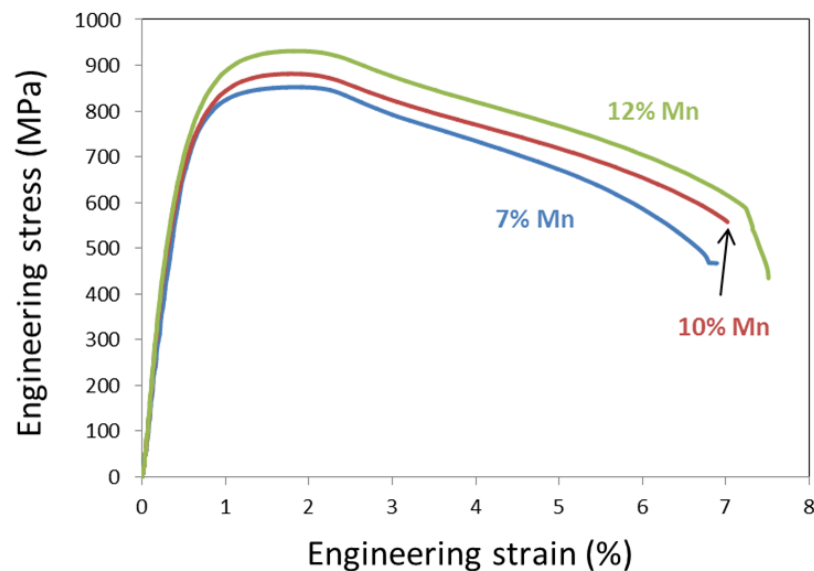


Figure 4-9 Engineering stress vs. strain of 7%, 10% and 12% Mn alloys in the SHT state.

Chapter 4 Brief study on microstructure and mechanical properties of Mn-based maraging steels

Table 4–1 Summary of the mechanical properties of 7% Mn, 10% Mn and 12% Mn alloys in the SHT state.

	YS (MPa)	UTS (MPa)	TE (%)
7% Mn	770	852	6.9
10% Mn	790	882	7.1
12% Mn	820	931	7.5

4.5.2 The embrittlement of aged samples

After aging, the three alloys suffered from poor ductility at lower aging temperature or at higher temperature but for short time. Most of them failed before approaching the yield point (see Figure 4-10(a)). The images of the fracture surface reveal that there was no visible necking (reduction of area), and cracks along grain boundaries can be clearly observed (Figure 4-10(b) and (c)). Aging at higher temperatures or for longer times were demonstrated to significantly improve the embrittlement. Besides, the Mn content of alloy was also found to affect the ductility. In the following section, the tensile behaviour of Mn-based maraging steels will be studied in terms of the aging time, aging temperature and the Mn content, respectively.

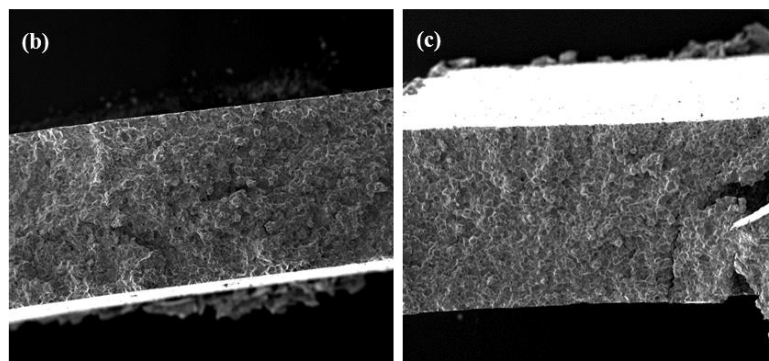
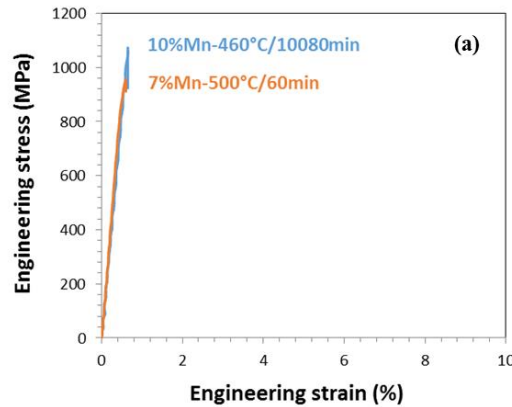


Figure 4-10 (a) Engineering stress-strain curves of 10% Mn alloy in 460 °C / 10080 min state and 7% Mn alloy in 500 °C / 60 min state with their corresponding fracture images: (b) 10% Mn alloy in 460 °C / 10080 min state and (c) 7% Mn alloy in 500 °C / 60 min state.

4.5.3 The improvement of mechanical properties in overaged samples

The engineering stress-strain curves of 10% Mn alloys aged at 500 °C where the plastic deformation was clearly present are displayed in Figure 4-11. The samples showing early embrittlement are not displayed here. After aging at 500 °C for over 2880 minutes, both UTS and TE were considerably improved. The UTS was increased from 832 MPa in the SHT state to 1113 MPa in 500 °C / 2880 min state, whereas the TE increased from 7.0% to 12.1%. Further aging for 5760 minutes led to the TE gradually increasing up to 17.0% but the UTS slightly reducing to 1062 MPa. Aging up to 10080 minutes unexpectedly resulted in a decrease in TE to 13.7%, whereas the UTS stayed at the same level. A summary of YS, UTS and TE are listed

Chapter 4 Brief study on microstructure and mechanical properties of Mn-based maraging steels

in Table 4–2. It is worth noting that, compared to the engineering stress-strain curves of the solution-treated samples, the engineering stress of aged samples in Figure 4-11 reached a plateau after the yield point and stayed at the plateau over a wide strain range.

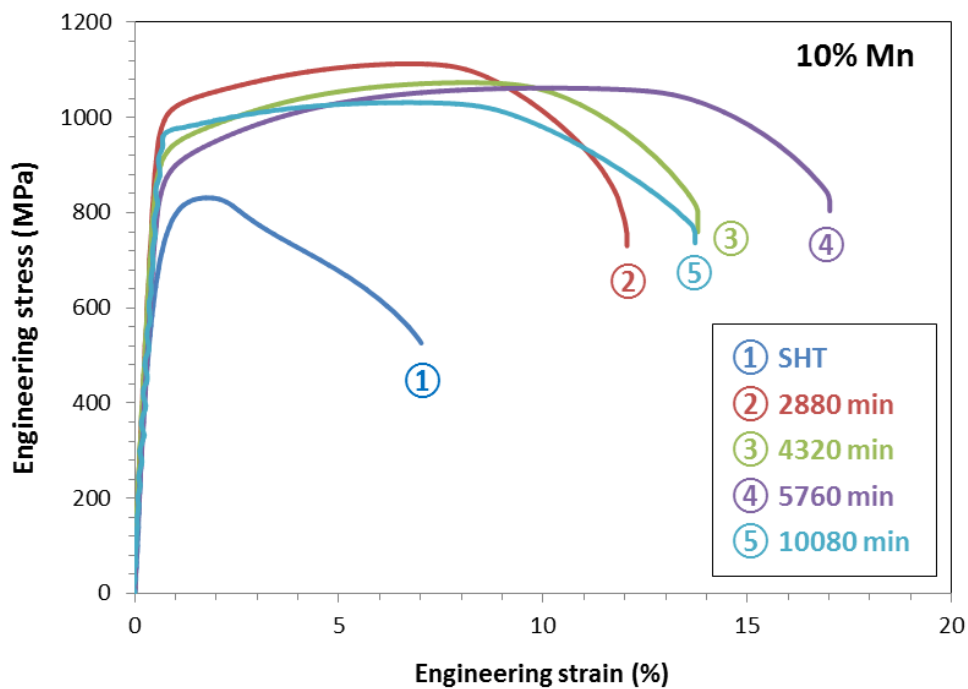


Figure 4-11 Engineering stress vs. engineering strain of 10% Mn alloy aged at 500 °C for different durations.

Table 4–2 Summary of the mechanical properties of 10% Mn alloys aged at 500 °C for different durations.

	YS (MPa)	UTS (MPa)	TE (%)
2880 min	1010	1113	12.1
4320 min	920	1074	13.8
5760 min	860	1062	17.0
10080 min	970	1032	13.7

Chapter 4 Brief study on microstructure and mechanical properties of Mn-based maraging steels

Similarly in the 12% Mn alloy aged at 500 °C, the aging led to the increase in strength but uncertain changes in ductility (Figure 4-12 and Table 4-3). In the early aging stage, samples failed without exhibiting any ductility (not displayed). After aging for 240 min, an improved TE to 5.5% with a remarkable UTS of 1306 MPa was noticed. Longer aging improved the ductility but was found detrimental to the strength (e.g. the sample in 500 °C / 2880 min state: UTS of 1142 MPa, TE of 17.8%). However, further extended aging did not result in any obvious variation in the mechanical properties (④⑤⑥⑦ in Figure 4-12). What is worth emphasising is that similar but more flattened engineering stress-strain curves than 10% Mn alloy was present in 12% Mn alloy. It is evident that the decrease of engineering stress during the necking period was smaller than that in 12% Mn alloy for the same conditions.

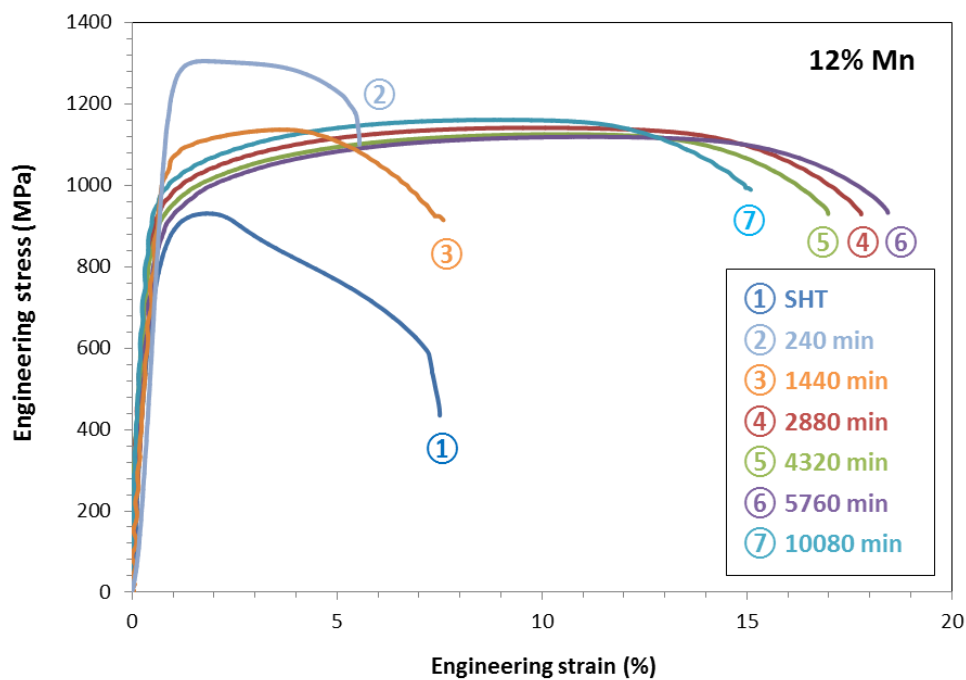


Figure 4-12 Engineering stress vs. strain of 12% Mn alloy aged at 500 °C for different durations.

Chapter 4 Brief study on microstructure and mechanical properties of Mn-based maraging steels

Table 4–3 Summary of mechanical properties of 12% Mn alloy aged at 500 °C for different durations.

	YS (MPa)	UTS (MPa)	TE (%)
240 min	1250	1306	5.5
1440 min	1015	1137	7.6
2880 min	940	1142	17.8
4320 min	910	1126	17.0
5760 min	870	1120	18.4
10080 min	960	1162	15.1

In terms of the effects of aging temperature, all the three alloys exhibited poor ductility when aging at 420 °C even for 10080 minutes (Figure 4-13 exhibits the tensile curve of 12% Mn alloy in 420 °C / 10080 min state). Increasing aging temperature to 460 °C improved the embrittlement. The 12% Mn alloy in 460 °C / 10080 min state attained a limited TE of 7.7% with a UTS of 1330 MPa. Significantly improved ductility but decreased strength existed when aging at 500 °C.

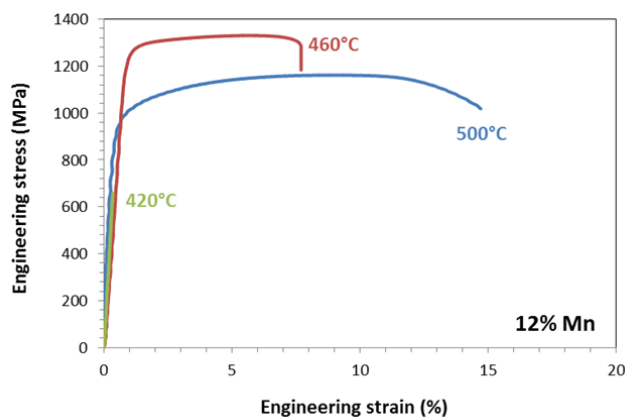


Figure 4-13 Engineering stress-strain curves of 12% Mn alloy aged for 10080 minutes at different temperatures.

Increasing the Mn content of alloy is considered to another effective method to improve both the strength and ductility. As stated above, at lower aging temperatures

Chapter 4 Brief study on microstructure and mechanical properties of Mn-based maraging steels

(420 °C and 460 °C), 7% Mn and 10% Mn alloy failed before plastic deformation initiated. Only the 12% Mn alloy in 460 °C /10080 min state exhibited an acceptable combination of strength and ductility (Figure 4-13). At the aging temperature of 500 °C where the embrittlement was supposed to be much improved, 7% Mn alloy in 500 °C / 10080 state yielded a TE of 6.6%, while both the 10% Mn and 12% Mn alloys yielded even better ductility (13.7% and 15.3%, respectively). Moreover, the UTS was also increased from 1005 MPa of 7% Mn alloy to 1162 MPa of 12% Mn alloy (Figure 4-14). Figure 4-15 further compares the UTS and TE between 10% Mn and 12% Mn alloys aged at 500 °C for different durations, which reveals that both the UTS and TE of 12% Mn alloy were higher than those of 10% Mn alloy for the same conditions.

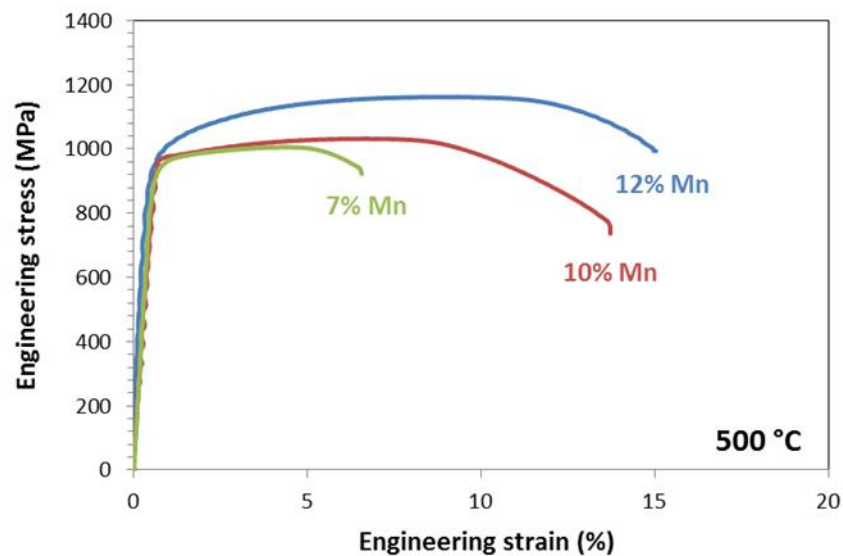


Figure 4-14 Engineering stress-strain curves of 7% Mn, 10% Mn and 12% Mn alloys in 500 °C / 10080 min state.

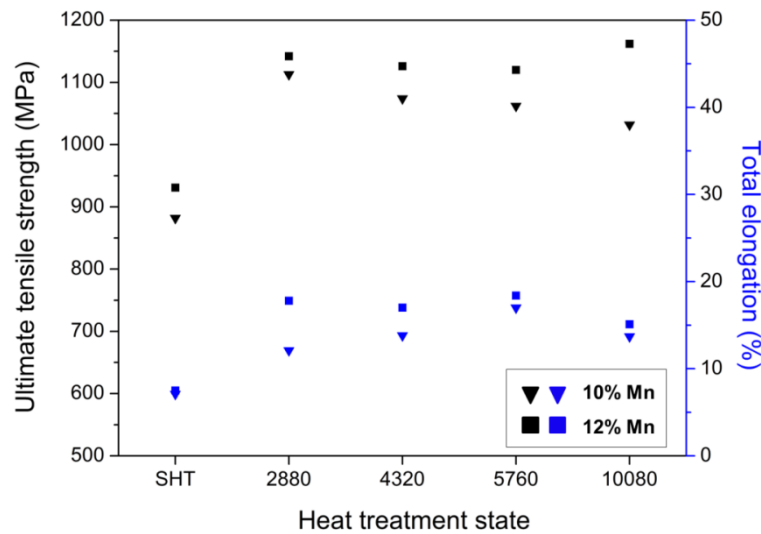


Figure 4-15 Comparison of UTS and TE between 10% Mn and 12% Mn alloys aged at 500 °C for different durations.

4.6 Fractography analyses

4.6.1 The fracture surface after solution heat treatment

Figure 4-16 displays the SEM fractographs of fracture surfaces in the SHT state. Figure 4-16(a) reveals a mixed fracture mode in solution-treated 7% Mn alloy. Specifically, the flat facets exhibiting river patterns are typical of cleavage brittle fracture while cup-and-cone dimples are the characteristic feature of good, ductile fracture. Increasing Mn content led to the improvement of ductility. As shown in Figure 4-16(b), the proportion of dimple fracture in solution-treated 10% Mn alloy is much higher than that in 7% Mn alloy. 12% Mn alloy exhibits a complete transgranular dimpled ductile fracture (Figure 4-16(c)). Compared to the uniform and shallow dimples in 7% Mn and 10% Mn alloys, the dimples in 12% Mn alloy are relatively larger and deeper. Besides, bimodal dimples, i.e. both large and small dimples were observed in the 12% Mn alloy.

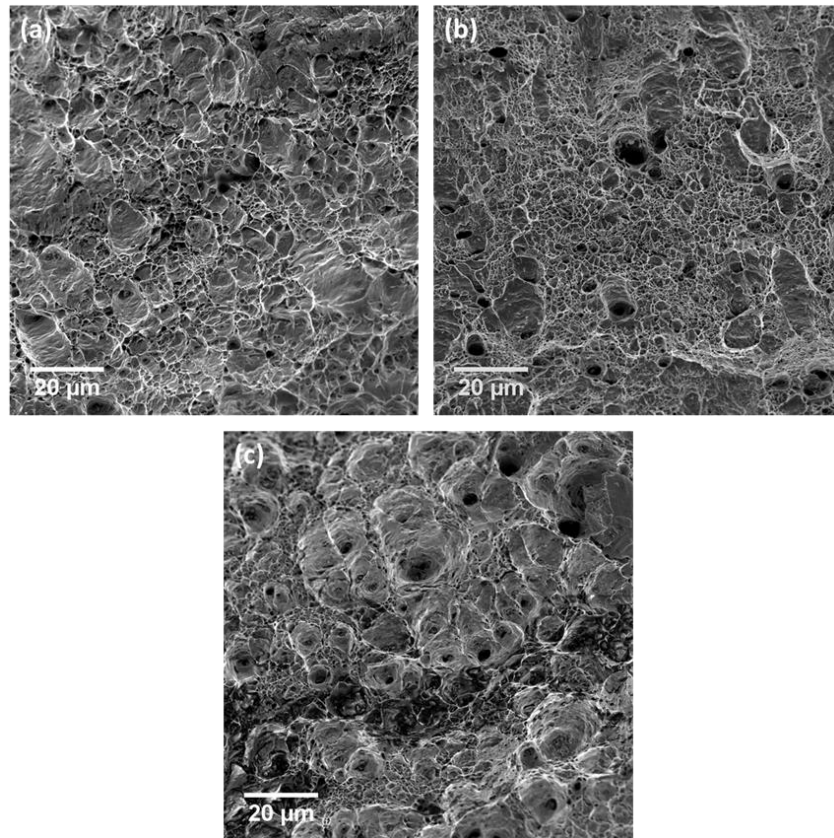


Figure 4-16 The fracture surface of solution-treated (a) 7% Mn; (b) 10% Mn and (c) 12% Mn alloys.

4.6.2 Intergranular brittleness in aged 7% Mn alloy

As the intergranular brittleness was most severe in 7% Mn alloy, the 7% Mn alloy was taken as example to study the effect of aging parameters on brittleness. Figure 4-17(a) reveals a nearly complete intergranular brittle fracture surface when aging at 420 °C for 10080 min. Clear cracks along grain boundaries can be observed. Increasing aging temperature to 460 °C led to a small amount of cleavage fracture as shown in Figure 4-17(b). But the intergranular brittleness was still the dominant fracture mode. When subjected to the aging temperature of 500 °C, the intergranular brittleness was still evident in the initial aging stage (Figure 4-17(c)), then the fracture mode gradually transformed into cleavage fracture as the aging time increases (Figure 4-17(d)).

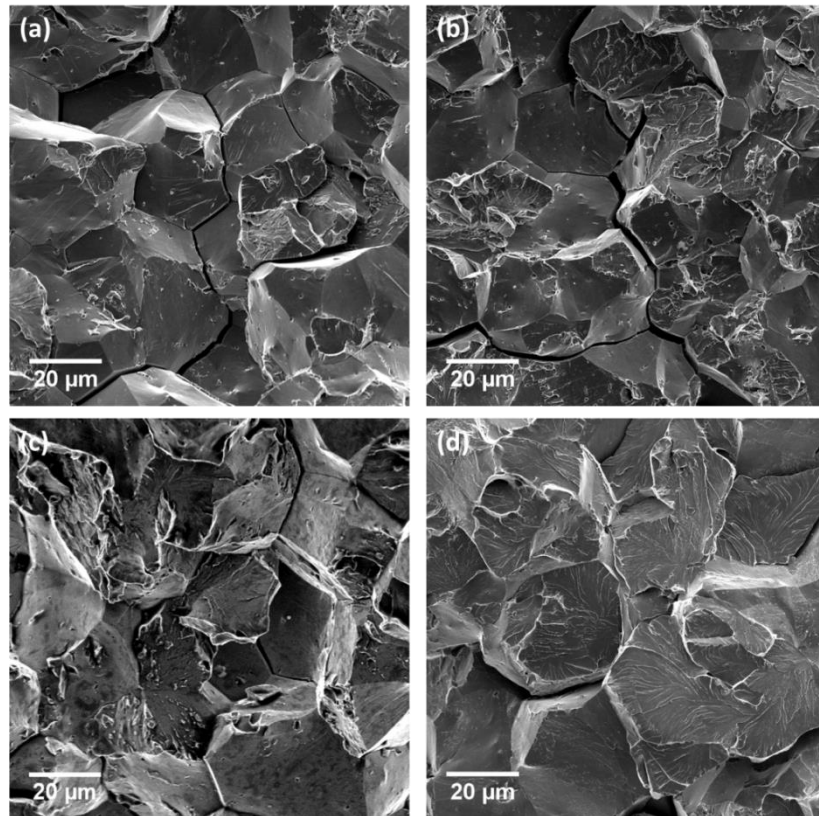


Figure 4-17 The fracture surface of 7% Mn alloy aged at: (a) 420 °C / 10080 min; (b) 460 °C / 10080 min; (c) 500 °C / 60 min and (d) 500 °C / 10080 min.

4.6.3 Improved fracture behaviour in aged 12% Mn alloy

As both the tensile result and microstructural observation indicated, 10% and 12% Mn alloys revealed similar mechanical properties and microstructure with a small variation in austenite fraction, the 12% Mn alloy is representatively studied here to explore the effects of aging parameters on the fracture behaviour. At the aging temperature of 420 °C, the 12% Mn alloy revealed severe intergranular brittle fracture like 7% Mn alloy shown in Figure 4-17(a). Increasing the aging temperature to 460 °C led to the improvement of fracture behaviour. The fracture mode transformed from cleavage fracture in the 460 °C / 4320 min state (Figure 4-18(a) and (b)) to quasi cleavage fracture mode in the 460 °C / 10080 min state (Figure 4-18(c) and (d)). The quasi cleavage is similar to the cleavage fracture but with an

increased ductile proportion. As illustrated in Figure 4-18(c) and (d), small dimples seem to become dominant although intergranular fracture can still be observed.

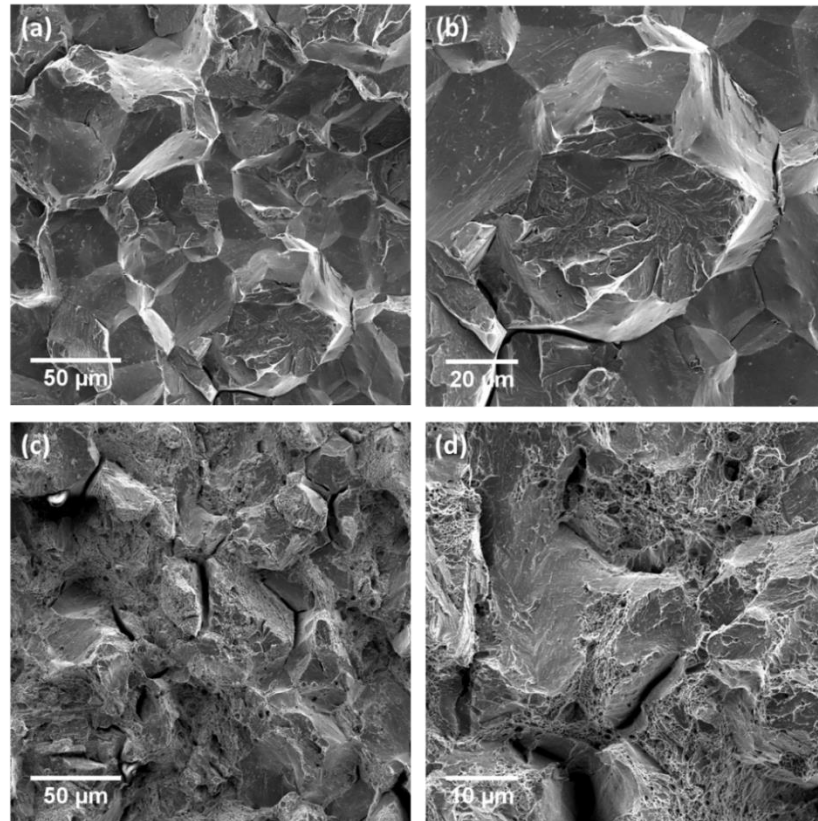


Figure 4-18 The fracture surface of 12% Mn alloys aged at 460 °C for (a)(b) 4320 min and (c)(d) 10080 min. The right column is the enlarged fractographs.

Although intergranular brittleness occurred at the onset of aging process (500 °C / 10 min state, Figure 4-19(a)), further aging at 500 °C significantly improved the fracture performance of 12% Mn alloy. After aging for 1440 min, a microvoid coalescence fracture mode related to dimples was present with a small amount of river pattern (Figure 4-19(b)). In 500 °C / 10080 min state, obvious necking and large reductions in area were clearly observed (not displayed here) and the fractograph is fully occupied by dimpled fracture mode (Figure 4-19(c)). It is found that the proportion of intergranular fracture increased immediately at the start of aging and with prolonged aging it gradually decreased. Besides, granular inclusions in the size range 100-200 nm were found at the bottom of some dimples as shown in Figure 4-19(d). It is worth noting that compared to the dimples in solution-treated

Chapter 4 Brief study on microstructure and mechanical properties of Mn-based maraging steels

stage (Figure 4-16), dimples were smoother and smaller in ductile aged samples (Figure 4-19(c) and (d)).

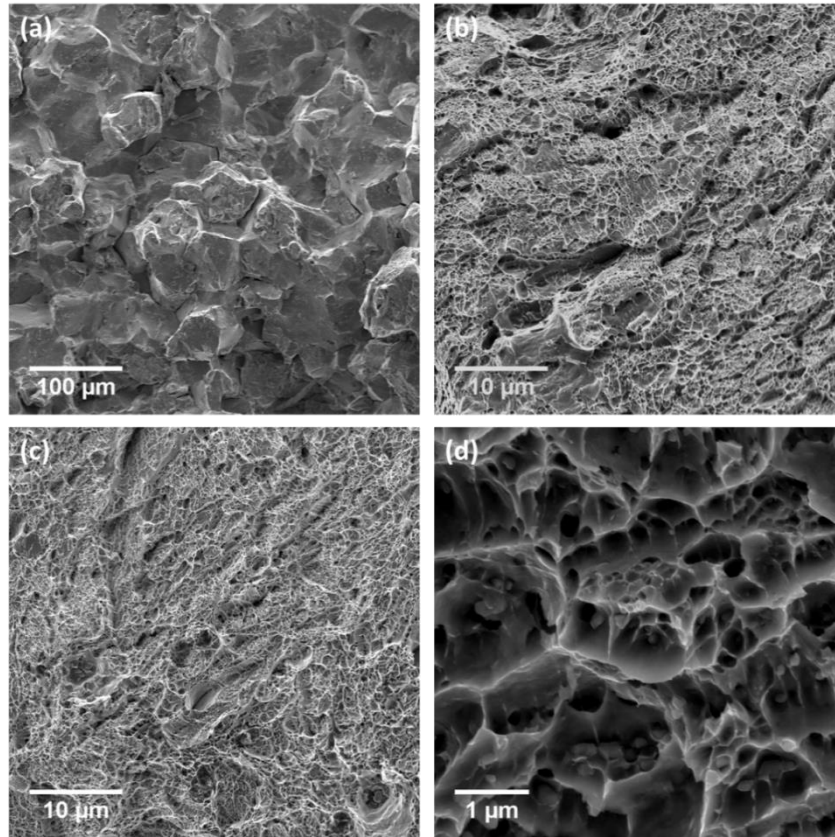


Figure 4-19 The fracture surface of 12% Mn alloys aged at 500 °C for (a) 10 min; (b) 1440 min and (c)(d) 10080 min.

4.7 Summary

1. Thermodynamic calculation by MatCalc confirmed that the dominant equilibrium phases at aging temperature 420-500 °C are ferrite and austenite. The only precipitate phase predicted by MatCalc was Laves phase $\text{Fe}_3\text{Ti}(\text{Mo})$. A trace of fcc phase TiC was found thermally stable over a wide temperature range up to 1300 °C. The equilibrium γ/α transformation temperatures (A_{e3}) are calculated as: 7% Mn alloy: 722 °C; 10% Mn alloy: 644 °C; 12% Mn alloy: 614 °C.
2. The addition of Mn has been demonstrated to refine both the prior austenite grains and martensite packets via reducing A_{e3} and M_s temperatures. This

grain refinement is partially responsible for the higher strength and ductility in 12% Mn alloy in the SHT state.

3. Phase identification by XRD confirmed the formation of reverted austenite during aging. Besides, XRD analyses revealed the existence of ϵ -martensite in over-aged samples, but no evidence of precipitates was found in XRD patterns.
4. Aging at 460 °C or 500 °C exhibited a typical hardness evolution of precipitation-strengthened alloys. Higher aging temperature led to a more rapid hardening towards peak hardness followed by a moderate decrease in hardness in the overaged region. A slower hardening kinetics but more significant hardening effect existed at 420 °C. In terms of the Mn content of alloy, a quicker response to thermal treatment and more significant hardening effect were observed in 12% Mn alloy when compared to other two alloys.
5. Embrittlement occurred in the samples aged at lower temperatures or at higher temperatures but for short times. Increasing aging temperatures and durations could significantly improve the embrittlement phenomenon. Higher Mn content was also demonstrated to benefit the ductility as well. The 12% Mn alloy aged at 500 °C for 5760 min exhibited a UTS of 1120 MPa with TE of 18.4%.
6. The fracture mode of solution-treated samples is a mix of cleavage brittle fracture and dimples fracture. Higher Mn content corresponded to an increase of the proportion of dimples fracture. Intergranular brittle fracture was observed in the early aging stage. The embrittlement phenomena were much improved after prolonged aging process and the fracture mode gradually transformed to a transgranular dimpled ductile fracture. Both higher Mn content and higher aging temperature were found to accelerate the improvement of ductility.

Chapter 5 Characterization of L₂₁-ordered Ni₂TiAl intermetallic phase and its precipitation behaviour

5.1 Introduction

The previous hardness study in Section 4.4 revealed a rapid and significant hardening during aging in the three Mn-based maraging steels and evidence has suggested that the hardening is mainly attributed to the formation of an unknown type of precipitate. Therefore, the primary objective addressed in this study is to investigate the nature of the precipitate. In this chapter, the chemical composition, coarsening behaviour, crystal structure and coherency of precipitates will be studied aiming to understand their effects on the strengthening behaviour of Mn-based maraging steels respectively.

5.2 Experimental details

The precipitates formed in 7%, 10% and 12% Mn alloys under different aging treatments were investigated. The solution-treated samples were aged at 420 °C, 460 °C and 500 °C for 10, 30, 60, 120, 240, 480, 1440, 2880, 4320, 5760 and 10080 mins. Various TEM techniques including bright field, electron diffraction, dark field and EDS were employed to obtain the information about size, composition and the crystal structure of precipitates. Most of these investigations were carried out on overaged samples as the ultrafine precipitates formed prior to the peak strengthening were difficult to be identified under conventional TEM observation. In this case, carbon extracted replicas were used for the investigation of early precipitation. Complementary studies on the crystal structure and core/shell structure were performed on HREM and HAADF.

5.3 Microstructural evolution

5.3.1 The effect of Mn content on the precipitation

Figure 5-1 presents the bright-field TEM micrographs of precipitates in 7% Mn and 12% Mn alloys aged at 500 °C. The microstructural evolution of precipitates in the 7% Mn alloy aged at 500 °C is illustrated in the left column. The 480 min aged sample (Figure 5-1(a)), corresponding to the peak aging hardening, exhibited a fine, highly dispersed distribution of precipitates with weak contrast. Further aging led to the increase of the size of precipitates, as shown in the 2880 min aged sample (Figure 5-1(c)). Precipitate coarsening, which resulted in a significant decrease of the number density, was obvious in the 10080 min aged sample (Figure 5-1(e)). For the 12% Mn alloy, the precipitates in the 480 min aged sample have a larger average size and higher number density compared to the precipitates in the 7% Mn alloy for the same aging condition. Analogous to the 7% Mn alloy, further aging to 2880 min and then 10080 min resulted in a significant increase in the precipitate size but a decrease in the number density (Figure 5-1(d) and (f)).

Chapter 5 Characterization of L₂₁-ordered Ni₂TiAl intermetallic phase and its precipitation behaviour

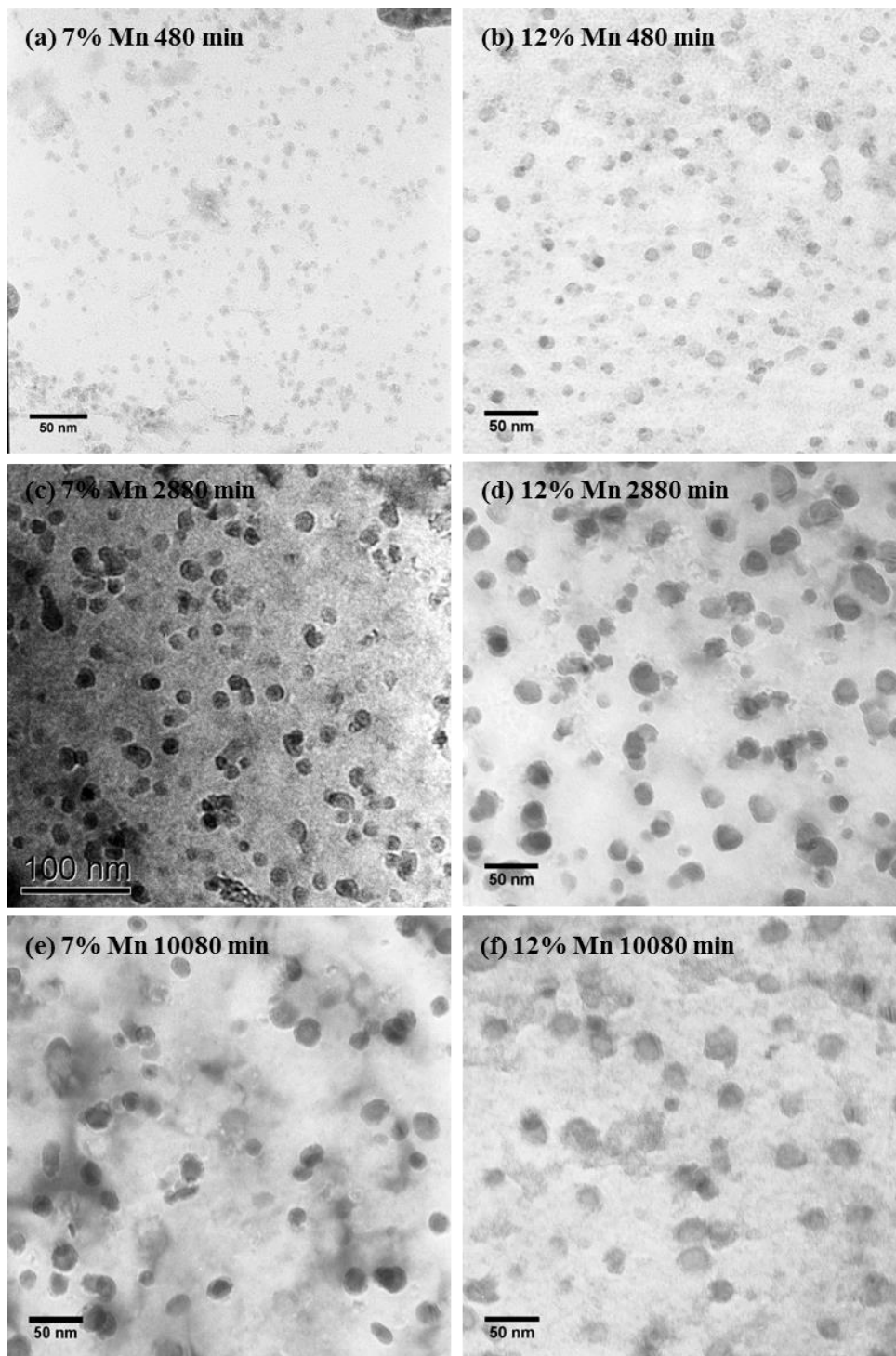


Figure 5-1 Bright-field TEM micrographs of precipitates formed at 500 °C. Left: 7% Mn alloy for (a) 480 min (c) 2880 min and (e) 10080 min; right: 12% Mn alloy for (b) 480 min (d) 2880 min and (f) 10080 min.

5.3.2 The effect of aging temperature on precipitation

The aging temperature is one of the key factors to determine the population and size of precipitates. It is believed that lower aging temperatures can introduce a high number density of fine precipitates, and thus a better strengthening contribution. On the other hand, the kinetics of precipitation is, to a large extent, also associated with the aging temperature. A relatively high temperature is generally desired by steelmakers to reduce the cycle time of aging process. Therefore, investigation is needed to determine the optimum aging temperature meeting both the thermodynamics and kinetics requirement.

The representative 12% Mn alloy subjected to different aging temperatures was studied. As shown in Figure 5-2(a), the precipitates experienced an extremely slow growth process when aging at 420 °C. A small average size of ~5.5 nm was achieved after aging for 10080 min. A more rapid growth was observed at 460 °C where the average size grew up to ~7.5 nm after aging for 10080 min (Figure 5-2(b)), and a moderate increase in the number density is also visible. Further increasing the aging temperature to 500 °C led to a significant increase in the size but a decrease in the number density: the precipitates in the 10080 min aged sample have an average size of 19.4 ± 6.4 nm (Figure 5-2(c)).

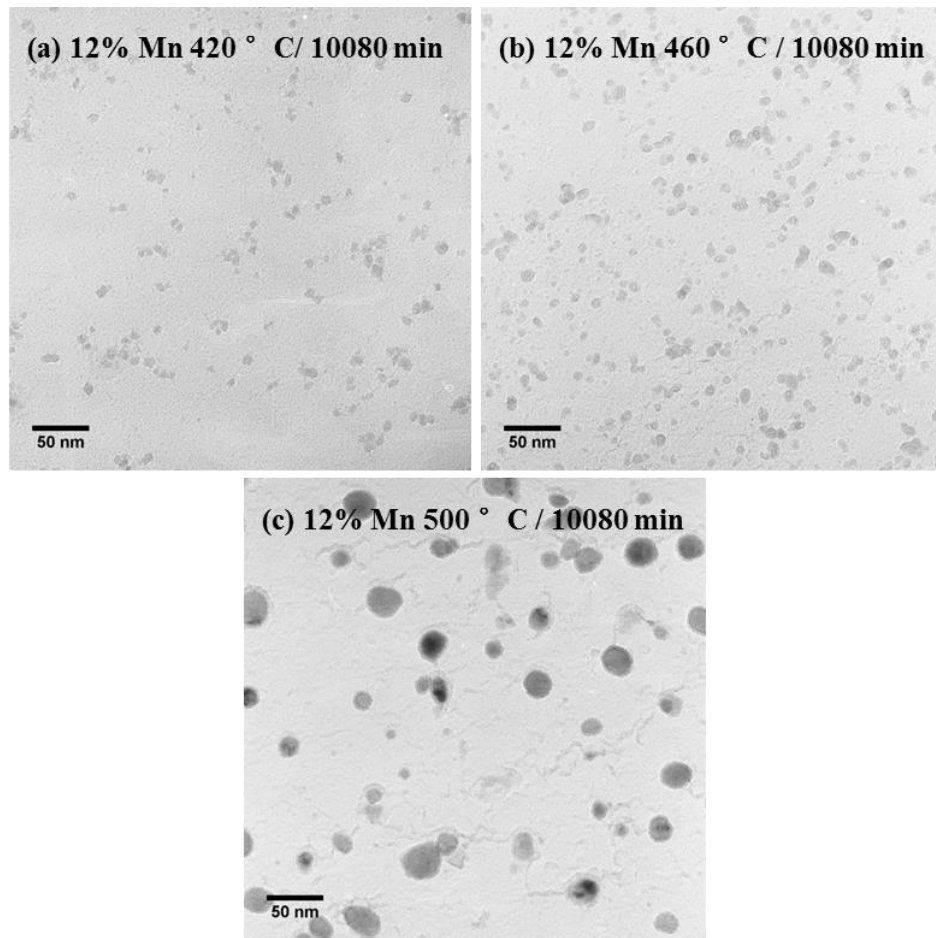


Figure 5-2 TEM micrographs of precipitates on carbon extraction replicas of 12% Mn alloy aged at (a) 420 °C, (b) 460 °C and (c) 500 °C for 10080 min.

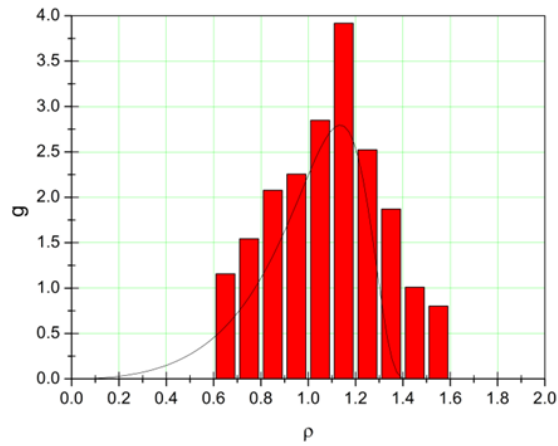
5.4 Coarsening of precipitates

5.4.1 Size distribution of precipitates

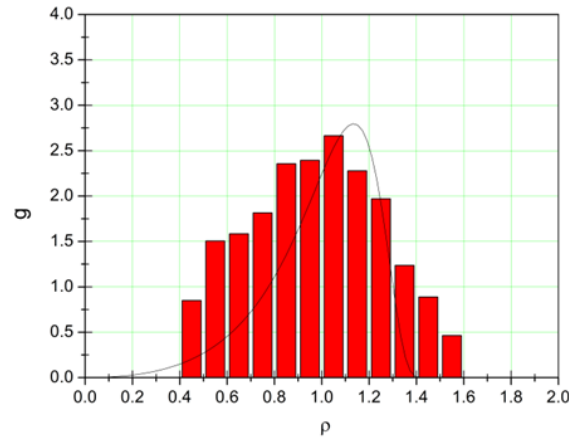
Based on the TEM observation of precipitates, the precipitate size distributions (PSDs) were analysed and the representative results are displayed in Figure 5-3. Due to the limitation of the resolution of extraction replicas under TEM observation, precipitates with an equivalent radius below 1 nm could not be counted. The PSD function (g) was plotted as a function of reduced precipitate radius ($\rho = r/\bar{r}$) to allow comparison with the LSW model expressed as [76]:

$$\int_0^{3/2} \rho^2 h(\rho) d\rho = \frac{9}{4} \quad (5.1)$$

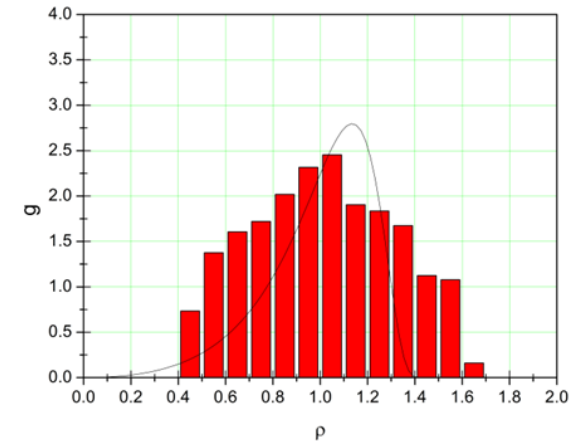
where $\rho^2 h(\rho)$ is the theoretical distribution function. As displayed in Figure 5-3, the experimental PSDs results roughly agree with the theoretical PSD function superimposed on the histograms and the agreement in the early aging stage is better than that after long-term aging. Despite the variation of the average precipitate size, the PSDs of the three alloys exhibit a similar shape for the same aging condition, which means that the effect of Mn content was not that significant on the precipitate size distributions. In terms of the aging time, the PSDs of the three alloys were all narrow in the beginning (500 °C / 480 min) and fitted well with the PSD function predicted by LSW theory (Figure 5-3(a), (d) and (g)), but after aging for 2880 min the PSDs yielded a broader shape than the theoretical PSD distribution (Figure 5-3(b), (e) and (h)), and this discrepancy maintained at this level to the end of aging process (10080 min state), as shown in Figure 5-3(c), (f) and (i).



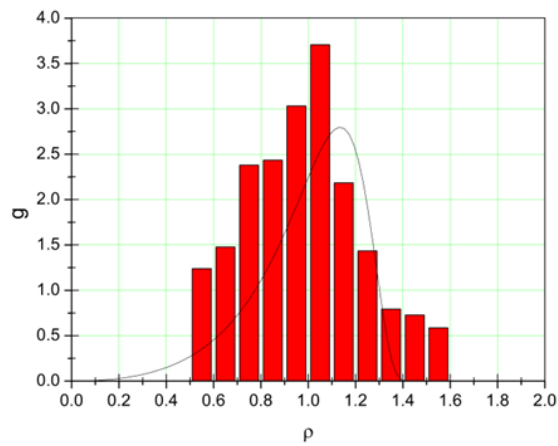
(a) 7% Mn, 500 ° C / 480 min



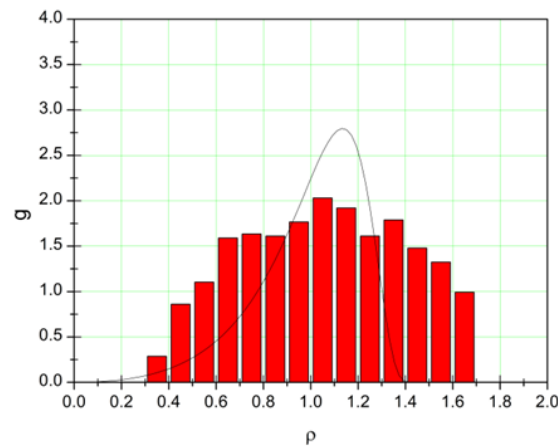
(b) 7% Mn, 500 ° C / 2880 min



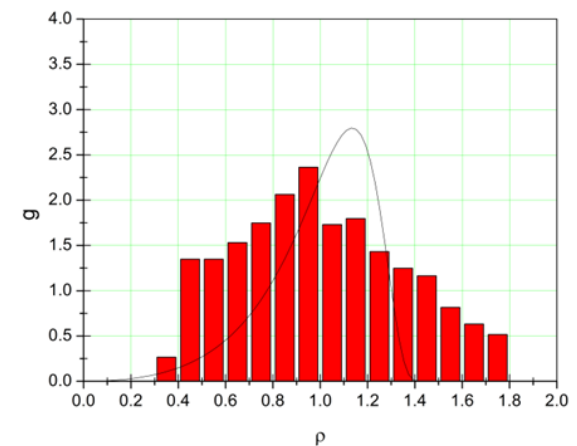
(c) 7% Mn, 500 ° C / 10080 min



(d) 10% Mn, 500 ° C / 480 min



(e) 10% Mn, 500 ° C / 2880 min



(f) 10% Mn, 500 ° C / 10080 min

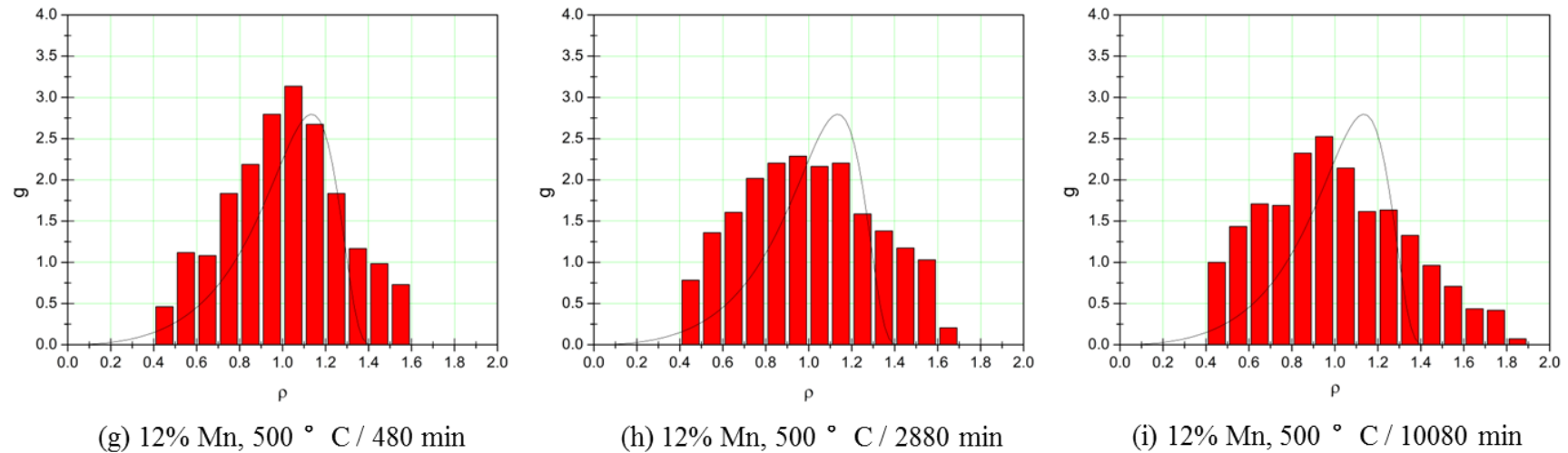


Figure 5-3 Examples of PSDs plotted for various aged samples: 7% Mn alloy (a) 500 °C / 480 min, (b) 500 °C / 2880 min and (c) 500°C / 10080 min; 10% Mn alloy (d) 500 °C / 480 min, (e) 500 °C / 2880 min and (f) 500°C / 10080 min; 12% Mn alloy (g) 500 °C / 480 min, (h) 500 °C / 2880 min and (i) 500°C / 10080 min. The histograms of the PSD function, g , are plotted as a function of reduced precipitate radius ($\rho = r/\bar{r}$). Theoretical LSW distribution is presented as well for comparison.

5.4.2 The growth and coarsening kinetics of precipitate

The growth kinetics at the early stage of precipitation was studied. It is found that the size of early precipitates followed a linear increase with aging time, after which the rate of increase appeared to change indicating the initiation of the coarsening process (Figure 5-4). The trend of curves is consistent with the description of precipitate size-time relationship in Figure 2-5. Besides, the growth rate of precipitates in 7% Mn alloy is found slower than that in 12% Mn alloy.

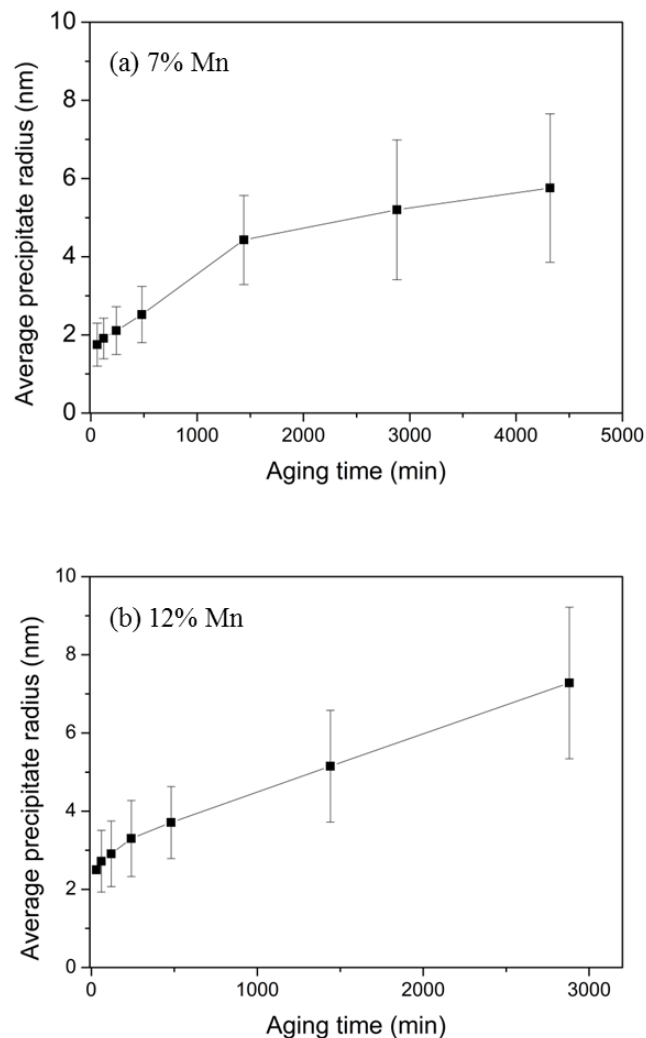


Figure 5-4 Evolution of the mean precipitate size \bar{r} as a function of aging time at 500 °C in (a) 7% Mn alloy and (b) 12% Mn alloy.

Chapter 5 Characterization of L2₁-ordered Ni₂TiAl intermetallic phase and its precipitation behaviour

The precipitate coarsening in the 7%, 10% and 12% Mn alloys aged at 500 °C was assessed by plotting mean precipitate radius \bar{r}^3 (Table 5–1) as a function of aging time t (Figure 5-5). Except the point of 500 °C / 10080 min state in 12% Mn alloy, the linear slopes in Figure 5-5 confirm to the relationship between the mean precipitate radius and aging time:

$$\bar{r}^3 - r_{c5}^3 = K_R t \quad (5.2)$$

This indicates that the coarsening kinetics of precipitates in the three alloys follows the diffusion-controlled coarsening kinetics predicted by LSW theory. The slopes in Figure 5-5 reveal that the coarsening rate constants increase with the Mn contents of alloy. Besides, the \bar{r}^3 of 12% Mn alloy aged at 500 °C / 10080 min, which shows a deviation from the expected value by LSW model. This could indicate a change in coarsening mechanism or possibly a change in precipitate structure. Further work would be required to understand this change.

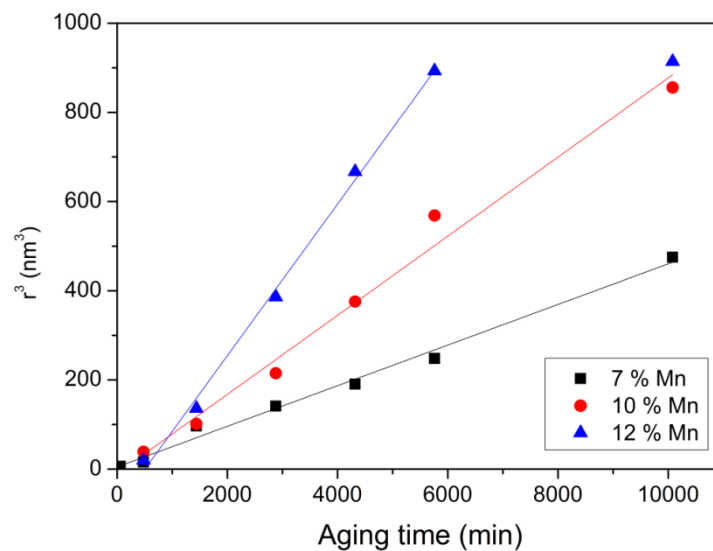


Figure 5-5 Evolution of the mean precipitate radius \bar{r}^3 as a function of aging time t , in 7% Mn, 10% Mn and 12% Mn alloys aged at 500 °C.

Chapter 5 Characterization of L2₁-ordered Ni₂TiAl intermetallic phase and its precipitation behaviour

Table 5–1 Experimental mean size of precipitates (\bar{r}) and coarsening rate constant (K_R) of different alloys aged at 500 °C.

Aging time (min)	7% Mn		10% Mn		12% Mn	
	\bar{r} (nm)	K_R (m ³ s ⁻¹)	\bar{r} (nm)	K_R (m ³ s ⁻¹)	\bar{r} (nm)	K_R (m ³ s ⁻¹)
480	2.52 ± 0.72	-	3.39 ± 1.28	-	3.71 ± 1.43	-
1440	4.43 ± 1.14	-	4.66 ± 1.56	-	5.15 ± 1.94	-
2880	5.2 ± 1.79	-	5.99 ± 2.41	-	7.28 ± 2.21	-
4320	5.76 ± 1.9	-	7.22 ± 2.44	-	8.74 ± 3.15	-
5760	6.29 ± 1.8	-	8.29 ± 2.78	-	9.63 ± 3.17	2.83 × 10 ⁻³⁰
10080	7.81 ± 2.38	0.76 × 10 ⁻³⁰	9.5 ± 3.33	1.48 × 10 ⁻³⁰	9.71 ± 3.19	-

5.5 Chemical composition of precipitates

The chemical composition of precipitates in Mn-based maraging steels is under debate in the literature [18][44][135][217][218]. Apart from the commonly reported θ -NiMn precipitates in Fe- Mn-Ni maraging steels, Heo et al. [217] found a type of precipitate with the chemical composition agreeing with Ni₂MnAl phase in an Fe-8.3Mn-8.2Ni-4.2Al alloy. The investigation of the newly developed 9-12% Mn maraging steels with minor additions of Ni, Ti, Al and Mo, which are chemically similar to the materials in our study, reported the precipitates were enriched in Ni, Ti and Al [18][44]. It was initially speculated the precipitates might be γ' -Ni₃(Ti,Al) phase which is the most common precipitates in conventional 18Ni maraging steels. Later, APT analysis, revealed that the average chemical composition was close to Ni₅₀(Al,Ti,Mn)₅₀ [135]. However, a more recent study proposed the formation of NiMn or/and Ni₂MnAl precipitates depending on the Al contents in these Mn maraging steels [219]. Moreover, in a ternary Fe-10Mn-1Pd biodegradable maraging steel, the addition of Pd was found to promote the formation of (Pd,Mn)-rich precipitates. All the evidence suggests that the chemical compositions of precipitates in Mn-based maraging steels are variable and, to a large extent, depend on the elemental concentrations of alloys.

TEM-EDS analyses were conducted on thin foil samples and the representative spectra of both precipitates and matrix (7% Mn, 500 °C / 12960 min) are presented in Figure 5-6. The spectrum in Figure 5-6(b) indicates that the precipitate contained Ni, Ti and Al when compared to the surrounding matrix (Figure 5-6(c)). The major elements of the matrix, Fe and Mn, were also detected by the EDS analysis of precipitates (Figure 5-6(b)). Some researchers suggested that the Fe and Mn concentrations were due to the residual matrix above or below precipitates [85], but this viewpoint is doubtful as the Mn/Fe mass ratio in Figure 5-6(b) is much higher than that in Figure 5-6(c).

Chapter 5 Characterization of L₂₁-ordered Ni₂TiAl intermetallic phase and its precipitation behaviour

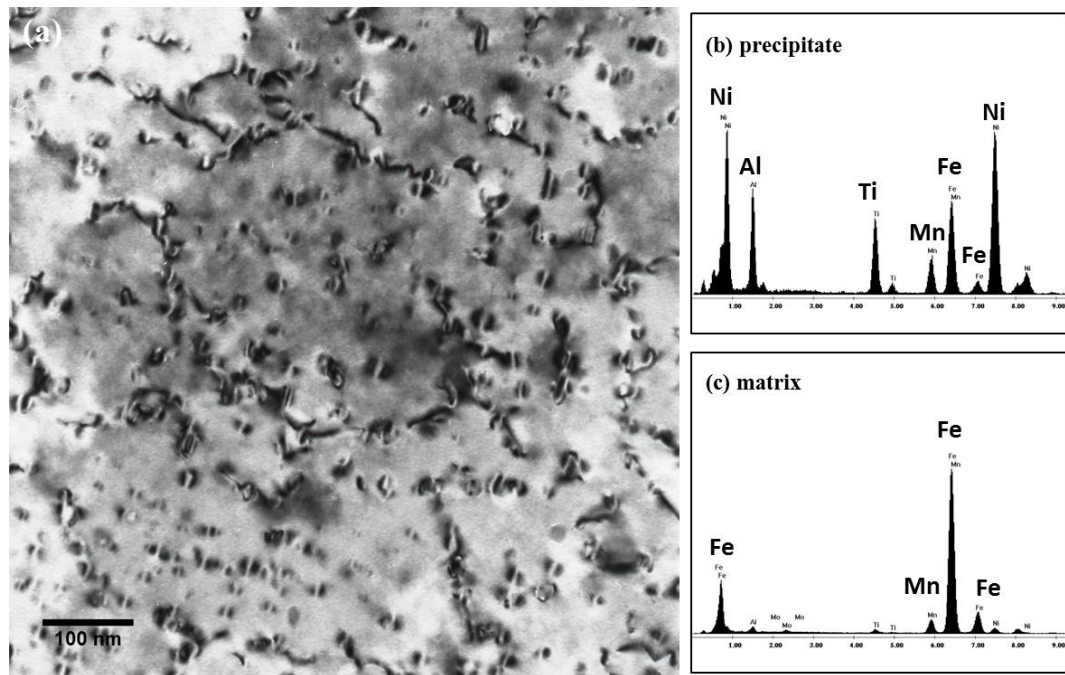


Figure 5-6 (a) Bright-field TEM image of 7% Mn alloy aged at 500 °C for 12960 min and TEM-EDS spectra of (b) precipitate and (c) matrix.

In order to minimize the interference from the matrix, carbon extraction replicas were utilized for further compositional analyses. Representative STEM-EDS analysis was conducted on 12% Mn alloy aged at 500 °C for 2880 min along the horizontal line crossing a precipitate, as shown in Figure 5-7. The corresponding concentration profiles of Al, Ti, Mn, Fe and Ni are plotted below the STEM micrograph.

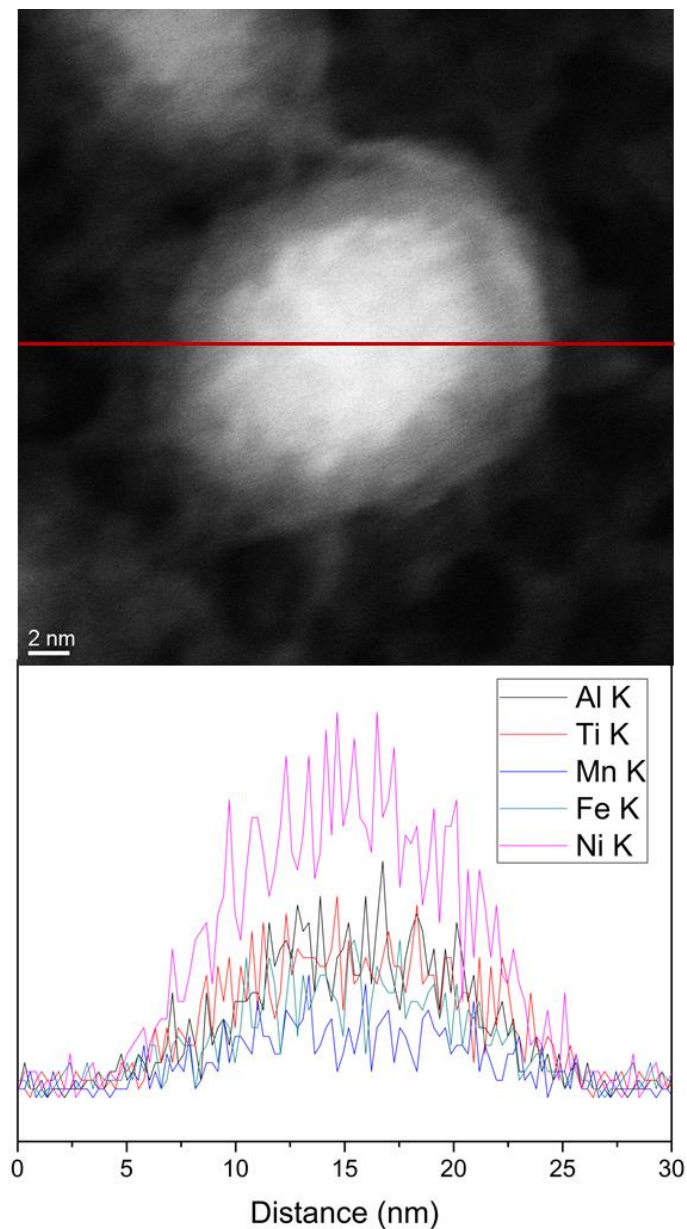


Figure 5-7 STEM micrograph of precipitates in 12% Mn alloy aged at 500 °C for 2880 min and EDS results of concentration profiles measured along the red line.

As displayed in Figure 5-7, the STEM-EDS analysis on replica sample confirms that the precipitates mainly comprised Ni, Ti and Al with some segregation of Fe and Mn. The considerable Fe and Mn concentration detected demonstrates that the segregation of Fe and Mn in precipitates is not an artefact. The APT study conducted by Millán et al. [135] also confirmed the existence of Fe and Mn atoms in precipitates and 20 at.% Fe and 25 at.% Mn were detected by APT in the precipitates

Chapter 5 Characterization of L₂-ordered Ni₂TiAl intermetallic phase and its precipitation behaviour

in a 9% Mn alloy aged at 450 °C for 192 h. As mentioned in Section 2.2.3.1, similar phenomenon of matrix elements segregating to precipitates has been reported in several NiAl-strengthened steels [32][40][60][78][81]. It is worth noting that in an Fe-Ni-Al-Ti-Cr alloy, two independent precipitates, NiAl and Ni₃Ti, were formed after a splitting of the precursor clusters. NiAl precipitates were found to contain a significant amount of Fe while Ni₃Ti precipitates were Fe-free [32]. It is generally believed that NiAl precipitates which are formed out of the solute-rich clusters have a high solubility of Fe, thus the Fe atoms in precursor clusters tend to be retained in NiAl precipitates rather than in Ni₃Ti precipitates [38][82]. Therefore, the presence of Fe atoms in the precipitates of Mn-based maraging steels in this study implies that the precipitate is more likely to be NiAl phase or similar phases with high Fe solubility, rather than the Ni₃Ti phase in the conventional maraging steels. On the other hand, another possibility proposes that the existing of Fe and Mn in precipitates is associated with the lateral diffusion of Fe and Mn atoms from the matrix during aging [135]. Therefore, further investigation is needed to determine which viewpoint is more reliable.

In order to quantify the elemental constituents of precipitates, standardless quantitative analysis on at least 10 precipitates within each sample was undertaken and the results are summarized in Table 5–2. As discussed in Section 3.3.4.2, standardless quantitative analysis cannot provide accurate quantitative results, but given that the precipitate forming elements in this study are not trace and their atomic numbers are not small, the standardless quantitative results should be acceptable.

The data in Table 5–2 did not reveal significant variation in the chemical composition of precipitate among the three alloys. This suggests that the precipitates are quite chemically stable within the aging time up to 10080 min. The 7% Mn alloy is chosen to study the Fe evolution in precipitate in order to eliminate the interference from austenite reversion. In the 500 °C / 480 min state, 15.8 at.% Fe is detected in the precipitate followed by a decrease to 9.8 at.% Fe after aging for 2880 min. Further aging to 10080 min did not further change the Fe concentration which suggests that the Fe in precipitates had reached its equilibrium concentration after prolonged aging. Owing to the limitation of the TEM-EDS technique, compositional

Chapter 5 Characterization of L₂-ordered Ni₂TiAl intermetallic phase and its precipitation behaviour

analysis was not carried out on the precipitates in the very beginning of aging process. But Millán et al. [135], who employed APT to measure the chemical composition of precipitates in a 9% Mn maraging steel, reported the precipitates with an average composition of 35 at.% Ni, 11 at.% Mn, 2 at.% Al, 2 at.% Ti, and 50 at.% Fe after aging for 0.5 hours. The evolution of Fe concentration in precipitates confirms our speculation that the Fe atoms in the precipitate are retained from the precursor clusters rather than via the diffusion from the Fe matrix during aging.

Owing to the partitioning of Fe and Mn, the precipitates have a non-stoichiometric composition which can be described as Ni₂TiAl or Ni(Ti,Al) phase. This deviation from the stoichiometric composition due to the element substitution is proposed to increase the local disordering and dislocation climb or cutting, thereby enhancing the ductility of phases [103].

It is important to emphasize that in Raabe et al.'s APT study [135], the Al and Ti concentrations of precipitates were relatively low and these low levels maintained up to aging for 196 h which was contradictory to the present results. On the other hand, as the Ni and Mn concentrations in their study increased moderately with the aging time, the composition of the precipitates in their work was Ni₄₄Fe₂₀Mn₂₄Al₆Ti₄ which, in their opinion, was more close to Ni₅₀(Mn,Al,Ti)₅₀.

Table 5–2 Average chemical composition in at.% of the nano-sized precipitates evolved at 500 °C measured by TEM-EDS.

		Al-K	Ti-K	Mn-K	Fe-K	Ni-K
7% Mn	480 min	30.2 ± 1.4	17.4 ± 1.0	4.3 ± 0.6	15.8 ± 0.6	32.4 ± 0.8
	2880 min	33.1 ± 1.2	17.2 ± 1.3	5.6 ± 0.5	9.8 ± 0.6	34.3 ± 0.9
	10080 min	33.4 ± 0.4	14.9 ± 0.5	7.1 ± 0.5	9.8 ± 0.3	35.0 ± 0.3
10% Mn	480 min	30.4 ± 0.5	15.6 ± 0.8	6.5 ± 0.6	14.7 ± 0.4	32.8 ± 0.8
	2880 min	33.0 ± 0.7	17.7 ± 0.6	5.4 ± 0.5	12.2 ± 0.4	31.8 ± 0.7
	10080 min	33.5 ± 0.7	18.1 ± 0.9	4.7 ± 0.5	13.4 ± 1.3	30.3 ± 1.5
12% Mn	480 min	30.2 ± 0.9	15.6 ± 1.1	6.7 ± 0.4	15.1 ± 0.9	32.5 ± 1.1
	2880 min	32.9 ± 0.2	16.8 ± 0.5	5.7 ± 0.4	12.2 ± 0.3	32.5 ± 0.5
	10080 min	33.4 ± 0.8	17.3 ± 1.1	5.4 ± 0.9	12.7 ± 1.0	31.2 ± 1.3

5.6 Crystal structure of precipitates

5.6.1 Determination of crystal structure

According to the compositional study, the intermetallic precipitates in Mn-based maraging steels may be Ni₂TiAl or Ni(Al,Ti). XRD analyses of the aged samples (see Section 4.3) did not reveal any diffraction signal of the precipitates even when the microstructural observation clearly showed a significant amount of precipitates, which further suggests that the precipitates are highly likely to be B2-Ni(Al, Ti) or L₂₁-Ni₂TiAl phase as most of their diffraction peaks overlap with the peaks of α' -martensite matrix. Since the crystallographic constitution of the phase determines its electron diffraction behaviour which plays an important role in the precipitate characterization, the crystallographic details of B2-NiAl and L₂₁-Ni₂TiAl are discussed.

- B2-ordered NiAl

Figure 5-8 displays the crystal structure of B2-NiAl phase and its simulated electron diffraction patterns along low-index zone axis directions. The B2 phase has a CsCl-type crystal structure. It is constituted by two primitive cubic lattices which are stacked alternatively along the vector $1/2\langle 111 \rangle$ [17]. This structure can also be described as a body-centred cubic (bcc) lattice of Ni with the centre positions being replaced by Al atoms. The lattice parameter of the stoichiometric composition is 0.2887 nm which is very close to that of α' -martensite (0.2884 nm) (see Appendix).

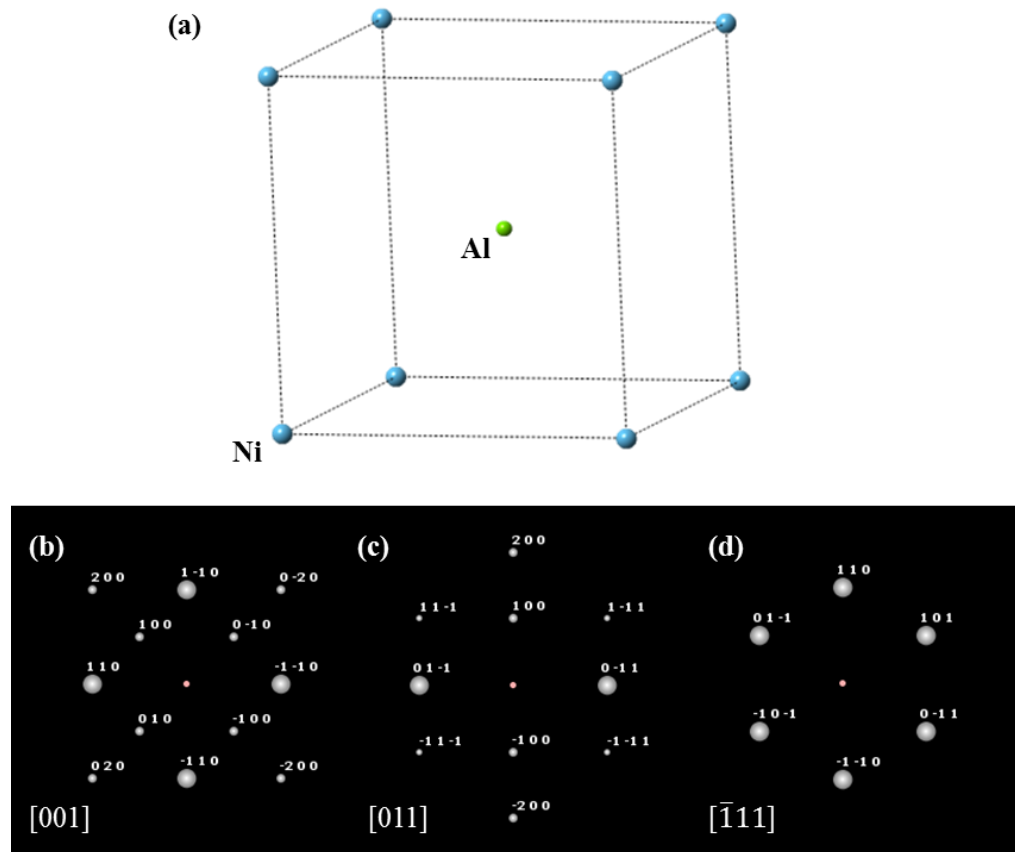


Figure 5-8 Crystal structure of the B2-ordered NiAl phase and simulated electron diffraction patterns along low-index zone axis directions simulated using ICDD PDF-4+ software.

- $L2_1$ -ordered Ni_2TiAl

The $L2_1$ structure simply involves a further ordering of the Al and Ti atoms on the Al sublattice in B2 structure. The structure can be regarded as possessing three sets of sublattice (Figure 5-9(a)), among which two interpenetrating face centred cubic lattices are occupied by Al and Ti atoms respectively and a primitive cubic lattice of Ni atoms is shifted by the vector $1/4\langle 111 \rangle$. Figure 5-10(a) is an equivalent way to illuminate the $L2_1$ structure but easier to understand. The unit cell is built up by eight small bcc lattices. The corners of each small cubic lattice are occupied by Ni atoms with the centre positions being orderly occupied by Al and Ti atoms. Thus, two different types of B2 structure are arranged successively in each direction. The lattice parameter of the small body centred cubic lattice (0.295 nm) is half that of the

Chapter 5 Characterization of $L2_1$ -ordered Ni_2TiAl intermetallic phase and its precipitation behaviour

entire unit cell and is close to that of B2-NiAl phase (0.2887 nm). When the centre positions are fully occupied by one type of atom, for example Al, the phase is transformed to B2-ordered NiAl phase; when the Al and Ti atoms are randomly arranged, the phase is degraded to B2-ordered Ni(Al,Ti) phase.

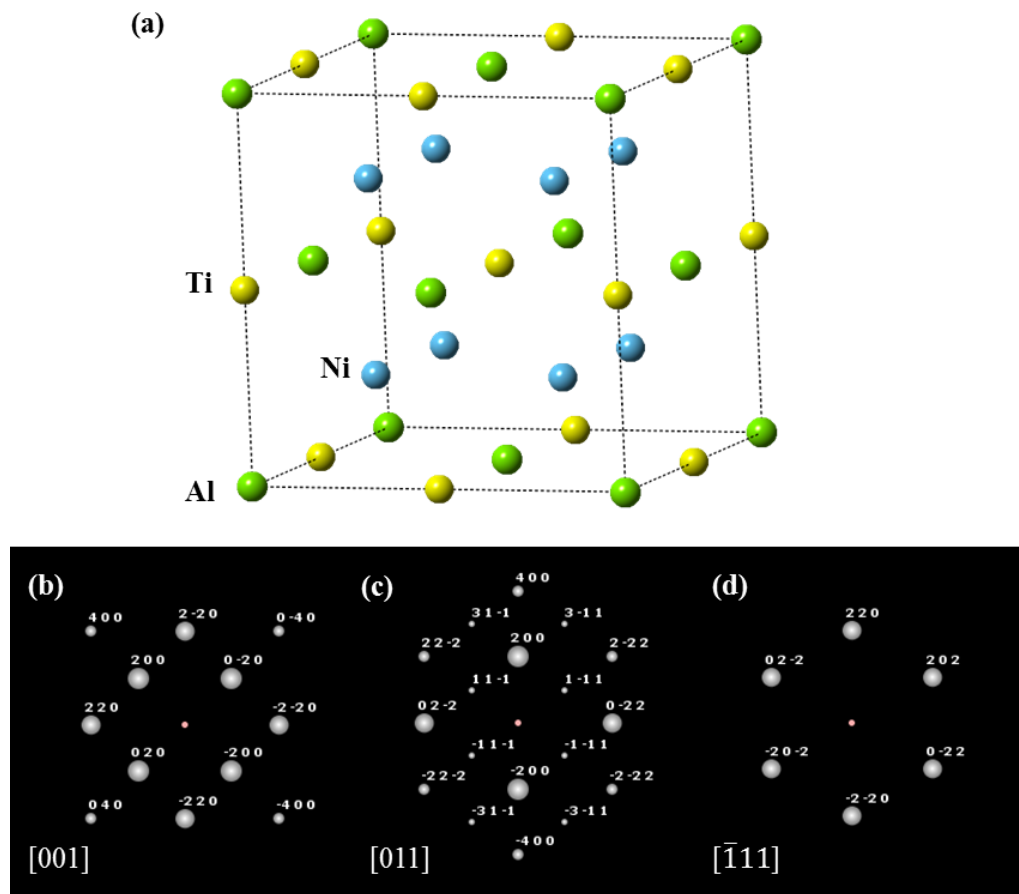


Figure 5-9 Crystal structure of the $L2_1$ -ordered Ni_2TiAl phase and its simulated electron diffraction patterns along low-index zone axis directions simulated using ICDD PDF-4+ software.

The phase with the fully ordered $L2_1$ structure is named as Heusler phase. The Heusler phases become strongly ferromagnetic after quenching from 800 °C [220]. The structure is body centred cubic but with a face centred superlattice, as illustrated in the electron diffraction patterns (Figure 5-9(b), (c) and (d)). Comparing their standard electron diffraction pattern, it is found that the B2 and $L2_1$ structures have

Chapter 5 Characterization of L₂₁-ordered Ni₂TiAl intermetallic phase and its precipitation behaviour

similar diffraction patterns along the [001] and $[\bar{1}11]$ zone axes. In the [001] zone axis, the {220} and {002} reflections of L₂₁-ordered Ni₂TiAl coincide with the {110} and {001} reflections of B2-ordered NiAl, respectively (Figure 5-8(b) and Figure 5-9(b)). In the $[\bar{1}11]$ zone axis, the {220} reflections of L₂₁-ordered Ni₂TiAl coincide with the {110} reflections of B2-ordered NiAl (Figure 5-8(d) and Figure 5-9(d)). Although the theoretical intensity difference exists between the two phases, it is difficult to distinguish it under the real beam condition. The characteristic reflections to distinguish the two phases are only visible along the [011] zone axis. Figure 5-10 presents the electron diffraction patterns of both L₂₁-ordered Ni₂TiAl and B2-ordered NiAl along the [011] zone axis for a better comparison. The {222} and {002} reflections of L₂₁-ordered Ni₂TiAl coincide with the {111} and {001} reflections of B2-ordered NiAl, whereas the {111} and {311} reflections exclusively exist in the L₂₁-ordered Ni₂TiAl phase. Therefore, the {111} and {311} reflections along the [011] zone axis are considered as the characteristic diffraction spots for L₂₁ structure.

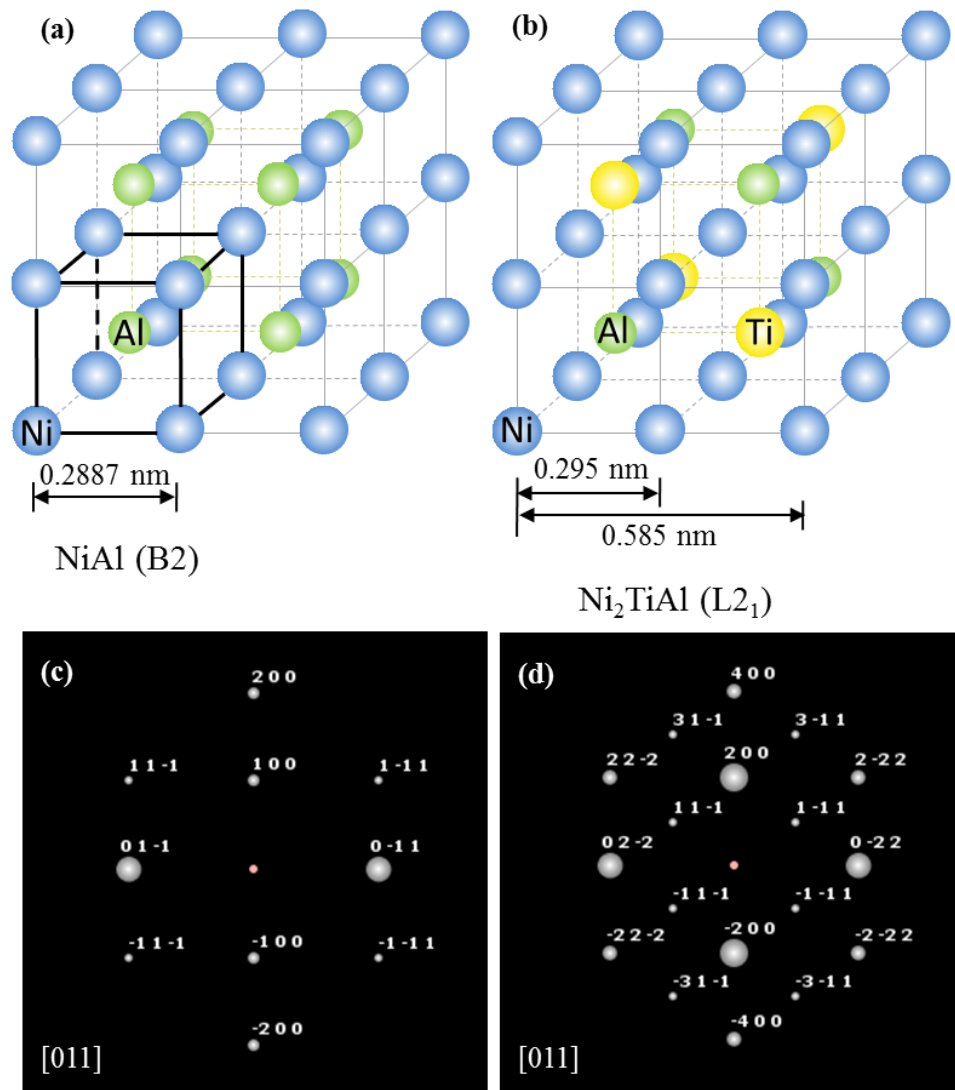


Figure 5-10 (a) Eight unit cells of the B2-ordered NiAl for a better comparison with (b) the unit cell of L₂₁-ordered Ni₂TiAl; diffraction patterns along the [011] zone axis of (c) B2-ordered NiAl and (d) L₂₁-Ni₂TiAl simulated using ICDD PDF-4+ software.

A HREM study was carried out to identify the crystal structure of the precipitates. Figure 5-11 shows the HREM micrographs of precipitate along the [011] and $[\bar{1}11]$ zone axes, respectively. To better clarify the crystalline structure of the precipitate, fast Fourier transform (FFT) analysis is displayed as inset. The characteristic {111} reflections along the [011] zone axis of L₂₁-ordered Ni₂TiAl phase are indexed (see inset). Figure 5-11(b) and (d) reveal the inverse fast Fourier transform (IFFT) image by removing the background noise. The atomic arrangement is coincident with that

Chapter 5 Characterization of L₂₁-ordered Ni₂TiAl intermetallic phase and its precipitation behaviour

of Ni₂TiAl; the indexed d-spacing of 0.3335 nm for the {111} planes and 0.206 nm for the {220} planes are very close to the standard d-spacing of Ni₂TiAl phase (0.3377 nm for {111} plane and 0.2068 nm for {220} plane) given by the ICDD database. The slight deviation may be associated with either the non-stoichiometric composition or the error from the measurement and/or equipment.

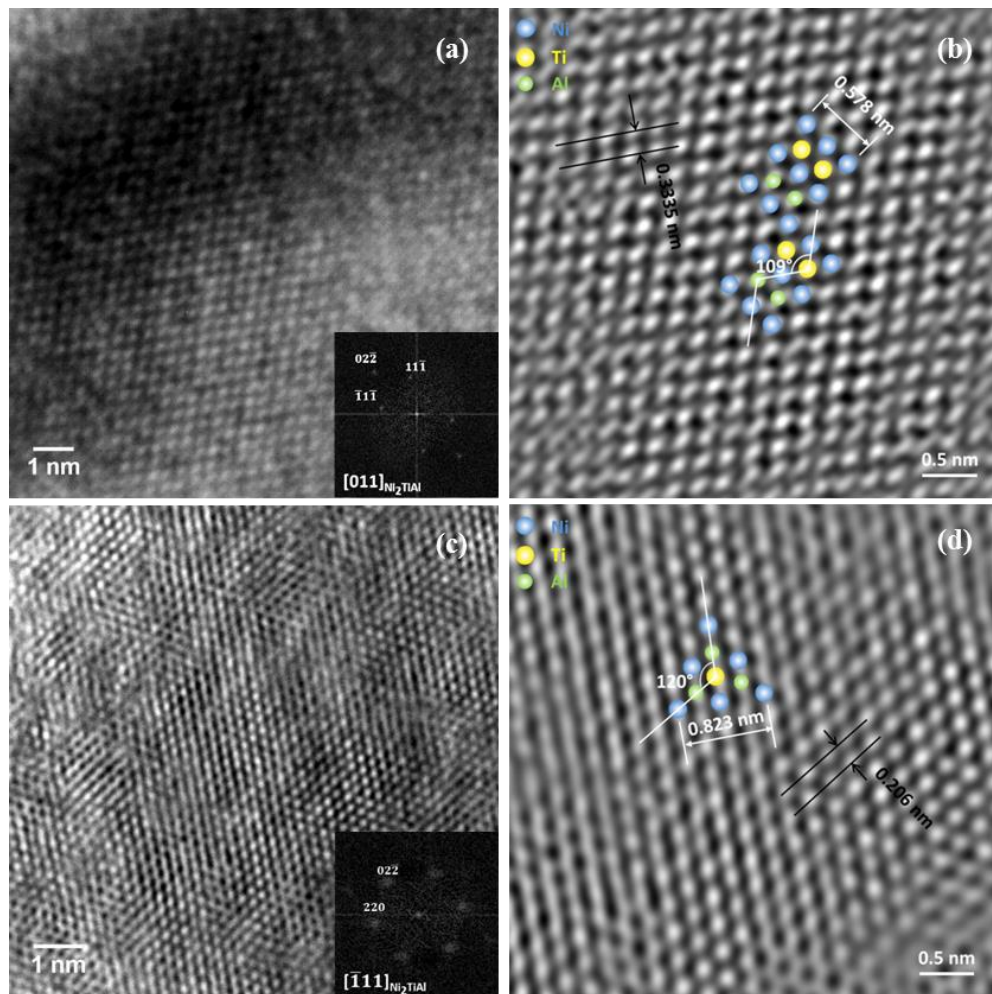


Figure 5-11 HREM micrographs of precipitates in 12% Mn alloy aged at 500 °C for 10080 min, (a) [011] zone axis; (b) IFFT of (a); (c) $[\bar{1}11]$ zone axis; (d) IFFT of (c).

More information about the crystal structure is obtained by SAED analyses (Figure 5-12). The {111} and {311} reflections along the [011] zone axis, which are unique to the L₂₁ structure, are displayed in the inset of Figure 5-12(b). The presence of L₂₁-ordered Ni₂TiAl phase in the dark-field images (white spherical phase in Figure

Chapter 5 Characterization of L₂₁-ordered Ni₂TiAl intermetallic phase and its precipitation behaviour

5-12(b)), which was acquired by using the (11 $\bar{1}$) superlattice spots, further confirms the precipitate is, or at least consists of, L₂₁-ordered Ni₂TiAl phase.

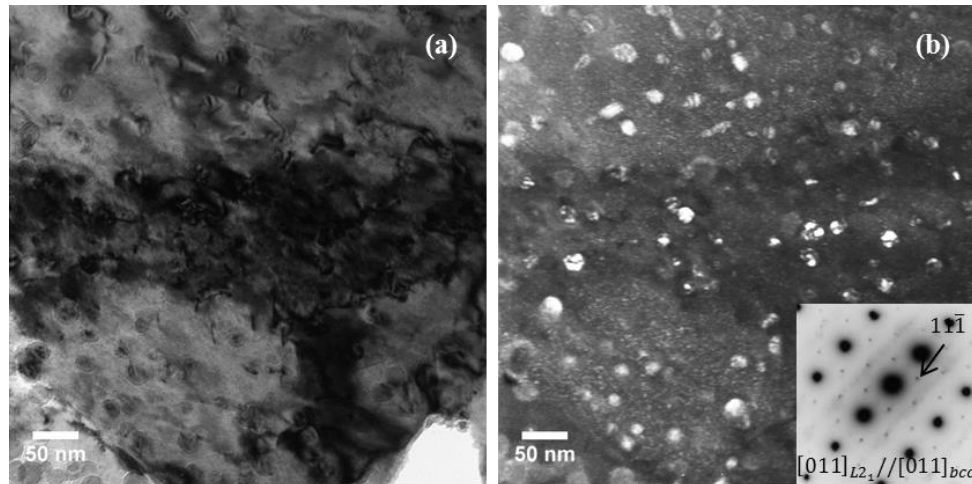


Figure 5-12 (a) Bright-field TEM micrograph of 7% Mn alloy aged at 500 °C for 10080 min along [011] zone axis and (b) corresponding dark-field micrograph using the [11 $\bar{1}$] superlattice spots of precipitates (inset is the corresponding diffraction pattern).

5.6.2 The orientation relationship between the precipitate and martensite matrix

Representative selected area diffraction patterns (SADPs) along low-index zone axis directions (10% Mn alloy, 500 °C / 10080 min state) are shown in Figure 5-13.

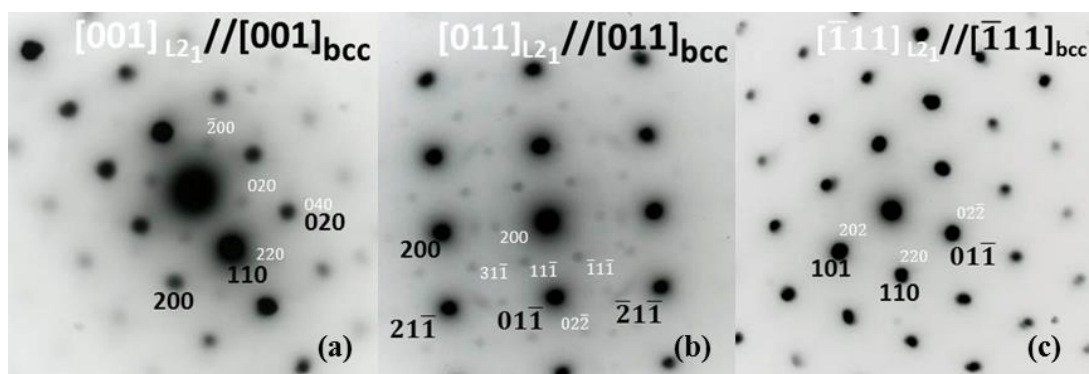


Figure 5-13 Selected area diffraction patterns taken on thin foil samples (500 °C / 10080 min, 10% Mn alloy) along (a) [001], (b) [011] and (c) [1 $\bar{1}$ 1] zone axes.

Chapter 5 Characterization of L₂₁-ordered Ni₂TiAl intermetallic phase and its precipitation behaviour

The coherency between precipitates and martensite matrix was investigated. The SADPs reveal that the orientation of L₂₁-ordered Ni₂TiAl precipitate is exactly coincident with that of the α' -martensite matrix (Figure 5-13). In both the [001] and [011] zone axes (Figure 5-13(a) and (b)), the {040} and {220} reflections of L₂₁-Ni₂TiAl phase are overlapping with the {020} and {110} reflections of the bcc matrix, respectively; in the $[\bar{1}11]$ zone axis, the diffraction pattern of Ni₂TiAl exactly matches that of the matrix, so no extra spots originating from the precipitate were observed (Figure 5-13(c)).

The lattice parameter of L₂₁-ordered Ni₂TiAl phase was determined according to the SADPs. The camera length was calibrated using the lattice parameter of α' -martensite matrix obtained from the XRD analysis. Based on this calibration, the lattice parameter of the L₂₁-ordered Ni₂TiAl phase was calculated as 0.5819 nm. Half of the lattice parameter of L₂₁-ordered Ni₂TiAl, which is the dimension of the small cubic lattice in Figure 5-10(b), is close to the lattice parameter of α' -martensite matrix. The misfit between them is calculated as

$$\delta = \frac{2 \times \left| \frac{1}{2} a_{\text{Ni}_2\text{TiAl}} - a_{\text{bcc}} \right|}{\frac{1}{2} a_{\text{Ni}_2\text{TiAl}} + a_{\text{bcc}}} \times 100\% = 1.24\% \quad (5.3)$$

where $a_{\text{Ni}_2\text{TiAl}}$ is the lattice parameter of Ni₂TiAl and a_{bcc} is the lattice parameter of the martensitic matrix measured by XRD. Owing to the small misfit of the lattice parameters and the special orientation relationship between the two phases, it is proposed that the L₂₁-ordered Ni₂TiAl precipitate is coherent and coplanar with the martensite matrix. Figure 5-14 presents the nano-scale precipitates were uniformly dispersed in martensite matrix in both the 7% Mn and 10% Mn alloys aged at 500°C for 10080 min. The dumbbell-shaped precipitates reveal that they remain coherent with the matrix even after aging at 500 °C for 10080 min, according to Ashby-Brown contrast theory [221].

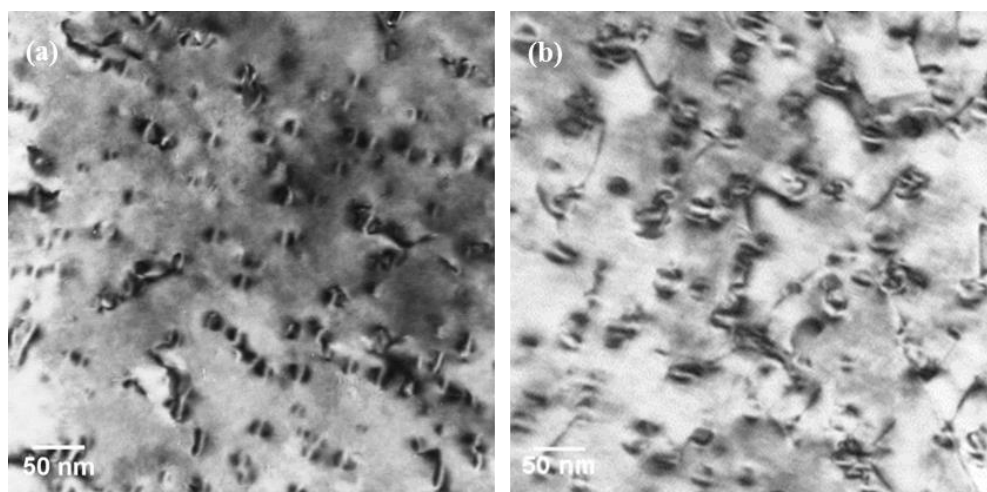


Figure 5-14 Two-beam bright field micrographs of (a) 7% Mn and (b) 10% Mn alloys after aging at 500 °C for 10080 min.

5.7 Core/shell precipitates

Figure 5-15 shows the representative bright-field TEM micrographs (left column) of precipitates formed when aging at 500 °C for 10080 min in 7% Mn alloy (Figure 5-15(a)), 10% Mn alloy (Figure 5-15(b)) and 12% Mn alloy (Figure 5-15(c)), respectively. Corresponding high-magnification TEM micrographs obtained from carbon extraction replicas are correspondingly displayed in the right column. As shown in Figure 5-15, precipitates with a well-developed core/shell structure can be distinguished by the darker central region surrounded by a periphery with brighter contrast. For the 7% Mn alloy aged at 500 °C for 10080 min (Figure 5-15(a)), the average size of precipitates ranges from less than 10 nm to ~20 nm with shells being 2-3 nm thick. Similar microstructure is found in the 10% Mn alloy aged at 500 °C for 10080 min (Figure 5-15(b)). The thickness of the shell is approximately constant at 2-3 nm despite the sizes of precipitates varying from 12 nm to 24 nm, which indicates that the thickness of the shell did not increase with the growth of the core.

Chapter 5 Characterization of L₂₁-ordered Ni₂TiAl intermetallic phase and its precipitation behaviour

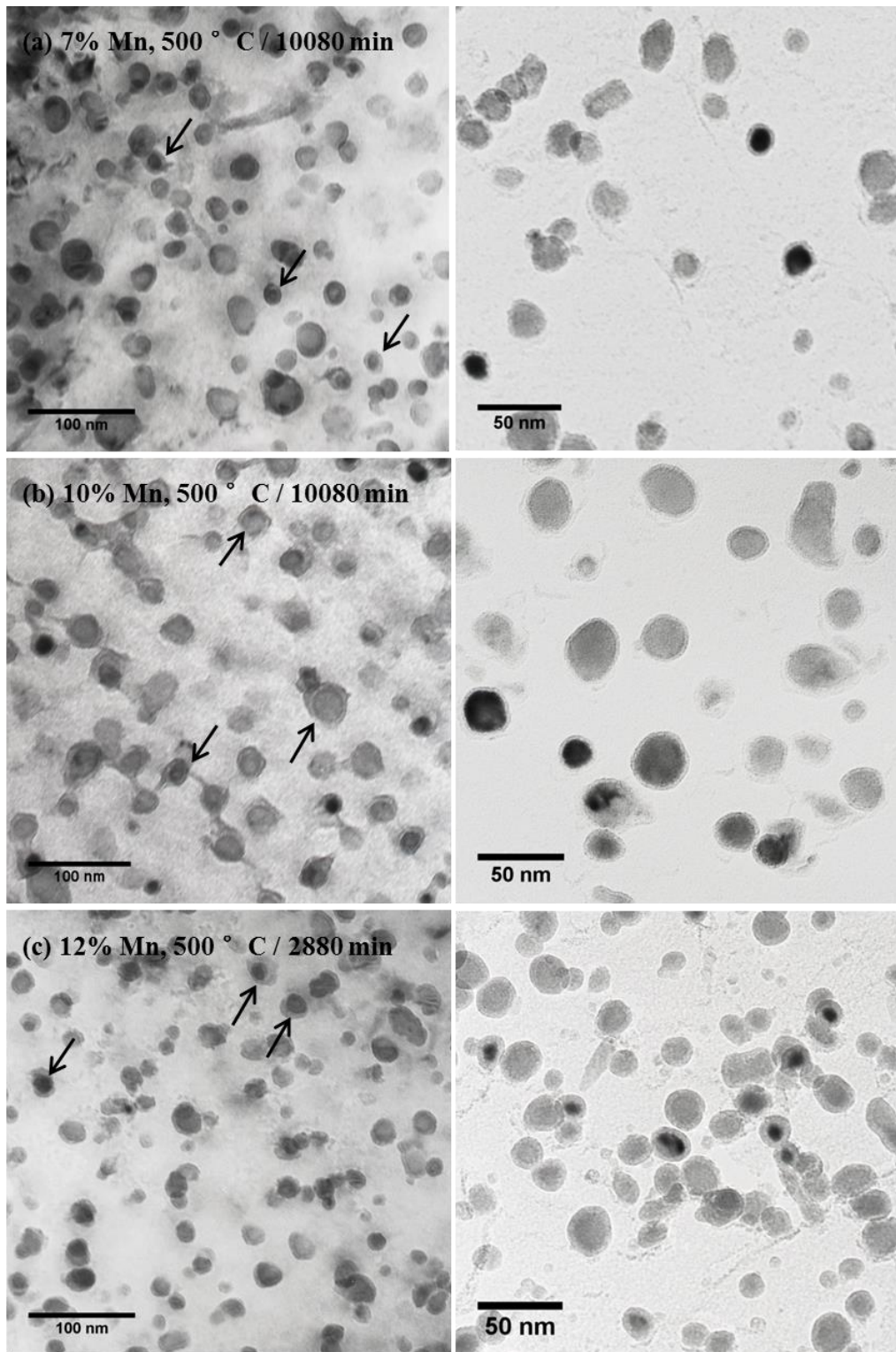


Figure 5-15 Left column: representative bright-field TEM micrographs. Right column: magnified carbon extraction replica TEM micrographs of precipitates. (a) 7% Mn alloy, 500 °C / 10080 min; (b) 10% Mn alloy, 500 °C / 10080 min and (c) 12% Mn alloy, 500 °C / 2880 min.

Chapter 5 Characterization of L₂-ordered Ni₂TiAl intermetallic phase and its precipitation behaviour

As shown in the HAADF micrograph (Figure 5-16), the contrast variation within each precipitate is evident. HAADF image was taken under conditions excluding any diffraction effect, and the image contrast under HAADF mode is Z contrast which depends on the mass and thickness. For the thickness contrast, the following equation describes the relationship between the beam intensity detected by camera, I' , and the thickness of the object, t [222]:

$$I' = I_0(1 - \exp(-\mu t)) \quad (5.4)$$

where I_0 is the beam intensity before it enters the object and μ is the attenuation coefficient. If the object is spherical like the precipitate in this study, the beam intensity detected I' should be continuous along the diameter. The mass contrast, on the other hand, is demonstrated to be roughly proportional to the square of atomic number [223]. Therefore, the sharp contrast at the periphery should be correlated to the mass contrast.

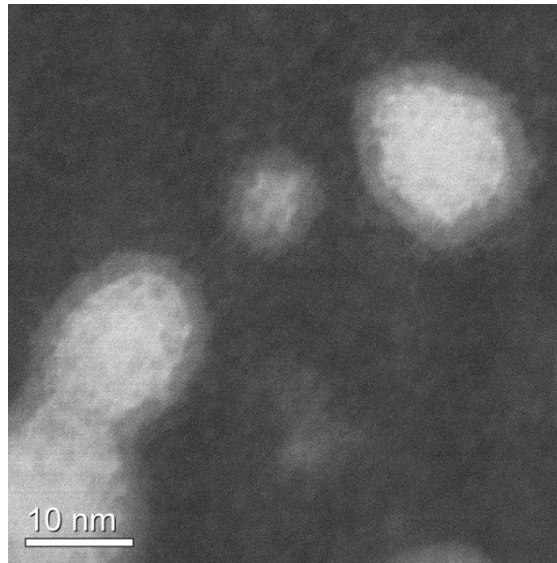


Figure 5-16 HAADF image of core/shell precipitates in 12% Mn alloy aged at 500 °C for 2880 min.

HREM micrographs of precipitates on carbon extraction replicas were acquired to study the core/shell structure. Precipitates with evident core/shell structure can be observed in Figure 5-17(a). Although the interface is visible between the core and shell, the shell is found coherent and coplanar with the core (Figure 5-17(b)). A

Chapter 5 Characterization of L₂₁-ordered Ni₂TiAl intermetallic phase and its precipitation behaviour

magnified HREM micrograph at the periphery of precipitate (Figure 5-17(c)) suggests that the precipitate is one single crystal. The lattice structure is uniform despite a slight distortion at the smearing core/shell interface.

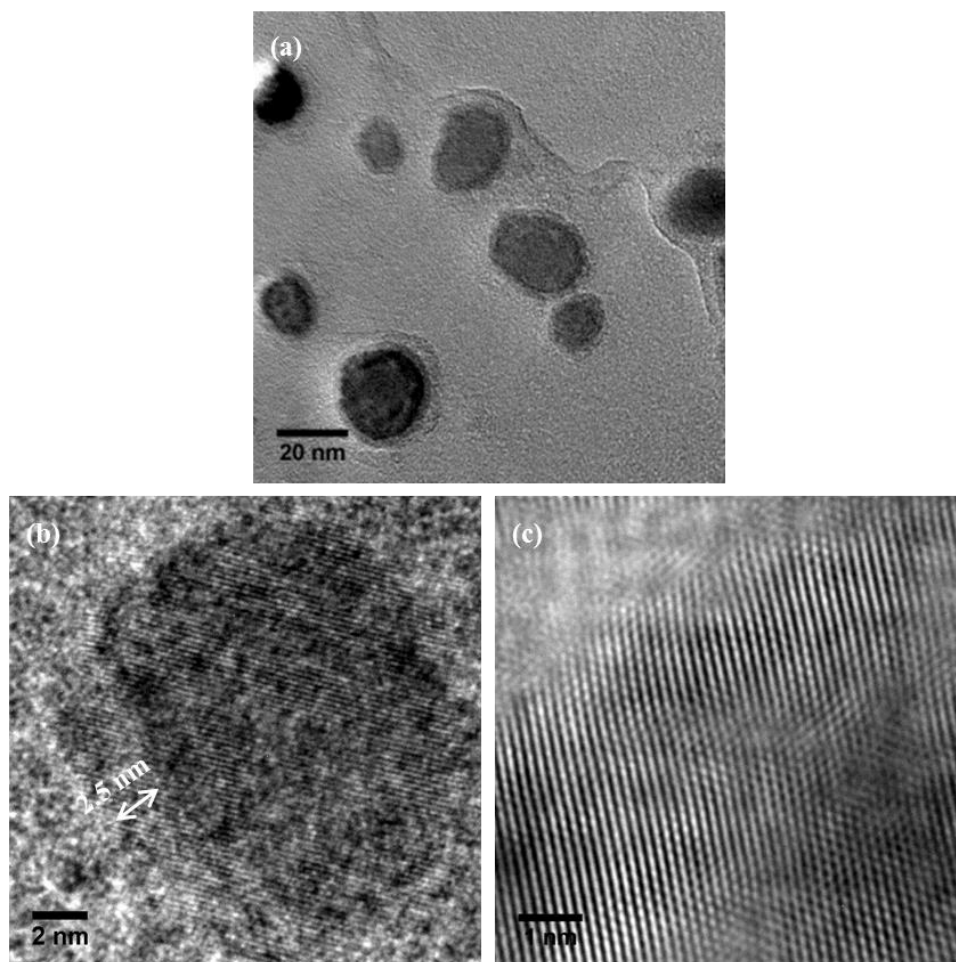


Figure 5-17 HREM micrographs of the precipitate in 12% Mn alloy aged at 500 °C for 10080 min. (a) The low-magnification images of precipitates, (b) core/shell structure at a higher magnification and (c) lattice information at the periphery of precipitate.

The discussion on the non-stoichiometric composition of precipitates (especially the high Al concentration) in Section 5.5 implies the precipitates may be constituted by more than one phase. The existence of the core/shell structure in precipitates is another evidence for this speculation. It is proposed that the precipitate may possess a NiAl/Ni₂TiAl structure. As discussed in Section 5.6.1, these two phases have very similar crystal structure, so they can be regarded as one single crystal. As the spherical phase in the dark-field micrograph in Figure 5-12 was acquired by using

the characteristic (11 $\bar{1}$) superlattice spot of L₂₁ structure, and the brighter core in HAADF micrograph (Figure 5-7) corresponds to a Ti-rich area of the precipitate as Ti has a higher atomic number than Al (²²Ti vs. ¹³Al), we further propose that the core should be L₂₁-Ni₂TiAl phase and the shell should be B2-NiAl. A further investigation is required to examine the core/shell structure within precipitate.

5.8 Discussion

5.8.1 The effects of volume fractions on the coarsening behaviour

- Precipitate size distribution (PSD)

PSDs provide us a pathway to estimate the goodness of fit of the LSW theory to the precipitate coarsening. As discussed in Section 2.3.3, LSW model is strictly valid under the assumption that the volume fraction of precipitates (f_p) is approaching zero and time-invariant. Modern theoretical and simulation studies, however, revealed a discrepancy between the LSW theory and experiment due to $f_p \neq 0$ in reality [224][225]. According to the modified LSW theories, the PSDs are predicted to broaden rapidly when f_p is low and approach the distribution model for interface-dominated coarsening when the limit $f_p \rightarrow 1$ [224]. The TK model (Tokuyama and Kawasaki, [226]) includes a correction for f_p leading to the broadening in PSD function and decrease in the peak height compared to those of LSW model (see Figure 5-18). The results of TK model are in good agreement with LSW theory in the limit $f_p \rightarrow 0$ [136].

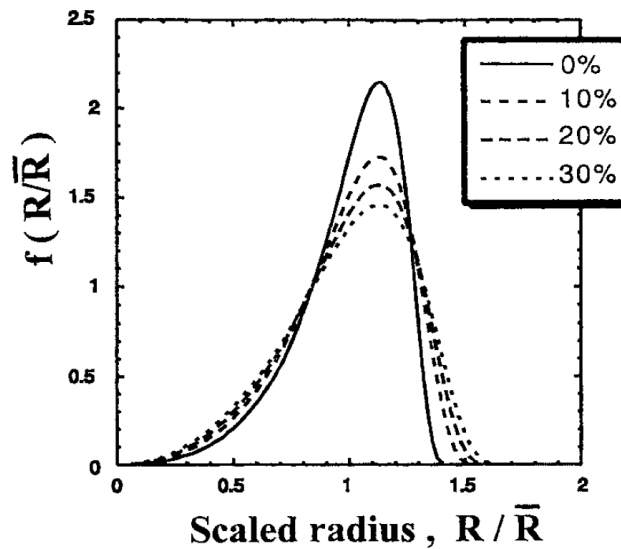


Figure 5-18 The precipitate size distribution as a function of reduced precipitate radius R/\bar{R} for different volume fractions of precipitate f_p [226].

The PSDs of the three alloys in different aging conditions were constructed to demonstrate the evolution of PSDs with aging time. As shown in Figure 5-3, the experimental PSD in the 500 °C / 480 min state follows the LSW theory which indicates that f_p can be roughly regarded as zero. After that the width of PSDs grew significantly (500 °C / 2880 min and 500 °C / 10080 min state) and the PSDs were more consistent with the TK model.

Apart from the volume fraction of precipitates, other attempts were also made to relate this discrepancy to the misfit of lattice parameter [224][227][228]. In this study, as the misfit of lattice parameters between phases has been demonstrated to be small, the broadening of the PSDs is not likely to be associated with the lattice misfit.

- Precipitate coarsening

Precipitate coarsening is controlled by either interface reaction or lattice diffusion, or sometimes by the combination of both. Generally the interface-dominated coarsening occurs at small size while the diffusion-dominated coarsening occurs at larger size. A combination of the two mechanisms takes effect at the transition stage. Experimental results in Section 5.4.2 reveal that at the early aging stage at 500 °C, the precipitates exhibited an interface-dominated growth (coarsening) kinetics

followed by a decrease in the growth rate indicating the initiation of the diffusion-dominated coarsening kinetics (Figure 5-4). The coarsening evolution of precipitate size obeys the diffusion-controlled coarsening kinetics predicted by LSW theory (Figure 5-5). In contrast to the significant broadening of PSDs with the increase of f_p , experimental observation revealed that the dependence of coarsening rate constant on f_p was small and the diffusion-controlled coarsening kinetic form $\bar{r}^3 \sim Kt$ can be maintained even when f_p was high.

Many efforts have been made to investigate the effects of precipitated volume fraction on the coarsening kinetics and the shape of PSDs. Based on these studies, modified LSW theories, in which the precipitated volume fraction is taken into consideration, are established for the realistic case. All the modified theories agree that the non-zero volume fraction does not change the exponents of the temporal laws given by LSW (Equation (2.4), (2.5) and (2.6)) or the time-irrelevance of PSDs, but does change the amplitudes of the temporal power laws and the shapes of PSDs [136][137][138][139]. The presence of non-zero volume fraction, which leads to the interparticle diffusional interactions, can affect the coarsening of precipitates in two ways: (a) Different from the LSW theory claiming that the coarsening rate of a precipitate is solely a function of the precipitate size, the coarsening rate in the modified theories takes the surrounding precipitates into consideration. The precipitate will coarsen when surrounded by precipitates smaller than it and shrink when the surrounding precipitates are larger. (b) In the case where LSW theory is applied, the spatial distribution is considered as random. While in modified theory where the diffusional interaction is included, it is unlikely to find a small and large precipitate almost touching, as the small precipitate tends to shrink when it is close to a larger precipitate. Thus, the average interparticle separation is larger than that in a system with a random spatial distribution. Nevertheless, large precipitates prefer to locate near small precipitates as the small ones can feed solute for their coarsening. Therefore, both precipitate size and spatial distribution have to be considered when discussing the effect of volume fraction on the coarsening behaviours.

According to the modified theories, the coarsening rate constants K_R increase with the volume fraction f_p , and the time-invariant PSDs become broader and more

symmetric as the precipitated volume fraction increases. However, Brailsford and Wynblatt [136] suggested that the coarsening rate constants are much less sensitive to the volume fraction and thus are more compatible with experimental observation. For the evolution of PSDs, the situation is complicated. One possible reason for the broadening is that the continuous nucleation during the precipitation provides an increase in the population of fine precipitates. Secondly, the coarsening of large precipitates at the expense of fine ones results in the increase of the number of large precipitates.

In terms of this work, experimental observations on the coarsening behaviour of precipitates in Mn-based maraging steels revealed that the evolution of PSDs with the increasing volume fraction coincides with the prediction by modified LSW theories, which indicates the effect of precipitate volume fraction cannot be ignored. In the case of coarsening kinetics, the experimental evidence reveal that at the early aging stage (Figure 5-4), precipitates exhibited an interface-dominated growth followed by a decrease in the growth rate indicating the initiation of the diffusion-dominated coarsening. The coarsening rate constant K_R obeys the diffusion-controlled coarsening kinetics predicted by LSW theory (Figure 5-5). It is also revealed that the Mn content of the alloy, which is not the main precipitate forming element, has a significant effect on the growth and coarsening kinetics of precipitates. This will be discussed in detail in Section 5.8.3.

5.8.2 The formation mechanism of core/shell structure

The most well-known precipitate with core/shell structure is, Al₃(Sc,Zr) precipitates in Al-Zr-Sc alloys which have been widely investigated based on both experimental analyses and complementary first-principle calculations [229]. Elagin et al. first claimed that Zr could substitute the Sc atoms in Al₃Sc precipitates in an Al-0.24Sc-0.04Zr alloy [230]. Later, HREM studies [229][231][232] revealed that Zr was detected at the α -Al/Al₃(Sc_{1-x}Zr_x) interfaces. Then APT analyses further quantified an 8-10 at.% Zr concentration at the interface [233]. It is suggested that Zr acts as a barrier to the diffusion of Sc, and contributes to lowering the coarsening rate of

Chapter 5 Characterization of L₂-ordered Ni₂TiAl intermetallic phase and its precipitation behaviour

precipitates [234]. These experimental observations agree with the prediction by the thermodynamic calculation and model simulations [235].

Another well-known group is Cu-bearing precipitation-strengthening Fe alloys. In Fe-Cr-Ni-Al-Cu alloys [38][39], the decomposition of the Ni+Al+Cu clusters leads to a core/shell precipitates with Cu-rich core surrounded by a NiAl shell. The thermally stable NiAl shells hinder the diffusion growth of Cu core and more importantly, reduce the misfit between the fcc Cu-rich core and bcc matrix. While in the conventional maraging steels strengthened by Ni₃Ti precipitates, the formation mechanism of core/shell structure is explained as: since the solubility of Cu in Ni₃Ti phase is low, the Cu-rich clusters usually act as nucleation sites for Ni₃Ti precipitates and thus a unique core/shell precipitate with Cu embedded in Ni₃Ti phase can be found in these maraging steels. Detailed discussion about the core/shell structure in Cu-containing Fe alloys has been given in Section 2.2.3.5.

Both thermodynamic and kinetic factors were studied in order to understand the formation of the core/shell structure in precipitates. Table 5–3 presents the diffusion rates of the constituent elements in bcc-Fe at 500 °C. Al possesses the highest diffusion rate followed by Ti and Mn which have the same order of magnitude. Ni, together with Fe itself, has the slowest diffusion rates in bcc-Fe at 500 °C. Except that Al has the highest diffusion rate which is about five or six orders of magnitude faster than other elements, the difference of the diffusion rates among Ti, Mn, Ni and Fe are not large. The APT analyses on a 9% Mn maraging steel reported that at the very early stage of precipitation (0.5 h at 450 °C), 50 at.% Fe, 35 at.% Ni, 11 at.% Mn, 2 at.% Al and 2 at.% Ti were detected [135]. It is obvious that Ni, which possesses the slowest diffusion rate at 450 °C, had a relatively high concentration in precipitates than other elements (except the matrix element Fe); while Al and Ti which possess the fastest diffusion rates, had very low concentrations, thus it is unlikely that the precipitate heterogeneity is associated with the kinetic effect.

Chapter 5 Characterization of L₂₁-ordered Ni₂TiAl intermetallic phase and its precipitation behaviour

Table 5–3 The diffusion rates of the constituent elements in bcc-Fe at 500 °C

Element	Diffusion rate (cm ² s ⁻¹)	Equation	References
Al	6.05×10^{-11}	$58600 \exp(-53000/RT)$	[236]
Ti	7.97×10^{-16}	$20.01 \exp(-58000/RT)$	[237]
Mn	5.01×10^{-16}	$0.35 \exp(-52500/RT)$	[238]
Ni	3.54×10^{-17}	$1.4 \exp(-58700/RT)$	[195]
Fe	2.17×10^{-17}	$2.0 \exp(-60000/RT)$	[239]

It is generally accepted that the precipitation process is governed by complex thermodynamic driving force [109]. The mixing enthalpy of elements, ΔH_{mix} , are displayed in Table 5–4 to discuss the precipitate stability in Mn-based maraging steels [240]. The three largest negative mixing enthalpy belong to Al-Ti, Ni-Ti and Al-Ni, which means there is a high tendency that these three elements will segregate and form a second phase. This conclusion agrees with the experimental results that Ni₂TiAl is the dominant precipitates in Mn-based maraging steels. In addition, no positive mixing enthalpy in Table 5–4 suggests the other two elements, Fe and Mn, may also partition to the precipitates, especially considering that both of them have high concentrations in the matrix. In view of the negative mixing enthalpy between elements, the precipitates are not likely to decompose during aging. Therefore, additional factors, such as interfacial energy are taken into consideration. The lattice parameter of B2-NiAl phase ($a = 0.2887$ nm) is larger than that of bcc-Fe ($a = 0.2884$ nm) but smaller than that of 1/8 Ni₂TiAl lattice ($a = 0.2925$ nm). Therefore, the formation of NiAl at the interface is believed to contribute to the further reduction of the lattice misfit between Ni₂TiAl and bcc-Fe matrix. Previous studies have reported the similar formation of B2 phase from the parent L₂₁ phase in a Ni-Ti-Al alloy [86]. Besides, a two phase L₂₁-Ni₂TiAl/B2-NiAl precipitates formed by spinodal decomposition: $L2_1 \rightarrow L2_1 + B2$ were also observed in a ferritic alloy [85].

Chapter 5 Characterization of L2₁-ordered Ni₂TiAl intermetallic phase and its precipitation behaviour

It is proposed that the L2₁-Ni₂TiAl/B2-NiAl precipitate is a more thermodynamically stable structure in the Mn-based maraging steels.

Table 5–4 The mixing enthalpy of elements in the Mn-based maraging steels [240].

$\Delta H_{mix}(kJmol^{-1})$	Al	Ti	Mn	Fe	Ni
Al	-	-30	-19	-11	-22
Ti	-	-	-8	-17	-35
Mn	-	-	-	0	-8
Fe	-	-	-	-	-2
Ni	-	-	-	-	-

5.8.3 The effect of Mn on the precipitation

The microstructural observation revealed that the nucleation of Ni₂TiAl was promoted by the Mn content of the alloy. As shown in Figure 5-1, a higher number density of precipitates was observed in the 12% Mn alloy compared to the 7% Mn alloy for the same aging conditions. Osamura et al. [241] found that Ni and Mn additions promoted the precipitation reaction in a Fe-Cu alloy. Jiao et al. [106] also reported that the additions of Ni and Mn in Fe-Cu alloy were beneficial to increasing the number density of precipitates. Complementary Langer-Schwartz simulation and first-principles calculation further demonstrated that Ni had a more significant effect than Mn on decreasing the critical energy for nucleation [242][243].

According to the classical nucleation theory [244], the nucleation of Ni₂TiAl precipitates can be described by:

$$\frac{dN}{dt} \propto \left(\frac{-\sigma_n}{kT}\right) \quad (5.5)$$

where σ_n is the critical energy for nucleation, k is the Boltzmann's constant and T is the temperature in kelvin. The critical energy for nucleation is expressed as:

$$\sigma_n = \frac{16\pi\sigma_{\alpha/\beta}^3}{3(\sigma_V + \sigma_{el})^2} \quad (5.6)$$

where $\sigma_{\alpha/\beta}$ is the interfacial free energy per unit area between the precipitate and matrix, ΔG_V is the chemical driving force of precipitates per unit volume and σ_{el} is the elastic strain energy. Therefore, the effect of Mn content on reducing σ_n can be discussed in two aspects: the elastic strain energy for nucleation and the precipitate/matrix interfacial energy. APT analyses on the early precipitation stage illustrated that the precipitates in a 9% Mn-based maraging steel contained a considerable Mn content (11 at.% Mn at 450 °C / 0.5 h) [135], which indicates that Mn was involved in the nucleation of precipitates. The study by Zhang et al. revealed that Mn has the capability of reducing the misfit strain energy at interface, namely, when Mn atoms enter the nuclei, the lattice parameter of the nuclei can be decreased and the strain energy barrier for nucleation is also decreased [242]. On the other hand, as the diffusivity of the constituent elements in Table 5–3 implies, Mn has a relatively fast diffusion rate. Moreover, the high mixing enthalpy of Fe/Mn (Table 5–4), indicates that Mn tends to segregate from the Fe matrix. Based on these two reasons, it is highly possible that these Mn-rich clusters acts as nucleation sites for further precipitation, and thus the number density of precipitate and its growth rate was largely dependent on the Mn content.

5.9 Summary

1. Conventional TEM-EDS and STEM-EDS analyses demonstrate that the nano-scale precipitates in Mn-based maraging steels is a non-stoichiometric Ni₂TiAl phase with a small amount of Fe and Mn substitution. This non-stoichiometric composition is believed to enhance the ductility of the phase [103].
2. HREM combined with SAED study identifies the crystal structure of the precipitate. The L₂₁-ordered Ni₂TiAl phase is expected to have a better creep resistance than B2-NiAl phase [91]. The orientation relationship between the L₂₁-ordered Ni₂TiAl phase and bcc martensite matrix is found to be $(220)_{L_{21}} \parallel (110)_{bcc}$, $[001]_{L_{21}} \parallel [001]_{bcc}$; $(220)_{L_{21}} \parallel (110)_{bcc}$,

$[011]_{L_{21}} \parallel [011]_{bcc}$; $(220)_{L_{21}} \parallel (110)_{bcc}$, $[\bar{1}11]_{L_{21}} \parallel [\bar{1}11]_{bcc}$. One eighth of the crystal structure of L₂₁-Ni₂TiAl phase is a bcc cubic lattice which has a similar lattice parameter with the bcc matrix. The lattice misfit between them is calculated as 1.24%. This small lattice misfit together with the special orientation relationship illustrates that the L₂₁-ordered Ni₂TiAl precipitates is not only coherent but also coplanar with the matrix. The dumbbell-shaped precipitates in the 10080 min aged sample demonstrate that the precipitates maintained the coherency with the matrix even after long-term aging treatment (Figure 5-14).

3. The shell of the precipitates in Mn-based maraging steels is found to have a strong resistance to coarsening and maintain a thickness of 2-3 nm regardless of the growth of core during aging. The presence of core/shell structure indicates the heterogeneity in precipitates. A sharp step of contrast at the periphery under HAADF observation (Figure 5-16) excludes the possibility of thickness contrast (assuming the precipitates are spherical) and thus confirms the sharp contrast corresponds to the mass difference. HREM analyses at the periphery suggest that the lattice structure of the shell is uniform with that of the core despite a slight distortion at interface. Along with the evidence of HAADF and dark-field micrograph, it is proposed that the core is Ni₂TiAl and the shell is NiAl. It is believed that the L₂₁-Ni₂TiAl/B2-NiAl structure can further decrease the lattice misfit between the precipitate and bcc-Fe matrix.
4. Owing to the non-zero volume fraction in reality, a broadening of the experimental PSDs than the theoretical PSD function is evident, especially at the longest aging time when the volume fraction of precipitates cannot be ignored. However, the discrepancy is not that obvious in the coarsening rate as the coarsening rate constants (K_R) are much less sensitive to the volume fraction compared to the PSDs [136]. Experimental results reveal that coarsening rate constants of precipitates in the three alloys follow the diffusion-controlled coarsening kinetic form $\bar{r}^3 \sim Kt$ predicted by LSW theory.

5. Microstructural observation reveals a higher number density and larger size of precipitates in 12% Mn alloy compared to 7% and 10% Mn alloys for the same aging condition. Both thermodynamic and kinetic analyses suggest that Mn atoms participated in the nucleation of precipitates and reduced the misfit strain energy at the interface [106]. Therefore, higher Mn content is believed to promote the nucleation and thus the growth and coarsening of precipitates. The faster coarsening rate as well as the higher volume fraction of precipitate in 12% Mn alloy is correlated to the large number of nucleation sites due to Mn segregation.

Chapter 6 The formation mechanism of reverted austenite and its mechanical stability

6.1 Introduction

As most Fe-Mn-(Ni) maraging alloys exhibit a poor ductility due to the Mn segregation at grain boundaries, many studies have been carried out to improve their ductility and some of them proposed that the ductility can be improved by generating reverted austenite via aging at higher temperatures or for longer times.

In terms of the Mn TRIP steels, in the 1960s Goldshtein et al. [12] first reported an excellent toughness in an 8% Mn steel with a considerable amount of austenite. Later Miller found that, by intercritical annealing, 20-40% austenite was obtained in 0.1-5 wt.% Mn steels with excellent stability [24]. Based on Miller's work, Luo et al. modified the composition of 5 wt.% Mn steels and 30% austenite was formed in the new alloy, and thereby, the tensile strength was improved to 1-1.5 GPa and total elongation to 31-44% [27].

In this study, the approach to form Mn-rich austenite is different from the above intercritical annealing process in Mn TRIP steels. The austenite reversion in Mn-based maraging steels took place simultaneously with precipitation when aging at relatively high temperature. The difference in the heat treatment process led to the microstructure and mechanical properties of reverted austenite being different from those of retained austenite. It is worth emphasising that as the austenite reversion occurred simultaneously with the precipitation, with Mn atoms involved in both processes, and therefore there might expect to be a competition in the role of Mn.

As discussed in Section 2.4.1, both the amount and stability of austenite are of great importance for the mechanical properties of steels containing austenite, based on which the optimization of microstructure/properties can be feasible. Therefore, the major aim of this chapter is to characterizing the austenite phase in different aging conditions and investigating its formation mechanisms. The influence of the quantity

of reverted austenite on the mechanical properties will be discussed in the next chapter.

6.2 SEM observation

6.2.1 The effect of aging parameters on austenite reversion

The typical microstructure of reverted austenite in α' -martensite matrix along with uniformly distributed precipitates has been given in Figure 4-7. In this section, the representative 12% Mn alloy was studied to explore the effects of aging temperatures/times on austenite reversion.

Aging at 420 °C even for 10080 minutes did not result in any detectable austenite phase, however, a very small amount of matrix austenite layers at the prior austenite grain boundaries at the martensite packet boundaries were observed (Figure 6-1(a)). In contrast to the sluggish austenite reversion, a large number density of nano-scaled precipitates has been formed at this stage (Figure 6-1(b)).

At 460 °C, the sample after aged for 2880 minutes also exhibited a typical microstructure of the austenite layers along boundaries (Figure 6-1(c)). The matrix austenite at prior austenite boundaries, denoted 'M', appears thinner and smoother than austenite layers at martensite lath/packet boundaries. As expected, prolonged aging for 10080 minutes led to the austenite layers growing into lath-like austenite, as shown in Figure 6-1(d).

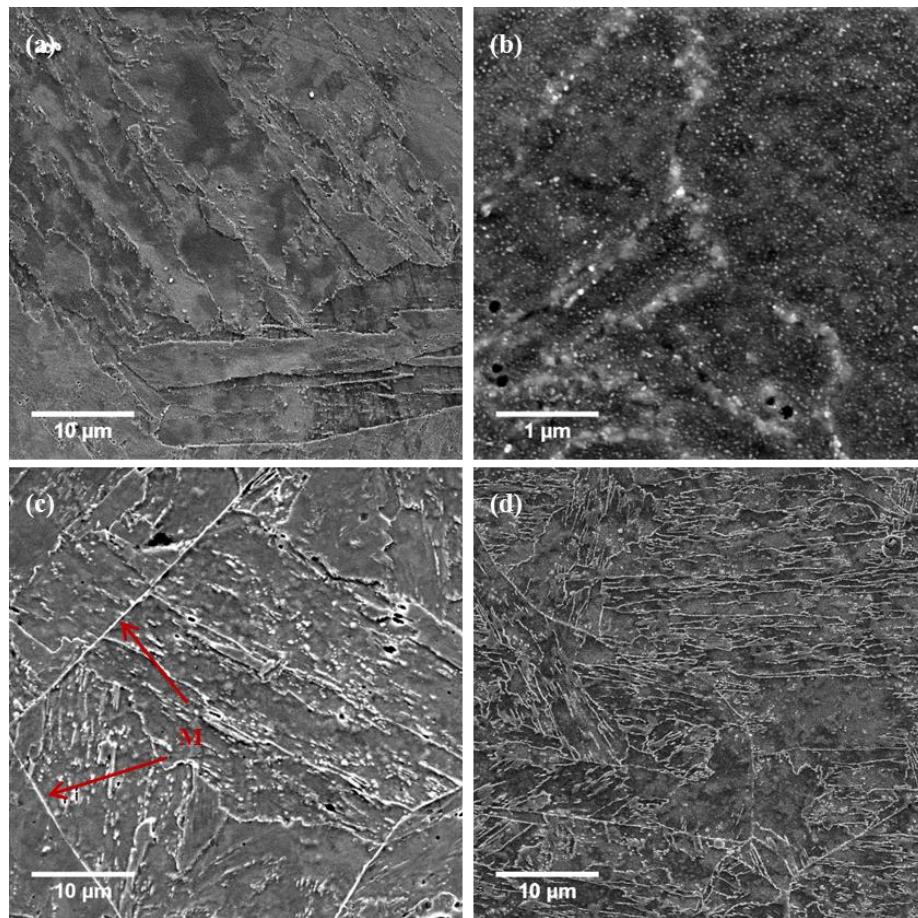


Figure 6-1 SEM micrographs showing the morphologies of reverted austenite in the 12% Mn alloy during aging. (a) Thin austenite layers formed along boundaries and (b) highly dispersed fine precipitates at 420 °C / 10080 min state; (c) evident matrix austenite and austenite layers at 460 °C / 2880 min state; (d) the amount of austenite increased after aging at 460 °C for 10080 min.

When increasing the aging temperature to 500 °C, ultrafine precipitates were generated at the onset of aging, as shown in Figure 6-2(a). Thin matrix austenite and austenite layers at boundaries were also visible in the 10 min aged state (Figure 6-2(b)). After a longer aging time, the austenite layers gradually grew into film-like and then lath-like austenite (Figure 6-2(c) and (d)). The lath-like austenite was formed not only along the boundaries, but also within the martensite laths. It is found that the lath-like austenite and residual martensite present a lamellar structure (see inset in Figure 6-2(d)).

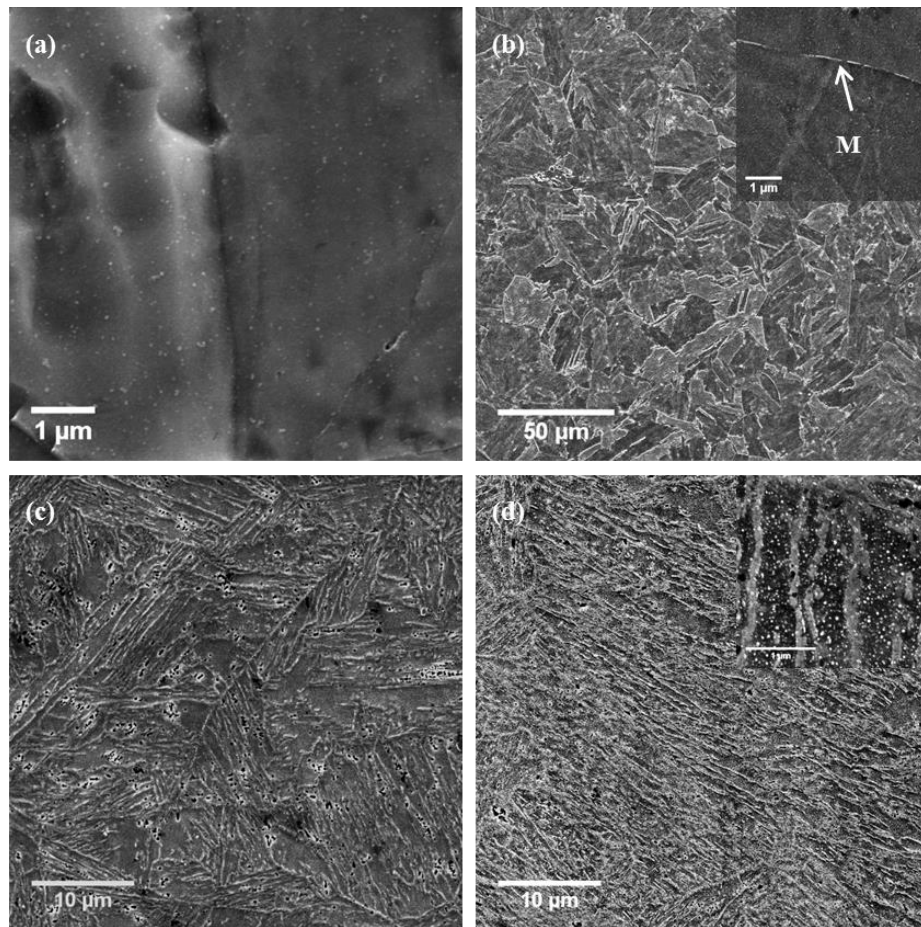


Figure 6-2 (a) Fine precipitates and (b) thin matrix austenite at the onset of aging in the 12% Mn alloy (500 °C / 10 min state); (c) the lath-like austenite became dominant after aging for 2880 min; (d) a lamellar structure of alternative lath-like austenite and residual martensite in the 10080 min aged sample.

Raising the aging temperature to 540 °C led to a further increase in the driving force for austenite reversion. The initial point for austenite reversion was shorter than 10 minutes, so it was not captured. The amounts of reverted austenite formed at 540 °C were higher than that formed at 500 °C for the same durations (Figure 6-3(a)). In addition, the thickness of lath-like austenite was also larger (Figure 6-3(b)).

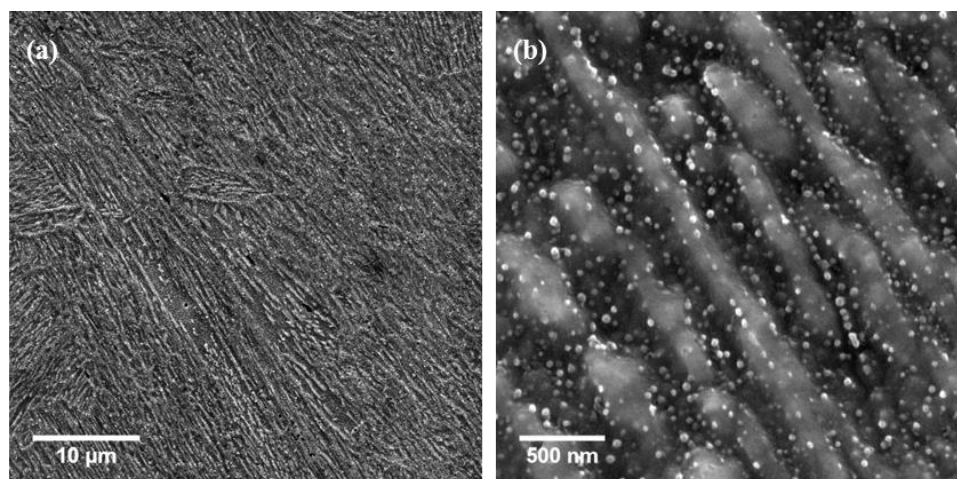


Figure 6-3 (a) Reverted austenite in the 12% Mn alloy after aging at 540 °C for 10080 min;
(b) reverted austenite is free of precipitates.

6.2.2 The effect of Mn content on austenite reversion

The kinetics of austenite reversion in the 7% Mn alloy was very slow. No reverted austenite was present within 2880 min when aging at 500 °C, but nano-precipitates have been found uniformly distributed in α' -martensite matrix (Figure 6-4(a)). Even after aging for 10080 min did not lead to an evident increase of the amount of reverted austenite, only matrix austenite layers was observed (Figure 6-4(b)). In the 10% Mn alloy, the amount of reverted austenite was much higher than that in 7% Mn alloy for the same aging conditions. It also appears that the aging time did not appreciably affect the quantity of reverted austenite in the late aging stage, with the amount of reverted austenite in the 10080 min aged sample (Figure 6-4(d)) not much higher than that in the 2880 min aged sample (Figure 6-4(c)). In addition, the amount of reverted austenite in the 12% Mn alloy (Figure 6-2) was also much higher than that in 10% Mn alloy (Figure 6-4) for the same aging conditions. Clearly, therefore, the higher the Mn content of the alloy, the greater the austenite reversion.

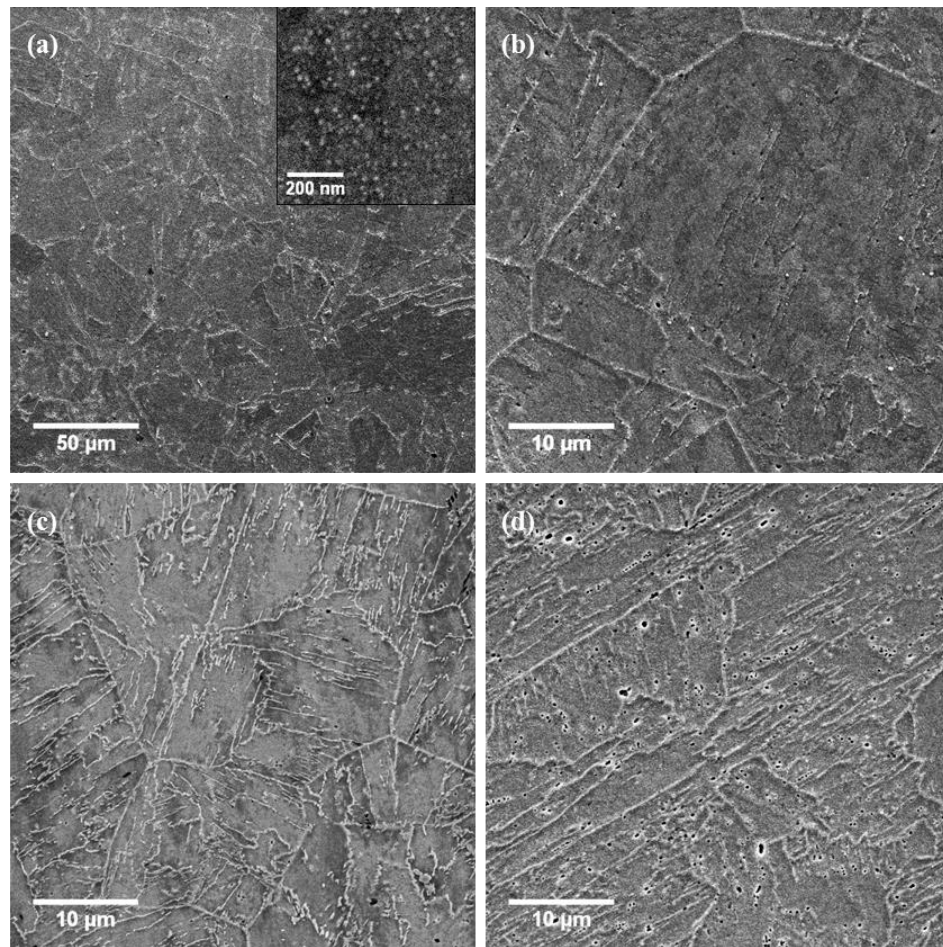


Figure 6-4 SEM observation of (a) 7% Mn alloy (500 °C / 2880 min state); (b) 7% Mn alloy (500 °C / 10080 min state); (c) 10% Mn alloy (500 °C / 2880 min state); (d) 10% Mn alloy (500 °C / 10080 min state).

6.3 TEM investigation

TEM investigations were conducted on samples in which reverted austenite could be observed. At the beginning of austenite reversion (e.g. 10% Mn alloy, 500 °C / 1440 min state (Figure 6-5(a)) or when the kinetics of austenite reversion was very slow, e.g. 7% Mn alloy, 500 °C / 10080 min state (Figure 6-5(b))), only thin matrix austenite, which looked like nanolayer, could be found along the prior austenite grain boundaries and this was consistent with what had been observed under SEM observations.

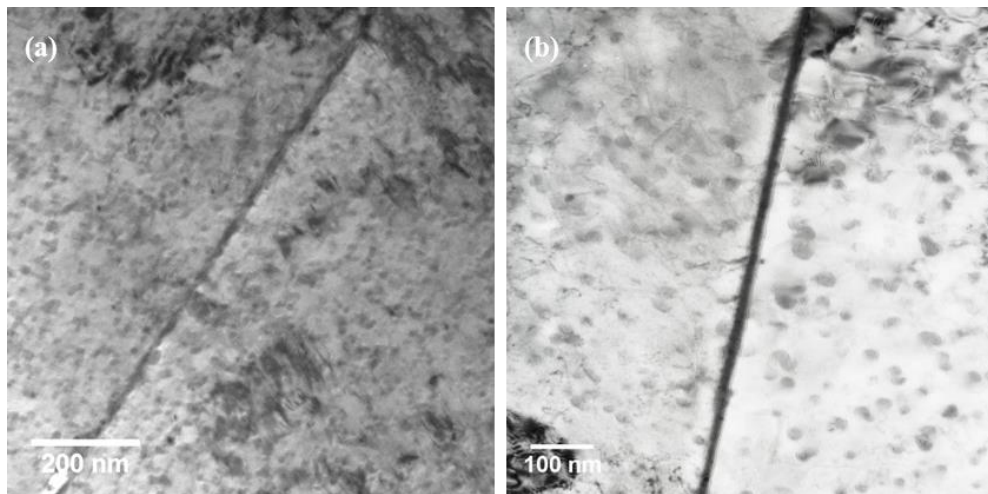


Figure 6-5 Matrix austenite formed along prior austenite grain boundaries in (a) 10% Mn alloy at 500 °C / 1440 min state and (b) 7% Mn alloy at 500 °C / 10080 min state.

With the growth of austenite, the dominant morphology of reverted austenite gradually became film-like and then lath-like. Images of lath-like austenite from different orientations parallel to the elongated austenite were shown in Figure 6-6. Besides, the TEM observation demonstrated that the reverted austenite was free of precipitates, whereas a high dislocation density induced from cooling was observed within the austenite grains.

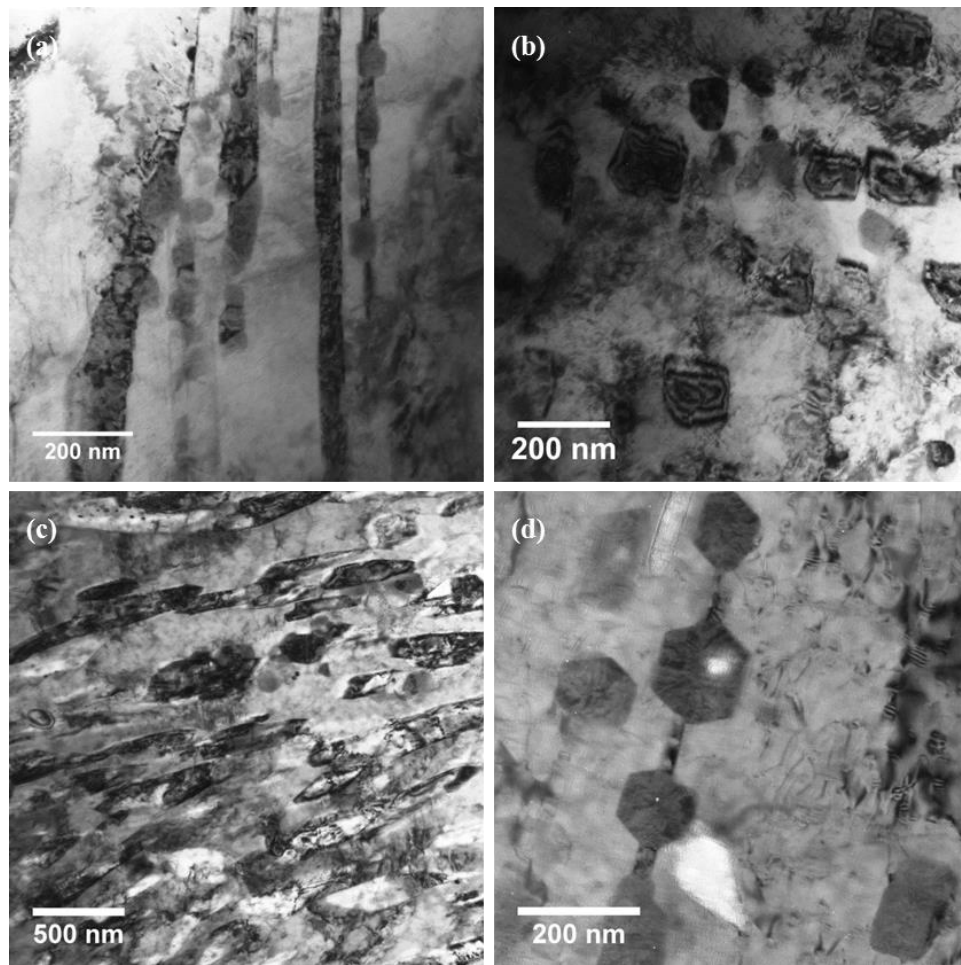


Figure 6-6 TEM micrographs of lath-like austenite in (a) 12% Mn alloy aging at 500 °C for 2880 min and (b) 12% Mn alloy aging at 540 °C for 2880 min; (c) and (d) are the corresponding images from a different orientation.

The evolution of the chemical composition in reverted austenite and adjacent martensite was analysed by TEM-EDS. The EDS analyses of the three alloys are presented in Table 6–1 and Table 6–2. Each data is the average of at least 5 measurements.

It is worth noting that the Al contents of solution-treated matrix in the three alloys were higher than the nominal content of the alloys (Al: ~2.5 at.%). This is probably due to the inaccuracy of the semi-quantitative analysis using EDS in the TEM, where Al gives the second highest peak per atomic fraction for the whole periodic table. Otherwise, the detected compositions of the martensite matrix in the SHT state are consistent with the nominal compositions of alloys. Schnitzer et al. [147] who

compared the composition results measured by TEM-EDS and APT when studying the reverted austenite in a PH 13-8 maraging steels, also stated that there was no evident difference between the results obtained by the two methods, except that the Al concentration by the TEM-EDS measurement was slightly higher than that obtained by the APT measurement.

Table 6–1 presents the chemical compositions of austenite and martensite in the 7% Mn alloy. As the kinetics of austenite reversion in the 7% Mn alloy was slow, the composition analysis was only performed on film-like austenite (nanolayer) formed after aging at 500 °C for a long time. The Mn concentration of austenite nanolayer increased with aging time, from 12.9 ± 0.6 at.% in the 500 °C / 5760 min state to 16.2 ± 0.3 at.% in the 500 °C / 10080 min state. What was unexpected is that the austenite nanolayer was also enriched in Ti and Mo. The Ti concentration of the austenite maintained at a level of 12.4-14.5 at.% and the Mo concentration maintained between 10.5 at.% and 13.6 at.%. A similar Ti and Mo enrichment in austenite was also observed in the 10% Mn alloy in the early stage of austenite reversion. This finding is very interesting as Ti is generally considered to raise the A_e^3 temperature and therefore is not expected in the austenite phase. However, Ni, as an austenite stabilizer element, was present at a low concentration of 1.2-1.9 at.% in the reverted austenite. On the other hand, the composition of martensite matrix was approximately constant during the aging process, for example, the composition of matrix in the 500 °C / 10080 min state was similar to that in the SHT state (Table 6–1).

Chapter 6 The formation mechanism of reverted austenite and its mechanical stability

Table 6–1 Chemical compositions (at.%) of reverted austenite and martensite in the 7% Mn alloy obtained by TEM-EDS

Elements	SHT	500 °C		
		5760 min		10080 min
	Matrix	Austenite	Matrix	Austenite
Al	5.0 ± 0.6	2.7 ± 0.5	3.7 ± 0.6	1.8 ± 0.4
Mo	1.4 ± 0.3	13.6 ± 1.0	1.3 ± 0.1	10.5 ± 0.3
Ti	1.1 ± 0.1	14.5 ± 0.8	1.1 ± 0.3	12.4 ± 0.5
Mn	6.3 ± 0.3	12.9 ± 0.6	6.4 ± 0.2	16.2 ± 0.3
Fe	84.4 ± 0.6	54.4 ± 1.5	85.3 ± 1.5	58.0 ± 0.6
Ni	1.8 ± 0.1	1.9 ± 0.4	1.9 ± 0.6	1.2 ± 0.4

The chemical compositions of lath-like reverted austenite in the 12% Mn alloy are listed in Table 6–2. The lath-like reverted austenite formed in the 12% Mn alloy had a considerably higher Mn concentration (24-26.1 at.%) compared to that in the 7% Mn alloy. While the Ti and Mo concentrations in the reverted austenite (Mo: 2.9-7.3 at.%, Ti: 2.9-8.0 at.%) were lower than those in the 7% Mn alloy. On the other hand, there was an inversed relationship between the Mn concentration of the matrix and the aging time (the Mn concentration reduced from 11.5 at.% in the SHT state to 6.9 at.% after aging at 500 °C for a long time), which is reasonable as the formation of reverted austenite consumed a large amount of Mn from the martensite matrix.

Chapter 6 The formation mechanism of reverted austenite and its mechanical stability

Table 6–2 Chemical compositions (at.%) of reverted austenite and martensite in the 12% Mn alloy under various heat treatment conditions obtained by TEM-EDS.

Elements	SHT	460 °C		500 °C				540 °C
		10080 min		2880 min		10080 min		2880 min
		Matrix	Matrix	Austenite	Matrix	Austenite	Matrix	Austenite
Al	3.8 ± 0.8	5.1 ± 1.4	1.5 ± 0.2	5.3 ± 1.0	2.8 ± 0.4	7.0 ± 1.5	4.4 ± 1.0	3.6 ± 0.7
Mo	1.6 ± 0.2	1.5 ± 0.4	4.4 ± 0.5	1.5 ± 0.6	2.5 ± 0.6	1.6 ± 0.5	7.3 ± 1.6	2.9 ± 0.4
Ti	1.1 ± 0.4	1.2 ± 0.2	3.3 ± 0.6	1.0 ± 0.3	2.9 ± 0.8	1.5 ± 0.4	8.0 ± 0.6	5.0 ± 0.6
Mn	11.5 ± 0.5	9.8 ± 0.8	26.1 ± 1.0	9.6 ± 0.5	24.1 ± 1.5	6.9 ± 0.8	24.7 ± 1.1	24 ± 0.8
Fe	80.1 ± 1.4	80.2 ± 1.5	63.5 ± 1.7	81.7 ± 1.9	66.4 ± 1.6	80.3 ± 1.4	53.0 ± 1.0	63.5 ± 1.7
Ni	1.9 ± 0.2	2.2 ± 0.4	1.2 ± 0.3	1.7 ± 0.2	1.3 ± 0.2	2.6 ± 0.6	2.5 ± 0.9	1.0 ± 0.2

The SAED analyses reveal that the K-S relationship ($(\bar{1}11)_\gamma \parallel (01\bar{1})_\alpha$, $[110]_\gamma \parallel [111]_\alpha$) and Nishiyama relationship ($(\bar{1}11)_\gamma \parallel (0\bar{1}\bar{1})_\alpha$, $[110]_\gamma \parallel [100]_\alpha$) coexisted between reverted austenite and martensite (Figure 6-7). Some researchers suggested that adjacent austenite grains had nearly the same orientation in low carbon steels and were twin-related [54][171][185]. Due to the limited statistics of the TEM observations, so far there was no evidence from the TEM investigation to prove this. An analysis technique which can provide better statistics, such as electron backscatter diffraction (EBSD), is required for the further study of the orientation relationships between austenite and martensite.

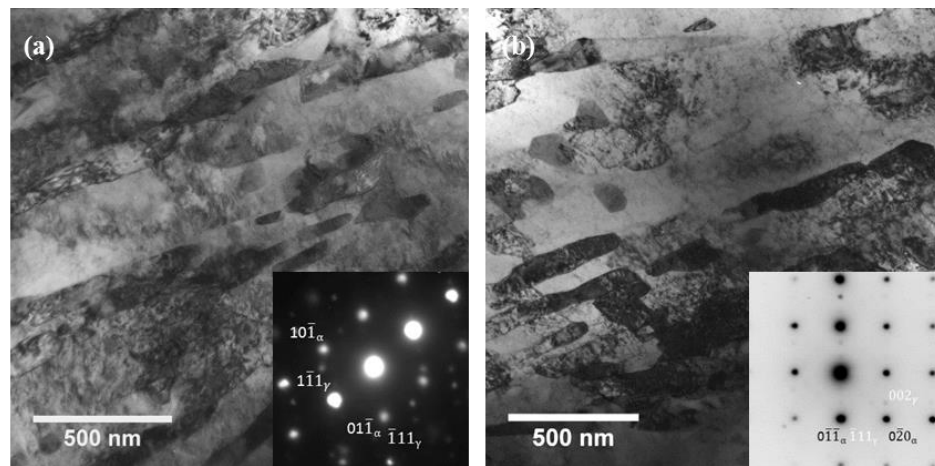


Figure 6-7 Bright-field TEM images of austenite in the martensite matrix and the corresponding selected area diffraction patterns presenting (a) K-S relationship and (b) Nishiyama relationship between austenite and martensite.

6.4 XRD quantitative analyses

As revealed by previous study, Mn-based maraging steels possessed a multi-phase structure comprised of α' -martensite matrix, Ni_2TiAl precipitates, reverted austenite and ϵ -martensite in some conditions. In this section, the volume fractions of reverted austenite formed in different aging conditions were measured by XRD and the results are presented in Table 6–3. In order to better understand the austenite reversion, the evolution of austenite phase fraction in the 10% and 12% Mn alloys aged at 500 °C is illustrated in Figure 6-8. As shown in Figure 6-8, aging at 500 °C

Chapter 6 The formation mechanism of reverted austenite and its mechanical stability

led to a nearly linear increase in the volume fraction of reverted austenite as a function of time up to the maximum was reached for both alloys. In the 10% Mn alloy, the austenite phase fraction reached a maximum of ~10 vol.% in the 500 °C / 5760 min state after which the content remained approximately constant; while in the 12% Mn alloy, the austenite fraction increased linearly up to ~25 vol.% after aging for 4320 min and then slightly decreased with longer aging time.

Table 6–3 The volume fractions (vol.%) of reverted austenite formed in different aging conditions.

Aging time (min)	10% Mn		12% Mn	
	500 °C	460 °C	500 °C	460 °C
1440	2.92 ± 0.67	-	8.48 ± 0.73	-
2880	6.03 ± 0.65	-	17.13 ± 1.76	-
4320	7.99 ± 0.49	-	24.78 ± 1.31	-
5760	10.35 ± 0.73	-	24.62 ± 1.49	5.58 ± 1.24
10080	10.69 ± 0.45	4.14 ± 1.03	23.06 ± 1.42	9.32 ± 2.48

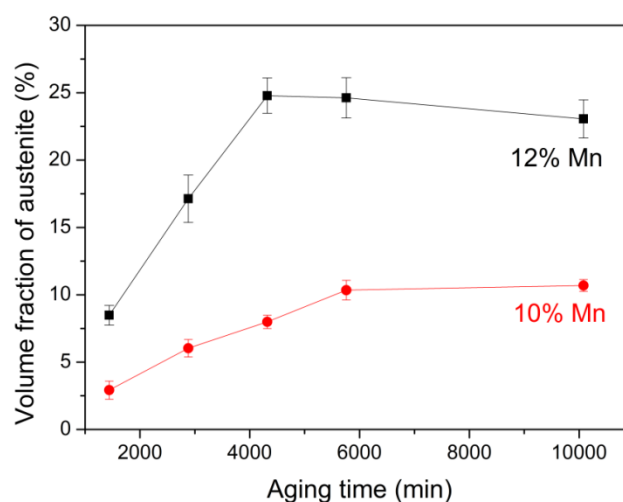


Figure 6-8 The evolution of volume fractions (vol.%) of reverted austenite formed as a function of aging time at the temperature of 500 °C.

6.5 Nanoindentation

As previously discussed, the key parameters of tensile deformation, i.e. yield strength (YS), ultimate tensile strength (UTS) and total elongation (TE) in multi-phase steels, are determined by the fractions of phases and their mechanical stability [140]. Therefore, the contribution of each phase to the strength of the Mn-based maraging steels is the main focus of this study.

In this study, the Mn-based maraging steels in aged conditions were mainly composed of tempered martensite decorated with uniformly dispersed nano-precipitates and various amount of elongated reverted austenite which depended on the aging conditions and Mn contents. In addition, a trace of ϵ -martensite or coarse carbide might be present in some cases. The following discussion only considers the martensite (with precipitates embedded within it) and reverted austenite, as previous studies have suggested that these two phases constituted the most relevant microstructure relating to the mechanical properties of materials.

As the mechanical characteristic of reverted austenite (with the size in the range 70-200 nm) in this study is hard to obtain by conventional testing methods, the nanoindentation combined with atomic-force microscopy (AFM) was utilized. A cube corner tip, which has a three-sided pyramidal with an apex angle of 90° and is much sharper than the conventional Berkovich tip, was selected to perform the indentation. In addition, a small load of 70 μN was applied. Nanoindentation tests were performed on a number of austenite grains and martensite matrix separately. The typical load-displacement ($P-h$) curves of the austenite and martensite in the 12% Mn alloy in the 500 $^\circ\text{C}$ / 10080 min state are given in Figure 6-9. Different phases were clearly characterized by different load-displacement relationships. Subject to the maximum load of 70 μN , the maximum penetration displacement was 10-15 nm for austenite phase and ~ 25 nm for martensite phase. This indicated that in this study the reverted austenite was unexpectedly harder than the martensite. It is generally accepted that the austenite phase, as a fcc crystal, has a low yield strength [245], especially compared to the martensite with highly dispersed nanoprecipitates in maraging steels [52][246][247]. Despite the low yield strength, the working hardening of austenite is remarkable and the higher load required for martensitic

transformation of austenite phase further increased the strength. In terms of martensite, its high strength is generally due to the high dislocation density and tetragonal lattice containing supersaturated carbon atoms (supersaturated Mn, Ni, Mo, Ti and Al atoms in Mn-based maraging steels). In this study, as these solid-solution strengthening elements in the martensite matrix were largely depleted by precipitation and austenite reversion and the dislocation density also reduced during the thermal aging process, the martensite could essentially be regarded as ferrite. In addition, a nanoindentation study on a similar medium-Mn TRIP steel revealed that retained austenite was significantly harder than ferrite (austenite: 7.7 GPa, ferrite: 3.4 GPa) [188]. Therefore, it is not surprising to see that the hardness of tempered martensite after a long-term aging was lower than that of austenite in this study.

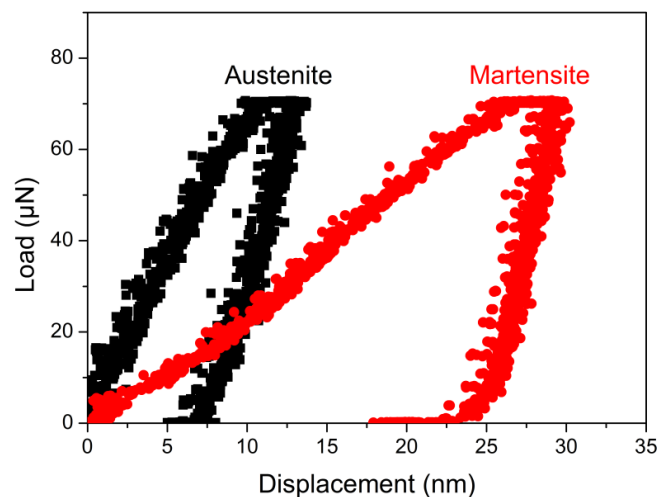


Figure 6-9 Load-displacement curves of martensite and austenite in the 12% Mn alloy in the 500 °C / 10080 min state.

The representative hardness values of the 10% Mn and 12% Mn alloys in the 500 °C / 10080 min state are given in Figure 6-10. In the 10% Mn alloy, the hardness of austenite and martensite are 8.5 ± 1.0 and 5.5 ± 0.3 GPa, respectively; in the 12% Mn alloy, the hardness of austenite and martensite are 9.0 ± 1.1 and 4.9 ± 0.5 GPa, respectively. It should be noted that the variation of austenite hardness in both alloys is larger than that of martensite.

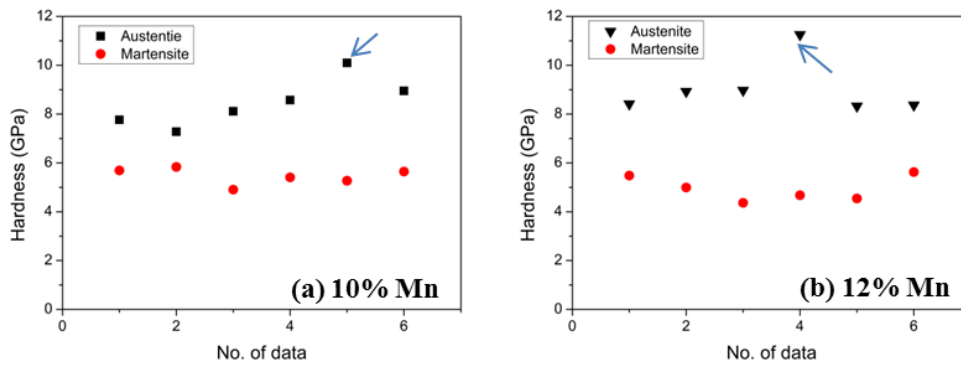


Figure 6-10 Hardness distribution of austenite and martensite phases in (a) 10% Mn alloy, in 500 °C / 10080 min state and (b) 12% Mn alloy, in 500 °C / 10080 min state.

The P - h curve of the indexed point in Figure 6-10(b) is representatively illustrated in Figure 6-11. A pop-in point near the top of the curve is visible. According to the study by He et al. [188], the pop-in point may correspond to a phase transformation. It is believed there is a critical load for the martensitic transformation (P_c), which is regarded as an indication of the mechanical stability of single austenite grain [188]. As the load applied in this study was small, most indentations on austenite did not lead to the martensitic transformation. Even in the indentation displayed in Figure 6-11, the martensitic transformation occurred when just approaching the maximum load, so the deformation behaviour of transformed martensite was not revealed. Otherwise a martensitic transformation strengthening is expected after the pop-in point. Furnemont et al. [245] reported that the slope of P - h curve after the pop-in point should be higher than that before the point. The martensitic transformation strengthening can be interpreted by dispersion hardening mechanism [248]. Accompanying with the phase transformation, a geometrically necessary dislocation (GND) prismatic loops [249] generate within the plastic zone close to the transformed martensite, leading to the increase of dislocation density and thereby strengthening the austenite phase [250]. During the loading, the untransformed austenite can be further strengthened when the GND prismatic loops bypass martensite and leave dislocation debris around the martensite. In terms of the martensite, the transformed martensite may have subjected severe deformation during the indentation which also contributes to the increase of hardness as higher

load is required to deform martensite. Another mechanism related to the pop-in point in $P-h$ curves was proposed by Wo et al. [251]. According to these researchers, the high-angle grain boundaries of austenite phase can prevent dislocations from passing through grain boundaries and thus leads to the grain boundary strengthening. Therefore, when the indentation position is just located at high-angle grain boundaries, a higher hardness than that on lower-angle grain boundaries or within plastic zone is expected. Both these two mechanisms may explain the pop-in point shown in Figure 6-11.

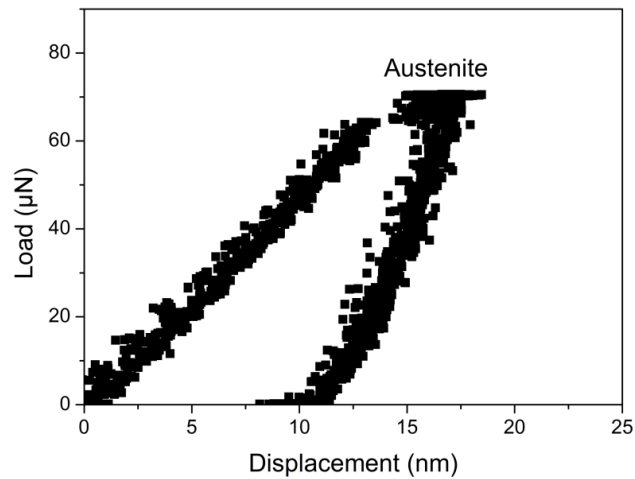


Figure 6-11 Load-displacement curve recording the martensitic transformation of an austenite grain.

6.6 Discussion

In the following sections the evolution of the grain size, chemical composition and volume fraction of reverted austenite will be discussed. Based on the discussion, the formation mechanism of reverted austenite is determined. Then the discussion will focus on the relationship between the mechanical stability of reverted austenite and its microstructure.

6.6.1 The size of reverted austenite grains

The average sizes of reverted austenite formed under different aging conditions were measured based on the SEM observation. Although the austenite reversion occurred in the very beginning of aging process, the size evolution of reverted austenite nanolayers in the early aging stage was difficult to capture due to the resolution limits of the microscope, and therefore, the discussion inevitably focuses on the size of lath-like reverted austenite in the over-aged condition. On the other hand, as lath-like austenite has a wide range of length and the length of lath-like reverted austenite may vary with different orientations, it is difficult to measure the average length accurately. Therefore, only the width of reverted austenite is analysed here. In Figure 6-12 and Figure 6-13, the width of reverted austenite was averaged from at least 80 measurements.

As shown in Figure 6-12, at 500 °C there was a slow increase in the average width of austenite grains with aging time for both the 10% Mn and 12% Mn alloys from 2880 min to 10080 min (Figure 6-12). This limited increase in the width is attributed to two reasons: (i) the decelerating kinetics of austenite growth for the over-aged stage, as a result of the slow diffusion of Mn atoms (EDS analyses revealed that the austenite formed at this stage had a high Mn concentration (~24 at.%) [27]; (ii) thermodynamic resistance to coalescence with adjacent reverted austenite grains as discussed in Section 2.4.2. In addition, the influence of the Mn content of alloy on the austenite width was not evident, and the widths of reverted austenite seemed to be irrelevant to the Mn content and are almost the same between the 10% Mn and 12% Mn alloys (Figure 6-12).

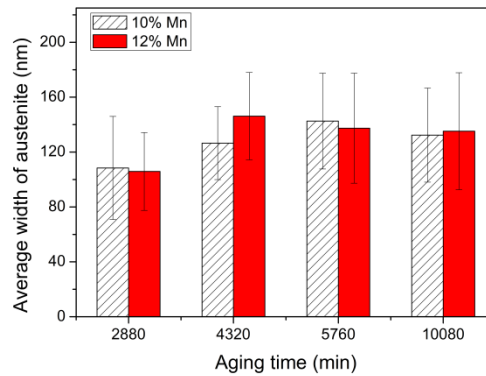


Figure 6-12 Average width of lath-like reverted austenite after aging at 500 °C for different times in the 10% Mn and 12% Mn alloys.

In contrast to the aging duration and alloying composition, the aging temperature had a more evident influence on the width of reverted austenite as presented in Figure 6-13, which showed an approximately linear increase with the aging temperature. It is not difficult to understand as the higher driving force for Mn diffusion at elevated temperature promoted the growth of reverted austenite.

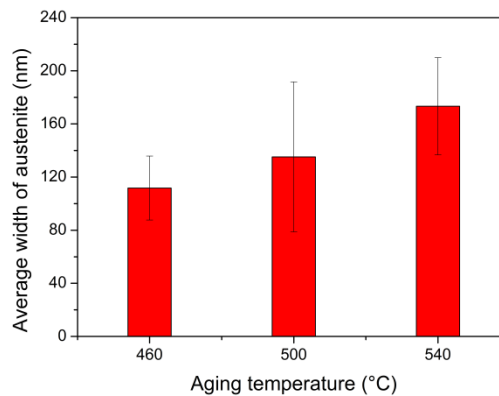


Figure 6-13 Average width of reverted austenite aged at different temperatures for 10080 min in the 12% Mn alloy.

6.6.2 Chemical composition of reverted austenite

In this study, Mo- and Ti-rich austenite was observed in some samples (see Table 6–1). This phenomenon is contradictory to the common knowledge that Ti is regarded

as ferrite stabilizing elements. A similar finding on the M-A-M (M: martensite, A: austenite) region using APT was reported in a 9 wt.% Mn maraging steel by Raabe et al. [50]. They summarized the experimental grain boundary segregation data of various elements [50] and reported that the grain boundary enrichment factor of Mn is 2.3, Ni is 1.7, Mo is 2.3 and Ti is 5.2. Therefore, in the current study, it is assumed that the Ti and Mo-rich austenite nanolayers in the 7% Mn and 10% Mn alloys was due to the fact that most of the austenite phase was formed along the prior austenite grain boundaries and martensite packet/lath boundaries. These interfaces were also the preferential segregation sites for Mo and Ti. As Ti has a higher grain boundary enrichment factor and a faster diffusivity, the notably high Ti concentrations in the austenite cannot be avoided. Subsequently, continuous diffusion of Mn led to the newly-formed Mn-rich austenite on top of the preceding Ti, Mo-rich grain boundaries. On the other hand, in this type of austenite, there was no segregation of Ti and Mo, so these austenite grains were observed with higher Mn concentration. Another reason relating to the Ti and Mo enrichment in austenite was proposed by Schnitzer et al. who suggested that the high solubility of C in austenite drove the formation of Ti- and Mo-rich carbides within the austenite phase [147]. However in the present Mn-based maraging steels, as the nominal carbon content of the alloys was very low (0.02-0.03 wt.%) and no carbide was observed, it is not likely that the limited carbon atoms within austenite could lead to such high concentrations of Ti and Mo in austenite.

The equilibrium binary Fe-Mn phase diagram is presented in Figure 6-14 to study the effects of temperature and nominal composition on the Mn concentration of austenite. According to the Fe-Mn phase diagram, the equilibrium compositions of Fe-10Mn alloy at 500 °C are ferrite with 3.7 at.% Mn and austenite with 21.3 at.% Mn. Increasing the Mn content of the alloy does not lead to the composition change in the ferrite or austenite, but different aging temperatures result in the variation of austenite composition. For example at 460 °C, ferrite with 3.9 at.% Mn and austenite with 25.0 at.% Mn can be formed regardless of the nominal Mn content.

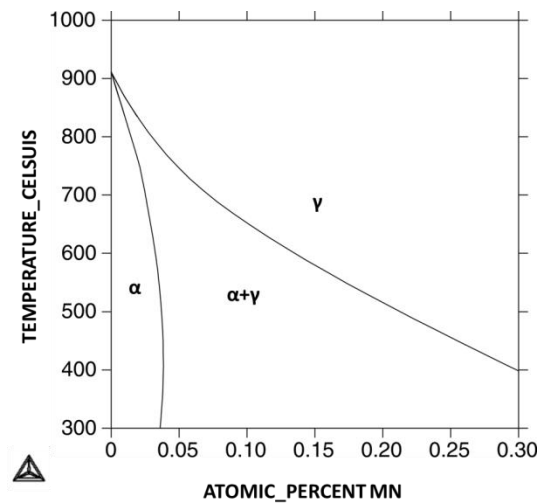


Figure 6-14 Equilibrium phase diagram of the Fe-Mn system.

The chemical composition profiles obtained by TEM-EDS are partially consistent with Fe-Mn phase diagram. The segregation of Ti and Mo on grain boundaries resulted in the Mn concentration of austenite nanolayers being far from that indicated by the equilibrium phase diagram. Although the phase diagram suggests that the Mn concentration of austenite is independent on the nominal Mn content of the alloy, experimental results reveal that higher Mn content contributed to a fast kinetics for the formation of reverted austenite and thus higher Mn concentration of reverted austenite for the same aging conditions. Otherwise, the chemical composition of ferrite and lath-like austenite exhibited good agreement with the phase diagram.

It is worth discussing the thermodynamic possibility of the austenite formation with relatively low Mn concentration along the grain boundaries in the initial stage of aging. Wilson and his colleagues [121][122] worked on the grain boundary segregation of Mn in a Fe-8Mn alloys at 450 °C and revealed by Auger spectroscopy that about 18 at.% Mn enrichment at the grain boundaries upon aging at 450 °C for 10-12 min. They suggested the Mn segregation to prior austenite grain boundaries supported the initial formation of reverted austenite at such sites. In our study, the Mn concentration of austenite nanolayers formed in the very beginning of aging was even lower owing to the Ti and Mo segregation at the grain boundaries. Raabe et al. [50] calculated the chemical driving force for the local austenite formation at 450 °C in different conditions. In the binary Fe-Mn system, a minimum 13.3 at.% Mn is required to approach the critical chemical driving force for austenite reversion. If

other alloying elements (Mo, Ti and Si) are included, the Mn concentration above 12.4 at.% Mn has the potential to form austenite. In the case with the local segregation of ferrite stabilizing elements, higher Mn concentration (above 15.3 at.%) is needed for the phase transformation to austenite. However, structural defects such as interface disorder, which is a significant factor, are not taken into consideration in the above calculations. Therefore, Raabe et al. [50] used a phase field model to model both the segregation and phase transformation, which revealed a high driving force for the formation of austenite at grain boundaries. The low nucleation energy at interface (0.5-1 eV based on 24 at.% Mn concentration at 450 °C) is attributed to not only the enrichment of Mn at grain boundaries, but also the low energy of K-S austenite/martensite interface and specifically, the high elastic relaxation energy of martensite induced by phase transformation.

In the present study, as the austenite reversion at the interface would be suppressed by the segregation of ferrite stabilizing elements (Ti and Mo), the critical Mn concentration for austenite reversion at the interface should be higher than that calculated on the basis of the nominal chemical composition. However, in view of the low nucleation energy at the interface due to structural defects, austenite reversion can still be realized with relatively low Mn concentrations at the grain boundaries. A detailed discussion on the formation of reverted austenite will be given in Section 6.6.4.

In addition, Raabe et al. performed an APT analysis on the M-A-M interface where retained austenite served as a template for further austenite reversion to study the difference between retained austenite and reverted austenite in maraging TRIP steels [50]. They reported that this special M-A-M interface presented a different compositional profile from the self-nucleated reverted austenite. Retained austenite in the centre region of Mn profile revealed a Mn concentration of 12 at.%, while the reverted austenite formed on top of it had a Mn concentration of ~25 at.%. This indicates that the Mn concentration of reverted austenite was much higher than that of retained austenite.

6.6.3 The volume fraction of reverted austenite

According to the Fe-Mn phase diagram, a sufficient long-time aging at 500 °C allows the formation of up to 36 vol.% austenite for a 10% Mn alloy. Increasing the Mn content of the alloy leads to an increase of the austenite fraction, so that at equilibrium, the volume fraction of austenite is 47.5 vol.% for the 12% Mn alloy. Different aging temperatures also result in the variation in composition and volume fraction of austenite. A summary of the equilibrium composition and volume fractions of phase as a function of aging temperature is presented in Table 6–4.

Table 6–4 A summary of the equilibrium Mn concentration (at.%) and volume fraction (vol.%) of austenite and ferrite phases at different aging temperatures based on the Fe-Mn phase diagram in Figure 6-14.

		7% Mn		10% Mn		12% Mn	
		at.%	vol.%	at.%	vol.%	at.%	vol.%
420 °C	Austenite	28.4	13.1	28.4	25.0	28.4	33.3
	Ferrite	4.0	86.9	4.0	75.0	4.0	66.7
460 °C	Austenite	25.0	15.4	25.0	29.3	25.0	39.0
	Ferrite	3.9	84.6	3.9	70.7	3.9	61.0
500 °C	Austenite	21.3	18.7	21.3	36.0	21.3	47.5
	Ferrite	3.7	81.3	3.7	64.0	3.7	52.5

The experimental results of the volume fraction of reverted austenite (Table 6–3) are compared to the data from the equilibrium Fe-Mn phase diagram (Table 6–4). It is obvious that the maximum austenite phase fractions (up to ~10 vol.% for 10% Mn alloy aged at 500 °C; up to ~24 vol.% for 12% Mn alloy aged at 500 °C) are significantly lower than the values predicted by the Fe-Mn phase diagram (~36.0 vol.% for 10% Mn alloy at 500 °C; ~47.5 vol.% for 12% Mn alloy at 500 °C). This may be attributed to the fact that a small amount of reverted austenite transformed to ϵ -martensite during cooling. In addition, the addition of Ti and Al could raise the A_e^3

and reduced the maximum volume fraction of austenite. The segregation of Ti and Mo at grain boundaries is considered to suppress the formation of reverted austenite as well.

6.6.4 The formation mechanism of reverted austenite

As revealed in Section 6.2, in the initial aging stage, austenite nanolayers were preferentially formed along prior austenite grain boundaries and martensite packet boundaries due to low nucleation energy at interface. Further aging led to those austenite nanolayers gradually growing to film-like and then lath-like austenite. In some cases (e.g. 12% Mn alloy after prolonged/high-temperature aging), lath-like reverted austenite was also found within martensite laths. In addition, as both the prior austenite grains and martensite packets were largely refined due to higher Mn content (see Figure 4-2), the 12% Mn alloy provided more nucleation sites for austenite formation and this partially explains why the austenite reversion of 12% Mn alloy kinetically exceed that of the other two alloys.

As discussed in Section 2.4.2, the formation of reverted austenite is generally considered to be dominated by a diffusion process [27][193][194]. but some researchers proposed that austenite reversion is shear-dominated and assisted by a prior or simultaneous diffusion mechanism [52][146]. In order to study the formation mechanism of reverted austenite in Mn-based maraging steels, the results of reverted austenite fraction were analysed. As the experimental study has confirmed that there was no retained austenite formed by quenching from solution heat treatment, the entire austenite detected in the aged samples is regarded as reverted austenite.

It is worth noting that the complexity of austenite reversion process in maraging steels, such as the competition with precipitation and the presence of coherency strains, may have led to the experimental results that are contradictory to the common knowledge [54]. On the other hand, previous microstructural observation has demonstrated that the formation of precipitates and reverted austenite started from the very beginning of aging simultaneously, and the computer simulation also indicates that the dissolution of precipitates is not necessary for the initial driving force for austenite reversion in maraging steels [147]. Therefore, it is assumed that

the formation of precipitates and reverted austenite are independent processes in this study. It should be highlighted that this analysis of the kinetics is only regarded as a semi-quantitative description of austenite reversion.

When the austenite reversion process is diffusion-controlled, its activation energy Q , can be calculated by the following equation [147]:

$$\ln(t) = \frac{Q}{RT} + c \quad (6.1)$$

where t is the time to form certain volume fraction of reverted austenite, T is the specific temperature at which austenite reversion occurs, and c is the constant. In the current study, the analyses of austenite formation were performed on the 10% and 12% Mn alloys by measuring the time required to form the certain amount of reverted austenite at 460 °C, 500 °C and 540 °C, respectively. The volume fraction for Equation (6.1) was set as 4 vol.% for the 10% Mn alloy and 9 vol.% for the 12% Mn alloy. These figures were chosen as the point before which ϵ -martensite was formed. Thus, the time to attain the certain amounts of reverted austenite as a function of aging temperature could be determined for both alloys. The results are presented in Figure 6-15 and a linear correlation is found between $1/T \cdot 1000$ and $\ln(t)$. Based on the slope of fitted line, the activation energy for austenite reversion was estimated as 63.5 kJ/mol for the 10% Mn alloy and 85.7 kJ/mol for the 12% Mn alloy. These values are significantly lower than those reported in conventional maraging steels and the activation energy for Mn diffusion in pure iron as well. The activation energy for Mn diffusion in Fe is reported to be 219.8-261.7 kJ/mol [252]. Nakagawa et al. [20] reported the activation energy for austenite reversion was about 240 kJ/mol in a 1.8Cu-7.3Ni-15.9Cr-1.2Mo steel. Schntizer et al. [147] reported the activation energy was 234 ± 20 kJ/mol in PH 13-8 Mo maraging steels. However in this study, the volume fraction of austenite chosen for the calculation is very low, which means that the calculation is mainly based on the early stage of austenite reversion. Therefore, it is considered that the austenite reversion in the early aging stage was not controlled by Mn diffusion. On the other hand, as the austenite reversion occurred at the onset of aging and the compositional change was small, the formation of reverted austenite is proposed to be a shear mechanism accompanied by a small amount of Mn diffusion.

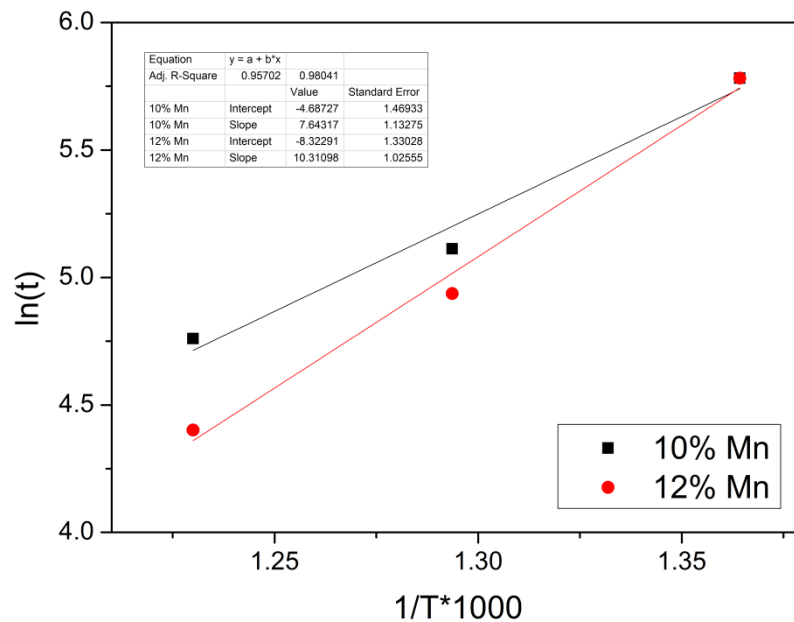


Figure 6-15 Arrhenius plot for the determination of the activation energy of austenite formation in the 10% Mn and 12% Mn alloy.

On the other hand, our TEM-EDS investigation on austenite reversion reveals that the Mn concentration of lath-like reverted austenite in the later aging stage (~24 at.%) was much higher than that of austenite nanolayers formed in the early aging stage (~12 at.%). The high concentration of Mn indicates that Mn was indeed involved in the formation of reverted austenite. Therefore, the variation of Mn concentration is considered as the result of the transition of austenite formation mechanism from diffusionless-dominant mechanism to diffusion-dominant mechanism.

Based on the experimental results and discussion presented above, the sequence for reverted austenite formation in these Mn-based maraging steels is proposed as following:

- 1) The nucleation of reverted austenite at prior austenite grain boundaries and martensite packet boundaries occurred at the onset of aging followed by the nucleation of austenite within martensite laths. The nucleation process was governed by a shear mechanism assisted by a prior or simultaneous diffusion of a small amount of Mn. Due to the structural disorder at interface, there is a higher

driving force for the segregation of Mn and phase transformation, which made the rapid nucleation of reverted austenite at grain boundaries easier. While the nucleation of reverted austenite within martensite laths needed higher Mn segregation and hence was kinetically slower.

- 2) During the further aging process, the accumulated Mn segregation to grain boundaries led to the austenite nanolayers growing to lath-like reverted austenite, which means the lateral growth of austenite was mainly supported by the diffusion of Mn. As the diffusion rate of Mn in the martensite matrix was relatively low, the diffusion-controlled austenite growth was fairly slow. In addition, the thermodynamic resistance to coalescence between adjacent reverted austenite is another reason why the reverted austenite could maintain nano-scale dimensions for a long time.

6.6.5 The stability of reverted austenite

As discussed in Section 2.4.1, studies on reverted austenite suggest that the size effect and enriched Mn concentration of austenite grains are the two main intrinsic factors that affect the stability of reverted austenite.

- **Chemical composition**

Yen et al. [26] stated that the essential concept of austenite engineering in Mn-based TRIP steels is to tailor the Mn concentration in austenite in order to attain metastable austenite after heat treatment. This metastable austenite can therefore lead to the TRIP effect which enables strain hardening.

The martensite transformation start temperature (M_s) is regarded as a parameter that directly controls the stability of the austenite. The M_s temperature based purely on the chemical compositions is designated M_s^0 . Therefore, the M_s^0 of the α' -martensite can be calculated by the following equation [253]:

$$M_s^0 (\text{°C}) = 545 - 330C + 2Al - 23Mn - 5Mo - 13Ni + 3Ti \quad (6.2)$$

where the elements stand for their concentrations in wt.%. The equation is simplified to only present the primary elements involved in this study.

According to Equation (6.2), the relationship between the austenite stability and chemical composition is quite straightforward. C and Mn significantly contribute to the stability of austenite while the Al and Ti additions lower the austenite stability. The influence of Ti and Mo enrichment on the initial formation of reverted austenite along the grain boundaries was discussed in Section 6.6.2. Here we mainly focus on the effects of Mn concentration on the austenite stability.

Figure 6-16 presents the average hardness values of austenite and martensite in various aged samples. As displayed in Figure 6-16(a), the austenite hardness of the 12% Mn alloy aged at 500 °C for 10080 min was higher than that of the 10% Mn alloy for the same aging condition, which is believed to be mainly attributed to the higher Mn concentration of austenite in the 12% Mn alloy (revealed by previous TEM-EDS analyses). On the other hand, the martensite hardness of the 12% Mn alloy was slightly lower than that of the 10% Mn alloy. This might be a result of the faster kinetics of the coarsening of precipitates and softening of martensite matrix in the 12% Mn alloy. In terms of the effect of aging temperature, it is clearly shown in Figure 6-16(b) that the hardness of both the austenite and martensite decreased as the aging temperature increased. The decrease of martensite hardness mainly resulted from the coarsening of precipitates and softening of martensite matrix at higher temperature. While the reverse relationship between the austenite hardness and aging temperature is considered to be related to the decreased Mn concentration of reverted austenite with the increase of aging temperature.

It should be noted that the above discussion is based on the average statistics. Due to the relatively low diffusion rate of Mn, the Mn concentration of each single austenite grain may vary from grain to grain, leading to the variation of austenite hardness which manifests the large scatter in Figure 6-10. Therefore, a detailed analysis on the hardness and Mn concentration of each single austenite grain may be a more direct method to explore the relationship between Mn concentration and the mechanical stability of austenite phase.

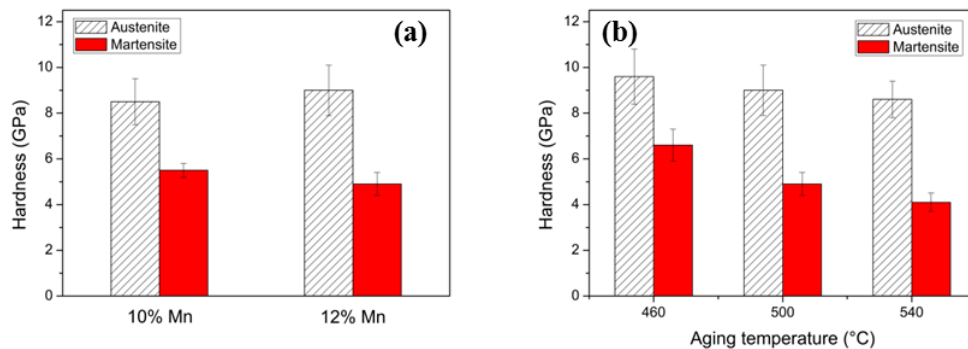


Figure 6-16 (a) The average hardness of austenite and martensite in the 10% Mn and 12% Mn alloys aged at 500 °C for 10080 min; (b) the hardness of austenite and martensite in the 12% Mn alloy as a function of aging temperature.

- **Austenite grain size**

It is generally accepted that the austenite with a small grain size has a high stability [154][34][158][159][162][163]. Although the interface is always a good site for heterogeneous nucleation, phase transformation is suppressed in materials with small grain sized even when there is a strong thermodynamic driving force. This has been shown to be true for both metals and ceramics.

In contrast, Wang et al. [171] reported a ‘smaller is less stable’ effect of austenite in a 9Mn maraging steel. They stated that the mechanical twinning was activated in larger austenite grains within which the deformation substructures stabilized grains. While for smaller austenite grains, mechanical twinning was less likely to occur. Another study by Wang et al. [166] proposed it is easier for the outer layer of reverted austenite to transform into martensite during deformation owing to the higher stress and lower concentration of austenite stabilizing elements. As the fraction of outer layer region is smaller the austenite grain with a larger dimension, the larger reverted austenite grains are more stable than the smaller ones. However, our study on Mn-based maraging steels did not find any evidence of mechanical twinning in the reverted austenite. Besides, the nanoindentation analysis confirmed that in the over-aged state when reverted austenite could be detected by AFM, reverted austenite was harder than the adjacent martensite matrix. On the other hand, the concentration variation between the outer layer and centre can be negligible

when the grain size of reverted austenite was so fine (e.g. < 200 nm in this study). Therefore, the above two ‘smaller is less stable’ effects apparently cannot be applied in the present work.

In this study, since the reverted austenite exhibited an elongated shape with a wide range of lengths, it was not possible to obtain an accurate equivalent size of reverted austenite grains. On the other hand, lath-like reverted austenite exhibited a strong resistance to coarsening in the lateral direction, maintaining a size in the range 70-200 nm under various aging conditions. Due to the resolution limit, nanoindentation study did not reveal a direct relationship between the stability and austenite size in this study. Although higher austenite hardness was found at lower aging temperature (Figure 6-12 (b)) where the average austenite size was smaller (Figure 6-13), it cannot be concluded that the smaller size of reverted austenite was the reason for the higher mechanical stability. Other factors, such as the higher Mn concentration at lower aging temperature (Table 6-4), have been demonstrated to have a more evident effect on the mechanical stability. Therefore, detailed investigation by performing nanoindentation on individual single austenite grain with measurable sizes and known Mn concentration is needed to understand the relationship between the size and the stability of austenite.

6.7 Summary

1. Owing to the high grain boundary enrichment factor of Ti and Mo, Ti and Mo-rich austenite along the grain boundaries was observed in the initial aging stage. The high concentrations of Ti and Mo gradually vanished with the enrichment of Mn during the succeeding aging process.
2. The experimental chemical composition profile of reverted austenite was partially consistent with that given by the Fe-Mn phase diagram. The segregation of Ti and Mo on grain boundaries resulted in the Mn concentration of austenite nanolayers in the initial aging stage being far from the value indicated by the equilibrium phase diagram. Otherwise, the chemical composition of ferrite and lath-like austenite exhibited good agreement with the phase diagram. The TEM-EDS analyses revealed the Mn concentration of

lath-like austenite was at the level of ~24 at.% which is much higher than that of retained austenite (8-12 at.%) reported in conventional Mn-based TRIP or Q&P steels [27][154][34][50]. The volume fraction of reverted austenite increased almost linearly with the logarithm of aging time until it was saturated. The experimental results of the equilibrium austenite fractions (e.g. ~10 vol.% for 10% Mn alloy aged at 500 °C and ~24 vol.% for 12% Mn alloy aged at 500 °C) were significantly lower than the values predicted by the Fe-Mn phase diagram (36.0 vol.% for Fe-10Mn at 500 °C and ~47.5 vol.% for Fe-12Mn at 500 °C). This is mainly attributed to the fact that an amount of reverted austenite transformed to ϵ -martensite during cooling. The addition of Ti and Al may be another reason for the discrepancy.

3. The formation of reverted austenite nanolayers initiated at the onset of aging by a diffusionless shear mechanism accompanied by a small amount of Mn diffusion like bainite. The nucleation of reverted austenite within martensite laths was kinetically slower due to a lower driving force for phase transformation. In the following aging process, the accumulated Mn segregation to the newly-formed austenite/martensite grain boundaries led to the austenite nanolayers growing to lath-like reverted austenite, which means the lateral growth of austenite in the later aging stage was supported by the diffusion of Mn.
4. As the diffusion rate of Mn in the martensite matrix was relatively low, the diffusion-controlled austenite growth was fairly slow. In addition, the thermodynamic resistance to coalescence between adjacent reverted austenite grains is another reason why the width of reverted austenite could maintain in the range 70-200 nm for a long time. The width of reverted austenite was not closely associated with the nominal Mn content of the alloy, but it is found that the width increased with the increase of aging temperature owing to the higher driving force for Mn diffusion at higher temperature.
5. Most of the reverted austenite in Mn-based maraging steels exhibited a K-S or N orientation relationship with the residual martensite. It is believed that both the K-S and N orientation relationships contributed to the mechanical stability of reverted austenite.

6. Nanoindentation testing revealed the high stability of reverted austenite in Mn-based maraging steels was mainly attributed to the high Mn concentration of austenite. The nano-size of reverted austenite was also considered to be responsible for the high stability, but more evidence is needed to support this viewpoint.

Chapter 7 Strengthening mechanisms of Mn-based maraging steels

Table 7–1 summarizes the tensile properties of Mn-based maraging steels in this study together with other research results on medium Mn steels (mainly with 5-7 wt.% Mn). As shown in Table 7–1, impressive tensile properties have been reported in other Mn-based steels subjected to various processing paths. Nevertheless, in view of the low carbon content (<0.03 wt.%) of the steels in this work, the tensile strength of 9-12% Mn steels are still remarkable compared to steels with the same level of carbon content in Table 7–1. It is proposed that the high UTS is attributed to the joint effect of the precipitation strengthening of Ni₂TiAl intermetallic phase and the work hardening of reverted austenite. On the other hand, the ductility of the 10% and 12% Mn alloys in this study is relatively mediocre. One possible reason is the relatively lower austenite fraction than other alloys. Another reason we speculated is associated with the high mechanical stability of reverted austenite. In this chapter, the strengthening mechanisms of Mn-based maraging steels will be investigated and based on the discussion, the optimal microstructure and relevant processing paths to obtain the microstructure will be determined with the aim to achieve better mechanical properties.

The strengthening mechanism for steels is complex and generally it can be expressed as:

$$\sigma_y = \sigma_B + \sigma_{SS} + \sigma_{GR} + \sigma_{PH} + \sigma_{dislocation} \quad (7.1)$$

where σ_y is the total yield strength, σ_B is the yield strength of base steel, σ_{SS} is the solid-solution strengthening, σ_{GR} is the grain refinement strengthening, σ_{PH} is the precipitation strengthening and $\sigma_{dislocation}$ is the dislocation strengthening. In the following sections, the dominant strengthening mechanism in different heat treatment conditions will be discussed.

Table 7–1 Summary of the tensile properties of Mn-based steels.

Materials (wt.%)	Heat treatment	V_γ (vol.%)	YS (MPa)	UTS (MPa)	TE (%)	Ref.
Fe-0.015C-10Mn-2Ni-1.2Mo-1Al-0.8Ti	500 °C / 5760 min, WQ	10.4	860	1062	17	*
Fe-0.022C-11.8Mn-2Ni-1.2Mo-1Al-0.8Ti	500 °C / 5760 min, WQ	24.6	870	1120	18.4	*
Fe-0.007C-8.86Mn-2.0Ni-1.07Mo-1.04Ti	450 °C / 48 h	-	984	~1000	~15	[18][26]
Fe-0.007C-8.86Mn-2.0Ni-1.07Mo-1.04Ti	450 °C / 48 h ^[a]	-	978	1011	12.7	[18][26]
Fe-0.01C-11.9Mn-2.06Ni-1.12Mo-1.09Ti	450 °C / 48 h	-	1142	~1300	21	[18][26]
Fe-0.01C-11.9Mn-2.06Ni-1.12Mo-1.09Ti	450 °C / 48 h ^[a]	-	1394	~1500	~10	[18][26]
Fe-0.01C-11.9Mn-2.06Ni-1.12Mo-1.09Ti	650 °C / 144 h, AC	32.7	~500	~980	~45	[27]
Fe-0.11C-5.7Mn	560 °C / 1 h, AC	11	955	981	12	[24]
Fe-0.11C-5.7Mn	520 °C / 4 h, AC	10	934	956	19.5	[24]
Fe-0.11C-5.7Mn	600 °C / 1 h, AC	23	874	914	18.5	[24]
Fe-0.11C-5.7Mn	640 °C / 1 h, AC	30	798	1145	30.5	[24]
Fe-0.11C-5.7Mn	600 °C / 16 h, AC	29	727	879	34	[24]
Fe-0.11C-5.7Mn	640 °C / 16 h, AC	30	87	174	18.5	[24]

Chapter 7 Strengthening mechanisms of Mn-based maraging steels

Fe-0.04C-5Mn	590 °C / 16 h ^[b]	75.5	952	1049	39.5	[13]
Fe-0.045C-5Mn-3Ni	590 °C / 4 h ^[b]	76.4	1104	1249	39.9	[13]
Fe-0.2C-4.72Mn	650 °C / 1 min, AC	4.54	~830	~970	~20	[27]
Fe-0.01C-7.09Mn	575°C / 1 week, WQ	26	766	800	33	[23]
Fe-0.01C-7.09Mn	625°C / 1 week, WQ	40	954	503	22	[23]
Fe-0.01C-7.09Mn	675°C / 1week, WQ	1.4	775	1368	7	[23]
Fe-0.08C-10.6Mn-0.36Si	550 °C / 2 h, WQ	47	1240	1360	8.5	[26]
Fe-0.08C-10.6Mn-0.36Si	610 °C / 8 min, WQ	54	1080	1390	26.7	[26]
Fe-0.12C-4.6Mn-1.1Al-0.55Si	720 °C / 2 min, 10°C/s ^[c]	28	766	1204	12.9	[16]
Fe-0.12C-4.6Mn-1.1Al-0.55Si	780 °C / 2 min, 10°C/s ^[c]	6	940	1461	6.2	[16]
Fe-0.12C-5.8Mn -3.1Al-0.47Si	720 °C / 2 min ^[c]	26	814	854	14.7	[16]
Fe-0.12C-5.8Mn -3.1Al-0.47Si	780 °C / 2 mi ^[c]	31	714	994	23.8	[16]
Fe-0.12C-5.8Mn -3.1Al-0.47Si	840 °C / 2 min ^[c]	18	444	1161	11.2	[16]
Fe-0.05C-9Mn	620 °C / 600 s, FC	30	830	1034	27	[254]
Fe-0.05C-9Mn	620 °C / 600 s, FC ^[d]	37	1110	1193	25	[254]

Chapter 7 Strengthening mechanisms of Mn-based maraging steels

Fe-0.1C-5.22Mn	650 °C / 1 h, WQ	-	-	794	29	[14]
Fe-0.1C-5.25Mn-2.09Si	675 °C / 1 h, FC	-	-	1029	27	[14]
Fe-0.01C-5Mn	625 °C / 3 h, WQ	~4	~500	~800	~10	[255]
Fe-0.1C-5Mn	650 °C / 3 h, WQ	~30	~450	~1050	~24	[255]
Fe-0.4C-5Mn	675 °C / 3 h, WQ	~56	~550	~1700	~20	[255]
Fe-0.4C-5Mn	675 °C / 3 h, FC	~15	~350	~1550	~10	[255]

AC: air cooling; WQ: water quenching; FC: furnace cooling.

* Tensile results of this work;

[a] Cold rolled before annealing

[b] four-step thermal cycling 2BT treatment, detail see [13]

[c] single-step heat treatment of intercritical annealing

[d] Cold rolled after hot rolling

7.1 The solid-solution and grain refinement strengthening

As a large amount of solute atoms (e.g. Mn, Ni, Ti, Al and Mo) were added, the strength of alloys in the SHT state was increased when compared to that of the base steel. The strengthening achieved by substitutional solute atoms is, in general, greater the larger the difference in atomic size of the solute from that of iron. On the other hand, the differences in the elastic behaviour of solute and solvent atoms are also important in determining the overall solid solution strengthening. Mn is an effective strengthener, but other elements, such as Mo and Al, have more significant effect [197]. Therefore, increasing Mn content did not result in a significant increase in the lattice distortions (Table 7–2). Hence, there is no evident difference of the solid-solution strengthening among the three alloys. While after aging for a long time, owing to the precipitation and the formation of reverted austenite which consumed a large number of solute atoms, the supersaturated α' -martensite matrix gradually restored (Table 7–2). This indicates that the solid-solution strengthening after long-term aging was less important than that in the SHT and earlier aging state.

Table 7–2 Lattice parameter (Å) of α' -martensite in the three alloy in different heat treatment conditions.

	SHT	500 °C / 10080 min
7% Mn	2.8820	2.8753
10% Mn	2.8863	2.8776
12% Mn	2.8878	2.8789

EBSM maps of the 7%, 10% and 12% Mn alloys in the SHT state (Figure 4-2) have demonstrated that increasing the Mn content of alloy significantly refined both the prior austenite grain size and packet size of lath martensite. Therefore, finer prior austenite grains and martensite packets were observed in the 12% Mn alloy in the SHT state compared to other alloys. Despite this, the tensile curves in Figure 4-9 reveal that the differences of YS, UTS and TE among the three alloys are small. It is

proposed that this is because the solid-solution strengthening prevailed in the SHT state. Another reason is the grain boundaries of martensite packets are too weak to resist dislocation. As experimental evidence reveals that the effective grain sizes had a good resistance against coarsening during aging owing to the segregation of Mn and the formation of reverted austenite (Figure 7-1), the grain refinement strengthening in the aged conditions was considered to be the same as in the SHT state.

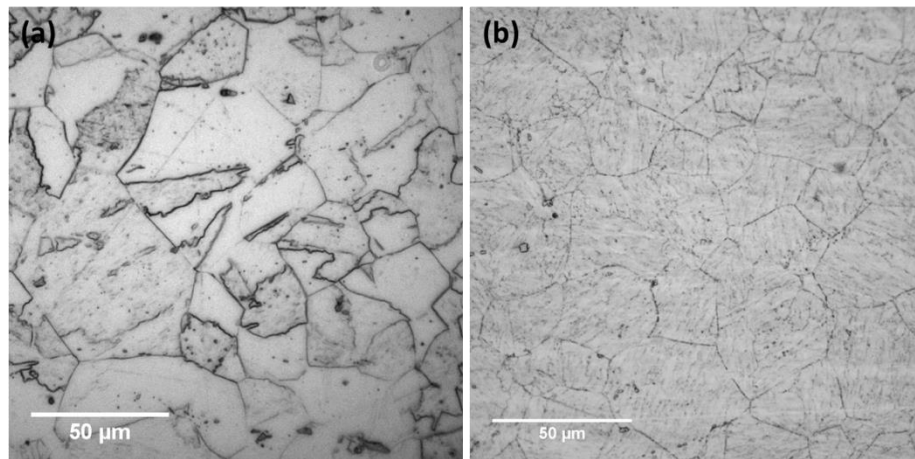


Figure 7-1 The optical micrographs of 7% Mn alloy (a) at SHT state and (b) 500 °C / 2880 min state.

7.2 Precipitation strengthening mechanism

For precipitation-strengthened alloys, if the sum of $\sigma_B + \sigma_{SS} + \sigma_{GR} + \sigma_{TR}$ is defined as σ_0 , the strengthening can be accounted for an Orowan mechanism [48]:

$$\sigma_y = \sigma_0 + \frac{T}{b\Lambda} \quad (7.2)$$

where T is the line tension, b is the Burgers vector and Λ is the interparticle spacing. After examining Orowan theory in detail, Ansell and his colleagues [256][257] proposed a modified form of the Orowan equation in which σ_y is expressed as:

$$\sigma_y = \sigma_0 + \frac{2Gb\phi \ln(\Lambda - d/2b)}{4\pi(\Lambda - d)} \quad (7.3)$$

where G is the shear modulus of matrix, ν is related to the Poisson's ratio of matrix by $\nu = \left[1 + \frac{1}{1-\nu}\right] / 2$ and d is the mean size of precipitates. In the present study, the peak hardness condition is considered to be strengthened mainly by the precipitation effects. However, in order to avoid the intergranular brittleness, a slightly overaged sample (12% Mn alloy, 500 °C / 240 min state) was studied to estimate the precipitation strengthening mechanism (see Figure 7-2(a)). Since this sample had a small amount of reverted austenite (below 3 vol.%), the effect of reverted austenite on strengthening would have been small. The value of σ_0 in peak hardness condition is assumed to be equal to that of σ_y in the SHT state. The average precipitate size of this sample is 7.4 nm (Table 5-1) and the interparticle spacing was ~40 nm. Taking $G = 71$ GPa [33], $|b| = 0.249$ nm [48], $\nu = 0.3$ [54] and $\sigma_0 = 820$ MPa, the calculated σ_y is 1258 MPa which is in good agreement with the experimental value (~1250 MPa). Moreover, this does suggest that the small amount of reverted austenite in this sample did not contribute greatly to strength.

Based on the Orowan mechanism, it is not surprising to see a decrease in the YS during the overaged period. However, the experimental σ_y in the 500 °C / 5760 min state (882 MPa) is much lower than the value calculated by Equation (7.3) (1090 MPa) and is almost at the same level with the YS in the SHT state (834 MPa). This discrepancy is attributed to two factors: (i) the precipitation and austenite reversion for the longer aging times consumed a large amount of solute atoms, which weakened the solid-solution strengthening of the α' -martensite matrix; (ii) the annihilation of dislocation slips as a result of the recovery of α' -martensite matrix after long-term aging will have reduced its strength. The softening of α' martensite matrix led to the fact that the hardness of α' martensite matrix was even lower than that of reverted austenite in the overaged stage.

Based on the above discussion, the precipitation strengthening mechanism is summarized as follows. At the early stage of aging, strengthening is associated with the stress required for dislocations to cut through coherent $L2_1$ -ordered Ni_2TiAl precipitates. The stress to cut through the precipitate is assumed to be governed by the coherency stresses and internal ordering of precipitates [33]. With the growth of the precipitates, the stress required for dislocation to cut through them increases and

so the yield strength increases. Unfortunately, it was not possible to investigate the strengthening behaviour at this stage due to the intergranular brittleness in this study. Further increasing in the precipitate size led to the initiation of Orowan mechanism. According to Orowan mechanism, the coarsening of precipitates featured with the increase of interparticle spacing after long-term aging result in the decrease of strength.

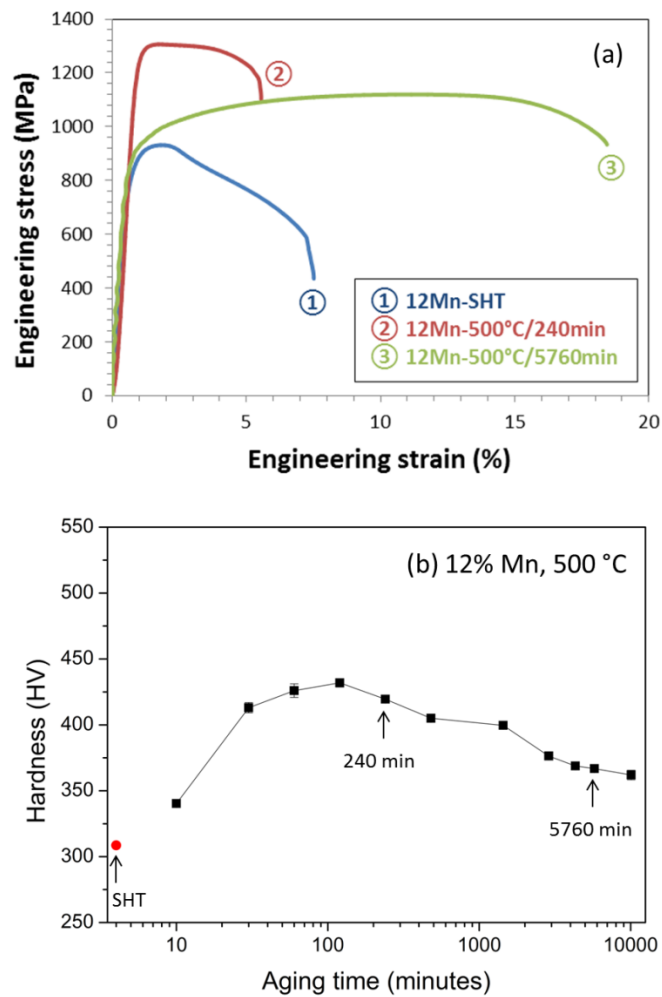


Figure 7-2 (a) The engineering stress-strain curves of 12% Mn alloy in different heat treatment conditions; (b) the corresponding hardness evolution of 12% Mn alloy aged at 500 °C.

7.3 Austenite engineering in overaged stage

There are three essential plastic deformation mechanisms in austenite at room temperature: dislocation slip, deformation-induced martensitic transformation and mechanical twinning [26]. In this section, an attempt will be made to understand which deformation modes occurred in these Mn-based maraging steels. This is significant if further improvement of the mechanical properties is required, as both theoretical and experimental studies have demonstrated that invoking the desired operation modes of plastic deformation in austenite can avoid the loss of ductility shortly after yielding [26].

Figure 7-3 displays the microstructural observation and XRD quantitative analysis of the over-aged 10% and 12% Mn alloys (500 °C / 5760 min state) after tensile testing. The plastic deformation did not lead to a significant decrease in the amount of austenite. A more evident decrease in the volume fraction of austenite after tensile testing was observed in the 10% Mn alloy, which might be associated with a lower stability of the austenite due to lower Mn concentration. All the evidence indicates that the reverted austenite possessed such a high stability against deformation-induced martensitic transformation that the TRIP effect was not a strong factor in the two alloys. This conclusion is in agreement with our previous nanoindentation study (Section 6.5) in which the TRIP effect was seldom observed during indentation.

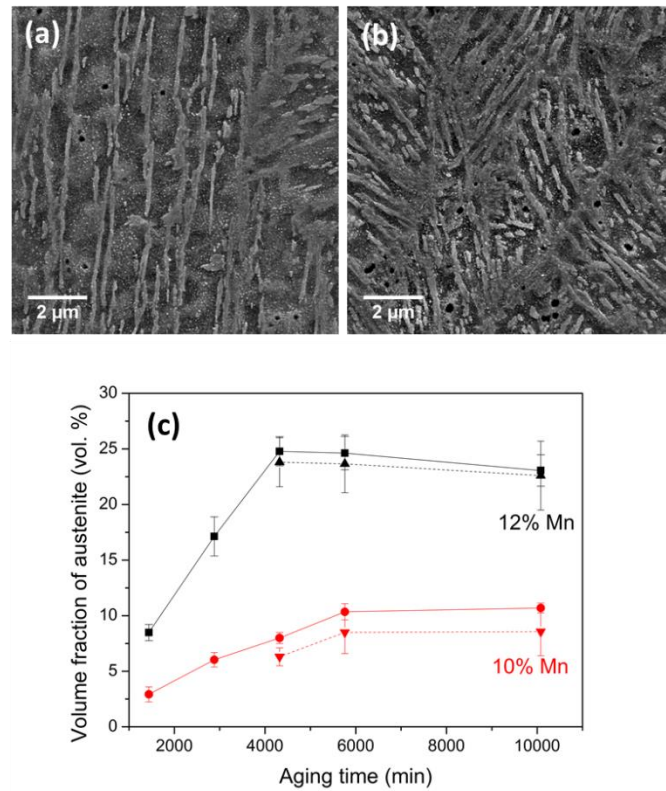


Figure 7-3 SEM images of samples after-tensile (a) 10% Mn and (b) 12% Mn alloys aged at 500 °C for 5760 min. (c) The volume fractions (vol.%) of reverted austenite as a function of aging time at the temperature of 500 °C (solid lines: before tensile testing; dash lines: after tensile testing).

7.3.1 The effect of reverted austenite on strengthening

As shown in Figure 4-8, when aging at 500 °C, the hardness of the 10 and 12% Mn alloys moderately decreased during the overaged stage. On the other hand, secondary hardening was observed at this stage in both alloys, which suggested the possible formation of an additional phase. Experimental evidence showed that it was associated with the austenite reversion in both alloys. As Figure 7-4(a) shows, it is clear that the formation of austenite (can be detected by XRD (> 3 vol. %)) in the 10% Mn alloy started from aging for 1440 min, which coincided with the onset of secondary hardening. Although the austenite nanolayers were observed earlier before the 500°C / 1440 min state, e.g. austenite layers along the prior austenite grain boundaries at the early aging stage in Figure 6-1, it is not believed that the plastic deformation mechanisms could occurred in the austenite nanolayers. A similar

coincidence of detecting reverted austenite formation and secondary hardening also existed in the 12% Mn alloys aged at 500 °C (Figure 7-4(b)).

In order to discuss the work hardening behaviour, true stress-strain curves are introduced in this section. Figure 7-5(a) displays the representative true stress-strain curves of 12% Mn alloy when aged at 500 °C for 480 min and 5760 min. True stress-strain curves of the 12% Mn alloy in the SHT state and 10% Mn alloy at 500 °C /5760 min state are also displayed in Figure 7-5(a) for a comparison. The following discussion about the tensile properties in this section is all based on the true stress-strain data.

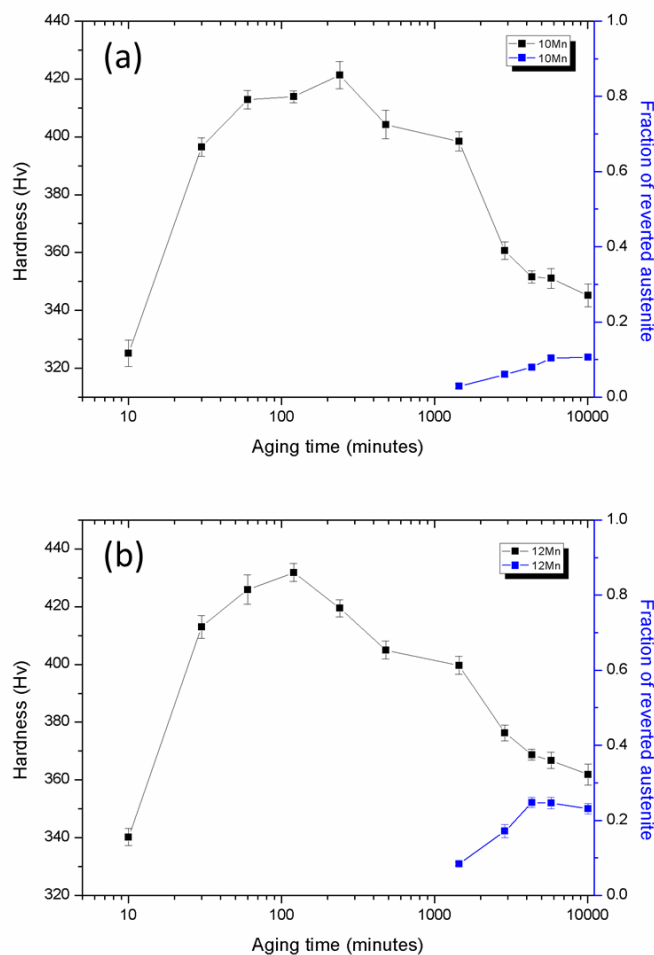


Figure 7-4 Hardness evolution vs. volume fraction of austenite as a function of time in (a) 10% Mn and (b) 12% Mn alloys when aged at 500 °C.

As shown in Figure 7-5, the 12% Mn alloy in the 500 °C / 480 min state exhibited an impressive yield stress of ~1320 MPa but failed shortly after yielding with a maximum true strain of 5.4%. The high yield stress was attributed to the precipitation strengthening mechanism which, however, could not provide sufficient work hardening after yielding, although the work hardening was still evident when compared to that of the SHT state. In contrast, the 12% Mn alloy in the 500 °C / 5760 min state exhibited steady work hardening after reaching the yield stress of ~900 MPa. This subsequent work hardening greatly enhanced both the strength (up to 1490 MPa) and ductility (~16.9%). A significant but lower level of work hardening (maximum true stress: 1366 MPa, maximum true strain: 15.7%) existed in the 10% Mn alloy in the 500 °C / 5760 min state (Figure 7-5). This work hardening apparently compensated the loss of yield stress after long-term aging, and more importantly, it was accompanied by an increase of ductility. As it has been shown that there was limited transformation of the reverted austenite to martensite during the deformation of both alloys, it is not likely that the work hardening could be primarily attributed to the TRIP effect. Given that the twinned structure of austenite was not observed in the two samples either, it is proposed that the deformation mechanism of reverted austenite was dominated by the dislocation slip with a small amount of the TRIP effect. This is quite possible when considering the high stability of the reverted austenite in the two alloys aged at 500 °C.

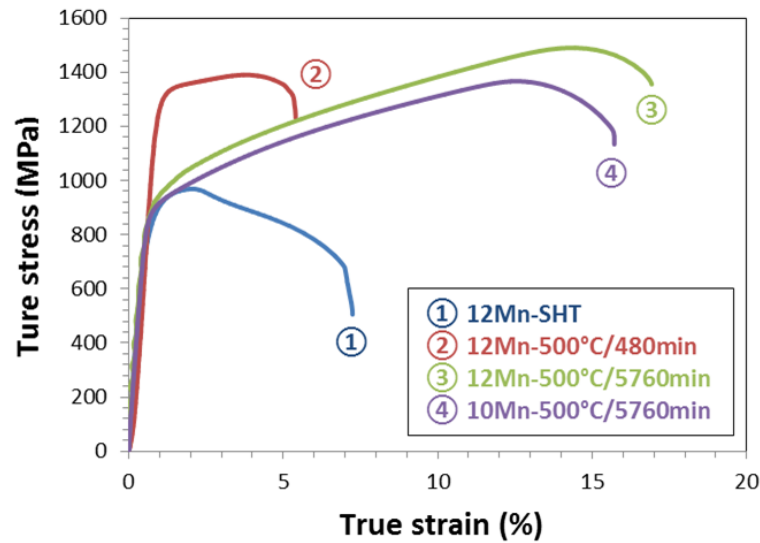


Figure 7-5 (a) The true stress-strain curves of the 12% Mn alloy in different heat treatment conditions; the true stress-strain curves of the 10% Mn alloy in the 500 °C /5760 min state is also displayed for comparison.

It is known that α' -martensite tends to nucleate at grain boundaries by a strain-controlled mechanism, or in some cases by stress-assisted nucleation process. Yen et al. [26] pointed out that when the grain size of austenite is small, it is difficult to form the multiple-variant fault structure which serve as the dominant sites for the nucleation of strain-induced martensite and therefore the stress-assisted martensite nucleation would become the predominant mechanism in this situation. In this work, a lot of evidence has confirmed that the reverted austenite formed in Mn-based maraging steels aged at 500 °C was very stable. Deformation-induced transformation to martensite did not occur by a large scale even when subjected to a true strain up to 16.9%. As the deformation behaviours of nano-scale austenite in this work coincided with the factors required for the stress-assisted nucleation mechanism in Ref. [26], it is proposed that the limited TRIP effect in this work was the result of a stress-assisted martensitic transformation process rather than the well-known strain-induced martensitic transformation.

The thermodynamic modelling has demonstrated that the stress-assisted mechanism for the deformation-induced α' -martensite transformation is very sensitive to the

chemical composition of austenite, particularly the Mn concentration [26]. Based on the principles of stress-assisted martensitic transformation, Yen et al. [26] suggested that the compositional differences in austenite could lead to a remarkable difference in the efficiency of TRIP effect. It has been demonstrated by experiment that an additional stress of 587 MPa is required to trigger the deformation-induced martensitic transformation in austenite with 2.6 wt.% higher of Mn concentration. Therefore, reverted austenite with relatively high Mn concentrations (in the range of 20-26.1 wt.%) in this study is believed to require a correspondingly high stress to induce the martensitic transformation. In reality, most austenite grains in Mn-based maraging steels reached the plastic instability before the stress threshold required for martensitic transformation was reached. Only a small amount of austenite grains with lower Mn concentrations had the martensitic transformation during deformation.

7.3.2 The effect of reverted austenite on ductility

In contrast to some literature suggesting that the brittleness was associated with the formation of reverted austenite [113], the present work suggests that the ductility is significantly improved by the formation of ductile austenite at grain boundaries.

Basically, the embrittlement is caused by two factors, first, the segregation of impurity or alloying elements along grain boundaries and second, preferential precipitation of second phase(s) at grain boundaries. As discussed in Section 2.2.4, researches presented numerous experimental results to support both mechanisms in Fe-Mn alloys [92][95][113][116][117][118][119][121]. The main difficulty in studying the embrittlement phenomenon is the observation of atomic scale segregation at boundaries. Initially, the results were only speculative. Later, Auger electron spectroscopy (AES) was applied to elucidate possible segregation at grain boundaries and these investigations indeed identified the segregation of Mn to boundaries [49][121][122]. In this study, the Auger electron spectroscopy was not performed to study the elemental segregation at the interface. However, high-resolution TEM-EDS analysis has confirmed the presence of Mn-rich nanolayer at grain boundaries in the early aging stage (Section 6.3).

The tensile results in conjunction with the fractographs of aged 10 and 12% Mn alloys revealed that the aging treatment resulted in the intergranular brittleness in the initial stage of aging. While after longer aging durations, or higher aging temperatures or increasing Mn content led to a transition in the fracture mode to transgranular dimpled ductile fracture. These factors have been demonstrated to benefit the formation of reverted austenite as well. For example, 12% Mn alloy aged at 500 °C exhibited intergranular embrittlement in the initial aging stage until the ductility suddenly increased to 5.5% after aging for 240 min. At this time, the volume fraction of austenite could not be detected by XRD, only thin austenite nanolayers were visible under SEM and TEM observations. As the increasing of aging time, the ductility gradually increased to 17.8% in the 500 °C /2880 min state with the austenite fraction of 17.2%. The whole transformation process can be described as: in the initial aging stage, the segregation of Mn at the grain boundaries increased the DBTT and thus gave rise to the intergranular embrittlement under external load. Although the subsequent formation of austenite nanolayers removed the intergranular embrittlement, the ductility was still unsatisfactory. Thanks to the growth of austenite layers via accumulated Mn segregation, the presence of ductile lath-like austenite significantly improved the ductility of these alloys. On the other hand, once the evident ductility was achieved, the further increase of austenite fraction did not lead to a corresponding improvement in ductility (Figure 4-11 and Figure 4-12). This finding once again confirmed that the TRIP effect was not likely to be extensive in these alloys, as the TRIP effect of austenite is known to improve the ductility and it is supposed that there is an approximately linear relationship between the volume fraction of austenite and the increment of ductility in the case of TRIP steels [15].

7.4 Summary

Studies on newly-developed materials mainly focus on optimizing the microstructure by tailoring the heat treatment parameters and chemical composition with the aim of obtaining the desired properties. Specifically in this work, the Mn content of the alloy, aging temperature and duration are the most important factors. Based on the

above discussion, the 12% Mn alloy, which had a relatively smaller grain size and higher amount of reverted austenite after aging, had many advantages. Further increasing the Mn content beyond 12 wt.%, however, would lead to the TWIP austenitic steels [18]. In terms of aging conditions, the effort to attain a good balance between the aging temperature and duration has been made. The 12% Mn alloy in the 500 °C / 480 min state exhibits a high yield stress (~1320 MPa) which is attributed to the interaction between dense precipitates and dislocations in the martensite matrix, whereas the poor ductility (5.4%) and limited work hardening is due to the small amount of reverted austenite nanolayers which cannot provide plastic deformation. In contrast, the lower yield stress (~900 MPa) of the 12% Mn alloy in the 500 °C / 5760 min state is the result of coarse precipitates and martensite softening after long-term aging. But owing to the considerable amount of lath-like reverted austenite formed at grain boundaries, the alloys exhibited a good work hardening leading to a maximum stress of 1490 MPa after yielding. Therefore, there is a contradiction between the requirement for short aging time to avoid the coarsening of precipitates and the softening of martensite matrix and the requirement for long-term aging to form a certain amount of lath-like austenite. Previous studies have revealed that the precipitation kinetics of Ni₂TiAl was very fast due to the rapid diffusivity of participating elements at 500 °C, whereas the formation of lath-like austenite was limited by the diffusion of Mn. The analyses on the formation of precipitates and reverted austenite have demonstrated that the kinetics of both processes were strongly associated with the aging temperature. Elevating aging temperature accelerated both processes, but some evidence indicates that the influence of aging temperature on the austenite formation was more prominent than that on the precipitation. For example, decreasing the aging temperature to 420 °C led to the volume fraction reducing to almost zero even after aged for 10080 min, whereas a number of precipitates with a size of ~5.5 nm could be observed in the 12% Mn alloy aged at 420 °C for 10080 min (Figure 5-2). Based on this discussion, the idea of aging at a higher temperature for a shorter duration is proposed. Most importantly, it is suggested by the MatCalc calculation that higher aging temperature corresponds to a lower Mn concentration of austenite. As it has been demonstrated that the stability of austenite is closely dependent on the concentration of austenite

stabilizing elements, the increase of aging temperature is believed to lead to a less stable austenite in which deformation-induced martensitic transformation is possible. In this case, a further improvement of both strength and ductility due to TRIP effect can be expected in these alloys.

Figure 7-6 shows the SEM images of the 12% Mn alloy aged at 540 °C for 360 min. It is clear that the reverted austenite had been formed at grain boundaries in this stage (Figure 7-6(a)). Besides, a large number of fine precipitates were observed as well (Figure 7-6(b)). In the future study, the tensile testing and nanoindentation will be carried out on this sample to examine its mechanical properties.

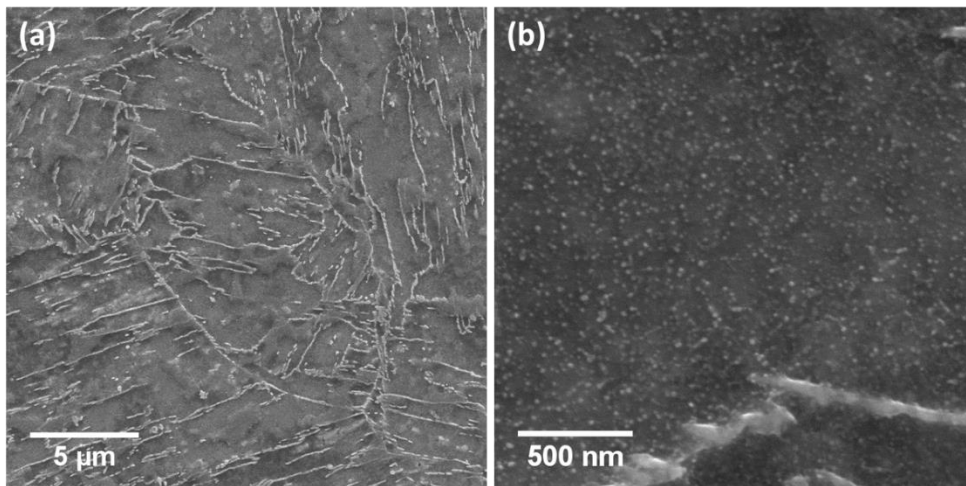


Figure 7-6 SEM images of 12% Mn alloy aged at 540 °C for 360 min: (a) reverted austenite formed along grain boundaries and (b) nano-precipitates.

Chapter 8 Conclusions and future work

8.1 Phase identification

Thermodynamic calculations by MatCalc indicated that the dominant equilibrium phases of Mn-based maraging steels at the aging temperatures 420-500 °C are ferrite and austenite. But it did not predict the existence of Ni₂TiAl intermetallic phase. Instead, a laves phase Fe₃Ti(Mo) is considered to be the precipitate phase according to the calculation. This discrepancy implies that an improvement to complete the thermodynamic database is required. Another reason may be that the real microconstituent is far from the equilibrium and is difficult to comprehensively predict. The situation is further complicated when considering the variety of alloying elements in this alloying system and the substantial variations in heat treatment paths.

Phase identification by XRD confirmed the formation of reverted austenite during aging at 420-500 °C. The amount of reverted austenite increased with the aging temperature and duration. Higher Mn content of the alloy also promoted the austenite reversion. In addition, XRD analyses revealed the existence of ϵ -martensite in the over-aged samples, but no evidence of precipitates was found in XRD patterns.

8.2 Hardness and tensile results

In the SHT state, the addition of Mn has been demonstrated to refine both the prior austenite grains and martensite packets via reducing the A_{e3} and M_s temperatures. This grain refinement is believed to contribute to the higher hardness of 12% Mn alloy in the SHT state.

Aging at 460 °C and 500 °C exhibited a typical hardness evolution of the precipitation-strengthened alloys. Increasing the aging temperature led to a more rapid hardening towards the peak hardness followed by a moderate decrease of hardness in the over-aged regime. Slower hardening kinetics but more significant hardening effect existed at 420 °C. In terms of the effect of Mn content, a quicker

response to thermal treatment and more significant hardening was found in the 12% Mn alloy.

Embrittlement occurred in samples aged at lower temperatures or for shorter times. Increasing the aging temperature and duration significantly improved the embrittlement phenomena. Increasing the Mn content of the alloy also benefited the ductility. The fracture mode of the solution-treated samples was a mix of cleavage brittle fracture and dimple ductile fracture. Intergranular brittle fracture was observed in the early aging stage. The embrittlement phenomenon was much improved after prolonged aging process and the fracture mode gradually transformed to a transgranular dimpled ductile fracture. Both increasing Mn content and aging temperature accelerated the improvement in the ductility. The 12% Mn alloy aged at 500 °C for 5760 min exhibited a UTS of 1120 MPa with TE of 18.4%.

8.3 Precipitation behaviour of L₂₁-ordered Ni₂TiAl phase

The compositional analyses identified that the nano-scale precipitates in the Mn-based maraging steels are a non-stoichiometric Ni₂TiAl intermetallic phase with minor Fe and Mn substitution. This non-stoichiometric composition is considered to enhance the ductility of the Ni₂TiAl phase.

HREM in conjunction with SAED study revealed the crystal structure of Ni₂TiAl phase is L₂₁-ordered which is expected to have a better creep resistance than B2-NiAl phase. The orientation relationship between the L₂₁-ordered Ni₂TiAl phase and *bcc* martensite matrix was: $(220)_{L_{21}} \parallel (110)_{bcc}$, $[001]_{L_{21}} \parallel [001]_{bcc}$; $(220)_{L_{21}} \parallel (110)_{bcc}$, $[011]_{L_{21}} \parallel [011]_{bcc}$; $(220)_{L_{21}} \parallel (110)_{bcc}$, $[\bar{1}11]_{L_{21}} \parallel [\bar{1}11]_{bcc}$. One eighth of the crystal structure of the L₂₁-Ni₂TiAl phase is a bcc cubic lattice which has a similar lattice parameter with the bcc matrix. The lattice misfit between them is calculated as 1.24%. This small lattice misfit together with the special orientation relationship indicates that the L₂₁-ordered Ni₂TiAl precipitates are not only coherent but also coplanar with the α' -martensite matrix. The coherent relationship is confirmed by the bright-field TEM observation which exhibited

classic dumb-bell dynamical diffraction contrast from the precipitates under two-beam conditions.

Various microstructural observations, such as by bright-field TEM, HREM and HAADF, suggested the existence of core/shell structure in the precipitates. So far, the exact nature of the heterogeneity is still not clear. The current evidence indicates that the two-phase $L2_1$ -Ni₂TiAl/B2-NiAl precipitates might be possible.

Experimental results revealed that the coarsening rate constants of precipitates in Mn-based maraging steels obey the diffusion-controlled coarsening kinetic form $\bar{r}^3 \sim Kt$ predicted by LSW theory (even though the alloy clearly broke the assumption of the LSW theory of a zero volume fraction of precipitates). On the other hand, the experimental particle size distributions (PSDs) were much broader than the theoretical PSD function, as the PSDs are believed to be more sensitive to the volume fraction than the coarsening rate constants.

Both thermodynamics and kinetics analyses supported the view that the Mn atoms participated in the nucleation of precipitation and reduced the misfit strain energy at the interface. Hence, higher Mn content is considered to promote the nucleation and increase the number density of precipitates, which has been confirmed by the microstructural observations.

8.4 Reverted austenite and its mechanical stability

The formation of reverted austenite nanolayers at grain boundaries initiated at the onset of aging by a diffusionless shear mechanism since the critical Mn concentration for austenite reversion at the interface was very low. The nucleation of reverted austenite within martensite laths was kinetically slower due to a lower driving force for phase transformation. In the following aging process, the accumulated Mn segregation to the new martensite/austenite grain boundaries led to the austenite nanolayers growing to lath-like reverted austenite, which means the lateral growth of austenite was supported by the diffusion of Mn. As the diffusion rate of Mn in the martensite matrix was relatively low, the diffusion-controlled austenite growth was fairly slow. In addition, the thermodynamic resistance to

coalescence between adjacent reverted austenite grains is another reason why the width of reverted austenite could maintain in the range 70-200 nm for a long time.

The width of reverted austenite was not closely associated with the nominal Mn content of the alloy, but it is found that it slightly increased with the increase of aging temperature owing to the higher driving force for Mn diffusion at higher temperature.

The experimental chemical composition profile of reverted austenite was partially consistent with that given by the Fe-Mn phase diagram. The segregation of Ti and Mo on grain boundaries in the initial aging stage resulted in the Mn concentration of austenite nanolayers being far from that indicated by the equilibrium phase diagram. The high concentration of Ti and Mo gradually vanished with the enrichment of Mn during the succeeding aging process. Therefore, the chemical composition of ferrite and lath-like austenite exhibited good agreement with the phase diagram. The TEM-EDS analyses revealed the Mn concentration of lath-like austenite was at the level of ~24 at.% which is higher than that of retained austenite (8-12 at.%) reported in conventional Mn-based TRIP or Q&P steels [27][154][34][50].

The volume fraction of reverted austenite increased almost linearly with the logarithm of aging time until it was saturated. The experimental results of the maximum austenite fractions (e.g. ~10 vol.% for 10% Mn alloy aged at 500 °C and ~24 vol.% for 12% Mn alloy aged at 500 °C) were significantly lower than the values predicted by the Fe-Mn phase diagram (36.0 vol.% for Fe-10Mn at 500 °C and ~47.5 vol.% for Fe-12Mn at 500 °C). This is mainly attributed to the fact that an amount of reverted austenite transformed to ϵ -martensite during cooling. The addition of Ti and Al may also be a reason for the discrepancy.

Most of the reverted austenite in the Mn-based maraging steels exhibited a K-S or N orientation relationships with the residual martensite. It is believed that both the K-S and N orientation relationships contributed to the mechanical stability of reverted austenite. However, nanoindentation results revealed that the high stability of reverted austenite in Mn-based maraging steels was mainly attributed to the high Mn concentration of austenite. The nano-size of reverted austenite was also considered to

be responsible for the high stability, but more evidence is needed to support this viewpoint.

8.5 Optimal heat treatment suggestions

Based on the above discussion, the 12% Mn alloy, which had a relatively smaller grain size together with a higher potential for austenite reversion, has been demonstrated to possess advantages for the automotive applications. In terms of the aging conditions, the optimum aging temperature for Mn-based maraging steels is 460 °C if the balance between the strengthening effect and production efficiency is considered, but in reality the serious embrittlement that occurs at this temperature would limit its use. Therefore, the aging temperature primarily studied in this work was 500 °C. The 12% Mn alloy aged at 500 °C / 480 min state exhibited a high yield stress (true stress: ~1320 MPa) but poor ductility (true strain: 5.4%), which resulted from the interaction between dense precipitates and dislocations. In contrast, the 12% Mn alloy aged at 500 °C / 5760 min state exhibited a lower yield stress (true stress: ~900 MPa) but good work hardening leading to a UTS of 1490 MPa (true stress), which was attributed to the formation of reverted austenite. Therefore, there is a contradiction between the requirement for a short aging duration to avoid the softening of martensite matrix (including the coarsening of precipitates) and the requirement for a long-term aging to form lath-like reverted austenite. Experimental studies revealed that the kinetics of both the precipitation and austenite reversion were strongly dependent on the aging temperature, but the influence of aging temperature on austenite formation was more prominent than that on precipitation. Therefore, it is proposed that aging at higher temperature for shorter duration might be a method to address the conflicting requirements. More importantly, higher aging temperature corresponds to a lower Mn concentration of austenite which made the occurrence of TRIP effect possible.

8.6 Future work

Based on the findings and discussions in this study, the following suggestions for future research are proposed:

1. It has been proposed that the 12% Mn alloy aged at higher temperature for a shorter duration to obtain a better combination of strength and ductility. The next step therefore is to define the optimal aging temperature and duration. Dilatometry measurements can be utilized to determine the austenite transformation kinetics instead of by trial and error method. A volume fraction of austenite (~20 vol.%) with a mechanical stability which enhances the capacity for work hardening during deformation is the main aim when designing the processing paths.
2. Atom probe analysis which provides the information about the chemical composition, particle size and number density of precipitates at atomic scale, should be used for further characterization of precipitates formed in early aging stage. In addition, APT in combination with HREM can assist the investigation on the core/shell structure.
3. The orientation relationship between the austenite and martensite needs to be further studied by EBSD which can provide better statistics than TEM observations, although this technique will be limited by its resolution.
4. Detailed nanoindentation study on the hardness of each single austenite grain with known Mn concentration and grain size is a direct method to explore the relationship between the mechanical stability and Mn concentration/grain size of austenite phase. Besides, nanoindentation is also an effective technology to estimate the occurrence of martensitic transformation under deformation (a higher maximum force at least above 70 μN should be applied to trigger TRIP effect).
5. As ϵ -martensite in Mn-based maraging steels vanished after tensile testing, investigation on its role in the deformation mechanism is required.

References

- [1] S. Keeler and M. Kimchi, Eds., *Advanced High-Strength Steels Application Guidelines Version 5.0*. WorldAutoSteel, 2014.
- [2] R. G. Davies, “The deformation behavior of a vanadium-strengthened dual phase steel,” *Metall. Trans. A*, vol. 9, no. 1, pp. 41–52, Jan. 1978.
- [3] R. G. Davies, “Influence of martensite composition and content on the properties of dual phase steels,” *Metall. Trans. A*, vol. 9, no. 5, pp. 671–679, May 1978.
- [4] N. J. Kim and G. Thomas, “Effects of morphology on the mechanical behavior of a dual phase Fe/2Si/0.1C steel,” *Metall. Trans. A*, vol. 12, no. 3, pp. 483–489, Mar. 1981.
- [5] M. Sarwar and R. Priestner, “Influence of ferrite-martensite microstructural morphology on tensile properties of dual-phase steel,” *J. Mater. Sci.*, vol. 31, no. 8, pp. 2091–2095, 1996.
- [6] G. B. Olson and M. Cohen, “Kinetics of strain-induced martensitic nucleation,” *Metall. Trans. A*, vol. 6, no. 4, pp. 791–795, Apr. 1975.
- [7] G. B. Olson and M. Azrin, “Transformation behavior of TRIP steels,” *Metall. Trans. A*, vol. 9, no. 5, pp. 713–721, May 1978.
- [8] G. B. Olson and M. Cohen, “Stress-assisted isothermal martensitic transformation: Application to TRIP steels,” *Metall. Trans. A*, vol. 13, no. 11, pp. 1907–1914, Nov. 1982.
- [9] S. Vercammen, B. Blanpain, B. C. De Cooman, and P. Wollants, “Cold rolling behaviour of an austenitic Fe–30Mn–3Al–3Si TWIP-steel: the importance of deformation twinning,” *Acta Mater.*, vol. 52, no. 7, pp. 2005–2012, Apr. 2004.
- [10] B. C. De Cooman, O. Kwon, and K.-G. Chin, “State-of-the-knowledge on TWIP steel,” *Mater. Sci. Technol.*, vol. 28, no. 5, pp. 513–527, May 2012.
- [11] B. C. De Cooman, “Phase transformations in high manganese twinning-induced plasticity (TWIP) steels,” in *Phase Transformations in Steels*, D. V. Edmonds and E. Pereloma, Eds. Woodhead Publishing, 2012.
- [12] Y. E. Goldshtein and G. A. Charushnikova, *Russ. Metall. Min.*, vol. 4, p. 72, 1963.

References

- [13] M. Niikura and J. W. Morris, "Thermal processing of ferritic 5Mn steel for toughness at cryogenic temperatures," *Metall. Trans. A*, vol. 11, no. 9, pp. 1531–1540, Sep. 1980.
- [14] T. Furukawa, "Dependence of strength–ductility characteristics on thermal history in lowcarbon, 5 wt-%Mn steels," *Mater. Sci. Technol.*, vol. 5, no. 5, p. 465, Jul. 1989.
- [15] H. Huang, O. Matsumura, and T. Furukawa, "Retained austenite in low carbon, manganese steel after intercritical heat treatment," *Mater. Sci. Technol.*, vol. 10, no. 7, p. 621, Jul. 1994.
- [16] D.-W. Suh, S.-J. Park, T.-H. Lee, C.-S. Oh, and S.-J. Kim, "Influence of Al on the Microstructural Evolution and Mechanical Behavior of Low-Carbon, Manganese Transformation-Induced-Plasticity Steel," *Metall. Mater. Trans. A*, vol. 41, no. 2, pp. 397–408, Dec. 2009.
- [17] J. Shi, X. Sun, M. Wang, W. Hui, H. Dong, and W. Cao, "Enhanced work-hardening behavior and mechanical properties in ultrafine-grained steels with large-fractioned metastable austenite," *Scr. Mater.*, vol. 63, no. 8, pp. 815–818, Oct. 2010.
- [18] D. Raabe, D. Ponge, O. Dmitrieva, and B. Sander, "Designing Ultrahigh Strength Steels with Good Ductility by Combining Transformation Induced Plasticity and Martensite Aging," *Adv. Eng. Mater.*, vol. 11, no. 7, pp. 547–555, Jul. 2009.
- [19] U. K. Viswanathan, G. K. Dey, and V. Sethumadhavan, "Effects of austenite reversion during overageing on the mechanical properties of 18 Ni (350) maraging steel," *Mater. Sci. Eng. A*, vol. 398, no. 1–2, pp. 367–372, 2005.
- [20] H. Nakagawa, T. Miyazaki, and H. Yokota, "Effects of aging temperature on the microstructure and mechanical properties of 1.8Cu-7.3Ni-15.9Cr-1.2Mo-low C, N martensitic precipitation hardening stainless steel," *J. Mater. Sci.*, vol. 35, no. 9, pp. 2245–2253, 2000.
- [21] A. Haldar, S. Suwas, and D. Bhattacharjee, Eds., *Microstructure and Texture in Steels*. London: Springer London, 2009.
- [22] B. C. De Cooman, P. Gibbs, S. Lee, and D. K. Matlock, "Transmission Electron Microscopy Analysis of Yielding in Ultrafine-Grained Medium Mn Transformation-Induced Plasticity Steel," *Metall. Mater. Trans. A*, vol. 44, no. 6, pp. 2563–2572, Feb. 2013.
- [23] P. J. Gibbs, E. De Moor, M. J. Merwin, B. Clausen, J. G. Speer, and D. K. Matlock, "Austenite Stability Effects on Tensile Behavior of Manganese-Enriched-Austenite Transformation-Induced Plasticity Steel," *Metall. Mater. Trans. A*, vol. 42, no. 12, pp. 3691–3702, Apr. 2011.

References

- [24] R. L. Miller, "Ultrafine-grained microstructures and mechanical properties of alloy steels," *Metall. Trans.*, vol. 3, no. 4, pp. 905–912, Apr. 1972.
- [25] J.-M. Jang, S.-J. Kim, N. H. Kang, K.-M. Cho, and D.-W. Suh, "Effects of annealing conditions on microstructure and mechanical properties of low carbon, manganese transformation-induced plasticity steel," *Met. Mater. Int.*, vol. 15, no. 6, pp. 909–916, Dec. 2009.
- [26] H.-W. Yen, S. W. Ooi, M. Eizadjou, A. Breen, C.-Y. Huang, H. K. D. H. Bhadeshia, and S. P. Ringer, "Role of stress-assisted martensite in the design of strong ultrafine-grained duplex steels," *Acta Mater.*, vol. 82, pp. 100–114, Jan. 2015.
- [27] H. Luo, J. Shi, C. Wang, W. Cao, X. Sun, and H. Dong, "Experimental and numerical analysis on formation of stable austenite during the intercritical annealing of 5Mn steel," *Acta Mater.*, vol. 59, no. 10, pp. 4002–4014, Jun. 2011.
- [28] S. Floreen, "The physical metallurgy of maraging steels," *Int. Mater. Rev.*, vol. 13, no. 1, pp. 115–128, 1968.
- [29] W. Sha and Z. Guo, *Maraging Steels: Modelling of Microstructure, Properties, and Applications*. Woodhead, Oxford, 2009.
- [30] R. F. Decker, J. T. Eash, and A. J. Goldman, "18% Nickel maraging steel," *Trans. ASM*, vol. 55, no. 1, p. 58, 1962.
- [31] Y. He, K. Yang, and W. Sha, "Microstructure and mechanical properties of a 2000 MPa grade co-free maraging steel," *Metall. Mater. Trans. A*, vol. 36, no. 9, pp. 2273–2287, 2005.
- [32] H. Leitner, M. Schober, and R. Schnitzer, "Splitting phenomenon in the precipitation evolution in an Fe–Ni–Al–Ti–Cr stainless steel," *Acta Mater.*, vol. 58, no. 4, pp. 1261–1269, 2010.
- [33] S. J. Kim and C. M. Wayman, "Strengthening behaviour and embrittlement phenomena in Fe-Ni-Mn-(Ti) maraging alloys," *Mater. Sci. Eng. A*, vol. 207, no. 1, pp. 22–29, 1996.
- [34] S. Lee, S.-J. Lee, and B. C. De Cooman, "Austenite stability of ultrafine-grained transformation-induced plasticity steel with Mn partitioning," *Scr. Mater.*, vol. 65, no. 3, pp. 225–228, Aug. 2011.
- [35] Y. Tomita and T. Okawa, "Effect of microstructure on mechanical properties of isothermally bainite-transformed 300M steel," *Mater. Sci. Eng. A*, vol. 172, no. 1–2, pp. 145–151, Nov. 1993.

References

- [36] H. Springer, M. Belde, and D. Raabe, "Bulk combinatorial design of ductile martensitic stainless steels through confined martensite-to-austenite reversion," *Mater. Sci. Eng. A*, vol. 582, pp. 235–244, Oct. 2013.
- [37] E. A. Wilson, "Discussion of 'precipitation of austenite particles at grain boundaries during aging of Fe-Mn-Ni steel,'" *Metall. Mater. Trans. A*, vol. 35, no. 1, pp. 352–355, Jan. 2004.
- [38] H. Leitner, R. Schnitzer, M. Schober, and S. Zinner, "Precipitate modification in PH13-8 Mo type maraging steel," *Acta Mater.*, vol. 59, no. 12, pp. 5012–5022, 2011.
- [39] R. Schnitzer, M. Schober, S. Zinner, and H. Leitner, "Effect of Cu on the evolution of precipitation in an Fe–Cr–Ni–Al–Ti maraging steel," *Acta Mater.*, vol. 58, no. 10, pp. 3733–3741, 2010.
- [40] S. Höring, N. Wanderka, and J. Banhart, "The influence of Cu addition on precipitation in Fe-Cr-Ni-Al-(Cu) model alloys," *Ultramicroscopy*, vol. 109, no. 5, pp. 574–9, Apr. 2009.
- [41] F. G. Wilson and F. B. Pickering, "A study of precipitation following reversion and high temperature ageing in a 25% Ni, 15% Cr, 4% Ti steel," *Acta Metall.*, vol. 18, no. 7, pp. 775–783, 1970.
- [42] M. Hättestrand, J.-O. Nilsson, K. Stiller, P. Liu, and M. Andersson, "Precipitation hardening in a 12%Cr–9%Ni–4%Mo–2%Cu stainless steel," *Acta Mater.*, vol. 52, no. 4, pp. 1023–1037, 2004.
- [43] P. Liu, A. H. Stigenberg, and J. O. Nilsson, "Quasicrystalline and crystalline precipitation during isothermal tempering in a 12Cr-9Ni-4Mo maraging stainless steel," *Acta Metall. Mater.*, vol. 43, no. 7, pp. 2881–2890, 1995.
- [44] D. Raabe, D. Ponge, O. Dmitrieva, and B. Sander, "Nanoprecipitate-hardened 1.5 GPa steels with unexpected high ductility," *Scr. Mater.*, vol. 60, no. 12, pp. 1141–1144, 2009.
- [45] Y. R. Wen, A. Hirata, Z. W. Zhang, T. Fujita, C. T. Liu, J. H. Jiang, and M. W. Chen, "Microstructure characterization of Cu-rich nanoprecipitates in a Fe–2.5 Cu–1.5 Mn–4.0 Ni–1.0 Al multicomponent ferritic alloy," *Acta Mater.*, vol. 61, no. 6, pp. 2133–2147, 2013.
- [46] E. V Pereloma, R. A. Stohr, M. K. Miller, and S. P. Ringer, "Observation of precipitation evolution in Fe-Ni-Mn-Ti-Al maraging steel by atom probe tomography," *Metall. Mater. Trans. A Phys. Metall. Mater. Sci.*, vol. 40, no. 13, pp. 3069–3075, 2009.

References

- [47] L.-T. Shiang and C. M. Wayman, "Maraging behavior of an Fe-19.5Ni-5Mn alloy. III: Mechanical properties," *Metallography*, vol. 22, no. 1, pp. 15–36, Jan. 1989.
- [48] E. V. Pereloma, A. Shekhter, M. K. Miller, and S. P. Ringer, "Ageing behaviour of an Fe-20Ni-1.8Mn-1.6Ti-0.59Al (wt%) maraging alloy: clustering, precipitation and hardening," *Acta Mater.*, vol. 52, no. 19, pp. 5589–5602, 2004.
- [49] N. H. Heo, J. W. Nam, Y. U. Heo, and S. J. Kim, "Grain boundary embrittlement by Mn and eutectoid reaction in binary Fe-12Mn steel," *Acta Mater.*, vol. 61, no. 11, pp. 4022–4034, 2013.
- [50] D. Raabe, S. Sandlöbes, J. Millán, D. Ponge, H. Assadi, M. Herbig, and P.-P. Choi, "Segregation engineering enables nanoscale martensite to austenite phase transformation at grain boundaries: A pathway to ductile martensite," *Acta Mater.*, vol. 61, no. 16, pp. 6132–6152, Sep. 2013.
- [51] W. Sha, A. Cerezo, and G. Smith, "Phase chemistry and precipitation reactions in maraging steels: Part I. Introduction and study of Co-containing C-300 steel," *Metall. Mater. Trans. A*, vol. 24, no. 6, pp. 1221–1232, 1993.
- [52] S.-J. Kim and C. M. Wayman, "Precipitation behavior and microstructural changes in maraging Fe-Ni-Mn-Ti alloys," *Mater. Sci. Eng. A*, vol. 128, no. 2, pp. 217–230, 1990.
- [53] A. Shekhter, H. Aaronson, M. Miller, S. Ringer, and E. Pereloma, "Effect of aging and deformation on the microstructure and properties of Fe-Ni-Ti maraging steel," *Metall. Mater. Trans. A*, vol. 35, no. 3, pp. 973–983, 2004.
- [54] V. K. Vasudevan, S. J. Kim, and C. M. Wayman, "Precipitation reactions and strengthening behavior in 18 Wt Pct nickel maraging steels," *Metall. Trans. A*, vol. 21, no. 10, pp. 2655–2668, Oct. 1990.
- [55] R. J. Rioja and D. E. Laughlin, "The early stages of GP zone formation in naturally aged Al-4 wt pct Cu alloys," *Metall. Trans. A*, vol. 8, no. 8, pp. 1257–1261, Aug. 1977.
- [56] W. Sha, A. Cerezo, and G. D. W. Smith, "Phase chemistry and precipitation reactions in maraging steels: Part IV. Discussion and conclusions," *Metall. Trans. A*, vol. 24, no. 6, pp. 1251–1256, 1993.
- [57] C. Servant, G. Maeder, and G. Cizeron, "A small-angle x-ray scattering investigation of the zone formation of 'maraging' type alloys," *Metall. Trans. A*, vol. 6, no. 5, pp. 981–990, May 1975.

References

- [58] C. Servant, N. Bouzid, and O. Lyon, "Small-angle X-ray scattering investigation of the martensite unmixing in maraging alloy using synchrotron radiation," *Philos. Mag. A*, vol. 56, no. 5, pp. 565–582, Nov. 1987.
- [59] A. Gemperle, J. Gemperlova, W. Sha, and G. D. W. Smith, "Aging behaviour of cobalt free chromium containing maraging steels," *Mater. Sci. Technol.*, vol. 8, no. 6, pp. 546–554, 1992.
- [60] Z. K. Teng, C. T. Liu, G. Ghosh, P. K. Liaw, and M. E. Fine, "Effects of Al on the microstructure and ductility of NiAl-strengthened ferritic steels at room temperature," *Intermetallics*, vol. 18, no. 8, pp. 1437–1443, Aug. 2010.
- [61] Z. K. Teng, F. Zhang, M. K. Miller, C. T. Liu, S. Huang, Y. T. Chou, R. H. Tien, Y. A. Chang, and P. K. Liaw, "New NiAl-strengthened ferritic steels with balanced creep resistance and ductility designed by coupling thermodynamic calculations with focused experiments," *Intermetallics*, vol. 29, pp. 110–115, Oct. 2012.
- [62] Z. Sun, C. H. Liebscher, S. Huang, Z. Teng, G. Song, G. Wang, M. Asta, M. Rawlings, M. E. Fine, and P. K. Liaw, "New design aspects of creep-resistant NiAl-strengthened ferritic alloys," *Scr. Mater.*, vol. 68, no. 6, pp. 384–388, 2013.
- [63] H. K. D. H. Bhadeshia, "Design of ferritic creep-resistant steels," *ISIJ Int.*, vol. 41, no. 6, pp. 626–640, 2001.
- [64] R. Viswanathan, J. F. Henry, J. Tanzosh, G. Stanko, J. Shingledecker, B. Vitalis, and R. Purgert, "U.S. Program on Materials Technology for Ultra-Supercritical Coal Power Plants," *J. Mater. Eng. Perform.*, vol. 14, no. 3, pp. 281–292, Jun. 2005.
- [65] G. Eggeler, "The effect of long-term creep on particle coarsening in tempered martensite ferritic steels," *Acta Metall.*, vol. 37, no. 12, pp. 3225–3234, Dec. 1989.
- [66] J. Pešička, R. Kužel, A. Dronhofer, and G. Eggeler, "The evolution of dislocation density during heat treatment and creep of tempered martensite ferritic steels," *Acta Mater.*, vol. 51, no. 16, pp. 4847–4862, Sep. 2003.
- [67] A. Kostka, K. Tak, R. Hellmig, Y. Estrin, and G. Eggeler, "On the contribution of carbides and micrograin boundaries to the creep strength of tempered martensite ferritic steels," *Acta Mater.*, vol. 55, no. 2, pp. 539–550, Jan. 2007.
- [68] Y. Wang, K.-H. Mayer, A. Scholz, C. Berger, H. Chilukuru, K. Durst, and W. Blum, "Development of new 11%Cr heat resistant ferritic steels with enhanced creep resistance for steam power plants with operating steam

References

- temperatures up to 650°C,” *Mater. Sci. Eng. A*, vol. 510–511, pp. 180–184, Jun. 2009.
- [69] A. Aghajani, C. Somsen, and G. Eggeler, “On the effect of long-term creep on the microstructure of a 12% chromium tempered martensite ferritic steel,” *Acta Mater.*, vol. 57, no. 17, pp. 5093–5106, Oct. 2009.
- [70] K. SC, “Precipitation processes in Fe-base ferritic NiAl alloys,” Northwestern University, 1971.
- [71] H. A. Calderon, M. E. Fine, and J. R. Weertman, “Coarsening and morphology of β' particles in Fe-Ni-Al-Mo ferritic alloys,” *Metall. Trans. A*, vol. 19, no. 5, pp. 1135–1146, May 1988.
- [72] S. M. Zhu, S. C. Tjong, and J. K. L. Lai, “Creep behavior of a β' (NiAl) precipitation strengthened ferritic Fe–Cr–Ni–Al alloy,” *Acta Mater.*, vol. 46, no. 9, pp. 2969–2976, May 1998.
- [73] C. Stallybrass and G. Sauthoff, “Ferritic Fe–Al–Ni–Cr alloys with coherent precipitates for high-temperature applications,” *Mater. Sci. Eng. A*, vol. 387–389, pp. 985–990, Dec. 2004.
- [74] C. Stallybrass, A. Schneider, and G. Sauthoff, “The strengthening effect of (Ni,Fe)Al precipitates on the mechanical properties at high temperatures of ferritic Fe–Al–Ni–Cr alloys,” *Intermetallics*, vol. 13, no. 12, pp. 1263–1268, Dec. 2005.
- [75] W. B. Pearson, *Handbook of Lattice Spacing and Structure of Metals*. Pergamon Press, 1958.
- [76] R. Taillard, A. Pineau, and B. J. Thomas, “The precipitation of the intermetallic compound NiAl in Fe-19wt.%Cr alloys,” *Mater. Sci. Eng.*, vol. 54, no. 2, pp. 209–219, Jul. 1982.
- [77] Z. K. Teng, G. Ghosh, M. K. Miller, S. Huang, B. Clausen, D. W. Brown, and P. K. Liaw, “Neutron-diffraction study and modeling of the lattice parameters of a NiAl-precipitate-strengthened Fe-based alloy,” *Acta Mater.*, vol. 60, no. 13–14, pp. 5362–5369, Aug. 2012.
- [78] M. Schober, R. Schnitzer, and H. Leitner, “Precipitation evolution in a Ti-free and Ti-containing stainless maraging steel,” *Ultramicroscopy*, vol. 109, no. 5, pp. 553–562, 2009.
- [79] H. C. Burnett, R. H. Duff, and H. C. Vacher, “Identification of Metallurgical Reactions and Their Effect on the Mechanical Properties of 17-7 PH Stainless Steel,” *J. Res. Natl. Bur. Stand.*, vol. 66C, no. 2, 1962.

References

- [80] V. Seetharaman, M. Sundararaman, and R. Krishnan, "Precipitation hardening in a PH 13-8 Mo stainless steel," *Mater. Sci. Eng.*, vol. 47, no. 1, pp. 1–11, 1981.
- [81] Z. Guo, W. Sha, and D. Vaumousse, "Microstructural evolution in a PH13-8 stainless steel after ageing," *Acta Mater.*, vol. 51, no. 1, pp. 101–116, 2003.
- [82] D. H. Ping, M. Ohnuma, Y. Hirakawa, Y. Kadoya, and K. Hono, "Microstructural evolution in 13Cr–8Ni–2.5Mo–2Al martensitic precipitation-hardened stainless steel," *Mater. Sci. Eng. A*, vol. 394, no. 1–2, pp. 285–295, 2005.
- [83] A. Gemperle, J. Gemperlová, W. Sha, and G. D. W. Smith, "Aging behaviour of cobalt free chromium containing maraging steels," *Mater. Sci. Technol.*, vol. 8, no. 6, pp. 546–554, Jun. 1992.
- [84] H. Leitner, M. Schober, R. Schnitzer, and S. Zinner, "Strengthening behavior of Fe–Cr–Ni–Al–(Ti) maraging steels," *Mater. Sci. Eng. A*, vol. 528, no. 15, pp. 5264–5270, Jun. 2011.
- [85] C. H. Liebscher, V. Radmilovic, U. Dahmen, M. Asta, and G. Ghosh, "On the formation of hierarchically structured L2 1 -Ni₂TiAl type precipitates in a ferritic alloy," *J. Mater. Sci.*, vol. 48, no. 5, pp. 2067–2075, 2013.
- [86] L. A. Bendersky, P. W. Voorhees, W. J. Boettinger, and W. C. Johnson, "The role of elastic energy in the morphological development of a NiTiAl alloy," *Scr. Metall.*, vol. 22, no. 7, pp. 1029–1034, Jan. 1988.
- [87] W. J. Boettinger, L. A. Bendersky, F. S. Biancaniello, and J. W. Cahn, "Rapid solidification and ordering of B2 and L21 phases in the NiAl–NiTi system," *Mater. Sci. Eng.*, vol. 98, pp. 273–276, Feb. 1988.
- [88] R. D. Field, R. Darolia, and D. F. Lahrman, "Precipitation in NiAl/Ni₂AlTi alloys," *Scr. Metall.*, vol. 23, no. 9, pp. 1469–1474, Sep. 1989.
- [89] J. Jung, G. Ghosh, D. Isheim, and G. B. Olson, "Precipitation of heusler phase (Ni₂TiAl) from B2–TiNi in Ni–Ti–Al and Ni–Ti–Al–X (X=Hf, Zr) alloys," *Metall. Mater. Trans. A*, vol. 34, no. 6, pp. 1221–1235, 2003.
- [90] J. Jung, G. Ghosh, and G. B. Olson, "A comparative study of precipitation behavior of Heusler phase (Ni₂TiAl) from B2–TiNi in Ni–Ti–Al and Ni–Ti–Al–X (X=Hf, Pd, Pt, Zr) alloys," *Acta Mater.*, vol. 51, no. 20, pp. 6341–6357, 2003.
- [91] P. R. Strutt, R. S. Polvani, and J. C. Ingram, "Creep behavior of the heusler type structure alloy Ni₂AlTi," *Metall. Trans. A*, vol. 7, no. 1, pp. 23–31, Dec. 1976.

References

- [92] N.-H. Heo, "Theory of nonequilibrium segregation in an Fe-Mn-Ni ternary alloy and a ductile-brittle-ductile transition," *Acta Mater.*, vol. 44, no. 7, pp. 3015–3023, Jul. 1996.
- [93] Y. M. Kim, C. D. Yim, and B. S. You, "Grain refining mechanism in Mg–Al base alloys with carbon addition," *Scr. Mater.*, vol. 57, no. 8, pp. 691–694, Oct. 2007.
- [94] R.-Y. Li, J.-Y. Qin, T.-K. Gu, and X.-F. Bian, "Structure of liquid Al80Mn20 alloy by Reverse Monte Carlo simulation," *J. Non. Cryst. Solids*, vol. 354, no. 15–16, pp. 1736–1739, Mar. 2008.
- [95] D. R. Squires and E. A. Wilson, "Aging and brittleness in an Fe-Ni-Mn alloy," *Metall. Trans.*, vol. 3, no. 2, pp. 579–585, Feb. 1972.
- [96] D. R. Squires, F. G. Wilson, and E. A. Wilson, "The influence of Mo and Co on the embrittlement of an Fe-Ni-Mn alloy," *Metall. Trans.*, vol. 5, no. 12, pp. 2569–2578, Dec. 1974.
- [97] Z. W. Zhang, C. T. Liu, X.-L. Wang, K. C. Littrell, M. K. Miller, K. An, and B. A. Chin, "From embryos to precipitates: A study of nucleation and growth in a multicomponent ferritic steel," *Phys. Rev. B*, vol. 84, no. 17, p. 174114, Nov. 2011.
- [98] G. Fourlaris, A. J. Baker, and G. D. Papadimitriou, "Microscopic characterisation of ϵ -Cu interphase precipitation in hypereutectoid Fe-C-Cu alloys," *Acta Metall. Mater.*, vol. 43, no. 7, pp. 2589–2604, Jul. 1995.
- [99] M. D. Mulholland and D. N. Seidman, "Nanoscale co-precipitation and mechanical properties of a high-strength low-carbon steel," *Acta Mater.*, vol. 59, no. 5, pp. 1881–1897, Mar. 2011.
- [100] N. Maruyama, M. Sugiyama, T. Hara, and H. Tamehiro, "Precipitation and Phase Transformation of Copper Particles in Low Alloy Ferritic and Martensitic Steels," *Mater. Trans. JIM*, vol. 40, 1999.
- [101] A. Ghosh, S. das, and S. Chatterjee, "Ageing behavior of a Cu-bearing ultrahigh strength steel," *Mater. Sci. Eng. A*, vol. 486, no. 1–2, pp. 152–157, Jul. 2008.
- [102] R. Prakash Kolli and D. N. Seidman, "The temporal evolution of the decomposition of a concentrated multicomponent Fe–Cu-based steel," *Acta Mater.*, vol. 56, no. 9, pp. 2073–2088, May 2008.
- [103] Z. Zhang, C. T. Liu, M. K. Miller, X.-L. Wang, Y. Wen, T. Fujita, A. Hirata, M. Chen, G. Chen, and B. A. Chin, "A nanoscale co-precipitation approach for property enhancement of Fe-base alloys," *Sci. Rep.*, vol. 3, p. 1327, Jan. 2013.

References

- [104] M. Kapoor, "Design and Development of bcc - Cu - and B2 NiAl - Precipitation - Strengthened Ferritic Steel," Northwestern University, 2013.
- [105] P. J. Othen, M. L. Jenkins, and G. D. W. Smith, "High-resolution electron microscopy studies of the structure of Cu precipitates in α -Fe," *Philos. Mag. A*, vol. 70, no. 1, pp. 1–24, Jul. 1994.
- [106] Z. B. Jiao, J. H. Luan, Z. W. Zhang, M. K. Miller, W. B. Ma, and C. T. Liu, "Synergistic effects of Cu and Ni on nanoscale precipitation and mechanical properties of high-strength steels," *Acta Mater.*, vol. 61, no. 16, pp. 5996–6005, Sep. 2013.
- [107] K. Stiller, M. Hättestrand, and F. Danoix, "Precipitation in 9Ni–12Cr–2Cu maraging steels," *Acta Mater.*, vol. 46, no. 17, pp. 6063–6073, 1998.
- [108] N. Maruyama, M. Sugiyama, T. Hara, and H. Tamehiro, "Precipitation and phase transformation of copper particles in low alloy ferritic and martensitic steels," *Mater. Trans. JIM*, vol. 40, no. 4, pp. 268–277, 1999.
- [109] Y. R. Wen, Y. P. Li, A. Hirata, Y. Zhang, T. Fujita, T. Furuhashi, C. T. Liu, A. Chiba, and M. W. Chen, "Synergistic alloying effect on microstructural evolution and mechanical properties of Cu precipitation-strengthened ferritic alloys," *Acta Mater.*, vol. 61, no. 20, pp. 7726–7740, Dec. 2013.
- [110] M. K. Miller, B. D. Wirth, and G. R. Odette, "Precipitation in neutron-irradiated Fe–Cu and Fe–Cu–Mn model alloys: a comparison of APT and SANS data," *Mater. Sci. Eng. A*, vol. 353, no. 1–2, pp. 133–139, Jul. 2003.
- [111] L. T. Shiang and C. M. Wayman, "Maraging behavior in an Fe-19.5Ni-5Mn alloy I: Precipitation characteristics," *Metallography*, vol. 21, no. 4, pp. 399–423, Nov. 1988.
- [112] S.-J. Kim and C. M. Wayman, "Electron microscopy study of precipitates in Fe-Ni-Mn maraging alloys," *Mater. Sci. Eng. A*, vol. 136, pp. 121–129, Apr. 1991.
- [113] S.-H. Mun, M. Watanabe, D. B. Williams, X. Li, K. Hwan Oh, and H.-C. Lee, "Precipitation of austenite particles at grain boundaries during aging of Fe-Mn-Ni steel," *Metall. Mater. Trans. A*, vol. 33, no. 4, pp. 1057–1067, Apr. 2002.
- [114] J. Singh and C. M. Wayman, "Age-hardening characteristics of a martensitic Fe-Ni-Mn alloy," *Mater. Sci. Eng.*, vol. 94, pp. 233–242, Oct. 1987.
- [115] H. C. Feng, E. A. Wilson, and C. J. McMahon, in *3rd Int. Conf. on the Strength of Metals and Alloys*, 1973, p. 129.

References

- [116] H. Suto and T. Murakami, "On the Grain Boundary Embrittlement in an Aged 12Ni-6Mn-Fe Martensite," *Trans. Japan Inst. Met.*, vol. 20, p. 365, 1979.
- [117] N.-H. Heo and H.-C. Lee, "The embrittlement and de-embrittlement of grain boundaries in an Fe-Mn-Ni alloy due to grain boundary segregation of Mn," *Metall. Mater. Trans. A*, vol. 27, no. 4, pp. 1015–1020, Apr. 1996.
- [118] H.-C. Lee, S.-H. Mun, and D. McKenzie, "Electron microscopy study on the grain-boundary precipitation during aging of Fe-10Ni-5Mn steel," *Metall. Mater. Trans. A*, vol. 34, no. 11, pp. 2421–2428, Nov. 2003.
- [119] S. Hossein Nedjad, M. Nili Ahmadabadi, and T. Furuhashi, "Transmission Electron Microscopy Study on the Grain Boundary Precipitation of an Fe-Ni-Mn Maraging Steel," *Metall. Mater. Trans. A*, vol. 39, no. 1, pp. 19–27, 2008.
- [120] S. Hossein Nedjad, M. Nili Ahmadabadi, and T. Furuhashi, "Correlation between the intergranular brittleness and precipitation reactions during isothermal aging of an Fe-Ni-Mn maraging steel," *Mater. Sci. Eng. A*, vol. 490, no. 1–2, pp. 105–112, 2008.
- [121] F. Nikbakht, M. Nasim, C. Davies, E. A. Wilson, and H. Adrian, "Isothermal embrittlement of Fe-8Mn alloys at 450°C," *Mater. Sci. Technol.*, vol. 26, no. 5, pp. 552–558, May 2010.
- [122] M. Nasim, B. C. Edwards, and E. A. Wilson, "A study of grain boundary embrittlement in an Fe-8%Mn alloy," *Mater. Sci. Eng. A*, vol. 281, no. 1–2, pp. 56–67, Apr. 2000.
- [123] J. K. Tien, P. G. Shewmon, and J. S. Foster, "On evaluating the duration of the interfacial rate controlling step in reactions involving diffusion," *Scr. Metall.*, vol. 7, no. 11, pp. 1171–1174, Nov. 1973.
- [124] R. Wagner, R. Kampmann, and P. W. Voorhees, "Homogeneous Second-Phase Precipitation, in Phase Transformations in Materials," G. Kostorz, Ed. Weinheim, FRG: Wiley-VCH Verlag GmbH & Co. KGaA, 2001.
- [125] R. Kampmann and R. Wagner, *Decomposition of Alloys: the Early Stages*. Elsevier, 1984.
- [126] I. M. Lifshitz and V. V. Slyozov, "The kinetics of precipitation from supersaturated solid solutions," *J. Phys. Chem. Solids*, vol. 19, no. 1–2, pp. 35–50, Apr. 1961.
- [127] C. Wagner, "Theorie der Alterung von Niederschlägen durch Umlösen (Ostwald-Reifung)," *Zeitschrift für Elektrochemie, Berichte der Bunsengesellschaft für Phys. Chemie*, vol. 65, no. 7-8, pp. 581–591, Sep. 1961.

References

- [128] L. Ratke and P. W. Voorhees, *Growth and Coarsening: Ripening in Materials Processing*, Springer V. Berlin, 2002.
- [129] A. J. Ardell, “An application of the theory of particle coarsening: The γ' precipitate in Ni-Al alloys,” *Acta Metall.*, vol. 16, no. 4, pp. 511–516, Apr. 1968.
- [130] C. FULLER and D. SEIDMAN, “Temporal evolution of the nanostructure of Al(Sc,Zr) alloys: Part II-coarsening of Al(ScZr) precipitates,” *Acta Mater.*, vol. 53, no. 20, pp. 5415–5428, Dec. 2005.
- [131] N. Bouzid, C. Servant, and O. Lyon, “Anomalous small-angle X-ray scattering from a maraging alloy during martensite unmixing,” *Philos. Mag. Part B*, vol. 57, no. 3, pp. 343–359, Mar. 1988.
- [132] E.-W. Huang, P. K. Liaw, L. Porcar, Y. Liu, Y.-L. Liu, J.-J. Kai, and W.-R. Chen, “Study of nanoprecipitates in a nickel-based superalloy using small-angle neutron scattering and transmission electron microscopy,” *Appl. Phys. Lett.*, vol. 93, no. 16, p. 161904, Oct. 2008.
- [133] a. Deschamps, L. Lae, and P. Guyot, “In situ small-angle scattering study of the precipitation kinetics in an Al–Zr–Sc alloy,” *Acta Mater.*, vol. 55, no. 8, pp. 2775–2783, May 2007.
- [134] P. Donnadiou, Y. Shao, F. De Geuser, G. A. Botton, S. Lazar, M. Cheynet, M. de Boissieu, and A. Deschamps, “Atomic structure of T1 precipitates in Al–Li–Cu alloys revisited with HAADF-STEM imaging and small-angle X-ray scattering,” *Acta Mater.*, vol. 59, no. 2, pp. 462–472, 2011.
- [135] J. Millán, D. Ponge, D. Raabe, P. Choi, and O. Dmitrieva, “Characterization of Nano-Sized Precipitates in a Mn-Based Lean Maraging Steel by Atom Probe Tomography,” *Steel Res. Int.*, vol. 82, no. 2, pp. 137–145, Feb. 2011.
- [136] A. . Brailsford and P. Wynblatt, “The dependence of ostwald ripening kinetics on particle volume fraction,” *Acta Metall.*, vol. 27, no. 3, pp. 489–497, Mar. 1979.
- [137] J. A. Marqusee and J. Ross, “Theory of Ostwald ripening: Competitive growth and its dependence on volume fraction,” *J. Chem. Phys.*, vol. 80, no. 1, p. 536, Jan. 1984.
- [138] K. Tsumuraya and Y. Miyata, “Coarsening models incorporating both diffusion geometry and volume fraction of particles,” *Acta Metall.*, vol. 31, no. 3, pp. 437–452, Mar. 1983.
- [139] S. P. Marsh and M. E. Glicksman, “Kinetics of phase coarsening in dense systems,” *Acta Mater.*, vol. 44, no. 9, pp. 3761–3771, Sep. 1996.

References

- [140] H. Ghassemi-Armaki, R. Maaß, S. P. Bhat, S. Sriram, J. R. Greer, and K. S. Kumar, “Deformation response of ferrite and martensite in a dual-phase steel,” *Acta Mater.*, 2013.
- [141] J.-B. Seol, D. Raabe, P.-P. Choi, Y.-R. Im, and C.-G. Park, “Atomic scale effects of alloying, partitioning, solute drag and austempering on the mechanical properties of high-carbon bainitic–austenitic TRIP steels,” *Acta Mater.*, vol. 60, no. 17, pp. 6183–6199, Oct. 2012.
- [142] S. Zhang and K. O. Findley, “Quantitative assessment of the effects of microstructure on the stability of retained austenite in TRIP steels,” *Acta Mater.*, vol. 61, no. 6, pp. 1895–1903, Apr. 2013.
- [143] S. Zaefferer, J. Ohlert, and W. Bleck, “A study of microstructure, transformation mechanisms and correlation between microstructure and mechanical properties of a low alloyed TRIP steel,” *Acta Mater.*, vol. 52, no. 9, pp. 2765–2778, May 2004.
- [144] W. Bleck, “Proceedings of the International Conference on TRIP-Aided High Strength Ferrous Alloys,” 2002, p. 13.
- [145] A. Markfeld and A. Rosen, “The effect of reverted austenite on the plastic deformation of maraging steel,” *Mater. Sci. Eng.*, vol. 46, no. 2, pp. 151–157, Dec. 1980.
- [146] L. T. Shiang and C. M. Wayman, “Maraging behavior of an Fe-19.5Ni-5Mn alloy II: Evolution of reverse-transformed austenite during overaging,” *Metallography*, vol. 21, no. 4, pp. 425–451, 1988.
- [147] R. Schnitzer, R. Radis, M. Nöhler, M. Schober, R. Hochfellner, S. Zinner, E. Povoden-Karadeniz, E. Kozeschnik, and H. Leitner, “Reverted austenite in PH 13-8 Mo maraging steels,” *Mater. Chem. Phys.*, vol. 122, no. 1, pp. 138–145, 2010.
- [148] S. Hossein Nedjad, M. R. Movaghar Garabagh, M. Nili Ahmadabadi, and H. Shirazi, “Effect of further alloying on the microstructure and mechanical properties of an Fe–10Ni–5Mn maraging steel,” *Mater. Sci. Eng. A*, vol. 473, no. 1–2, pp. 249–253, 2008.
- [149] A. Shekhter, H. I. Aaronson, M. K. Miller, S. P. Ringer, and E. V. Pereloma, “Effect of aging and deformation on the microstructure and properties of Fe–Ni–Ti maraging steel,” *Metall. Mater. Trans. A*, vol. 35, no. 13, pp. 973–983, Mar. 2004.
- [150] Y. He, K. Yang, W. Sha, and D. J. Cleland, “Microstructure and mechanical properties of a 2000 MPa Co-free maraging steel after aging at 753 K,” *Metall. Mater. Trans. A*, vol. 35, no. 9, pp. 2747–2755, 2004.

References

- [151] Y. He, K. Yang, K. Liu, W. Sha, and Z. Guo, "Age hardening and mechanical properties of a 2400 MPa grade cobalt-free maraging steel," *Metall. Mater. Trans. A*, vol. 37, no. 4, pp. 1107–1116, 2006.
- [152] R. Schnitzer, G. A. Zickler, E. Lach, H. Clemens, S. Zinner, T. Lippmann, and H. Leitner, "Influence of reverted austenite on static and dynamic mechanical properties of a PH 13-8 Mo maraging steel," *Mater. Sci. Eng. A*, vol. 527, no. 7–8, pp. 2065–2070, 2010.
- [153] V. P. Vylezhnev, A. A. Sukhikh, V. G. Bragin, and S. A. Kokovyakina, "Mechanical properties of maraging N18K9M5T steel with residual and reverted austenite," *Phys. Met. Metallogr.*, vol. 75, p. 448, 1993.
- [154] D. Duchateau and M. Guttman, "An X-ray microanalysis study of the partition of manganese in 6 and 9% Mn cryogenic steels and its influence on the stability of austenite dispersed in a tempered martensitic matrix," *Acta Metall.*, vol. 29, no. 7, pp. 1291–1297, Jul. 1981.
- [155] G. N. Haidemenopoulos and A. N. Vasilakos, "On the thermodynamic stability of retained austenite in 4340 steel," *J. Alloys Compd.*, vol. 247, no. 1–2, pp. 128–133, Jan. 1997.
- [156] C. K. Syn, B. Fultz, and J. W. Morris, "Mechanical stability of retained austenite in tempered 9Ni steel," *Metall. Trans. A*, vol. 9, no. 11, pp. 1635–1640, Nov. 1978.
- [157] P. J. Jacques, F. Delannay, and J. Ladrière, "On the influence of interactions between phases on the mechanical stability of retained austenite in transformation-induced plasticity multiphase steels," *Metall. Mater. Trans. A*, vol. 32, no. 11, pp. 2759–2768, Nov. 2001.
- [158] J. Wang and S. Van Der Zwaag, "Stabilization mechanisms of retained austenite in transformation-induced plasticity steel," *Metall. Mater. Trans. A*, vol. 32, no. 6, pp. 1527–1539, Jun. 2001.
- [159] D. Q. Bai, A. Di Chiro, and S. Yue, "Stability of Retained Austenite in a Nb Microalloyed Mn-Si TRIP Steel," in *Materials Science Forum*, 1998, vol. 284–286, pp. 253–262.
- [160] J. A. Jiménez, M. Carsí, O. A. Ruano, and G. Frommeyer, "Effect of testing temperature and strain rate on the transformation behaviour of retained austenite in low-alloyed multiphase steel," *Mater. Sci. Eng. A*, vol. 508, no. 1–2, pp. 195–199, May 2009.
- [161] L. Samek, E. Moor, J. Penning, and B. C. Cooman, "Influence of alloying elements on the kinetics of strain-induced martensitic nucleation in low-alloy, multiphase high-strength steels," *Metall. Mater. Trans. A*, vol. 37, no. 1, pp. 109–124, Jan. 2006.

References

- [162] H. YANG and H. BHADESHIA, “Austenite grain size and the martensite-start temperature,” *Scr. Mater.*, vol. 60, no. 7, pp. 493–495, Apr. 2009.
- [163] E. Jimenez-Melero, N. H. van Dijk, L. Zhao, J. Sietsma, S. E. Offerman, J. P. Wright, and S. van der Zwaag, “Martensitic transformation of individual grains in low-alloyed TRIP steels,” *Scr. Mater.*, vol. 56, no. 5, pp. 421–424, Mar. 2007.
- [164] X. C. Xiong, B. Chen, M. X. Huang, J. F. Wang, and L. Wang, “The effect of morphology on the stability of retained austenite in a quenched and partitioned steel,” *Scr. Mater.*, vol. 68, no. 5, pp. 321–324, Mar. 2013.
- [165] I. B. Timokhina, P. D. Hodgson, and E. V. Pereloma, “Effect of microstructure on the stability of retained austenite in transformation-induced-plasticity steels,” *Metall. Mater. Trans. A*, vol. 35, no. 8, pp. 2331–2341, Aug. 2004.
- [166] P. Wang, N. Xiao, S. Lu, D. Li, and Y. Li, “Investigation of the mechanical stability of reversed austenite in 13%Cr–4%Ni martensitic stainless steel during the uniaxial tensile test,” *Mater. Sci. Eng. A*, vol. 586, pp. 292–300, Dec. 2013.
- [167] J. I. Suk, S. H. Hong, and S. W. Nam, “Crystallographic orientation relationships among η -Ni₃Ti precipitate, reverted austenite, and martensitic matrix in Fe-10Cr-10Ni-2W maraging alloy,” *Metall. Trans. A*, vol. 24, no. 12, pp. 2643–2652, Dec. 1993.
- [168] G. Brückner, J. Pospiech, I. Seidl, and G. Gottstein, “Orientation correlation during diffusional $\alpha \rightarrow \gamma$ phase transformation in a ferritic low carbon steel,” *Scr. Mater.*, vol. 44, no. 11, pp. 2635–2640, Jun. 2001.
- [169] K. Verbeken, L. Barbé, and D. Raabe, “Evaluation of the Crystallographic Orientation Relationships between FCC and BCC Phases in TRIP Steels,” *ISIJ Int.*, vol. 49, no. 10, pp. 1601–1609, 2009.
- [170] G. N. Haidemenopoulos and A. N. Vasilakos, “Modelling of austenite stability in low-alloy triple-phase steels,” *Steel Res.*, vol. 67, no. 11, pp. 513–519, 1995.
- [171] M.-M. Wang, C. C. Tasan, D. Ponge, A. Kostka, and D. Raabe, “Smaller is less stable: Size effects on twinning vs. transformation of reverted austenite in TRIP-maraging steels,” *Acta Mater.*, vol. 79, pp. 268–281, Oct. 2014.
- [172] X. Li and Z. Yin, “Reverted austenite during aging in 18Ni(350) maraging steel,” *Mater. Lett.*, vol. 24, no. 4, pp. 239–242, 1995.

References

- [173] A. Grajcar, "Morphological features of retained austenite in thermo-mechanically processed C-Mn-Si-Al-Nb-Ti multiphase steel," *J. Achiev. Mater. Manuf. Eng.*, vol. 39, no. 1, pp. 7–18, 2010.
- [174] G. Kurdjumov and G. Sachs, "Over the mechanisms of steel hardening," *Z. Phys.*, vol. 64, p. 325, 1930.
- [175] Y. Mishima, R. M. Horn, V. F. Zackay, and E. R. Parker, "Direct decomposition of austenite in two Fe-V-C alloys," *Metall. Trans. A*, vol. 11, no. 3, pp. 431–440, Mar. 1980.
- [176] Z. Nishiyama, "X-ray investigation of the mechanism of the transformation from face centered cubic lattice to body centered cubic," *Sci. Rep. Tohoku Univ.*, vol. 23, p. 638, 1934.
- [177] G. Wassermann, "Influence of the transformation of an irreversible Ni steel onto crystal orientation and tensile strength," *Arch. Eisenhüttenwes.*, vol. 16, p. 647, 1933.
- [178] W. Pitsch, "Der Orientierungszusammenhang zwischen Zementit und Austenit," *Acta Metall.*, vol. 10, no. 9, pp. 897–900, 1962.
- [179] L. Sandoval, H. M. Urbassek, and P. Entel, "The Bain versus Nishiyama–Wassermann path in the martensitic transformation of Fe," *New J. Phys.*, vol. 11, no. 10, p. 103027, Oct. 2009.
- [180] E. C. Bain, *Trans. AIME*, vol. 70, p. 25, 1924.
- [181] J. J. Jonas, Y. He, and S. Godet, "The possible role of partial dislocations in facilitating transformations of the Nishiyama–Wassermann type," *Scr. Mater.*, vol. 52, no. 3, pp. 175–179, Feb. 2005.
- [182] B. Verlinden, P. Bocher, E. Girault, and E. Aernoudt, "Austenite texture and bainite/austenite orientation relationships in TRIP steel," *Scr. Mater.*, vol. 45, no. 8, pp. 909–916, Oct. 2001.
- [183] D. Raabe, "Texture and microstructure evolution during cold rolling of a strip cast and of a hot rolled austenitic stainless steel," *Acta Mater.*, vol. 45, no. 3, pp. 1137–1151, Mar. 1997.
- [184] Y. Katz, H. Mathias, and S. Nadiv, "Mechanical stability of austenite in maraging steels," *Metall. Trans. A, Phys. Metall. Mater. Sci.*, vol. 14 A, no. 5, pp. 801–808, 1983.
- [185] J. I. Suk, S. H. Hong, and S. W. Nam, "The formation of twinned austenite in Fe₁₀Cr₁₀Ni₂W maraging steel," *Scr. Metall. Mater.*, vol. 25, no. 12, pp. 2651–2656, Dec. 1991.

References

- [186] L. T. Shiang and C. M. Wayman, "The formation of twinned Widmanstätten austenite," *Metallography*, vol. 18, no. 2, pp. 193–198, May 1985.
- [187] K. Ameyama, T. Maki, and I. Tamura, "Morphology and crystallographic feature of intragranular gamma phase in (alpha+ gamma) two phase stainless steel," *Nippon Kinzoku Gakkai-si*, vol. 50, no. 1, pp. 10–19, 1986.
- [188] B. B. He, M. X. Huang, Z. Y. Liang, A. H. W. Ngan, H. W. Luo, J. Shi, W. Q. Cao, and H. Dong, "Nanoindentation investigation on the mechanical stability of individual austenite grains in a medium-Mn transformation-induced plasticity steel," *Scr. Mater.*, vol. 69, no. 3, pp. 215–218, Aug. 2013.
- [189] J. J. Vlassak and W. D. Nix, "Measuring the elastic properties of anisotropic materials by means of indentation experiments," *J. Mech. Phys. Solids*, vol. 42, no. 8, pp. 1223–1245, Aug. 1994.
- [190] M. Karlsen, Ø. Grong, M. Søfferud, J. Hjelen, G. Rørvik, and R. Chiron, "Scanning Electron Microscopy/Electron Backscatter Diffraction–Based Observations of Martensite Variant Selection and Slip Plane Activity in Supermartensitic Stainless Steels during Plastic Deformation at Elevated, Ambient, and Subzero Temperatures," *Metall. Mater. Trans. A*, vol. 40, no. 2, pp. 310–320, Jan. 2009.
- [191] Y. You, C. Shang, L. Chen, and S. Subramanian, "Investigation on the crystallography of reverted structure and its effect on the properties of low carbon steel," *Mater. Sci. Eng. A*, vol. 546, pp. 111–118, Jun. 2012.
- [192] T. Hara, N. Maruyama, Y. Shinohara, H. Asahi, G. Shigesato, M. Sugiyama, and T. Koseki, "Abnormal α to γ Transformation Behavior of Steels with a Martensite and Bainite Microstructure at a Slow Reheating Rate," *ISIJ Int.*, vol. 49, no. 11, pp. 1792–1800, 2009.
- [193] M. R. Plichata and H. I. Aaronson, "Influence of Alloying Elements upon the Morphology of Austenite Formed From Martensite in Fe-C-X Alloys," *Metall. Trans.*, vol. 5, no. 12, p. 2611, 1974.
- [194] P. P. Sinha, D. Sivakumar, N. S. Babu, K. T. Tharian, and A. Natarajan, "Austenite reversion in 18 Ni Co-free maraging steel," *Steel Res.*, vol. 66, no. 11, pp. 490–494, 1995.
- [195] K. Hirano, M. Cohen, and B. . Averbach, "Diffusion of nickel into iron," *Acta Metall.*, vol. 9, no. 5, pp. 440–445, May 1961.
- [196] J. Speer, D. K. Matlock, B. C. De Cooman, and J. G. Schroth, "Carbon partitioning into austenite after martensite transformation," *Acta Mater.*, vol. 51, no. 9, pp. 2611–2622, May 2003.

References

- [197] R. W. K. Honeycombe and H. K. D. H. Bhadeshia, *Steels: Microstructure and Properties*. Oxford: Butterworth-Heinemann, 2006.
- [198] N. Hansen, "Hall–Petch relation and boundary strengthening," *Scr. Mater.*, vol. 51, no. 8, pp. 801–806, Oct. 2004.
- [199] A. H. Cottrell, "Theory of brittle fracture in steel and similar metals," *Trans. Metall. Soc. AIME*, vol. 212, 1958.
- [200] N. J. Petch, "The ductile-brittle transition in the fracture of α -iron: I," *Philos. Mag.*, vol. 3, no. 34, pp. 1089–1097, Oct. 1958.
- [201] A.A. Griffith, "The theory of rupture," in *Proc. 1st Int. Congr. Appl. Mech.*, 1924.
- [202] N. S. Stoloff, in *Fracture*, H. Liebowitz, Ed. New York: Academic Press, 1969.
- [203] Z. Guo, "The Limit of Strength and Toughness of Steel," University of California, Berkeley, 2001.
- [204] J. W. Morris, Z. Guo, C. R. Krenn, and Y.-H. Kim, "The limits of strength and toughness in steel," *ISIJ Int.*, vol. 41, no. 6, pp. 599–611.
- [205] Z. Guo, K. Sato, T. K. Lee, and J. W. Morris, "Ultrafine grain size through thermal treatment of lath martensitic steels," in *Ultrafine grained materials*, 2000.
- [206] B. Fultz, J. I. Kim, Y. H. Kim, and J. W. Morris, "The chemical composition of precipitated austenite in 9Ni steel," *Metall. Trans. A*, vol. 17, no. 6, pp. 967–972, Jun. 1986.
- [207] D. B. Williams and C. B. Carter, *Transmission Electron Microscopy*. New York: Springer Science, 2009.
- [208] C. Yang, S. Luo, and W. Yu, *GB: Retained austenite in steel-Quantitative determination-method of X-ray diffractometer*. Standardization Administration of the People's Republic of China, 2006.
- [209] W. Conshohocken, *ASTM Standard, Standard Practice for X-Ray Determination of Retained Austenite in Steel with Near Random Crystallographic Orientation* Standard E975-03, vol. 03, no. Reapproved 2008. American Society for Testing and Materials, 2003.
- [210] G. E. Dieter, *Mechanical Metallurgy*. NEW: New York: McGraw-Hill, 1986.
- [211] J. R. Cahoon, "An improved equation relating hardness to ultimate strength," *Metall. Trans.*, vol. 3, no. 11, p. 3040, 1972.

References

- [212] A. C. Fischer-Cripps, *Nanoindentation*. Springer New York, 2011.
- [213] Y. Matsuoka, T. Iwasaki, N. Nakada, T. Tsuchiyama, and S. Takaki, “Effect of Grain Size on Thermal and Mechanical Stability of Austenite in Metastable Austenitic Stainless Steel,” *ISIJ Int.*, vol. 53, no. 7, pp. 1224–1230, Aug. 2013.
- [214] H. Schumann, *Neue Hütte*, p. 12, 1970.
- [215] J. Martínez, S. M. Cotes, A. F. Cabrera, J. Desimoni, and A. Fernández Guillermet, “On the relative fraction of ϵ martensite in γ -Fe–Mn alloys,” *Mater. Sci. Eng. A*, vol. 408, no. 1–2, pp. 26–32, 2005.
- [216] P. Marinelli, A. Baruj, A. Fernández Guillermet, and M. Sade, “Lattice parameters of metastable structures in quenched Fe–Mn alloys. Part II: hcp phase,” *Zeitschrift fuer Met. Res. Adv. Tech.*, vol. 92, no. 5, pp. 489–493, 2001.
- [217] Y.-U. Heo, M. Takeguchi, K. Furuya, and H.-C. Lee, “Discontinuous coarsening behavior of Ni₂MnAl intermetallic compound during isothermal aging treatment of Fe–Mn–Ni–Al alloys,” *J. Electron Microsc. (Tokyo)*, vol. 59, no. S1, pp. S135–S140, 2010.
- [218] F. Moszner, A. S. Sologubenko, M. Schinhammer, C. Lerchbacher, A. C. Hänzi, H. Leitner, P. J. Uggowitzer, and J. F. Löffler, “Precipitation hardening of biodegradable Fe–Mn–Pd alloys,” *Acta Mater.*, vol. 59, no. 3, pp. 981–991, 2011.
- [219] J. Millán, S. Sandlöbes, A. Al-Zubi, T. Hickel, P. Choi, J. Neugebauer, D. Ponge, and D. Raabe, “Designing Heusler nanoprecipitates by elastic misfit stabilization in Fe–Mn maraging steels,” *Acta Mater.*, vol. 76, pp. 94–105, Sep. 2014.
- [220] A. J. Bradley and J. W. Rodgers, “The Crystal Structure of the Heusler Alloys,” *Proc. R. Soc. A Math. Phys. Eng. Sci.*, vol. 144, no. 852, pp. 340–359, Mar. 1934.
- [221] M. F. Ashby and L. M. Brown, “Diffraction contrast from spherically symmetrical coherency strains,” *Philos. Mag.*, vol. 8, no. 91, pp. 1083–1103, Jul. 1963.
- [222] W. Van den Broek, A. Rosenauer, B. Goris, G. T. Martinez, S. Bals, S. Van Aert, and D. Van Dyck, “Correction of non-linear thickness effects in HAADF STEM electron tomography,” *Ultramicroscopy*, vol. 116, pp. 8–12, May 2012.
- [223] A. V. Crewe, J. P. Langmore, and M. S. Isaacson, *Physical aspects of electron microscopy and microbeam analysis*. New York: Wiley, 1975.

References

- [224] A. . Ardell, “The effect of volume fraction on particle coarsening: theoretical considerations,” *Acta Metall.*, vol. 20, no. 1, pp. 61–71, Jan. 1972.
- [225] J. J. Hoyt, “On the steady-state particle size distributions during coarsening,” *Scr. Metall. Mater.*, vol. 24, no. 1, pp. 163–166, 1990.
- [226] M. Tokuyama and K. Kawazaki, “Statistical-mechanical theory of coarsening of spherical droplets,” *Phys. A Stat. Mech. its Appl.*, vol. 123, no. 2–3, pp. 386–411, Feb. 1984.
- [227] P. K. Rastogi and A. J. Ardell, “The coarsening behavior of the γ' precipitate in nickel-silicon alloys,” *Acta Metall.*, vol. 19, no. 4, pp. 321–330, Apr. 1971.
- [228] D. . Chellman and A. . Ardell, “The coarsening of γ' precipitates at large volume fractions,” *Acta Metall.*, vol. 22, no. 5, pp. 577–588, May 1974.
- [229] E. Clouet, L. Laé, T. Epicier, W. Lefebvre, M. Nastar, and A. Deschamps, “Complex precipitation pathways in multicomponent alloys,” *Nat. Mater.*, vol. 5, no. 6, pp. 482–8, Jun. 2006.
- [230] V. I. Elagin, V. V. Zakharov, S. G. Pavlenko, and T. D. Rostova, “Influence of Zirconium Additions on Ageing of Al-Sc Alloys,” *Phys. Met. Met.*, vol. 60, p. 88, 1985.
- [231] C. Fuller, J. Murray, and D. Seidman, “Temporal evolution of the nanostructure of Al(Sc,Zr) alloys: Part I – Chemical compositions of Al(ScZr) precipitates,” *Acta Mater.*, vol. 53, no. 20, pp. 5401–5413, Dec. 2005.
- [232] A. Tolley, V. Radmilovic, and U. Dahmen, “Segregation in Al₃(Sc,Zr) precipitates in Al–Sc–Zr alloys,” *Scr. Mater.*, vol. 52, no. 7, pp. 621–625, Apr. 2005.
- [233] B. Forbord, W. Lefebvre, F. Danoix, H. Hallem, and K. Marthinsen, “Three dimensional atom probe investigation on the formation of Al₃(Sc,Zr)-dispersoids in aluminium alloys,” *Scr. Mater.*, vol. 51, no. 4, pp. 333–337, Aug. 2004.
- [234] C. B. Fuller, “Temporal Evolution of the Microstructures of Al(Sc,Zr) Alloys and Their Influences on Mechanical Properties,” Northwestern University, 2003.
- [235] E. Clouet, “Séparation de Phase dans les Alliages Al-Zr-Sc: du Saut des Atomes à la Croissance de Précipités Ordonnés,” Feb. 2004.
- [236] S. R. Teixeira, P. H. Dionisio, E. F. da Silveria, F. L. Freire, W. H. Schreiner, and I. J. R. Baumvol, “Interdiffusion and reaction in the Fe□Al bilayer: I: Rutherford backscattering analysis of furnace-annealed samples,” *Mater. Sci. Eng.*, vol. 96, pp. 267–277, Dec. 1987.

References

- [237] V. P. Shapovalov and A. N. Kurasov, "Diffusion of titanium in iron," *Met. Sci. Heat Treat.*, vol. 17, no. 9, pp. 803–805, Sep. 1975.
- [238] K. Nohara and K. Hirano, "Diffusion of manganese into iron," in *Proc Int Conf Sci Technol Iron Steel*, 1970, p. 11.
- [239] F. . Buffington, K. Hirano, and M. Cohen, "Self diffusion in iron," *Acta Metall.*, vol. 9, no. 5, pp. 434–439, May 1961.
- [240] A. Takeuchi and A. Inoue, "Classification of Bulk Metallic Glasses by Atomic Size Difference, Heat of Mixing and Period of Constituent Elements and Its Application to Characterization of the Main Alloying Element," *Mater. Trans.*, vol. 46, no. 12, pp. 2817–2829, 2005.
- [241] K. Osamura, H. Okuda, K. Asano, M. Furusaka, K. Kishida, F. Kurosawa, and R. Uemori, "SANS Study of Phase Decomposition in Fe-Cu Alloy with Ni and Mn Addition.," *ISIJ Int.*, vol. 34, no. 4, pp. 346–354, May 1994.
- [242] C. Zhang and M. Enomoto, "Study of the influence of alloying elements on Cu precipitation in steel by non-classical nucleation theory," *Acta Mater.*, vol. 54, no. 16, pp. 4183–4191, Sep. 2006.
- [243] A. Seko, S. R. Nishitani, I. Tanaka, H. Adachi, and E. F. Fujita, "First-principles calculation on free energy of precipitate nucleation," *Calphad*, vol. 28, no. 2, pp. 173–176, Jun. 2004.
- [244] H. I. Aaronson and F. K. LeGoues, "An assessment of studies on homogeneous diffusional nucleation kinetics in binary metallic alloys," *Metall. Trans. A*, vol. 23, no. 7, pp. 1915–1945, Jul. 1992.
- [245] Q. Furnemont, M. Kempf, P. J. Jacques, M. Goken, and F. Delannay, "On the measurement of the nanohardness of the constitutive phases of TRIP-assisted multiphase steels," *Mater. Sci. Eng. A*, vol. 328, no. 1, pp. 26–32.
- [246] P. W. Hochanadel, C. V. Robino, G. R. Edwards, and M. J. Cieslak, "Heat treatment of investment cast PH 13-8 Mo stainless steel: Part I. Mechanical properties and microstructure," *Metall. Trans. A, Phys. Metall. Mater. Sci.*, vol. 25 A, no. 4, pp. 789–798, 1994.
- [247] J. M. Cloué, B. Viguier, and E. Andrieu, "Effect of the metallurgical variables on the yield stress of PH 13-08 steel," *Metall. Mater. Trans. A Phys. Metall. Mater. Sci.*, vol. 36, no. 10, pp. 2633–2639, 2005.
- [248] R. Ebeling and M. F. Ashby, "Dispersion hardening of copper single crystals," *Philos. Mag.*, vol. 13, no. 124, pp. 805–834, Apr. 1966.

References

- [249] W. D. Nix and H. Gao, "Indentation size effects in crystalline materials: A law for strain gradient plasticity," *J. Mech. Phys. Solids*, vol. 46, no. 3, pp. 411–425, Mar. 1998.
- [250] K. Durst, B. Backes, O. Franke, and M. Göken, "Indentation size effect in metallic materials: Modeling strength from pop-in to macroscopic hardness using geometrically necessary dislocations," *Acta Mater.*, vol. 54, no. 9, pp. 2547–2555, May 2006.
- [251] P. C. Wo and A. H. W. Ngan, "Investigation of slip transmission behavior across grain boundaries in polycrystalline Ni₃Al using nanoindentation," *J. Mater. Res.*, vol. 19, no. 1, pp. 189–201, 2004.
- [252] H. Mehrer, Ed., *Diffusion in Solid Metals and Alloys*, vol. 26. Berlin/Heidelberg: Springer-Verlag, 1990.
- [253] K. Ishida, "Calculation of the effect of alloying elements on the Ms temperature in steels," *J. Alloys Compd.*, vol. 220, no. 1–2, pp. 126–131, 1995.
- [254] J. Han, S.-J. Lee, J.-G. Jung, and Y.-K. Lee, "The effects of the initial martensite microstructure on the microstructure and tensile properties of intercritically annealed Fe–9Mn–0.05C steel," *Acta Mater.*, vol. 78, pp. 369–377, Oct. 2014.
- [255] T. Furukawa, H. Huang, and O. Matsumura, "Effects of carbon content on mechanical properties of 5%Mn steels exhibiting transformation induced plasticity," *Mater. Sci. Technol.*, vol. 10, no. 11, p. 964, Jul. 1994.
- [256] G. S. Ansell and F. J. Lenel, "Criteria for yielding of dispersion-strengthened alloys," *Acta Metall.*, vol. 8, no. 9, pp. 612–616, Sep. 1960.
- [257] G. S. Ansell, "Fine particle effect in dispersion-strengthening," *Acta Metall.*, vol. 9, no. 5, pp. 518–519, May 1961.

Appendix Crystallographic information of the phases in maraging steels

Phase	Formula	Crystal structure	Lattice parameter (nm)	Space group	Atomic position			
					Atom	X	Y	Z
α'	$\text{Fe}_{83.5}\text{Mn}_{16.5}$	bcc	a = 0.2884	$Im\bar{3}m$ (229)	Fe	0	0	0
					Mn	0	0	0
γ	$\text{Fe}_{65}\text{Mn}_{35}$	fcc	a = 0.3605	$Fm\bar{3}m$ (225)	Fe	0	0	0
					Mn	0	0	0
ε	$\text{Fe}_{83.5}\text{Mn}_{16.5}$	hexagonal	a = 0.2536	P63/mmc (194)	Fe	1/3	2/3	1/4
			c = 0.4089		Mn	1/3	2/3	1/4
η -NiAl	NiAl	B2	a = 0.2887	$Pm\bar{3}m$ (221)	Ni	0	0	0
					Al	1/2	1/2	1/2

Appendix

Appendix 1 (continued)

Phase	Formula	Crystal structure	Lattice parameter (nm)	Space group	Atomic position			
					Atom	X	Y	Z
Ni ₂ TiAl	Ni ₂ TiAl	L2 ₁	a = 0.585	<i>Fm</i> $\bar{3}$ <i>m</i> (225)	Al	0	0	0
					Ti	1/2	1/2	1/2
					Ni	1/4	1/4	1/4